THESE DE DOCTORAT DE

L'ÉCOLE CENTRALE DE NANTES
COMUE UNIVERSITE BRETAGNE LOIRE

ECOLE DOCTORALE N° 602
Sciences pour l'Ingénieur
Spécialité : *Mécanique des Solides, des Matériaux, des Structures et des Surfaces.*

Par
Laura OTER CARBONELL

Process-induced microstructure in industrial SMC compression: quantitative descriptive analysis and predictability of a state-of-the-art numerical model.

Thèse présentée et soutenue à Nantes, le 12 decembre 2018.
Unité de recherche : Institut de Recherche en Génie Civil et Mécanique.

Rapporteurs avant soutenance :

Pierre Dumont. Professeur. Institut National des Sciences Appliquées de Lyon.

Chung Hae Park. Professeur. Ecole Nationale Supérieure Mines Télécom Lille Douai.

Composition du Jury :

Suresh G. Advani. Professeur. University of Delaware.

Pierre Dumont. Professeur. Institut National des Sciences Appliquées de Lyon.

Président du jury :
Julien Férec. Professeur. Université de Bretagne Sud.

Patrice Laure. Directeur de Recherche CNRS. Université de Nice.

Chung Hae Park. Professeur. Ecole Nationale Supérieure Mines Télécom Lille Douai.

Luisa Rocha da Silva. Chargée de Recherche. Ecole Centrale de Nantes.

Directeur de thèse
Christophe Binetruy. Professeur. Ecole Centrale de Nantes.

Invité
Benedikt Eck. Dr. Composites Simulation Expert. Faurecia.

Process-induced microstructure in industrial SMC compression: quantitative descriptive analysis and predictability of a state-of-the-art numerical model.

Laura Oter Carbonell

Aknowledgements

I would like to begin by expressing my deepest appreciation to Faurecia for the opportunity to perform this thesis, and to all the members of the company I had the chance to work with, for considering me as just another collegue.

I would like to thank the Ecole Centrale de Nantes to trust me with the task of developping such a challenging and exciting work.

I would like to express my deepest, sincerest gratitude and appreciation to my thesis director, prof. C.Binetruy, for his continuous inconditional support, confidence, patience and undrestandign. And I would like to extend this same recognition to prof. S.Advani for all his support and motivation. Their guidance and inmense knowledge made me to grow in dimensions much further than the professional one. I would also like to include in this aknowledgement prof. S.Comas-Cardona for offering me his infinite wisdom whenever I needed it.

I would also like to thank all my collegues, many of whom I have the fortune of calling friends, for their invaluable help during my thesis work. Thank you for selflessly helping, listening and supporting at anytime. I will never forget the time we spent together.

Finally, my most sincere gratitude and love to my parents and my sister. And also thank you to those friends who have proved to be family. I would have never arrived here without you. I love you so much.

Contents

List of Figures

List of Tables

Chapter 1

Introduction.

Compression moulding is a popular processing technology for reactive polymers reinforced with long or continuous fibres in a composite material. While some compression processes give rise to little or no flow (as in continuous fibre reinforced prepregs), other cases involve moderate to large extent flow and deformation to transform the initial raw material into its final shape. This second situation is typical of the Sheet Moulding Compound (SMC) compression. One of the important characteristics of SMC is their unusual ability to flow in the mold as heat and pressure are applied. The SMC material is a prepreg manufactured as a sheet and processed by the so-called Compression Moulding process. Parts made from SMC material are molded using matched metal moulds. The SMC flows during compression moulding under the action of pressure and heat, and then polymerize to the mould cavity shape. The mechanical performance of the molded components is controlled by the final state of fiber orientation, degree of cure and the properties of the constituents. In theory, one optimize the part performance by steering process variables such as charge size, shape and location, mould temperature and closing speed, and cure time. The performance of a SMC components can be adjusted by mixing the proper required ratio of ingredients. The approximate composition by weight of a SMC is [5] [61] :

- Resin (25-35%), mostly unsaturated polyester, but vinylester are also used to improve chemical resistance and tensile strength
- Reinforcements (20-30%) to improve the mechanical properties and reduce shrinkage. Fibreglass is the most commonly used in bundles of several hundred of individual filaments, with fibre diameters ranging from 9 to 14 microns and lengths from 12 to 50 mm. An adapted sizing covers fiberglass to improve adhesion to resin. Sometimes hollow microspheres of glass are introduced to reduce the density and improve impact resistance. SMC coumpound made of carbon fibers have been developed. Nowadays, greener materials start to be used as reinforcement, like natural fibres, leading to more sustainable SMC materials.
- Catalyst (0.5 - 1.5%) to initiate the polymerization reaction. It controls gel, cure time and shelf-life.
- Low-profile additive (2-5%) to control the shrinkage of the polyester resin.
- Filler (40-65 %) to control the viscosity of the mixture and gloss surface on the final product, to reduce shrinkage and price, and to improve chemical resistance and physical properties. One of the most commonly used is calcium carbonate.
- Thickener (0.5-1.5%) to increase the viscosity of the moulding compound after maturation (M9), making the SMC compound easy to handle. The common thickeners used are the oxides and hydroxides of calcium and magnesium.

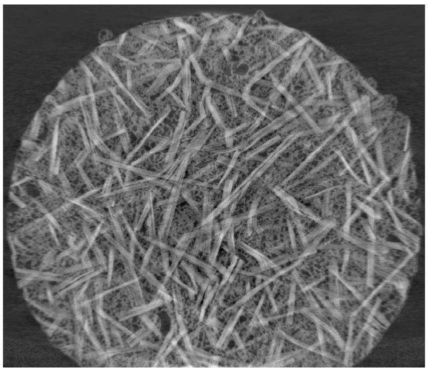

Figure 1.1: X-ray micro-tomograph scanner image of SMC material reinforced with glass fibres.

Figure 1.2: Structural automotive part. Courtesy of Faurecia.

- Release agent (0.5-2%) to ease the demoulding.
- Pigments (3-5%) to modify the colour of the moulding compound.
- Fire retardants (2-5%) to provide the moulding compound with self-extinguishing properties. The more commonly used are aluminium trihydrate (ATH).

In the following matrix will refer to the resin with all the above-mentioned additives, then the SMC compound is a mixture between matrix and the fibrous reinforcement.

Compression moulding of SMC is used in many applications in various industrial sectors like electrical and electronics, mass transportation, truck, buidling and construction, engineering but it is particularly popular in the automotive industry. As a matter of fact, the automotive industry fuelled the latest developments in SMC compression moulding. What makes SMC interesting for automotive applications are the good mechanical properties/weight ratio of SMC parts when compared to metallic materials, the short cycle time, high volume production, high freedom in design, high material usage rate and the level of automation that can be reached in the compression moulding process. Structural as well as semi-structural parts can be made out of SMC materials.

In the compression moulding process of SMC materials, a charge of the SMC compound is placed on the lower surface of a preheated mould of a hydraulic or mechanic press (Fig.1.3). The SMC material is usually provided in uncured continuous sheets of a thickness between 1 and 4 mm. Pieces of the sheets are cut forming strategic shapes, and then staked in a few layers, conforming what is called 'the charge'. The selection of charge size, weight, shape and placement is still today a matter of trial and error. The temperature of the surface of the mould is usually about 150 °C. The charge can cover from 30 up to 80% of the total surface of

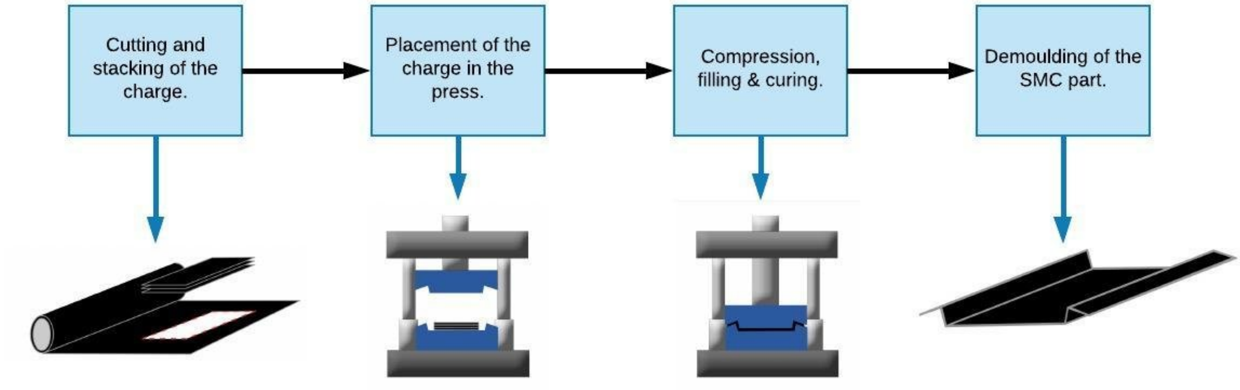

Figure 1.3: Schematic description of the SMC compression moulding process.

the bottom mould. The upper half of the mould is closed rapidly at a speed of between 1 to 10 mm/s, in an operation that lasts a few seconds. The compression performed by the press, united to the heating, forced the charge to flow inside the mould cavity. The reinforcing fibres of the charge are dragged by the resin and experience a change from their original configuration, initially considered as isotropic (no preferential direction of orientation of the reinforcement fibers), during the flow. The reinforcement fibres will end up oriented forming very different patterns, depending on the flow pattern of the polymer matrix in the mould.

A major need is to understand of how the flow affects the structural characteristics of moulded parts. It is a critical step in the processing-microstructure-property workflow of the composite part design. The shape and position of the charge is important in determining the possible generation of flow-induced defects (e.g. weld-lines), distribution of mechanical properties, and product stiffness and strength. The best mechanical properties of the produced part are found in the principal direction of orientation of the reinforcement fibres, but at the price of lowering the other directions. Therefore, being able to anticipate, or even control, the orientation of the reinforcement fibres in a SMC part constitutes a way to control its mechanical behaviour. Theoretical models have been developed to correlate the orientation of the reinforcement fibres with its mechanical behaviour (see [38], [60], [66]). Two well known models are the Tandon-Weng model, for unidirectionally aligned composites [81], and the Halpin-Tsai equations; a set of empirical relations developed by curve fitting. To model the evolution of the distribution of the reinforcement fibers with the flow, the current commercial packages use Folgar-Tucker's equation for the orientation of the reinforcement fibres [31]. It is an improvement of Jeffery's equation where a phenomenological term that tailors the kinetics of the *alignment* or *intensity of orientation* of the fibres, the latter being faster in Jeffery's model than in actual experiments. Jeffery's expression was first introduced for the motion of a single ellipsoidal particle moving in a viscous fluid in 1922 in [48]. Other outstanding works on fiber suspensions followed Jeffery's work, like Batchelor's [11], Cox and Brenner's [22] or Hinch and Leal's [42] [43]. Their simplicity when compared to the reinforcement structure of the SMC explain its shortcomings, although when considering the limit case of very slender ellipsoids, Jeffery's model gives reasonably good results when applied to real SMC problems in terms of intensity and directions of the orientation of the fibres. In 1984, Folgar and Tucker introduce in Jeffery's model their phenomenological term that represents the effect of the interaction between fibres, and adjust it to match their experimental results. The inconvenience of Folgar-Tucker's model is the necessity of adjusting the value of the term to each particular SMC material.

The adequate simulation of the squeeze flow along with the fibre orientation are the main concerns of manufacturing engineers [86]. The initial placement of the SMC charge in the mould for each particular part has a crucial influence on the final orientation of the reinforcement fibres and therefore, in the final mechanical properties of the part; as well, of course, on the productivity of the industrial process. For the time being, despite the support of a few commercial software packages, manufacturing engineers are still constrained to proceed by the 'trial and error' approach to find the optimal configuration of the SMC charge in the mould. A great amount of time and material resources could be saved with a software that can simulate realistically the SMC compression moulding process.

Besides the reorientation of the reinforcement fibres, there are many other phenomena involved in the compression moulding process. Other important issues in the computational modeling of SMC is the simulation of the complex flows and effects that appear in some features of SMC parts like ribs, welding lines, inserts or attachments. Here, some defects and undesirable characteristics, like segregation or air voids, may affect the characteristics of the final SMC part. Being able to reproduce in the model the factors that may trigger the occurrence of these defects is desirable. Among the listed factors, welding lines are critical because they cause poor mechanical properties in the direction normal to the welding line, since the reinforcement fibres tend to align parallel to them, reducing the resistance to traction and shear of the part in this zone. Being able to accurately predict the existence and the placement of the welding lines in the final part is another requirement for a good SMC compression simulation. Ribs in SMC parts, which are introduced to stiffen the part, are also a challenge for SMC models. The existence of the ribs in the part produces a complex behaviour of the reinforcement fibres. It is suspected that the flow of the SMC through ribs may be the origin of the fiber/matrix segregation, resulting in an anisotropy in the fibre concentration in the final part.

The modelling of the SMC compression is a complex task, especially if done at the micro-scale where all the details about the constituents and physics of the SMC material and the compression moulding process have to be described. So far, some rheological models have been developed, mostly based on phenomenological approaches, and at very different scales of description. They may be very complex, three-dimensional, and capable to describe the non-linearities of SMC behaviour, as in the work by Dumont et al. [29]. But this complexity becomes an issue when one has to implement them into commercial packages to assist the design of SMC parts and production processes. Then, these advanced and complex models become cumbersome and make the codes computationally very expensive and inefficient. As a consequence, the most popular models implemented in commercial packages to describe the squeeze flow of the SMC material rely on the well known Hele-Shaw [77] [52] or plug-flow model [46] [9] [47] [10] [25] for the fluid flow, along with the Jeffery's based model for the reorientation of the reinforcement fibres [31].

This work was achieved within the frame of the Faurecia Chaire at ECN and motivated by some issues experienced by design engineers in the company as they design a SMC part with one of these commercial packages. A benchmark conducted by the company evidenced some lacks in the current commercial packages to accurately model an SMC compression moulding process. Other authors have recently adressed the issue in [49] or [82]. The goal of this PhD study was then to:

- develop a 2D numerical model where the latest theoretical contributions to the SMC squeeze flow modelling are introduced,
- provide a new insight in some behaviours encountered in industrial-scale SMC compression and improve the fundamental understanding of this process
- validate the proposed numerical model experimentally.

Within the frame of this continuum (macro-scale) approach, it is possible to model the main features of the SMC rheology that, so far, have only been retrieved by scaling down the models

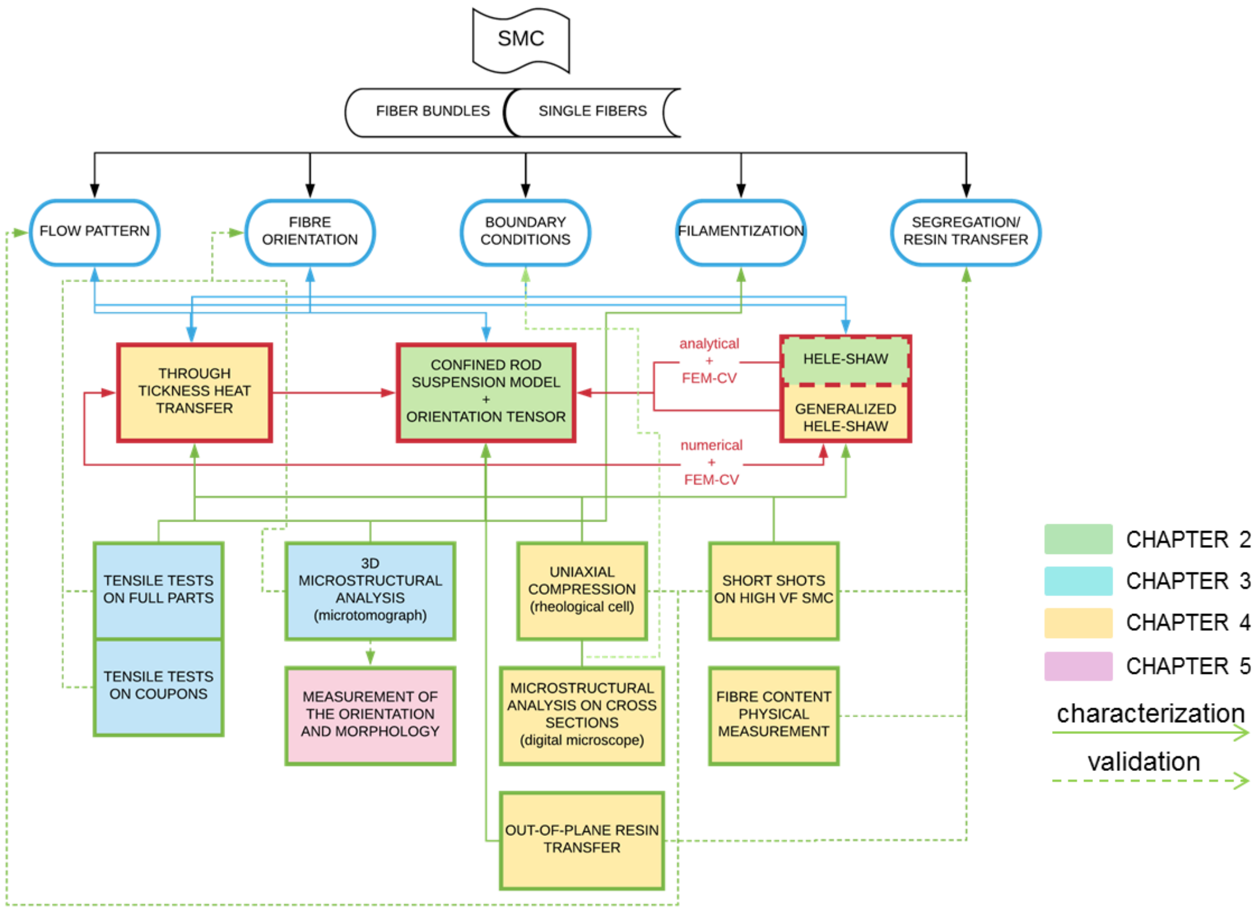

Figure 1.4: Organization of the work

(micro-scale approach). The desired features of the model to simulate complex shape parts with inserts are :

- to be robust to simulate 2D and 3D parts, even through a planar flow assumption,
- able to simulate transitions between a squeeze flow to a simple shear flow without losing mass (both types of flow can occur in the mould during the compression of SMC).

  To achieve this objective, this study is organized as described in Fig. 1.4 .

The overall organization of the work is presented in fig.1.4. The development of the proposed numerical model is presented in Chapter 2. Chapter 3 addresses the qualitative and quantitative validation of the model through various experimental techniques, at both the industrial- and Lab- scales, for different quantities of interest. The model developed in Chapter 2 is upgraded in Chapter 4 to simulate the non-isothermal compression. Chapter 5 focuses on the quantitative and critical comparison of fiber bundle orientation methods.

Chapter 2

2D isothermal numerical model.

As discussed in the introduction, one of the main motivation of this work is to build a SMC compression moulding simulation tool more adapted to the peculiarities of this process than what is proposed in the current commercial packages. The formulation on which the initial 2D code is based is presented in detail in this section. To start with, only flow in a thin flat section will be considered. The case of 3D geometries will be addressed in a second step.

2.0.1 General governing equations.

The general governing equations to describe the motion of fluids are a set of equations which include the mass conservation of the fluid, the conservation of the momentum (Navier-Stokes Eq.) and one last equation describing the conservation of the energy.

Navier-Stokes equations are coupled non-linear partial differential equations in four variables equations, what makes necessary to make some assumptions in order to simplify them and find the analytical solution. Reynold's Lubrication Theory in tandem with Navier-Stokes' continuity equation leads to the well known problem , representative of the squeeze flow of a composite material, that generates the so called Hele-Shaw model (see section 2.0.2 for the full development of the formulation).

The equation of continuity in a fluid domain free from sink effects, is defined by equation 2.1.

$$\frac{\partial \rho}{\partial t} + \nabla \cdot (\rho \mathbf{u}) = 0 \tag{2.1}$$

where ρ is the density of the fluid and $\mathbf{u}$ is the velocity of the fluid. We assume in the model that no mass of polymer matrix is lost during the squeeze process, and that the fluid is incompressible, that is to say, it's density remains constant. Therefore, equation 2.1 simplifies in

$$\nabla \cdot \mathbf{u} = 0 \tag{2.2}$$

which is the well-known equation of continuity for incompressible fluids. It will be used in the next subsection to simplify the momentum conservation equations in order to make them handier.

2.0.1.1 Momentum Conservation Equations.

The momentum conservation equations for a fluid in motion, in vectorial notation, read as in equation 2.3.

$$\rho \frac{D\mathbf{u}}{Dt} = -\nabla p + \nabla \cdot \tau + \mathbf{F} \tag{2.3}$$

where p is the pressure in the fluid, $\mathbf{F}$ are the body forces acting on the fluid and τ is the *viscous stress tensor* which, for a Newtonian fluid, displays as in linear expression 2.4.

$$\tau_{ij} = \lambda \left(\nabla \cdot \mathbf{u}\right) \delta_{ij} + \mu \dot{\gamma}_{ij} \tag{2.4}$$

$\dot{\gamma}$ being the *rate of strain tensor* (rate of change of shape of the material) and $\lambda = -\frac{2}{3}\mu$, where μ is the dynamic viscosity of the fluid.

Assuming the fluid incompressible, the continuity equation states that the divergence of the velocity is zero and, introducing 2.2 into 2.4, the components of the viscous stress tensor reduce to the ones in equation 2.5.

$$\tau_{ij} = \mu \dot{\gamma}_{ij} \tag{2.5}$$

$\dot{\gamma}$ can be obtained as the half of the symmetric part of the tensor gradient of velocity, so it can be expressed as in equation 2.6.

$$\dot{\gamma}_{ij} = \frac{1}{2}\left(u_{j,i} + u_{i,j}\right) \tag{2.6}$$

Taking 2.6 into account, the momentum conservation equations, for an incompressible Newtonian fluid, can be written as in equation 2.7.

$$\rho \frac{D\mathbf{u}}{Dt} = -\nabla p + \mu \nabla^2 \mathbf{u} + \mathbf{F} \tag{2.7}$$

Furthermore, due to the high viscosity and relatively small mass of SMC charges [1], inertia is usually neglected where a quasi-steady state is assumed at every instant. Then the left hand term in equation 2.7 can be discarded. Neglecting the body force, the final reduced form of the equation of motion is given by the well-known Stokes equation 2.8.

$$0 = -\nabla p + \mu \nabla^2 \mathbf{u} \tag{2.8}$$

Then the viscous forces developed by the incompressible material due to the pressure resulting from the mold closing, are the ones that drive the flow in this specific process.

2.0.2 Lubrication Theory.

There are physical peculiarities that have to be taken into account in order to make the equation of the conservation of the momentum more specific and analytically solvable to address the squeeze flow. The distribution of the velocity field in this specific fluid flow can be modelled by taking advantage of the Reynold's Lubrication Theory for viscous fluids. If so, one obtains the well known Hele-Shaw flow model [1], where the velocity vector at any location of the fluid domain is a function of the in-plane coordinates, but not of the out of plane one (see section 2.0.3).

In 1886, O.Reynolds described the effect of lubrication in the behaviour of viscous fluids between solid surfaces, studied the results given by the experiments of Mr.Tower on surfaces completely immersed in oil, and gave the so needed general laws for the phenomena in [73].

Reynolds adapted Navier-Stokes equation to the circumstances of Mr.Tower's experiments and integrated the expression, finding the mathematical relation between the pressure at the solid surfaces and the distribution of the velocity of the lubricating fluid (Fig.2.1).

The hypothesis formulated by Reynolds to deal with Navier-Stokes equation (which are, in consequence, the conditions to apply what would be the so on known as *Reynold's lubrication approximation*) concern, as well to the fluid of the model, as to the geometry of the domain and to the regime of the flow (Reynold's number of the flow). For a fluid to be susceptible to apply

Fig. 6.

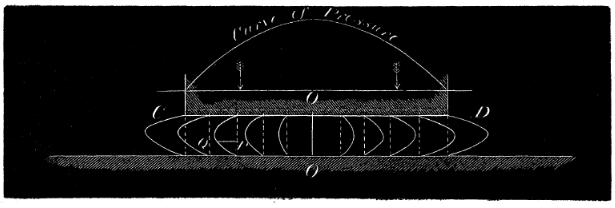

Case 3. *Parallel Surfaces approaching with Tangential Motion.*—The lines representing the motions in Cases 1 and 2 may be superimposed by adding the distances PQ in fig. 6 to the distances PN in fig. 5.

Figure 2.1: Reynolds,O. (1886). *On the theory of lubrication and its application to Mr.Beauchamps Tower's experiments, including an Experimental determination of the viscosity of olive oil.* Recovered from http://rstl.royalsocietypublishing.org

the lubrication approximation it needs to be viscous and incompressible, and it should be kept at isothermal conditions. For the geometry to fit the conditions, it should be such as that one of the dimensions (which will be called the gap) is orders of magnitude smaller than the other two and, if the gap is not constant over the geometry, at least it should vary smoothly. Finally, the flow have a Reynold's number below one, so that the viscous forces are the ones to drive the flow, not the inertial ones, and that there is no slip of the fluid in contact with the solid walls of the domain.

To be rightfully able to use the lubrication approximation, the conditions and elements that constitute the problem in hands must suit Reynolds' hypothesis. As just mentioned, the fluid has to be viscous and incompressible, which suits the initial assumptions here made. In addition, as pointed out in subsection 2.0.1.1, due to the high viscosity of SMC charges, the Reynolds' number of the fluid will not exceed the unitary value. Furthermore, no thermal coupling will be made in this model, and therefore, no influence of the temperature in the flow is allowed. In conclusion, for the fluid, the conditions of the lubrication approximation are met.

Regarding the geometry of the domain where the flow takes place in compression moulding of an SMC, we need to analyse the flow of a viscous fluid configured as a thin layer or a liquid film, confined in a very narrow gap between two solid walls. Usually, the thickness of the layer of SMC will be of the order of millimetres while the in-plane dimensions of the part will be of the order of meter. Again, the problem fits Reynold's conditions for the geometry aspect.

As extensively explained in [12], when the thickness of the layer is small enough compared to the other in-plane dimensions, large stresses due to the viscosity of the fluid arise, developing a large positive pressure between the solid bodies. As a consequence of the magnitude of the pressure, the confined fluid will rapidly flow through the gap of the cavity. The viscous forces are, consequently, the ones to steer the motion of the fluid in the mould, as required by the lubrication approximation.

To conclude, the lubrication approximation can be applied to the formulation of a simplified SMC squeeze flow problem.

Let's consider u,v and w to be the components of the velocity of the fluid, $\mathbf{u}$, in the x, y and z directions respectively, the direction z being parallel to the direction of the gap of the mould (the smaller dimension of the geometry) and the directions x and y being perpendicular to the gap (and further referred to as 'the in-plane' directions). Applying the hydrodynamic lubrication theory, the component w of the velocity of the fluid will be very small compared to the other two components, and so will be the variations of u and v in the in-plane directions. This is mathematically expressed as in 2.9.

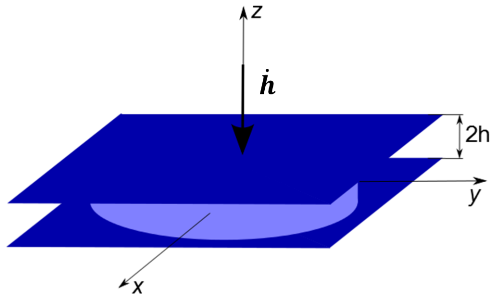

Figure 2.2: Geometry of the problem. Uni-axial load over parallel squared plates.

$$\begin{gathered}\frac{\partial u}{\partial z} \gg \frac{\partial u}{\partial x} \\ \frac{\partial u}{\partial z} \gg \frac{\partial u}{\partial y} \\ \frac{\partial v}{\partial z} \gg \frac{\partial v}{\partial x} \\ \frac{\partial v}{\partial z} \gg \frac{\partial v}{\partial y} \\ w \sim 0\end{gathered} \tag{2.9}$$

In the next subsection these conditions will be combined to the momentum equation to simplify it, in order to perform the analytical integration of Stokes' equation, and then to be able to obtain the equations that describe the velocity distribution of the flowing material. As will be seen, because of this manipulation of the equations, a full 3D flow can be translated into a 2D shell type flow, reducing the complexity of the formulation and the computational effort in the analysis of squeeze-flow problems.

This approach has been followed by Ghnatios, Chinesta and Binetruy in [34], in a study conducted to explore the potential of the lubrication approximation to model the consolidation of thermoplastics composite laminates. In that study, the use of the lubrication theory is shown to be of special interest for Newtonian and power-law monolayer resins, which is the frame of the fluid in this work.

2.0.3 Formulation of the theoretical velocity field.

To obtain the expression of the velocity field in the squeezed viscous material, the reference system introduced in section 2.0.2 is kept. Moreover the dimension of the gap will be referred as h.

It must be pointed out that, in a compression moulding process, the closure of the plates of the press can be performed in two different ways, depending on what parameter is more convenient to control: the closing speed or the applied pressure. The first option consists in closing the press by displacing the upper plate at a constant velocity and, consequently, the variation of the pressure in the fluid will not be constant. The second way to proceed would consist in closing the cavity of the mould by keeping the pressure applied by the plates in the fluid constant. In this case, it is the closing speed the parameter whose value will variate during the compression. Clearly, each one of this mechanics will generate a very different evolution of the velocity field in the time. In this case, it has been chosen to work with the first configuration, that is to say, with the plates moving at a constant velocity, which is usually referred to as *the squeeze rate*, and which is represented in this work as $\dot{h}$.

Using the Cartesian coordinate system, the 3 components of the Stokes equation 2.8 are :

$$\frac{\partial p}{\partial x} = \mu\left(\frac{\partial^2 u}{\partial x^2} + \frac{\partial^2 u}{\partial y^2} + \frac{\partial^2 u}{\partial z^2}\right)$$
$$\frac{\partial p}{\partial y} = \mu\left(\frac{\partial^2 v}{\partial x^2} + \frac{\partial^2 v}{\partial y^2} + \frac{\partial^2 v}{\partial z^2}\right)$$
$$\frac{\partial p}{\partial z} = \mu\left(\frac{\partial^2 w}{\partial x^2} + \frac{\partial^2 w}{\partial y^2} + \frac{\partial^2 w}{\partial z^2}\right) \tag{2.10}$$

While considering the assumptions stated above, the velocity gradients in the the x,y directions are smaller than the ones in the z direction. Then, only the shear stresses in the x-z and y-z planes are non negligible. In addition, the thickness of the SMC material is much smaller than the in-plane direction dimensions, hence the pressure in the z direction can be considered to be uniform. This results in the simplified model :

$$\frac{\partial p}{\partial x} = \mu\left(\frac{\partial^2 u}{\partial z^2}\right)$$
$$\frac{\partial p}{\partial y} = \mu\left(\frac{\partial^2 v}{\partial z^2}\right) \tag{2.11}$$

The resulting second order differential equations can now be easily adapted to the characteristics that a SMC domain (2.2) would have, to obtain the unknown velocity field.

In order to obtain the expression of the components of the velocity field of the flow, equations 2.11 are now integrated with respect to the z direction, which is the direction of the thickness of the gap of the mould. Equations 2.12 and 2.13 show the process of integration of the component of the velocity in the direction parallel to axis x. The process remains exactly the same for the other in-plane component.

$$\int \frac{\partial^2 u}{\partial z^2} dz = \int \frac{1}{\mu}\frac{\partial p}{\partial x} dz \tag{2.12}$$

$$\frac{\partial u}{\partial z} = \frac{1}{\mu}\frac{\partial p}{\partial x} z + C_1 \tag{2.13}$$

$$\int \frac{\partial u}{\partial z} dz = \int \left(\frac{1}{\mu}\frac{\partial p}{\partial x} z + C1\right) dz$$
$$u(x,z) = \frac{1}{2\mu}\frac{\partial p}{\partial x} z^2 + C_1 z + C_2 \tag{2.14}$$

The value of the integration constants C_1 and C_2 is then obtained by taking into account the non-slip condition of the fluid in contact with the boundary, to comply with the hydrodynamic lubrication hypothesis. Considering the origin of the reference system placed in the mid-plane of the mold gap, both components of the velocity in the in-plane directions need to be zero at $h/2$ and $-h/2$ ($u(z = h/2) = u(z = -h/2) = 0$). The system of equations that is obtained from the particularization of 2.14 to these conditions in the boundaries of the fluid with the plate is solved to get Eq. 2.15.

$$u\left(\frac{h}{2}\right) = 0 \rightarrow 0 = \frac{1}{2\mu}\frac{\partial p}{\partial x}\left(\frac{h}{2}\right)^2 + C_1\left(\frac{h}{2}\right) + C_2$$
$$u\left(-\frac{h}{2}\right) = 0 \rightarrow 0 = \frac{1}{2\mu}\frac{\partial p}{\partial x}\left(-\frac{h}{2}\right)^2 + C_1\left(-\frac{h}{2}\right) + C_2 \tag{2.15}$$

Solving this two equations system, the value of the integration constants is obtained.

$$C_1 = 0$$

$$C_2 = -\frac{1}{2\mu}\frac{\partial p}{\partial x}\left(\frac{h}{2}\right)^2$$

Finally, substituting these values on equation (2.14), the first component of the velocity field is obtained, being a function of the viscosity, the out-of-plane coordinate, the thickness of the gap and the gradient of pressure induced by the press, in the same in-plane direction as the integrated velocity component Eq. (2.16).

$$u(x, z) = \frac{1}{2\mu}\frac{\partial p}{\partial x}\left(z^2 - \left(\frac{h}{2}\right)^2\right) \tag{2.16}$$

The second in-plane component of the velocity field is obtained following the same derivation, and results in equation 2.17.

$$v(y, z) = \frac{1}{2\mu}\frac{\partial p}{\partial y}\left(z^2 - \left(\frac{h}{2}\right)^2\right) \tag{2.17}$$

These equations describe a parabolic-like profile of the velocity in the thickness of the flow, perfectly symmetrical to its mid-plane, giving a null value of the velocity of the fluid in the contact of the fluid with the mould. This is the same that assuming that there in no slip between the fluid and the walls of the mould, which is a hard assumption to make.

To completely determinate the value of the velocity field of the viscous fluid at each point of the fluid domain, it is necessary then, to find the local value of the gradient of the pressure distribution at each point of the fluid domain, which remains an unknown. In section 2.0.4, the expression of the gradient of pressure as a function of the squeeze rate is derived from the mass conservation principle. Since the value of the squeeze rate is a parameter of the compression moulding process, whose value is fixed a priori, this equation guarantees the complete definition of the velocity field.

2.0.4 Mass Conservation Equation.

As explained in the previous subsection, we need the expression of the continuity equation of the SMC flow to establish the way in which the value of pressure distribution and the velocity field of the fluid are related, so we can have complete knowledge of the evolution of the fluid domain.

Let's consider an infinitesimal volume in the viscous fluid that represents the polymer matrix of the SMC material, like the one we displayed in figure 2.3. As the flow proposed by Reynolds is planar ($w \sim 0$), the fluid will enter and leave this infinitesimal volume through the planes parallel to the xy plane, and will never cross the surfaces of the control volume parallels to the xy plane. Q_x and Q_y in the picture represent the flow rate incoming to the infinitesimal volume and Q'_x and Q'_y represent the out-going flow rate. The infinitesimal volume is being squeezed from its upper plane with a velocity $\dot{h}$, that is, at the squeeze rate.

Due to the assumption of incompressibility of the fluid that has been made, the flow trough the volume must verify the equation of balance 2.18, since there is no change in the density of the fluid inside the infinitesimal volume and no sink effects are possible.

$$Q_x dy + Q_y dx + \dot{h} dx dy - Q'_x dy - Q'_y dx = 0 \tag{2.18}$$

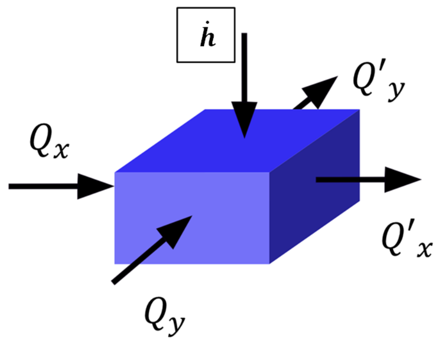

Figure 2.3: Infinitesimal volume of fluid representative of a squeeze flow problem.

Thinking in terms of volume, this equation describes how the volume of fluid that comes into the infinitesimal element during a certain period of time, leaves the element increased by the difference of volume that the element can hold at the beginning, and the volume that it can hold at the end of the period of time, after being squeezed constantly at the squeeze ratio.

Expressing the mass balance equation in this way as in 2.19 and operating on it, equation 2.20 is obtained.

$$Q_x dy + Q_y dx + \dot{h} dx dy - (Q_x + \frac{\partial Q_x}{\partial x} dx) dy - (Q_y + \frac{\partial Q_y}{\partial y} dy) dx = 0 \tag{2.19}$$

$$\dot{h} dx dy - \frac{\partial Q_x}{\partial x} dx dy - \frac{\partial Q_y}{\partial y} dy dx = 0$$

$$\dot{h} - \frac{\partial Q_x}{\partial x} - \frac{\partial Q_y}{\partial y} = 0 \tag{2.20}$$

The components of the flow ratio Q_x and Q_y can be expressed as a function of the gradients of the pressure distribution, from the integration of the expressions of the components of the velocity field, obtained in section 2.0.3, through the thickness of the gap of the mould, as is done in equation 2.21.

$$Q_x = \int_{-\frac{h}{2}}^{\frac{h}{2}} \frac{1}{2\mu} \frac{\partial p}{\partial x} \left(z^2 - \left(\frac{h}{2} \right)^2 \right) dz$$

$$Q_x = -\frac{h^3}{12\mu} \frac{\partial p}{\partial x} \tag{2.21}$$

And the component of the flow rate, as a function of the gradient of the pressure in the other in-plane direction, is obtained in similarly, obtaining equation 2.22.

$$Q_y = \int_{-\frac{h}{2}}^{\frac{h}{2}} \frac{1}{2\mu} \frac{\partial p}{\partial y} \left(z^2 - \left(\frac{h}{2} \right)^2 \right) dz$$

$$Q_y = -\frac{h^3}{12\mu} \frac{\partial p}{\partial y} \tag{2.22}$$

By substitution of the expressions of the flow rate as a function of the gradients of pressure in equations 2.21 and 2.22, into equation 2.20, we have the relation between the distribution of the pressure in the fluid domain and the squeeze ratio that is being applied all over the geometry of the domain (2.23). Being able to solve this equation means to be able to obtain the full velocity field of the fluid and so, to be able to describe the evolution of the fluid domain in time and to be able to describe the flow pattern of the fluid viscous charge in between the plates of the press through the process of compression moulding.

$$\dot{h} - \frac{\partial}{\partial x}(-\frac{h^3}{12\mu}\frac{\partial p}{\partial x}) - \frac{\partial}{\partial y}(-\frac{h^3}{12\mu}\frac{\partial p}{\partial y}) = 0$$
$$-\frac{h^3}{12\mu}(\frac{\partial^2 p}{\partial x^2} + \frac{\partial^2 p}{\partial y^2}) = \dot{h}$$
$$-\frac{h^3}{12\mu}\Delta p = \dot{h} \tag{2.23}$$

2.0.4.1 Boundary Conditions.

Equation 2.23 is a linear second order partial differential equation of elliptic character with two variables (Poisson's equation). To solve it, either analytically or numerically, boundary or initial conditions of the problem need to be defined. The physical domain in the problem is the closed cavity of the punch-die mould where the SMC charge flows.

In the region of the domain which is not covered with material, and at the flow front, the pressure is supposed to be zero (atmospheric pressure).

The known condition for the material that is in contact with the limits of the domain is the value of the derivative of the pressure normal to the mould walls. It has to be zero since the material cannot cross the walls, so there can be no gradient of the pressure in that direction, neither component of the velocity of the fluid.

At this stage the mathematical formulation of the problem does not explicitly give the evolution in time of the unknowns in the fluid domain. While an analytic solution of Eq. 2.23 completed by the above-mentioned boundary conditions is achievable in simple geometries, it is worth noting that a numerical solution suitable for more complex and realistic situations is preferred. It is developed in the next subsection.

2.0.5 Finite element resolution.

The Finite Element Method is the most popular numerical method for solving engineering problems due to its versatility [89]. The FEM methodology allows to formulate the problem as a series of algebraic equations which are solved simultaneously, instead of solving analytically the second order differential equation in 2.23 at every moment in time. The first step must be to discretize the continuous domain of the problem formed by an infinity of points, into a series of points where to obtain a local solution, so that the number of degrees of freedom of the problem is also reduced from infinity to a limited finite number. In the FEM framework, these points are called nodes, since they define a mesh that subdivides the geometrical domain of the problem. The mesh would be built by relating each node to its neighbours by means of a line.

The enclosure defined by the lines between each node and its neighbours is called element. The union of all the elements constitute an approximation of the initial geometry, that can be more or less accurate depending on the number of nodes considered, or depending on the size and shape of the defined elements. For example, let's define a geometry defined by a red circle inside a blue square and centred on it, like the one shown in figure 2.4. It can be discretized as a regular mesh of nodes defining triangular elements as shown in figure 2.5. The more the number of nodes chosen to discretize the domain, the smallest will be the triangular elements and the closer the discretized geometry will be to the real one. Of course, with the number of nodes also increases the richness of the solution, but so will the computational resources needed.

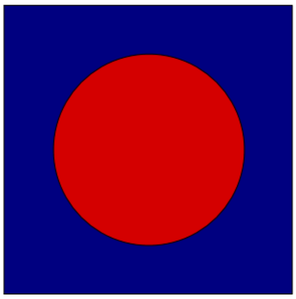

Figure 2.4: Initial geometry.

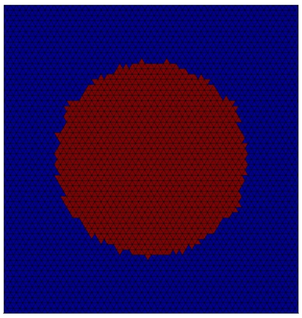

Figure 2.5: Discretized geometry.

As explained before, the value of the unknowns is evaluated at the nodes of the elements, leaving the distribution of its magnitude in the rest of the element to be interpolated. No need to say that the choice of an adequate interpolation function is of main importance; moreover, the quality of the results is very sensitive to it.

2.0.5.1 Geometry of the mesh.

The geometry presented in Fig.2.4 can be viewed as a simple square mould (represented by the blue part) where a round SMC charge (represented by the red part) has been placed in its centre.

The discretization into elements used to apply the FEM, allows to solve the problem to first predict the pressure field inside the material and then compute its velocity field.

The nodes of the resulting mesh will be the points where the pressure values are to be directly calculated by the algebraic system obtained through the variational formulation described in subsection 2.0.5.2. These nodes are distributed forming the shape of equilateral triangles of equal surface. Inside the elements, the value of the distribution of the pressure will be obtained by interpolation, using linear interpolation functions, as will be further explained, also in subsection 2.0.5.2.

The Finite Element Technique used follows the Eulerian approach, consequently, the mesh is stationary, although it would be possible to attach it to fixed points in the fluid to move with them, as in the Lagrangian approach. Even though both can be applied, the error generated by proceeding with the last approach would be very big due to the enormous deformations that would be suffered by the mesh, making it not suitable for fluid flows. It is in problems of solids, where displacements are small, where it is useful to be applied. In flow problems, the mesh is usually taken fixed and stationary, and the flow is transported through it. In the SMC compression moulding problem, the polymer fluid covers an increasing number of elements as it is squeezed by the press and as the gap of the mould becomes smaller, occupying elements of the mesh that were empty at the beginning.

At this point, we assume a quasi-steady state to deal with the change of cavity thickness.

The time dependence of the pressure is not present in equation 2.23 neither in equations 2.16 or 2.17. Therefore, we assume a state in which for each element, for each instant in time and for an instantaneous thickness of the gap, there are representative instantaneous values of pressure and velocity.

To solve for each mould closing state, a fixed thickness is assigned to every finite element. If the thickness of the SMC part to mould is uniform, the assigned thickness will be the same for all the elements. It is assumed to be constant during the whole compression. Therefore, the volume associated to each element changes at the same ratio than the thickness between time steps.

With respect to the boundary conditions, the squeeze flow describes a mix problem, since either Dirichlet conditions and Neumann conditions are present.

Dirichlet conditions are, in the FEM, those that assign a fixed value in a certain region of the domain. In this case, as discussed in section 2.0.4.1, they are set in the area of mould which is not covered with the SMC and at the flow front.

Neumann conditions consist in the restriction imposed to the derivative of the velocity in the region of the material in contact with the mould walls, to prevent the material to cross these limits.

2.0.5.2 Variational formulation.

.

As a previous step to apply the FEM, the Variational Methodology is applied to the initial formulation of the problem, called *strong formulation*, to obtain the *weak form* or *variational form* of equation 2.23, in order to reduce the order of the derivatives of the initial problem. This subsection exhibits the development of the weak solution of the elliptic problem.

Equation 2.23 can be written as follows.

$$\dot{h} = \nabla \cdot \left(\left(-\frac{h^3}{12\mu} \right) \nabla p \right) \tag{2.24}$$

The minimization of the residual of equation 2.24 when approximating the unknown function p by an approximation function of the form $p \simeq \hat{p} = \sum_{i=1}^{j} p_i N_i$, where p_i are the values of pressure at nodes, and N_i are a set of shape functions (to be defined), leads to equation 2.25.

$$\int_{\Omega} p^* \left[\nabla \cdot \left(\left(-\frac{h^3}{12\mu} \right) \nabla \hat{p} \right) - \dot{h} \right] d\Omega = 0 \tag{2.25}$$

where p^* is a weight function and Ω is the domain the integral is defined.

$$\int_{\Omega} p^* \left[\nabla \cdot \left(\left(-\frac{h^3}{12\mu} \right) \nabla \hat{p} \right) \right] d\Omega - \int_{\Omega} p^* \dot{h} d\Omega = 0 \tag{2.26}$$

Following of the variational methodology, the integral term on the left of equation 2.26 must be integrated by parts to obtain the weak form of the original equation, leading to Eq. 2.27.

$$\int_{\partial\Omega} p^* \left(\left(-\frac{h^3}{12\mu} \right) \nabla \hat{p} \right) \mathbf{n} \, d\partial\Omega - \int_{\Omega} \left[(\nabla p^*) \left(\left(-\frac{h^3}{12\mu} \right) \nabla \hat{p} \right) + p^* \dot{h} \right] d\Omega = 0 \tag{2.27}$$

where $\partial\Omega$ is the frontier of the domain. From the analysis of equation 2.27, it can be deduced that the integral term in the frontier of the domain can be neglected. On the one hand, the Dirichlet condition in the border of the fluid domain, forces the value of the pressure in there to be zero, as well as in the part of the domain which is not covered by fluid, and consequently, the value of the gradient of the pressure in this parts of the domain will be zero too. On the other hand, because of the Neumann condition in the frontier of the mould, the gradient of pressure in the direction perpendicular to the line of the frontier, that is given by vector **n**, must be zero to prevent the material to cross it. All in all, the integral of the gradient of pressure in the frontier of the domain can be removed from the equation, leading to Eq. 2.28.

$$\int_\Omega (\nabla p^*)\left(-\frac{h^3}{12\mu}\nabla\hat{p}\right)d\Omega = \int_\Omega p^*\dot{h}d\Omega \tag{2.28}$$

It has been already proposed to take as approximation to the unknown function, the one in equation 2.29, where p_j are the solutions of the distribution of pressure at the nodes in the mesh.

$$p \simeq \hat{p} = \sum_{j=1}^{3} p_j N_j \tag{2.29}$$

For the weight functions, we propose to take them as in expression 2.30.

$$p_i^* = N_i \tag{2.30}$$

Eq. 2.29 and Eq. 2.30 can be replaced into equation 2.28 to obtain equation 2.31.

$$\left(-\frac{h^3}{12\mu}\right)\int_\Omega \nabla N_i \nabla\left(\sum_{j=1}^{3} p_j N_j\right)d\Omega = \int_\Omega N_i\dot{h}d\Omega \tag{2.31}$$

Equation 2.31 can be rewritten into equation 2.32.

$$\left(-\frac{h^3}{12\mu}\right)\sum_{j=1}^{3}\left[\int_\Omega \nabla N_i \nabla N_j d\Omega\right] p_j = \int_\Omega N_i\dot{h}d\Omega \tag{2.32}$$

And equation 2.32 can be written in compact form as

$$\sum_{j=1}^{3} k_{ij}p_j = f_i \tag{2.33}$$

where

$$k_{ij} = \left(-\frac{h^3}{12\mu}\right)\int_\Omega \nabla N_i \nabla N_j d\Omega \tag{2.34}$$

$$f_i = \int_\Omega N_i\dot{h}d\Omega$$

Expression 2.34 represents the elements of the known *stiffness* matrix and, thanks to the property of additivity that it holds, it can be obtained for each element of the domain and then be assembled into a global matrix for the hole of the domain. This same property is maintained by the *vector of independent terms* $\mathbf{F} = (f_i)$.

An approximation, based on linear form functions to interpolate the values of the pressure inside each finite element, is proposed. At any point of the element, the value of the unknown function will be given by a linear combination of the value of pressure at the nodes in elements, according to equation 2.35, also illustrated in figure 2.7.

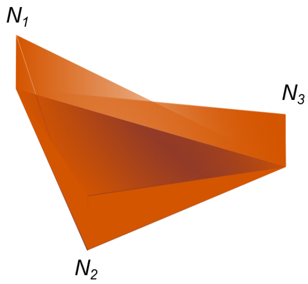

Figure 2.6: Linear form functions.

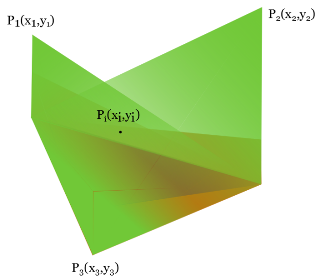

Figure 2.7: Value of the pressure in the nodes.

$$\hat{p}\,(x, y) = a + bx + cy \tag{2.35}$$

The pressure at the very same nodes of the elements can be expressed in the same way (see figure 2.7).

$$\hat{p}_i\,(x, y) = a + bx_i + cy_i \qquad i = 1, 2, 3 \tag{2.36}$$

Once the pressure at nodes is known, the value of the coefficients a, b and c is easily obtained by solving the linear system of equations 2.37.

$$\mathbf{p} = \begin{pmatrix} p_1 \\ p_2 \\ p_3 \end{pmatrix} = \begin{pmatrix} 1 & x_1 & y_1 \\ 1 & x_2 & y_2 \\ 1 & x_3 & y_3 \end{pmatrix} \begin{pmatrix} a \\ b \\ c \end{pmatrix} \tag{2.37}$$

Equivalent to the system 2.38.

$$\begin{pmatrix} a \\ b \\ c \end{pmatrix} = \begin{pmatrix} 1 & x_1 & y_1 \\ 1 & x_2 & y_2 \\ 1 & x_3 & y_3 \end{pmatrix}^{-1} \begin{pmatrix} p_1 \\ p_2 \\ p_3 \end{pmatrix} \tag{2.38}$$

Now, writing the relation 2.35 in matrix form like in 2.39 and using the linear system 2.38 to express the coefficients of the variables, expression 2.40 is obtained.

$$p\,(x, y) = \begin{pmatrix} 1 & x & y \end{pmatrix} \begin{pmatrix} a \\ b \\ c \end{pmatrix} \tag{2.39}$$

$$P\,(x, y) = \begin{pmatrix} 1 & x & y \end{pmatrix} \begin{pmatrix} 1 & x_1 & y_1 \\ 1 & x_2 & y_2 \\ 1 & x_3 & y_3 \end{pmatrix}^{-1} \begin{pmatrix} p_1 \\ p_2 \\ p_3 \end{pmatrix} \tag{2.40}$$

$$\mathbf{N} = \begin{pmatrix} N_1 & N_2 & N_3 \end{pmatrix} = \begin{pmatrix} 1 & x & y \end{pmatrix} \begin{pmatrix} 1 & x_1 & y_1 \\ 1 & x_2 & y_2 \\ 1 & x_3 & y_3 \end{pmatrix}^{-1} \tag{2.41}$$

In equation 2.40, the vector 2.41 configures the 'shape functions' of each element, which provides directly the value of the pressure at any point of the finite element, from the value of pressure at nodes. The shape functions are only dependent on the geometry of the finite elements, since they are obtained directly from the coordinates of the nodes of the element.

The derivatives of the shape functions with respect to x and y show that their spatial gradient is constant in all the element, as shown in 2.42 and 2.43.

$$\begin{pmatrix} \frac{\partial N_1}{\partial x} & \frac{\partial N_2}{\partial x} & \frac{\partial N_3}{\partial x} \end{pmatrix} = \begin{pmatrix} 0 & 1 & 0 \end{pmatrix} \begin{pmatrix} 1 & x_1 & y_1 \\ 1 & x_2 & y_2 \\ 1 & x_3 & y_3 \end{pmatrix}^{-1} \tag{2.42}$$

$$\begin{pmatrix} \frac{\partial N_1}{\partial y} & \frac{\partial N_2}{\partial y} & \frac{\partial N_3}{\partial y} \end{pmatrix} = \begin{pmatrix} 0 & 0 & 1 \end{pmatrix} \begin{pmatrix} 1 & x_1 & y_1 \\ 1 & x_2 & y_2 \\ 1 & x_3 & y_3 \end{pmatrix}^{-1} \tag{2.43}$$

From now on, the matrix of the gradient of the form functions will be referred to as B (2.44).

$$\mathbf{B} = \begin{pmatrix} \frac{\partial N_1}{\partial x} & \frac{\partial N_2}{\partial x} & \frac{\partial N_3}{\partial x} \\ \frac{\partial N_1}{\partial y} & \frac{\partial N_2}{\partial y} & \frac{\partial N_3}{\partial y} \end{pmatrix} \tag{2.44}$$

Now, the left hand side term of equation 2.32 can be rewritten in matrix form to get 2.45.

$$\left(-\frac{h^3}{12\mu}\right) \int_{y_1}^{y_2} \int_{x_1}^{x_2} \mathbf{B}^T \mathbf{I} \mathbf{B}\, \mathbf{p}\, dxdy \tag{2.45}$$

and

$$\left(-\frac{h^3}{12\mu}\right) \mathbf{B}^T \mathbf{I} \mathbf{B}\, \mathbf{p} \int_{y_1}^{y_2} \int_{x_1}^{x_2} dxdy = \left(-\frac{h^3}{12\mu}\right) \mathbf{B}^T \mathbf{I} \mathbf{B}\, \mathbf{p} A_e$$

The stiffness matrix of the element e can be expressed as in 2.46.

$$\mathbf{K}_e = \left(-\frac{h^3}{12\mu}\right) \mathbf{B}_e^T \mathbf{B}_e A_e \tag{2.46}$$

The right hand side term in Eq. 2.32 is obtained following the same procedure.

$$\mathbf{f}_e = \int_{y_1}^{y_2} \int_{x_1}^{x_2} \mathbf{N}\, \dot{h}\, dxdy$$

Now, when needed, the pressure gradients with respect to x and y can be easily obtained as in Eq. 2.47.

$$\nabla \mathbf{p} = \begin{pmatrix} \frac{\partial N_1}{\partial x} & \frac{\partial N_2}{\partial x} & \frac{\partial N_3}{\partial x} \\ \frac{\partial N_1}{\partial y} & \frac{\partial N_2}{\partial y} & \frac{\partial N_3}{\partial y} \end{pmatrix} \begin{pmatrix} p_1 \\ p_2 \\ p_3 \end{pmatrix} \tag{2.47}$$

$$
\begin{array}{cc}
 & \begin{matrix} & i-1 & i & i+1 & \\ & \downarrow & \downarrow & \downarrow & \end{matrix} \\
K_{glob} = & \begin{pmatrix} \cdots & \cdots & \cdots & \cdots & \cdots \\ \cdots & K^e_{11} & K^e_{12} & K^e_{13} & \cdots \\ \cdots & K^e_{21} & K^e_{22} & K^e_{23} & \cdots \\ \cdots & K^e_{31} & K^e_{32} & K^e_{33} & \cdots \\ \cdots & \cdots & \cdots & \cdots & \cdots \end{pmatrix} \begin{matrix} \\ \leftarrow i-1 \\ \leftarrow i \\ \leftarrow i+1 \\ \\ \end{matrix}
\end{array}
$$

Figure 2.8: Position of the nodes of the element e in the global stiffness matrix.

2.0.5.3 Assembly of the Stiffness Matrix.

All local matrices belonging to each element are now assembled into a global matrix which contains all the nodes that form the mesh. Therefore, the equivalent global linear system matrix will have as many rows and columns as nodes there are in the mesh. The elements of the local stiffness matrix need to be placed in the global matrix in the rows and columns whose number coincide with the numbers of the nodes of the finite element. That is to say, if the nodes of a given element of the mesh are numbered as $i-1$, i and $i+1$, then the components of the stiffness matrix of the element will be placed, in the global stiffness matrix of the mesh, in positions row $i-1$/column $i-1$, row $i-1$/column i, row $i-1$/column $i+1$, row i/column $i-1$, etc..., as shown in Eq.2.8. The numeration of the nodes will not be always correlative, since the same node belongs to more than one finite element.

$$\mathbf{K}_{glob}\,\mathbf{p}_{glob} = \mathbf{f}_{glob} \tag{2.48}$$

When the same node belongs to more than one element, a component of the local matrix of each of those elements will need to be placed in the very same position in the global matrix. In this case, due to the additivity property of the matrix, the values of this different components will be added and the result placed at the right position.

The last step before solving the linear system is to include the boundary conditions of the problem. For the Dirichlet boundary conditions, the pressure at the nodes of elements which do not contain any material during a given time step, is zero. Therefore, the components of the vector of pressure corresponding to these nodes will be forced to be zero. To avoid making the global matrix $\mathbf{K}_{glob}$ singular, in those elements of the stiffness matrix that multiply the elements of the vector of independent terms corresponding to the 'empty nodes', a unitary value is given.

Neumann boundary conditions are directly introduced in the formulation, so no further operations are needed to take them into account.

Once the boundary conditions are introduced, the system can be solved and the pressure at nodes are obtained. In the figure 2.9, the evolution of the distribution of pressure is displayed by a sequence of figures corresponding to different time sptes of the simulation of the compression process applied to the geometry proposed in subsection 2.0.5.1. For further clarity, the same sequence is reproduced in the figure **??**, where this time, the initial geometry of the sample is square instead of round.

From one step to another, the changing of the Dirichlet boundary conditions occurs in the following way: the press will close the mould cavity to reach a thickness of $\dot{h}\Delta t$, increasing the pressure in the SMC material, which will flow into the empty area of the mould cavity represented by elements that were empty during the previous time step. Now, to solve the linear system in a second time step, the new boundary conditions to introduce in the system depends on the new position of the flow front (the pressure needs to be forced to be zero in the nodes of the mesh that are 'empty'). Therefore, the new position of the flow front is needed at this point.

With equations 2.16 and 2.17, the velocity of the fluid at each element can be obtained from

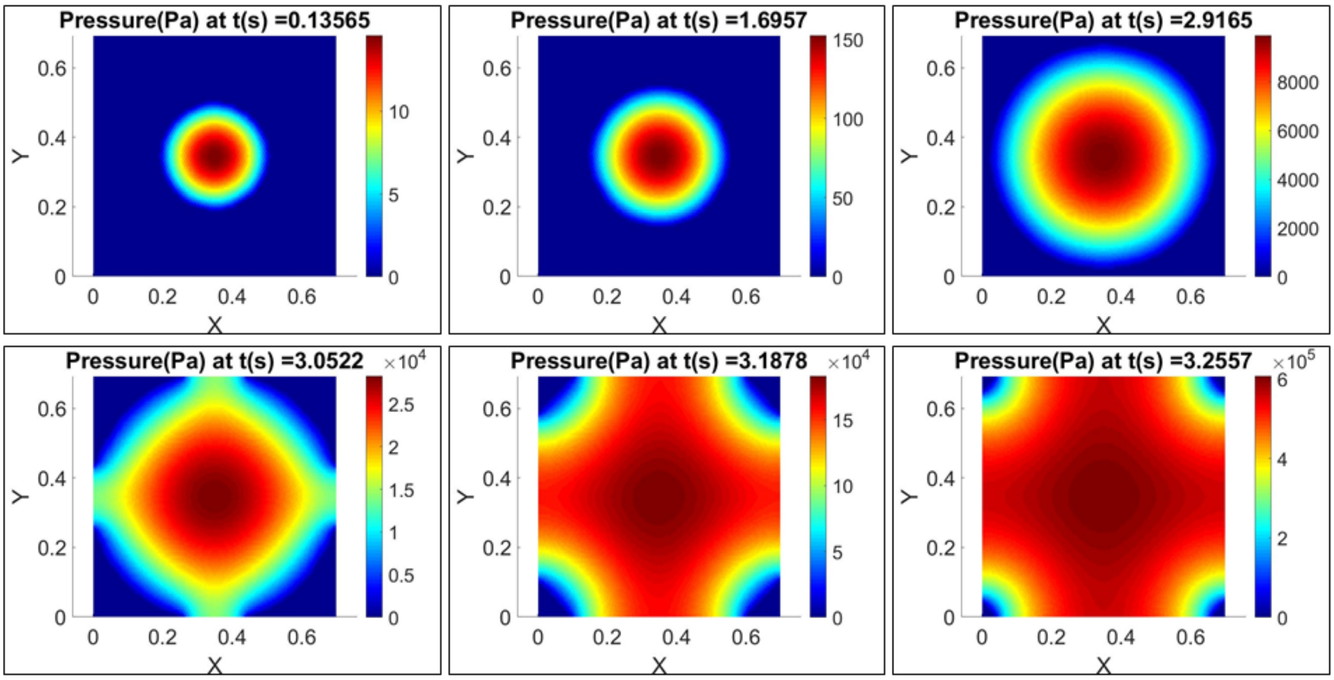

Figure 2.9: Round charge. Evolution of the pressure distribution during the compression process. Values in Pa.

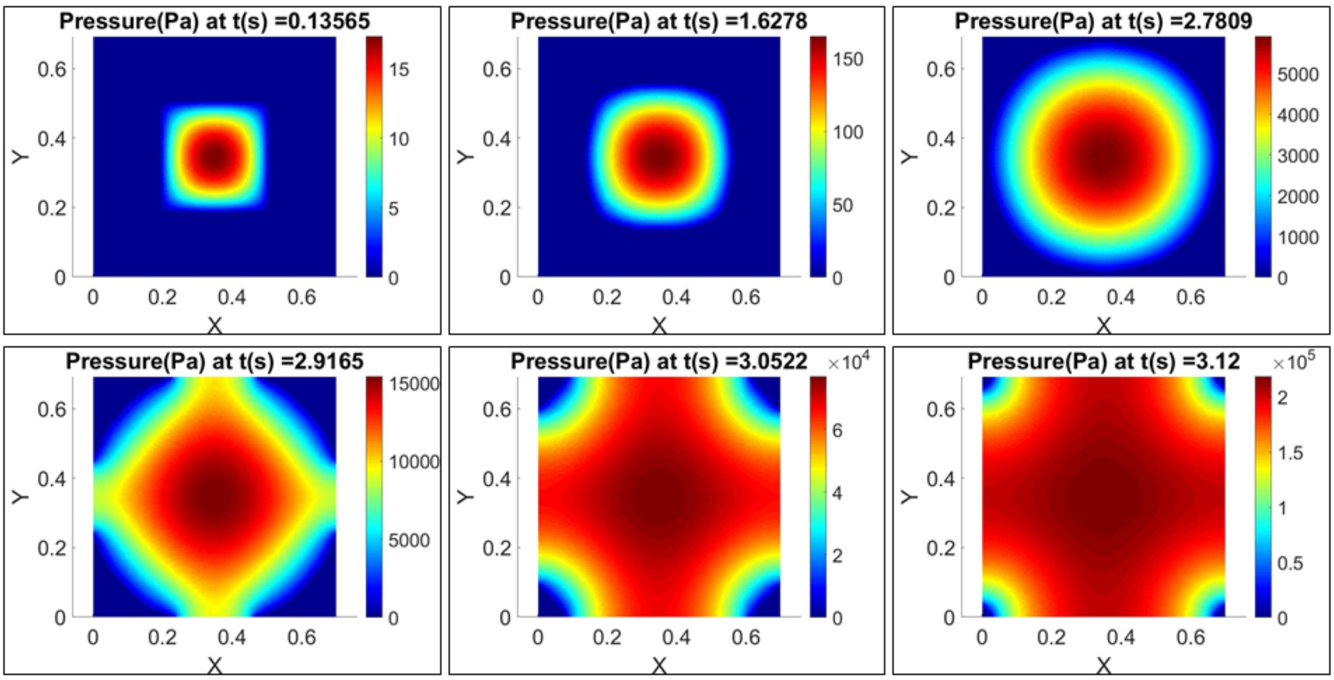

Figure 2.10: Square charge. Evolution of the pressure distribution during the compression process. Values in Pa.

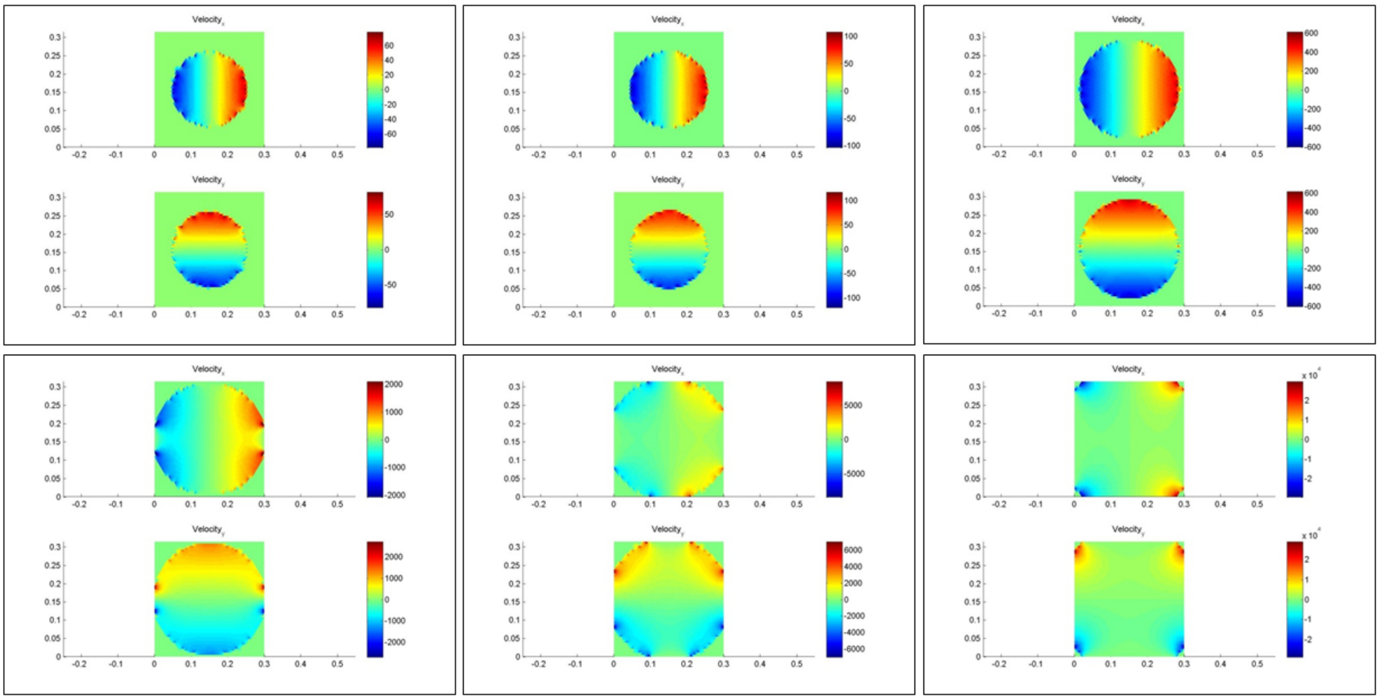

Figure 2.11: Evolution of the components of the velocity in the time steps 1, 11, 46, 58, 64, and 69. Values in m/s.

its value of the gradient of pressure, given by equation 2.50. Figure 2.11 shows the evolution of the components of the velocity of each element, at three different time steps.

Then, for each element, the rate at which the fluid is entering and leaving is known. So, at each time step, a balance of mass needs to be performed, always taking into account the change in the volume of the elements, whose thickness decreases due to the compression. This methodology is known as the *control-volume technique*. The process is illustrated in figure 2.12.

$$\mathbf{u}^e = \frac{h^2}{8\mu}\,\nabla\mathbf{p}^e \tag{2.49}$$

where

$$\nabla\mathbf{p}^e = \begin{pmatrix} \frac{\partial N_1^e}{\partial x} & \frac{\partial N_2^e}{\partial x} & \frac{\partial N_3^e}{\partial x} \\ \frac{\partial N_1^e}{\partial y} & \frac{\partial N_2^e}{\partial y} & \frac{\partial N_3^e}{\partial y} \end{pmatrix} \begin{pmatrix} p_1^e \\ p_2^e \\ p_3^e \end{pmatrix} \tag{2.50}$$

2.0.5.4 Control Volume method.

In order to perform the transport of fluid between the elements of the mesh, they are transformed into eulerian control volumes, where a mass balance is performed at each time step [4] [15] [53] [8]. For this purpose, two parameters are initially assigned to every element when the compression starts: the initial thickness of the element and the *fill factor*. Although the finite elements are two-dimensional, by assigning a value of thickness to each one of them, they can be associated with a certain storage volume, representative of a small space in the compression mould. They are called *control volumes* (CV) because they are used to control the space occupied by the flowing material at every instant of the compression process. The tracking of the fluid at the different elements is done by means of the fill factor; it takes a value between 0 and 1, indicating the percentage of volume of a CV that is filled with fluid (0 meaning that the CV is empty and 1 meaning that the CV is completely filled up).

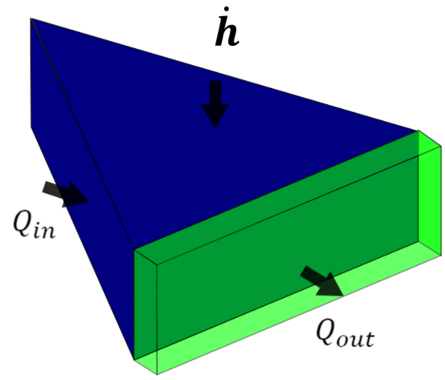

Figure 2.12: Representative control volume.

At the beginning of the compression stage, the SMC charge placed in the mould occupies a given space represented by certain CVs, to which a fill factor of 1 will be assigned, whereas the CV for the rest of the computational domain is 0. At each time step, the thickness h associated to each element decreases according to the squeeze ratio, of a quantity given by $\dot{h} \cdot dt$. The volume of material that the elements are able to store will also decrease, and the difference of volume between what was being stored and what can be hold in the next time step by the same element, will be redistributed between the downstream elements. This is achieved according to the direction of the flow, so that the total mass remains constant during the process and no mass is added. The fill factor of every CV is recalculated at each time step. The redistribution of the fluid between the elements will give the new position of the flow front at the end of the present time step. The position of the flow front is given by the elements whose fill factor is between 0 and 1 and have an empty CV as neighbour. The algebraic system 2.48 can be solved and the new pressure distribution can be obtained as initial conditions for the next time step.

This whole process is repeated until all the CVs are assigned with a value of fill factor of 1, that is, until all the elements are full and the mould is filled up with the SMC material. Figure 2.13 shows an example of *flow pattern* in the geometry that has been studied so far, through a sequence of figures corresponding to different time steps of the process.

The main weakness of this methodology arises when performing the mass balance in the control volumes, due to the choice of linear shape functions for the local distribution of the pressure. Because the velocity of the fluid at each element is a constant value at every point of the element, the variation of the velocity between elements is not continuous, and this discontinuity in the distribution of the velocity field leads to a loss of mass when computing a mass balance, since the volume of fluid leaving one element differs a little bit form the one entering its neighbour. This loss can be minimized by decreasing the size of elements and time steps.

Another problem can occur if the value of the time step is too large. If the value of the velocity of the material is such that it fills an element in less time than the current time step, the computation of pressure at the time step can give to unrealistic values. This issue is also avoided by adjusting the time stepping to the order of magnitude of the material velocity.

2.1 Validation in more complex 2D geometries

2.1.1 Convergent and divergent flow.

It has been proved that the proposed compression moulding fluid flow model works in a simple geometry. In this subsection a more complex situation is addressed where a rigid insert (obsta-

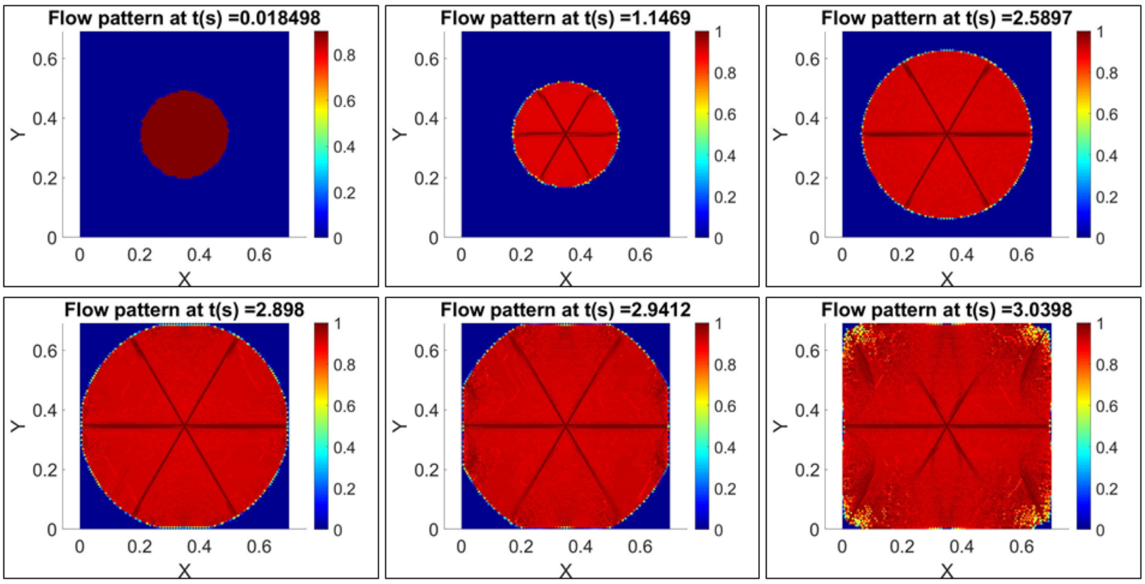

Figure 2.13: Evolution of the flow pattern during the compression phase.

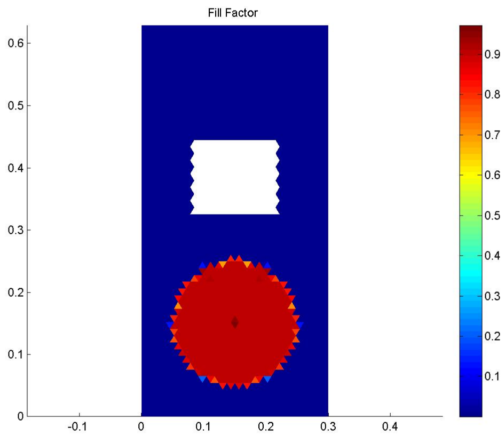

Figure 2.14: Rectangular geometry with inclusion.

cle) is placed inside the flow domain to give rise a divergent/convergent flow. The merging of two or more flow front leads to the so-called weld lines, that will create some weaker areas in the final part. For that purpose, the geometry shown in figure 2.14 has been defined accordingly.

In this geometry, a square rigid obstacle is located in the centre of the cavity; it is represented in the figure by the white square shaped void. A circular SMC charge, analogous to the one in the previous geometry, is placed inside the mould.

Progressive snapshots of the flow patterns is presented in figure 2.15 showing the effect of molding compound flowing around the insert. As explained in section 2.0.5.4, the flow pattern is represented by the evolution of the fill factor as the finite elements fill. The fill factor takes a zero value when the element is totally empty and a value of one when it is full. So, according to the color scale, the part of the domain in red represents the part of the mold covered with SMC at the corresponding time step. A small void or crack can result on the downstream side. The flow front adapts its shape to avoid the square insert. As expected, applying the same squeeze rate $\dot{h}$ as in the previous case, the flow front moves at the same velocity than in the squared geometry addressed in subsection 2.0.5.1, until it reaches the obstacle. Then, due to the reduction of the mould's cross-section while keeping a constant squeeze rate, the material speeds up till the obstacle is rounded and the initial cross-section available for the flow

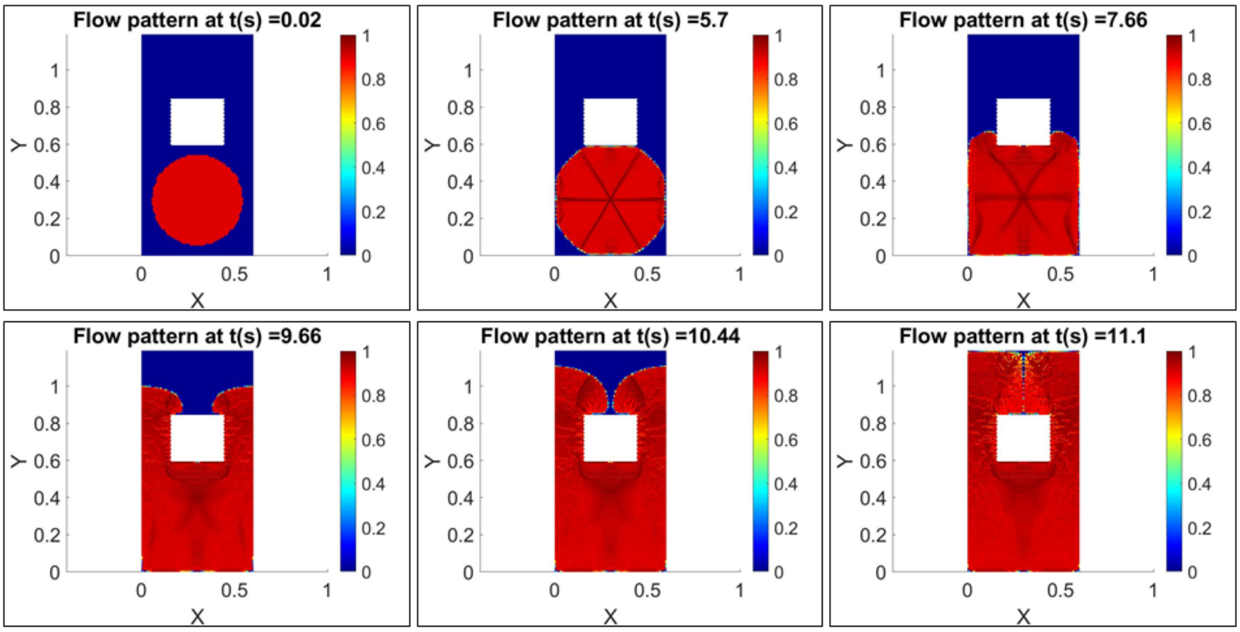

Figure 2.15: Evolution of the flow pattern during the compression phase.

is recovered. In that moment, the two flow fronts coming from each side of the inclusion merge to recover a smooth pattern.

2.1.2 Influence of the filling time.

One direct application of the FE model is to investigate the influence of the initial charge position and distribution to get a more robust process. Processing time can be saved by distributing the same volume of charge in a more optimal way. Of course, the benefit will grow with the size of the part. In this subsection, an example is given where a L-shaped mould is studied. Different initial configurations of the SMC charge are compared. In the first scenario, the charge is split in two parts, which are placed in the centre of each one of the branch of the mould. In the second scenario, the charge is placed in the interior angle of the mould, shaped itself like an L.

Figures 2.16 and 2.17 show that the second scenario results in a slightly longer filling time.

2.2 Three-dimensional geometries.

So far, a simple two dimensional geometry has been studied in order to simplify the understanding of the numerical model. Nevertheless, the same formulation can be applied to the analysis of more realistic three-dimensional geometries.

It is proposed to study the case of a punch-die cylindrical mould shown in figure 2.18. The mould is to be compressed from it's top, leaving a constant thickness gap between the two vertical walls. The SMC charge is circular with an initial diameter equal to the one of the upper base of the cylinder.

The interest of this specific geometry lies in testing the response of the model in the transition between a squeeze flow and a pure shear flow. These two flow modes are found in the proposed geometry when the fluid passes from the upper base, which is being compressed at a constant squeeze rate of value $\dot{h}$, to the vertical walls of the mould where, since no compression is applied and it's thickness remain constant, a pure shear flow profile is generated between the fix and moving vertical cylindrical walls.

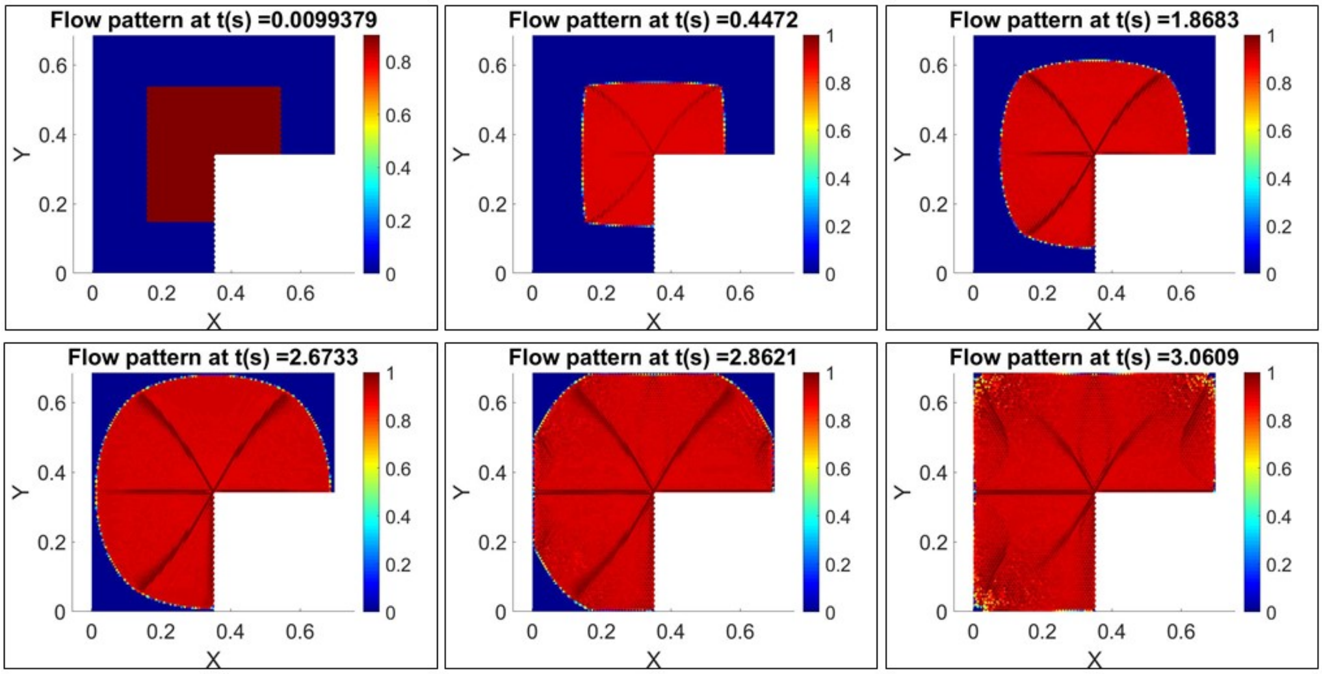

Figure 2.16: Comparative of the full filling times of a geometry with different initial configurations of the SMC charge.

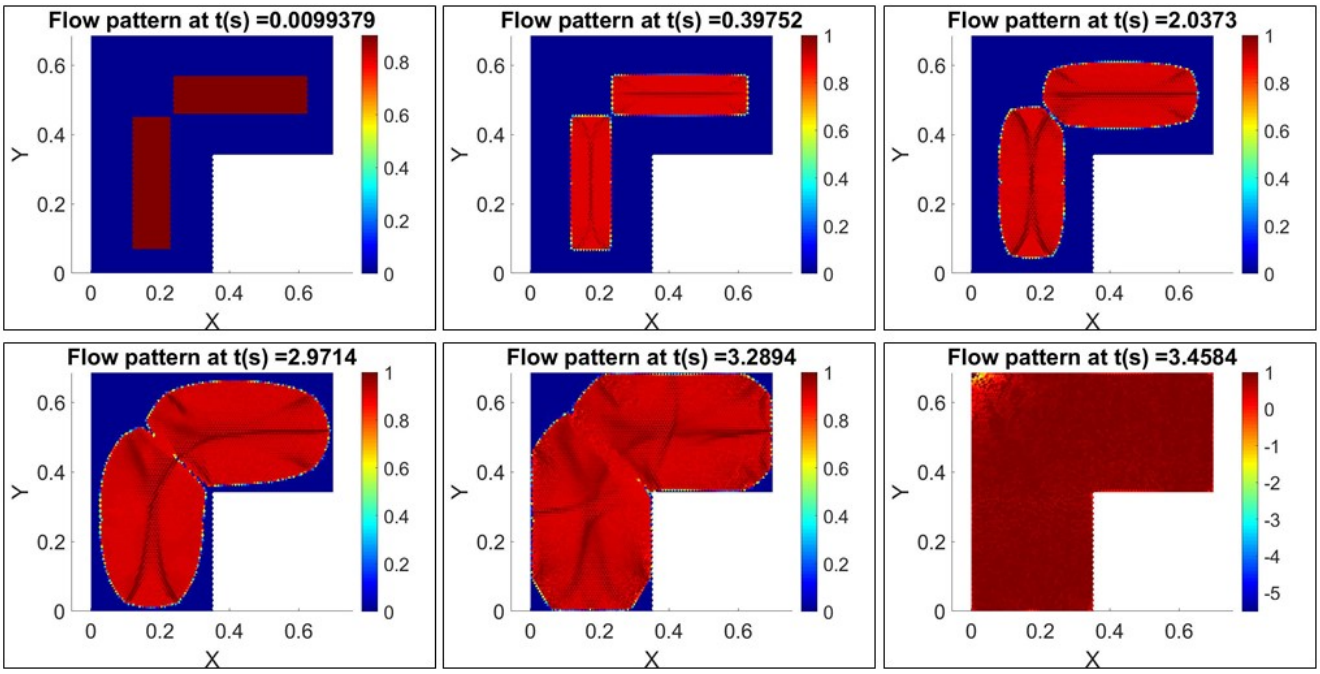

Figure 2.17: Comparative of the full filling times of a geometry with different initial configurations of the SMC charge.

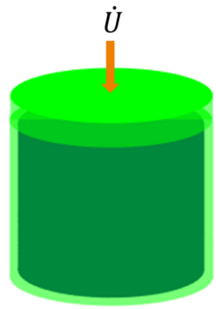

Figure 2.18: Cylindrical geometry for the estudy of a three-dimensional case.

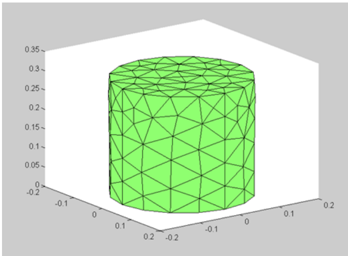

Figure 2.19: Discretization of the cylindrical geometry for the study of a three-dimensional case.

Due to the use of the lubrication approximation to obtain the current numerical flow the out-of-plane component of the velocity, in direction z, was neglected. The velocity vectors were described by two components, $\mathbf{u} = (u, v)$, the formulation for the pressure distribution does not involve the out-of-plane coordinate. However, in this new geometry the fluid flow will be defined in a three-dimensional space and a gradient of pressure in the z coordinate will appear, even if the flow remains planar (see figure 2.19). To face this problem, a local base can be defined for each finite element, on which to build the local algebraic two-dimensional system to obtain the distribution of the pressure, that afterwards can be translated to a global reference system to be assembled in the global matrix of the global linear system.

With the introduction of elements which are positioned out of the xy plane, a full three dimensional vector $\mathbf{u} = (u, v, w)$ is needed to define the velocity in those elements, even though the direction of this vector remains parallel to the plane of the element. Now, the in-plane velocity will be defined in reference to the individual element coordinate system, no longer with respect to the one of the full geometry. The motivation to define two coordinate systems (local and global) is to take advantage of the planar configuration of the flow at the scale of the element. The local reference system of each element is defined with the local plane $x'y'$ parallel to the plane of the element.

To obtain the variational formulation of that problem, the new shape functions and their derivatives will be defined in the local system of the element, and they will lead to a local stiffness system.

$$\mathbf{n}' = \begin{pmatrix} N_1' & N_2' & N_3' \end{pmatrix} = \begin{pmatrix} 1 & x' & y' \end{pmatrix} \begin{pmatrix} 1 & x_1' & y_1' \\ 1 & x_2' & y_2' \\ 1 & x_3' & y_3' \end{pmatrix}^{-1} \tag{2.51}$$

$$\mathbf{B}' = \begin{pmatrix} \frac{\partial N_1'}{\partial x'} & \frac{\partial N_2'}{\partial x'} & \frac{\partial N_3'}{\partial x'} \\ \frac{\partial N_1'}{\partial y'} & \frac{\partial N_2'}{\partial y'} & \frac{\partial N_3'}{\partial y'} \end{pmatrix} \tag{2.52}$$

$$\mathbf{K}'_e = \left(-\frac{h^3}{12\mu}\right)(\mathbf{B}')^T_e\mathbf{B}'_e A_e \tag{2.53}$$

$$\mathbf{K}'_e\,\mathbf{p}_e = \mathbf{f}'_e \tag{2.54}$$

To proceed to the ensemble of the local stiffness matrices in the global one, one may think in translating each local stiffness matrix into the global reference system, for all matrices to be expressed in the same basis. However, attention must be paid to the particular case of the problem in hands. In this case, the sought variable is a scalar one, whose its expression does not change in different bases. Moreover, it is affected by an isotropic differential operator and the transformation applied to it, consisting in a rotation of the axis, is an isometric one. In this case, it can be proved that the stiffness matrix of each element has the same expression in the local basis than in the global one, and no new change of basis is needed before the assembly of the local matrices into the global one.

$$\mathbf{K}^{e'} = \mathbf{K}^e \tag{2.55}$$

So the local stiffness matrices are directly assembled and the distribution of the pressure is obtained in the same way that in the two dimensional case.

To obtain the distribution of the velocity field, and since the gradient of the shape functions in the local reference system has already been obtained (equation 2.52), the local velocity vectors in each element can be directly calculated, to finally express them into the global reference system.

$$\nabla\mathbf{p}^{e'} = \begin{pmatrix} \frac{\partial N_1^{e'}}{\partial x'} & \frac{\partial N_2^{e'}}{\partial x'} & \frac{\partial N_3^{e'}}{\partial x'} \\ \frac{\partial N_1^{e'}}{\partial y'} & \frac{\partial N_2^{e'}}{\partial y'} & \frac{\partial N_3^{e'}}{\partial y'} \end{pmatrix} \begin{pmatrix} p_1^{e'} \\ p_2^{e'} \\ p_3^{e'} \end{pmatrix} \tag{2.56}$$

$$\mathbf{u}^{\mathbf{e}'} = \frac{h^2}{8\mu}\nabla\mathbf{p}^{e'} \tag{2.57}$$

Given the velocity field, the transport of mass is known for each time step by performing the mass balance at each element, as explained in subsection 2.0.5.3. The flow pattern can then be followed in the three-dimensional geometry, as shown in figure 2.20. In this example, a simulation has ben run on the described cylindrical geometry of dimensions: a base of 30 cm of radius and 30 cm of height. The initial charge has the same dimensions of the base and an initial thickness of 4 cm. The squeeze ratio for the simulation was fixed at 1 cm/s.

2.3 Orientation of the reinforcement fibres.

To introduce the reinforcement fibres in the SMC compression flow model, two different approaches can be followed: the discrete approach and the continuous approach. The discrete approach consists in a description of the evolution of the orientation of each individual fibre living in the fluid domain, while the continuous approach looks at the entire population of fibres from an statistical point of view, evaluating the probability of the fibres to be oriented in a certain direction. Due to the huge number of fibers in a typical SMC material, the use of the discrete approach to simulate industrial parts is intractable. In this work, the continuous approach is chosen as it is computationally more efficient and can still provide useful microstructural data for further analysis. The continuous approach, as just explained, is a statistical one, based on the description of the orientation of the population of fibres by means of their orientation probability distribution function, named *'pdf'* [13] [26] [41]. This pdf gives

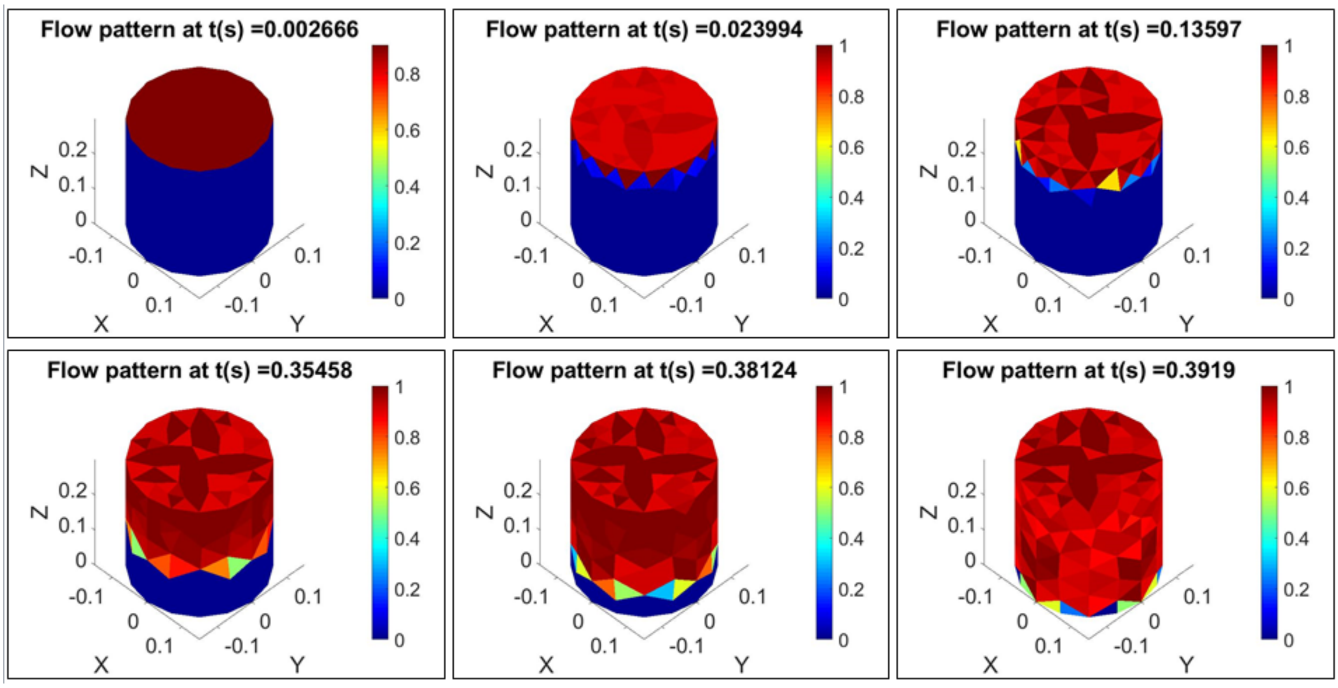

Figure 2.20: Evolution of the flow pattern during the compression process.

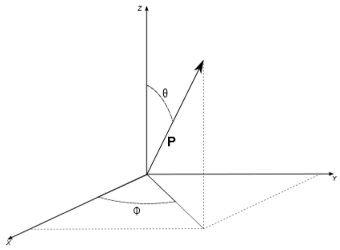

Figure 2.21: Directrion angles of the unitary vector $\mathbf{p}$.

the fraction of rods that, at a certain position $\mathbf{x}$, and at a certain moment t, are oriented in the direction of $\mathbf{p}$, where $\mathbf{p} = (p_x, p_y, p_z)$ is the unitary vector pointing in a direction defined by the in-plane angle θ and the out-of-plane angle ϕ (see figure 2.21).

$$
\begin{aligned}
p_x &= sin\theta cos\phi \\
p_y &= sin\theta sin\phi \\
p_z &= cos\theta
\end{aligned}
\tag{2.58}
$$

In other words, the pdf function allows to obtain the probability to find fibres that live in $\mathbf{x}$, in the moment $\mathbf{t}$, oriented in a specific range of directions, and it is obtained by integration of the pdf between the angles that describe this range. As any probability density function, it must fulfill the normalization condition, i.e., its integral over the entire space of definition of the pdf function S must be equal to one. It is equivalent to say that every fibre must have a specific orientation, so the integral over all possible orientations must be the unity.

$$\int_S \psi\left(\mathbf{x}, t, \mathbf{p}\right) d\mathbf{p} = 1 \qquad \forall \mathbf{x} \ \ \forall t \tag{2.59}$$

Considering physical requirements, the pdf must be a periodic function, since the orientation of a fibre directed like $\mathbf{p}$ is equivalent to the one of a fibre oriented like $-\mathbf{p}$, and so $\psi\left(\mathbf{x}, t, \mathbf{p}\right) = \psi\left(\mathbf{x}, t, -\mathbf{p}\right)$.

One must take into account that, in the case of the planar fluid flow model built in this work, the vector $\mathbf{p}$ must be bi-dimensional since it lives in the plane of the flow, and the pdf is a planar distribution function that must satisfy the same properties that the full tree-dimensional one. The simplification made to consider the orientation state as an in-plane one is pertinent due to the conditions of the SMC compression moulding process. In this process, fibres are much longer than the cavity thickness, and the possibility to rotate in the zenithal direction is very much limited; this issue will be more extensively discussed later on, when the model for *confined* fibres will be introduced, and in the next chapters.

However, despite the accuracy of the information given by the pdf, it is not in the appropriate form to use it in computationally demanding applications. Bearing this in mind, Advani and Tucker proposed in [2] for short fibres composites, the use of a set of moment tensors representative of the pdf, as a state variable that describes the instantaneous structure of orientation of fibres.

The tensors they propose, well known as *orientation tensors*, are obtained by integration of the product of the pdf with the successive dyadic products of the vector $\mathbf{p}$, over all the possible directions of orientation of the fibres, that conform a unit sphere referred to as S. Here so, the second order orientation tensor would be defined by equation 2.60.

$$\mathbf{a} = \int_S \mathbf{p} \otimes \mathbf{p} \, \psi \left(\mathbf{x}, t, \mathbf{p} \right) d\mathbf{p} \tag{2.60}$$

And the fourth order orientation tensor would be given by equation 2.61.

$$\mathbf{A} = \int_S \mathbf{p} \otimes \mathbf{p} \otimes \mathbf{p} \otimes \mathbf{p} \, \psi \left(\mathbf{x}, t, \mathbf{p} \right) d\mathbf{p} \tag{2.61}$$

Only even order tensors have been brought to attention because, as pointed out before, the pdf must be periodic and even, and that makes the integral of the odd-order dyadic products equal to zero.

This orientation tensors are symmetrical and their trace is unitary, due to the normalized distribution function and the unitary nature of the vector $\mathbf{p}$. The pdf function can be recovered from the the orientation tensors, developing a Fourier series of deviatoric versions of them.

Advani and Tucker prove also in [2] the appropriateness and accuracy of the orientation tensors to describe orientation states, by comparing the orientation distribution function recovered from a series comprising the second and fourth order orientation tensors, with experimentally obtained distribution functions. Furthermore, they provide the equation of the evolution of the orientation tensors as a function of the deformation of the fluid matrix.

2.3.1 Coupling of the orientation model with the flow model.

Due to their properties, the orientation tensors have been chosen to describe the evolution of the reinforcement structure in the SMC compression. As it will be extensively explained, they will be used as a representation of the population of fibres living in a certain finite element at a certain time step. They will also allow to describe the transportation of the orientation of the fibres between different elements at each time step.

In [48], Jeffery provides the equation that relates the evolution of the orientation of ellipsoidal particles to the deformation of the rate of deformation of the viscous fluid in which they are immersed. This work has been the starting point for many efforts to model the behaviour of slender bodies immersed in a viscous fluid.

$$\dot{\mathbf{p}}_i = \nabla \mathbf{v} \, \mathbf{p}_i - \left(\mathbf{p}_i^T \, \nabla \mathbf{v} \, \mathbf{p}_i \right) \mathbf{p}_i \qquad i = 1, ..., N \tag{2.62}$$

Chinesta derives this same equation in [17] considering of a rod particle with to beads at its ends (called a dumbell), immersed in a Newtonian fluid, submitted to hydrodynamic forces that depend on the difference of velocities between the fluid and the particle. He also describes the uspscaling process from the micro to the macro scale, to find the description of the evolution of the orientation tensors, providing the evolution process of reorientation of a population of fibres instead of a single particle.

Going back to the definition of the second order moment of the pdf function, its time derivatives are taken, obtaining equation 2.63.

$$\dot{\mathbf{a}} = \int_S \left(\dot{\mathbf{p}} \otimes \mathbf{p} + \mathbf{p} \otimes \dot{\mathbf{p}}\right) \psi d\mathbf{p} \tag{2.63}$$

Then, Jeffery's equation 2.62 can be substituted into 2.63, obtaining equation 2.64.

$$\frac{D\mathbf{a}}{Dt} = \mathbf{v} \cdot \nabla \mathbf{a} + \frac{\partial \mathbf{a}}{\partial t} = \nabla \mathbf{v}\ \mathbf{a} + \mathbf{a} \left(\nabla \mathbf{v}\right)^T - 2\ \mathbf{A} : \nabla \mathbf{v} \tag{2.64}$$

This equation allows to describe the time evolution of the orientation state of the population of fibres, in each finite element of the discretized domain. A closer look to equation 2.64 indicates that the instantaneous change of the velocity distribution will solely steer the reorientation of the reinforcement structure.

Attention must be paid to the fact that this equation requires a closure relation to express the fourth order moment of the pdf, $\mathbf{A}$, as a function of lower order moments. A common closure relation is the one given in equation 2.65, which will be used in this work [2] [63].

$$\mathbf{A} = \mathbf{a} \otimes \mathbf{a} \tag{2.65}$$

With this expression the update of the fibre orientation tensor in each element at each time step is straightforward in the two-dimensional case. The first element needed is the state of the orientation of the reinforcement structure at the beginning of the compression process, that is, the initial value of the second order orientation tensor $\mathbf{a}(t = 0)$. If an initial isotropic distribution of fibres is supposed, the initial orientation tensor, in a 2D domain, will have the form of equation 2.66.

$$\mathbf{a} = \begin{pmatrix} 0.5 & 0 \\ 0 & 0.5 \end{pmatrix} \tag{2.66}$$

Once it is identified, the gradient of velocity in the element $\nabla \mathbf{v}$, is obtained from the velocity field calculated as in subsection 2.0.5.3. Since linear shape functions are chosen to approximate the pressure, an uniform value of the orientation is obtained for each element; the velocity field is related to the pressure distribution by a spatial derivative in 2.16 and 2.17. Therefore, an unrealistic discontinuity in velocity is introduced between neighbour elements for the purpose of discretization in finite elements. This issue improved by refining the size of the finite mesh.

To circumvent the issue of constant velocity in each element, one can estimate a velocity gradient by comparing the velocity inside a given element to the ones of its neighbours. The more realistic local velocity of the element will be in between the computed one and the ones of its neighbours. The proposed solution consists in calculating the value of the velocity at each node of the finite mesh, by averaging the value of the velocities of the fluid in each element to which the node belongs, weighted by the area of the corresponding element. Now, three different values of velocity can be assigned to each element, and an actual gradient of velocity can be obtained on it, and the orientation tensor on the element too.

Finally, the closure relation is obtained by performing the dyadic product of the initial orientation tensor. All in all, the instantaneous variation of the second order orientation tensor,

$\dot{\mathbf{a}}$, can be obtained for every finite element. Given a time step Δt sufficiently small, the value of the second order orientation tensor in the time step $t+1$ will be obtained as $\mathbf{a}_{t+1} = \mathbf{a}_t + \dot{\mathbf{a}}\,\Delta t$.

At this point, the local variation of the second order orientation tensor, due to the variation of the evolution of the velocity field, has been obtained.

However, while the velocity field is changing throughout a time step, and the fibres at each finite element are changing their orientation, flow occurs and fibres coming from its neighbours are entering the element, whereas some fibres leave it. The population of fibres that enters the element modifies the orientation structure given in their original element. Their orientation is still described by the orientation tensor of the element they come from, and they will not have time to reorientate in the present time step. As well, there will be a fraction of fibres leaving the element during the time step to the element downstream, which will have assigned its orientation tensor. In few words, the transportation of the fibres by the flow means a 'transportation of the orientation tensors', that makes that, at the end of each time step, the value of the local orientation tensor in an element be not only the one given by Jeffery's equation, but a combination of this one with the one from the upstream elements .

The orientation balance proposed in equation 2.67 gives the value of the second order orientation tensor for each element at the end of the time step, that will be one to initialize the next time step.

$$\mathbf{a}'^{e}_{t+1} = \mathbf{a}^{e}_{t+1}\frac{V^{e}_{t+1}}{V_{tot}} + \mathbf{a}^{i}_{t+1}\frac{V^{i\to e}}{V_{tot}} - \mathbf{a}^{e}_{t+1}\frac{V^{e\to k}}{V_{tot}} \qquad i=1,2 \;\; k=1,2. \tag{2.67}$$

where $\mathbf{a}^{e}_{t+1}$ is the orientation tensor predicted with Jeffery's model, for the element e, in the current time step, $\mathbf{a}^{i}_{t+1}$ is the same orientation tensor but for the elements upstream from the element e, and V_{tot} is given by equation 2.68.

$$V_{tot} = V^{e}_{t+1} + V^{i\to e} - V^{e\to k} \qquad i=1,2 \;\; k=1,2. \tag{2.68}$$

where V^{e}_{t+1} is the volume of fluid in the element at the current time step $t+1$, $V^{i\to e}$ is the incoming volume to the element e from the upstream element i, and $V^{e\to k}$ is the outgoing volume from the element e towards the downstream element k. The indexes i and k can only take the values of 1 or 2 because the finite elements where chosen to be triangular, and, therefore, each element can receive material from up to two neighbour elements and can also supply material up to two elements.

In order to analyse the outputs of the orientation model, an adequate representation of the orientation tensors is needed. Hermans et al. propose in [40] a scalar parameter that measures the strength of orientation for axisymetric distribution functions, but that cannot be extended to other types of distributions [14]. Another scalar parameter used to represent the strength of the orientation in terms of the invariants of the second order orientation tensor is given in equation 2.69 [3].

$$f = 1 - \alpha det \mid a_{ij} \mid \tag{2.69}$$

Where α must be 4 for planar orientation states. The drawback of the parameter f is that it gives no clue about the direction of orientation.

It is also very common to directly represent the evolution of the eigenvalues of the orientation tensor in time. It gives the deviation of the principal directions of the orientation with respect to the principal direction of the flow.

Nevertheless, the most descriptive representation of the second order orientation tensors is, most likely, the well known 'orientation ellipsoid'. It is also defined from the eigenvalues and eigenvectors of the orientation tensor. The eigenvalues of the tensor indicate the length of the ellipsoid axis, and the eigenvectors describe the direction in which the axis are to be oriented.

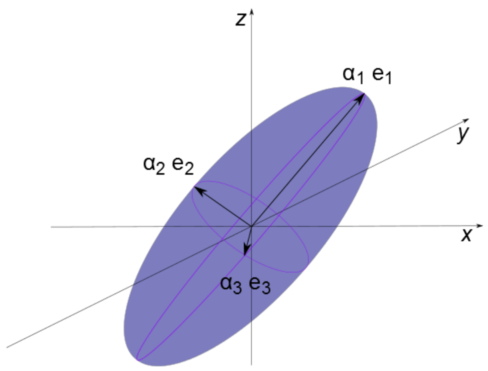

Figure 2.22: Orientation ellipsoid.

Thus, what the orientation ellipsoid illustrates is the proportion of fibres that are aligned in the direction of the axis of the ellipsoid. It is a very visual and intuitive representation of the orientation tensor. Eg., if the egienvalues of a given orientation tensor are $\alpha = (\alpha_1, \alpha_2, \alpha_3)$ and its eigenvectors are $\mathbf{e} = (\mathbf{e}_1, \mathbf{e}_2, \mathbf{e}_3)$, its associated orientation ellipsoid would be the one shown in figure 2.22.

Of course, in two dimensions, the projection of the ellipsoid in the planar flow becomes an ellipse.

Figure 2.23 shows the evolution of the orientation state in 2D by ellipses in the simple circular sample squeezed inside the square mould of dimensions 70x70 cm, being the initial radius of the charge of 15 cm and its initial thickness of 4 cm. The squeeze rate was set at 0.115 cm/s. As explained before, each orientation ellipse describes the population of fibres of a finite element, so there will be as many orientation ellipses as elements representing the SMC material. If the initial distribution of fibres is supposed to be isotropic, as it is almost the case, the ellipse will initially look like a circle, as it is shown in the first image of the sequence presented in figure 2.23. As the flow front advances, fibres start to orientate parallel to the flow front, as expected. As the oriented fraction of fibres increases, the orientation ellipses become more and more elongated as shown in the picture. When the flow front reaches the mould edges, they remain parallel to them. Since the chosen geometry is axisymetric, it is the same for the orientation structure. Irregularities visible in the picture are due to the triangular shape of the finite elements, that influence the advance of the flow.

2.3.2 Confined model.

Jeffery's model describes the kinematics of a single ellipsoidal particle immersed in a Newtonian fluid, where its movement is not affected by the presence of some outer factors like other fibres. In compression moulding processes, the reality couldn't be more different. Classical SMC material can have about 20% vol. of fibres, and high performance SMC can reach 40% vol. SMC material are actually concentrated suspension, and not dilute suspension addressed by Jeffery. Dinh and Armstrong developed a constitutive equation describing the rheology of semi-concentrated suspensions [24], based on the work by Batchelor [11].

One of the most popular model for concentrated suspensions is the one proposed by Folgar and Tucker in [31]. They model the interaction between fibres by introducing a rotary diffusion term in Jeffery's orientation model that contemplates, from a statistical approach, the interaction between fibres and the change in the orientation kinematics that it produces. Attempts have been made afterwords to improve the accuracy of Folgar-Tucker's diffusion term to specific cases, like in [65], where Phelps and Tucker modify it to better suit the orientation description in long-fibre thermoplastics, or in [69], where Ranganathan and Advani find a proportional-

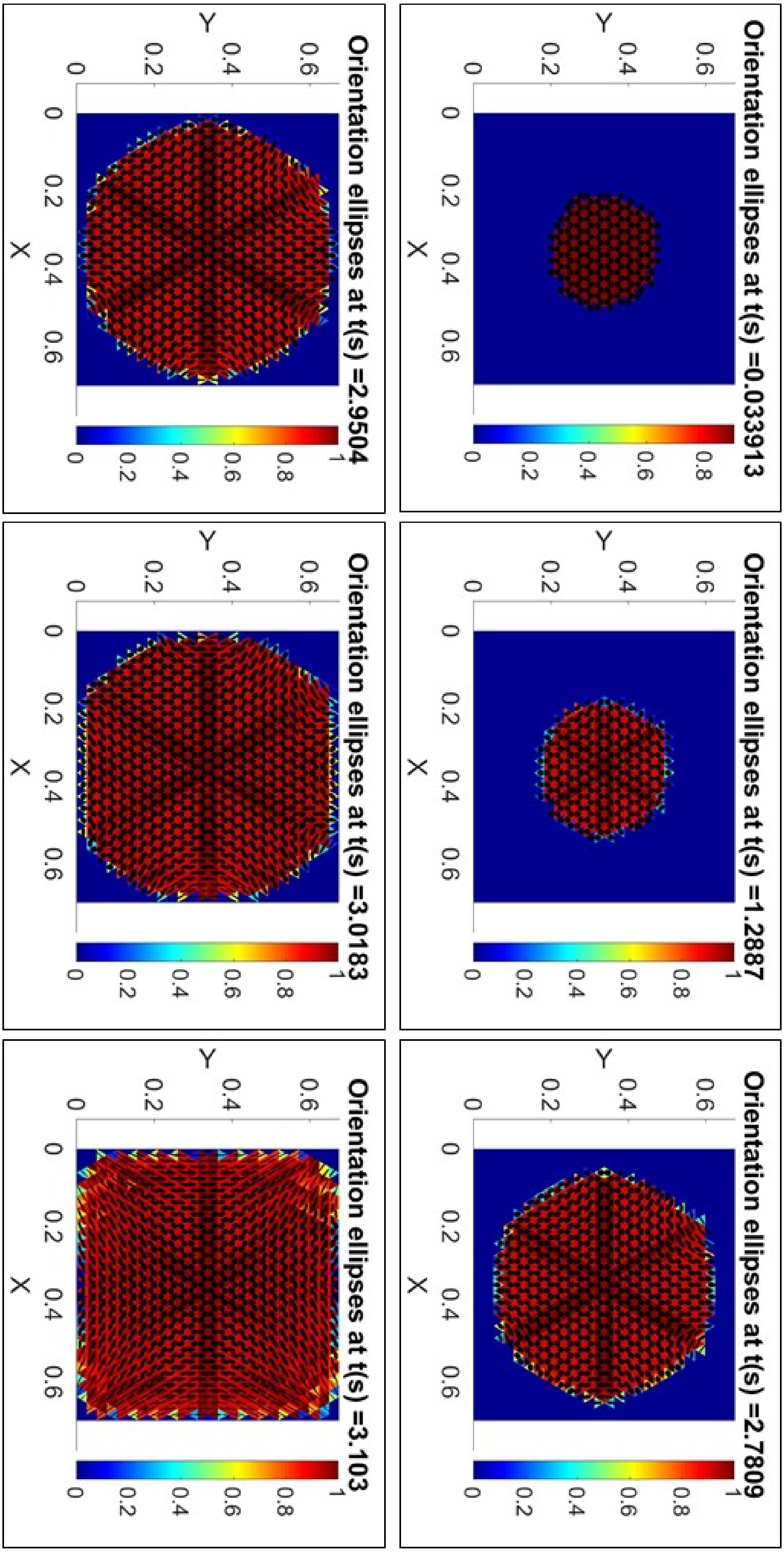

Figure 2.23: Evolution of the orientation state of the reinforcement fibres in geometry 1.

ity between the diffusion coefficient and the interfibres spacing in the short-fibres composite case. Direct numerical simulations to approach the interaction between fibres have also been attempted, like in [30], where Fan et al. distinguished between the short range interactions, simulated by means of lubrication forces, and long range interactions taken into account by the slender body approximation, or in [64].

Compared to results obtained from experimental tests, classical orientation models shown a delay in the orientation process. Different attempts have been made to adjust the timing between the physical and the numerical process as in [85].

However, any of this works have ever taken into account the effect of the confinement that the reinforcement fibres stand in most of the industrial processes of SMC materials. Perez et al. largely analyzed this issue in [63], where they dig to the microscale of the problem to provide of the constitutive equation for the evolution of the orientation of the reinforcement fibres, and then upscale it to the meso- and macro-scopic scales.

The effect of confinement consist in the lack of freedom of movement of fibres due to the very narrow space in which they live. In industrial SMC compression processes, the gap between the mould halves is much smaller than the typical fibre length. Inevitably, the movement of fibres to orientate will be slowed and will differ from the trajectory described by Jeffery, who assumed that the particles where free to move inside the suspension.

Perez et al. introduce, in the forces acting upon each particle immersed in the suspension, a contact force which prevents the fibre to cross it, enforcing the wall impermeability.

From the introduction of this contact force in the force balance, equation is 2.70 otained.

$$\dot{\mathbf{p}} = \dot{\mathbf{p}}^J - \frac{1}{1-p_z^2}\left[\dot{\mathbf{p}}^J\right](\mathbf{n} - p_z\mathbf{p}) \tag{2.70}$$

Where $\dot{\mathbf{p}}^J$ is the unconfined Jeffery's kinematics, given by equation 2.62, and the right hand term on the left side of the equation, which will be refereed to as $\dot{\mathbf{p}}^C$, prevents fibre to cross the mould wall. The confined term $\dot{\mathbf{p}}^C$ will be 'activated' when $L\mathbf{p}(t)\cdot\mathbf{n} > H$, i.e., when the fibre touches the wall, L being the half of the fibre length.

$$\dot{\mathbf{p}}^C = -\frac{1}{1-p_z^2}\left[\dot{\mathbf{p}}^J\right](\mathbf{n} - p_z\mathbf{p}) \tag{2.71}$$

Finally, the kinematics of a fibre of length $2L$ immersed in a flow occurring in a narrow gap of thickness $2H$ is given by the *confined Jeffery model*.

$$\begin{cases} \dot{\mathbf{p}} = \dot{\mathbf{p}}^J & \text{if} p_z L < H \\ \dot{\mathbf{p}} = \dot{\mathbf{p}}^J & \text{if} p_z L = H \;\&\; \dot{\mathbf{p}}^J\cdot\mathbf{n} \leq 0 \\ \dot{\mathbf{p}} = \dot{\mathbf{p}}^J + \dot{\mathbf{p}}^C & \text{if} p_z L = H \;\&\; \dot{\mathbf{p}}^J\cdot\mathbf{n} > 0 \end{cases} \tag{2.72}$$

However, fibres being much longer than the gap dimension, 'fully-confined conditions' will be assumed, i.e., fibres are always in contact with the mould walls, so the condition $\dot{\mathbf{p}} = \dot{\mathbf{p}}^J + \dot{\mathbf{p}}^C$ will always be applied.

Scaling to the macroscopic case (see [63]), Perez et al. propose the second order orientation tensor, and its derivative, as described in equations 2.73 and 2.77.

$$\mathbf{a}^C = \begin{pmatrix} \mathbf{b} & \mathbf{c} \\ \mathbf{c}^T & \frac{H^2}{L^2} \end{pmatrix} \tag{2.73}$$

where $\mathbf{b}$ is the in-plane second order orientation tensor given by equation 2.74.

$$\mathbf{b} = \int_C \mathbf{q}\otimes\mathbf{q}\,\psi(\mathbf{p})\,d\mathbf{p} \tag{2.74}$$

where $\mathbf{q}$ are the planar components of vector $\mathbf{p}$, that in the confined case is given by equation 2.75. C is the space of the permitted trajectories for the fibres, obtained removing from the unit sphere all possible trajectories of the fibre S, i.e. leanthe polar regions beyond the parallels $z = H$ and $z = -H$.

$$\mathbf{p} = \begin{pmatrix} \mathbf{q} \\ p_z \end{pmatrix} \tag{2.75}$$

Vector $\mathbf{c}$ in equation 2.73 is given by equation 2.76.

$$\mathbf{c} = \int_C \mathbf{q}\, p_z\, \psi\left(\mathbf{p}\right) d\mathbf{p} \tag{2.76}$$

The derivative of the confined second order orientation tensor will be expressed as follows.

$$\dot{\mathbf{a}}^C = \begin{pmatrix} \dot{\mathbf{b}} & \dot{\mathbf{c}} \\ \dot{\mathbf{c}}^T & 0 \end{pmatrix} \tag{2.77}$$

The derivatives of the in-plane second order orientation tensor ($\dot{\mathbf{b}}$), and of the vector $\mathbf{c}$ ($\dot{\mathbf{c}}$), depend on the components of the local velocity gradient, that will be renamed as in equation 2.78.

$$\nabla \mathbf{v} = \begin{pmatrix} \mathbf{G} & \mathbf{g} \\ \mathbf{j}^T & \mathcal{G} \end{pmatrix} \tag{2.78}$$

Based on this nomenclature, the derivative of the vector $\mathbf{q}$ is given by equation 2.79.

$$\dot{\mathbf{q}} = \mathbf{G}\,\mathbf{q} - \delta_1 \left(\mathbf{G} : (\mathbf{q} \otimes \mathbf{q})\right) \mathbf{q} + \delta_2 \mathbf{g} - \delta_3 \left(\mathbf{q}^T\ \mathbf{g}\right) \mathbf{q} \tag{2.79}$$

And the δ scalar coeficients are described like follows.

$$\delta_1 = \frac{1}{1 - p_z^2} \tag{2.80}$$

$$\delta_2 = p_z \tag{2.81}$$

$$\delta_3 = \frac{p_z}{1 - p_z^2} \tag{2.82}$$

The time derivative of tensor $\mathbf{b}$ is described by equation 2.83.

$$\dot{\mathbf{b}} = \mathbf{G}\,\mathbf{b} + \mathbf{b}\,\mathbf{G}^T - 2\delta_1 \mathbf{G} : \mathbf{B} + (\mathbf{g} \otimes \mathbf{c} + \mathbf{c} \otimes \mathbf{g}) - 2\delta_3\, \mathbb{B}\,\mathbf{g} \tag{2.83}$$

The terms $\mathbf{B}$ and $\mathbb{B}$ represent the third and fourth order in-plane orientation tensors respectively. Perez et al. propose to define them as in equations 2.84.

$$\begin{cases} \mathbb{B} = \frac{1}{p_z} \mathbf{b} \otimes \mathbf{c} \\ \mathbf{B} = \mathbf{b} \otimes \mathbf{b} \end{cases} \tag{2.84}$$

And the time derivative of vector $\mathbf{c}$ is given by equation 2.85.

$$\dot{\mathbf{c}} = \mathbf{G}\,\mathbf{c} - \delta_1 \delta_2 \mathbf{G} : \mathbb{B} + \delta_2^2\, \mathbf{g} - \delta_3 \delta_2 \mathbf{b}\,\mathbf{g} \tag{2.85}$$

2.3.3 Orientation in the case of convergent and divergent flow.

2.3.4 Adaptation of the orientation model to the three-dimensional case.

Due to the planar nature of the flow in the built model, applying the proposed orientation model to the three-dimensional geometry implies certain particularities and difficulties. To illustrate them, the three-dimensional geometry described in 2.2 will be used here.

First, the derivative of the orientation tensor (2.64) needs the gradient of pressure to be calculated. As explained in subsection 2.3.1, due to the chosen linear shape functions, the value of the velocity is uniform in each element, and to build a local gradient of pressure, a mean of the velocity between each element and its neighbours is needed. Because of that, it is necessary to obtain the nodal value of the velocity, in order to calculate the weighted mean of the velocity of all the elements that share the same node. But in the three dimensional case, the finite elements that conform the side of the cylinder do not share the same plane any more; each one of them define its own particular plane. Then, the velocity vector of each one of them lives in a different plane, so it is necessary to have all of them folded to the same plane before performing the calculation of the nodal velocity. Since the mesh consists in triangular elements, each node belongs to six elements, and it is necessary to perform, at least, five rotations of vectors to have them in the same plain and then be able to combine them.

If, instead the velocity gradient is computed from the velocities at the mid point of its edges, instead of from its nodes, the procedure simplifies. The number of rotations of vectors reduces to three, since it will only be necessary to take to the plane of each element the velocity vector of its neighbours and only three elements will be involved, instead of six. Once all the velocity vectors lay over the same plane, the value of the gradient of the velocity in a element can be obtained by applying the gradient theorem to the components of the tensor gradient of velocity of the element, like described in equation 2.86.

$$\int_{\Omega} \nabla \mathbf{v} \; d\Omega = \int_{\partial\Omega} \mathbf{v} \otimes \mathbf{n} \; d\partial\Omega = \sum_{i=1}^{3} \mathbf{v}_i \otimes \mathbf{n}_i l_i \tag{2.86}$$

Where $\mathbf{v}_i$ is the velocity vector of the neighbour element i, expressed in the plane of the actual element, $\mathbf{n}_i$ is the unitary vector pointing in the direction of the side between the element and its neighbour, and l_i is the length of the correspondent side.

Second, to transport the orientation tensor between two elements which are not coplanar, it is necessary to take the orientation tensor to the plane of the element to which it is 'being transported'. Great attention must be paid to the procedure of rotating a tensor from one plane to another. To fold the tensor between planes, the simplest way to proceed is to rotate the eigenvectors of the orientation tensor to the plane target; the eigenvalues do not change their value when changing of plane. Once the eigenvector is laying in the plane of the element downstream, it needs to be expressed in the same local reference system than the element downstream. Then, the orientation tensor is reconstructed from its eigenvalues and eigenvectors as shown in equations 2.87 and 2.88, and transported to the element downstream with the incoming flow as in equation 2.67.

$$\mathbf{a}\,\mathbf{P} = \mathbf{a} \begin{pmatrix} \mathbf{v}_{p1} & \mathbf{v}_{p2} & \mathbf{v}_{p3} \end{pmatrix} = \begin{pmatrix} \alpha_1 \mathbf{e}_1 & \alpha_2 \mathbf{e}_2 & \alpha_1 \mathbf{e}_3 \end{pmatrix} \tag{2.87}$$

Where $(\alpha_1, \alpha_2, \alpha_3)$ are the eigenvalues of the orientation tensor and $(\mathbf{e}_1, \mathbf{e}_2, \mathbf{e}_3)$ are its eigenvectors.

$$\mathbf{a} = \begin{pmatrix} \alpha_1 \mathbf{e}_1 & \alpha_2 \mathbf{e}_2 & \alpha_1 \mathbf{e}_3 \end{pmatrix} \mathbf{P}^{-1} \tag{2.88}$$

2.4 Conclusions of chapter 2

The main conclusions of this chapter are listed below.

- A simulation tool adapted to the peculiarities of the SMC compression moulding process has been developed (time evolving thickness of the charge, moving boundary conditions).
- The proposed model is the best suited for the particular case of SMC compression moulding because it takes into account the confinement which is experienced in thin parts by the fibers that are longer than the gap of the cavity of the mould.
- The proposed compression moulding fluid flow model with short confined fibers was implemented to numerically simulate flow and orientation with confinement in two and three dimensional geometries.

Chapter 3

Comparison of model predictions to experimental data.

3.1 Introduction.

To validate the numerical model developed in Chapter 2 to predict the macroscopic flow pattern and fibre orientation in the SMC compression process, three tests are proposed. The quality of a (semi)-structural SMC part is usually assessed through mechanical tests. One of the main objective of design engineers is to optimize the mechanical performance of SMC parts by tailoring the process-induced fibre orientation.

Then the first experimental analysis was to

- produce in industrial conditions flat SMC panels,
- simulate their manufacturing with the numerical model developed in Chapter 2,
- submit each panel to a tensile loading and measure the induced deformation field
- correlate the measured deformation field to the computed orientation field.

In the second test campaign tensile coupons were to cut out from the SMC panels according to the fiber direction predicted by the model. Stiffness and strength were measured and also compared to the computed orientation field.

Finally, samples cut out from the SMC parts were scanned in a X-ray microtomograph and analyzed to determine the fibre distribution.

3.2 Manufacturing of regular SMC parts.

A total number of 47 rectangular flat SMC panels were produced using a mould of dimensions 700 mm x 400 mm. The processed SMC material was the 15LP1393S (054-37B1), by IDITrans. It is a polyester SMC material reinforced with 29% wt. of 25 mm long chopped glass fibres.

For the production of the parts, the temperature of the lower mould half was kept at 150°C, while for the upper mould half it was 160°C. The filling time of the moulds was slightly under 2 s.

The 47 parts were classified into seven different series, according to the SMC charge coverage and shape, closing velocity, flow pattern and presence of insert. They are important compression moulding variables that must be under control for a satisfactory moulding operation.

The various configuration of each series of parts are described in table 3.2.

SERIES	INFLUENCE OF	SAMPLES	CHARGE CONFIGURATION	SPECIFICITIES
1	COVERAGE	1 to 3	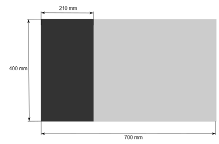	coverage : 30% closing force rate: 50 t/s [1]
		4 to 6	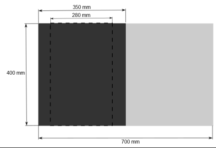	coverage : 50% closing force rate: 50 t/s
		7 to 9	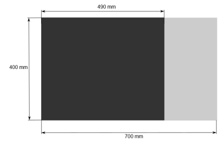	coverage : 70% closing force rate: 50 t/s
		35	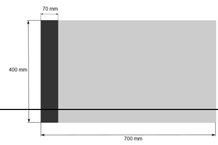	coverage : 10% closing force rate: 50 t/s
		36-37		coverage : 10% closing force rate: 20 t/s
2	SQUEEZE RATIO	10 TO 12	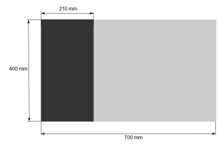	coverage : 30% closing force rate : 20 t/s
		13 TO 15		coverage : 30% closing force rate: 70 t/s
		16 TO 18		coverage : 30% closing force rate: 120 t/s
3	RADIAL FLOW	19-20	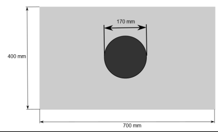	charge radius: 170 mm closing force rate: 50 t/s
		21 to 23	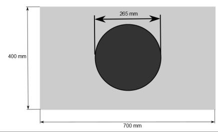	charge radius: 265 mm closing force rate: 50 t/s
4	WELD LINES	24 TO 28	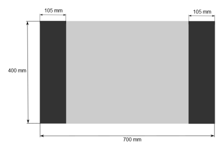	converging angle: 0° closing force rate: 50 t/s
		29 to 33	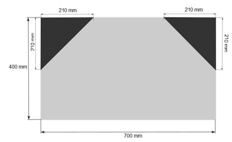	converging angle: 90° closing force rate: 50 t/s
		34 to 39	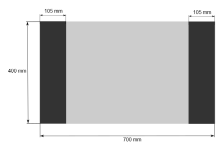	converging angle: 0° closing force rate: 10 t/s

[1] t/s = ton/second

SERIES	TARGET	SAMPLES	CHARGE CONFIGURATION	SPECIFICITIES
		42 to 44	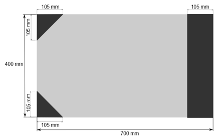	converging angle: 0° & 90° closing force rate: 10 t/s
5	SOLID INSERT	38	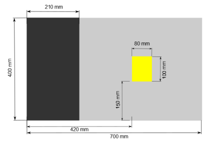	insert in the centre, closing force rate: 50 t/s
		39 to 41	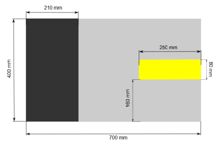	insert in the end, closing force rate 50 t/s
6	CHARGE SHAPE	45 to 47	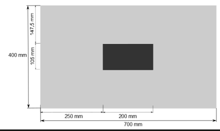	charge size: 200 mm x 105 mm closing force rate: 50 t/s

Table 3.1: Manufacturing conditions of regular SMC parts.

In all cases, the thickness of the initial charges corresponded to the minimum mass of SMC material necessary to fill up the mould.

3.3 Tensile tests on full SMC parts.

This specific procedure was chosen because, besides being a non-destructive test, it is closer to the manufacturers' uses and, if successful, it would constitute a way to avoid costly tests to measure the fibres orientation.

The quasi-static tensile properties were measured with an electro-mechanical Instron 5584 universal testing machine with a maximum capacity of 100 kN in tension. This machine is steered and controlled with the software Bluhill, developed by Instron.

The strain field measurement was carried out by means of a Digital Image Correlation technique (DIC) [59] [68][75], using two 29 Mpixel cameras to capture the displacement field. These raw data are post-processed with the software Vic 3D (Correlated Solutions) to compute the strain field. The full set-up is shown in figure 3.1.

3.3.1 Digital Image Correlation Technique.

Two operations are performed each time to get the strain field of the SMC part: a stereo-correlation of two images taken by each camera of the specimen before and after applying the tension loading, and a temporal matching or tracking of the same points of the part at each state of the test. The first operation provides the 3D topography of the SMC part before and after the traction and the matching allows to measure the displacement of each single point of this topography and, therefore, the strain induced in the SMC part.

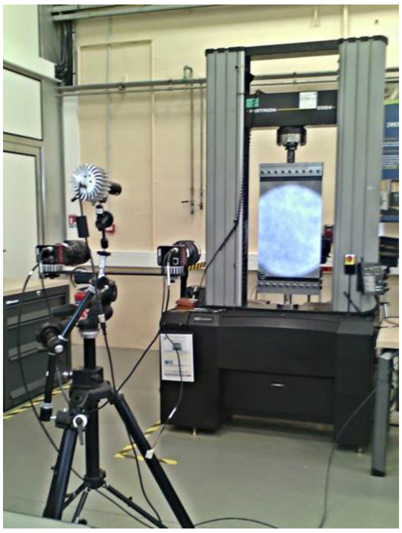

Figure 3.1: Set up for the tensile test on full SMC parts.

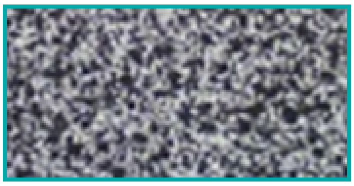

Figure 3.2: Speckle pattern for the stereo-correlation and tracking.

To make possible the identification of each point of the part, it is necessary to print a speckle pattern in its surface, like the one shown in fig.3.2. To ensure the correct identification of the points, the pattern must be non-repetitive, isotropic, and show high contrast [55]. Also, the pattern must satisfy some other requirements :

- it must deform with sample and not reinforce the specimen, then a certain flexibility is required,
- it must not degrade (too much) during the test,
- it should be uniform
- the specular reflection must be avoided so that the algorithm implemented in the software can establish all correspondences between the points in the pattern
- and it should be as dense as possible to achieve the maximum spatial resolution.

To draw the pattern, a uniform white layer is painted over the SMC part with a mat spray paint, over which a black speckles pattern is printed also with a spray paint.

To identify the different points of the designed pattern between two images, either they have been taken by the same camera at each state of the deformation, or by each camera at the same state of the deformation, the displacement of a pixels subset is tracked by maximizing a similarity function. When comparing between the images taken by each camera at the same moment of time, the software can identify a subset or window of pixels showing the same pattern of points, but when the comparison is done between images taken by the same camera at different stages of the deformation, the correspondence between points is not immediate since the strain in the part causes a relative displacement and the configuration of the subset of pixels changes. In this case, the maximization function is introduced in the identification

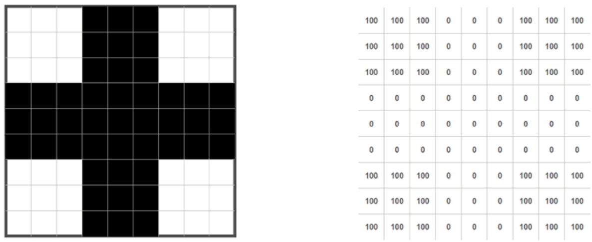

Subset of pixels on screen. Subset of pixels on memory.

Figure 3.3: Correspondence between the subset of pixels and a matrix of numerical values.

process. To translate the image into a set of numeric values meaningful for the function, the software assigns to each pixel a value on a scale from 0 to 100 depending on the intensity of gray of the pixel. This operation establishes a correspondence between the subset and a matrix whose elements are a numeric value (see fig. 3.3). The algorithm looks for the matrix with closest configuration of values between all possible subset of pixels in the image it is comparing with (target image from now on).

Although software companies do not usually specify the specific correlation functions implemented in their algorithm, they are functions of the form

$$C\left(x,y,x',y'\right)=\frac{\sum_{x=-N}^{N}\sum_{y=-N}^{N}\left[f\left(x,y\right)-\bar{f}\left(x,y\right)\right]\left[g\left(x',y'\right)-\bar{g}\left(x',y'\right)\right]}{\sqrt{\sum_{x=-N}^{N}\sum_{y=-N}^{N}\left[f\left(x,y\right)-\bar{f}\left(x,y\right)\right]^{2}}\sqrt{\sum_{x=-N}^{N}\sum_{y=-N}^{N}\left[g\left(x',y'\right)-\bar{g}\left(x',y'\right)\right]^{2}}} \tag{3.1}$$

where $f\left(x,y\right)$ is the gray scale value for the point $\left(x,y\right)$ of the reference image, and $g\left(x',y'\right)$ is the gray scale value for the point $\left(x',y'\right)$ of the target image, N is the size of the subset of pixels, eq. 3.2 gives the mean intensity of the subset of reference and eq. 3.3 gives the mean intensity of the target image.

$$\bar{f}\left(x,y\right)=\frac{1}{\left(2N+1\right)^{2}}\sum_{x=-N}^{N}\sum_{y=-N}^{N}\left[f\left(x,y\right)\right] \tag{3.2}$$

$$\bar{g}\left(x',y'\right)=\frac{1}{\left(2N+1\right)^{2}}\sum_{x=-N}^{N}\sum_{y=-N}^{N}\left[g\left(x',y'\right)\right] \tag{3.3}$$

The algorithm checks possible matches of the value assigned to the subset defined at several location, and uses a similarity score (the correlation function) to grade them.

Nevertheless, many difficulties affects the tracking process. For example, gray-scale images have many shades of gray in between, images are affected by noise, ambient changes in light and temperature may affect the resulting images, and the speckles pattern may change in color intensity when it is stretched by the tensile loading. It is of great importance to model the different aspects of the photometric transformation to design a robust correlation, like the change of shape of the reference subset with describing subset shape functions like the ones in fig. 3.4 [79], or reconstructing the continuous gray scale information between pixels from the discontinuous values, to allow to identify the displacements at a finer scale than the pixel scale.

A stereo-triangulation is required for the operation of matching between the two images taken by the two correlation cameras at each stage of the tensile test [80]. The stereo-triangulation requires computing the intersection of two optical rays, which must be formulated in a common coordinate system; a calibration of the stereo-rig is then necessary. The *calibration* consists in the identification of the *transference function.* The relative orientation of the stereo

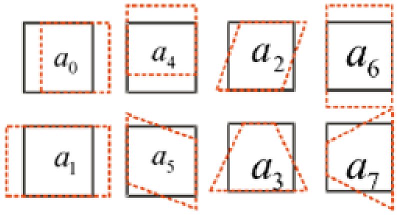

Figure 3.4: Subset shape functions correlation algorithms[79].

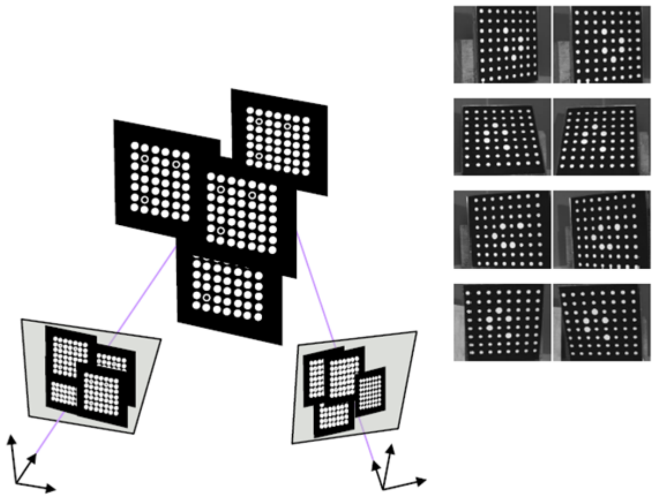

Figure 3.5: Subset shape functions correlation algorithms [79].

cameras has to be known for triangulation. Calibration is shape measurement process. It is performed by acquiring pairs of images of a known target that submitted arbitrary motions. Two constraints required to accomplish calibration: the calibration target must not deform between images, and the distance between two points on the target object must be known. For the calibration operation, calibration plates like the ones in fig.3.5 are used.

Special care to two different issues must be paid when setting both cameras. On the one side, the bias, consisting in systematic deviations from the correct result may appear that can be reduced or eliminated with proper setup and parameters tuning. On the other hand, the unavoidable noise, consisting on random, zero-mean deviations from the correct result, can be minimized with careful setup [33].

3.3.2 Tensile test on full SMC parts results.

The strain field induced by the tensile loading is measured with two 29 Mpixel cameras to capture the displacement field in the part and the processing software Vic-3D (DIC software developed by Correlated Solutions) is used to compute the strain field. Fig.3.6 shows the distribution of the value of the Green-Lagrange strain tensor measured with the VIC-3D 7 system over the surface of the part #2 (unidirectional flow, 33% mould coverage, closing velocity 50 t/s. See table 3.2 for further information on the configuration and moulding conditions of the part), mounted on the universal testing machine, as in fig3.1. The stress applied was kept in the elastic regime of the stress-strain curve of the sample, making sure that the part could recover from the deformation induced. Since the load applied varies from part to part, no comparison in absolute values of the strain field can be done. Therefore the results have been normalized and expressed as a percentage of the strain.

Table 3.2 reports the mean strain and the standard deviation as a measure of the variability

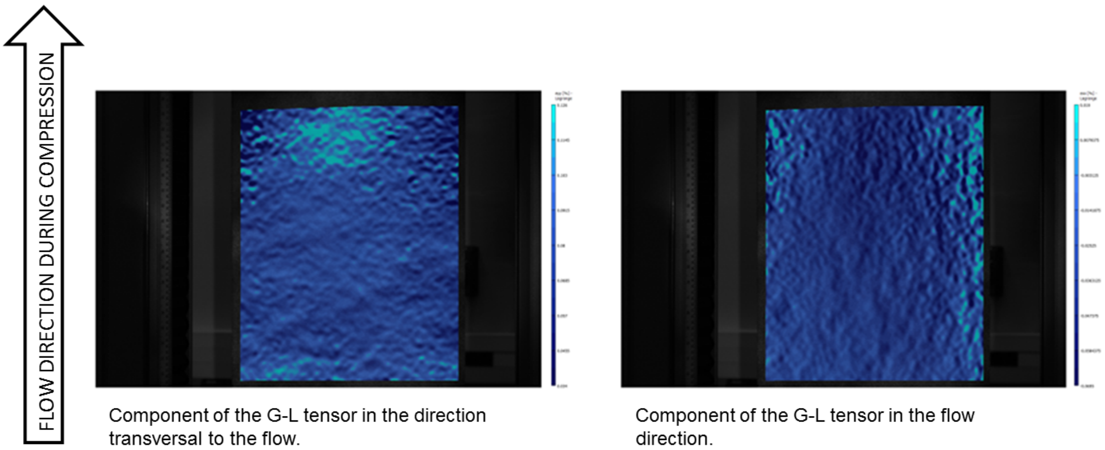

Figure 3.6: Distribution of the components of the Green-Lagrange strain tensor in part #2 under tensile loading.

Figure 3.7: Regions where the strain field was measured in part #2.

of the strain over the part, for parts #1 and #2, both produced with the same initial configuration of the charge and compression parameters. In the table, e_{fd} is the value of the component of the Green-Lagrange strain tensor in the direction of the flow and e_{ft} is the component in the direction transverse to the flow.

Strain component	Part	Mean (%)	Standard Deviation
e_{fd}	Part #1	2.16e-03	2.1e-04
	Part #2	1.69e-03	3.90e-04
e_{ft}	Part #1	-7.21e04	1.49e-04
	Part #2	-6.01e-04	2.68e-04

Table 3.2: Components of the trace of the Green-Lagrange strain tensor for parts #1 and #2.

Results in Table 3.2 reveals very similar values of strain in both parts. The standard deviations, of the order of 10^{-4}, evidences the homogeneity of the strain field over the parts. In addition, for a deeper analysis of the strain field, the same analysis was performed in smaller regions in part #2. Fig.3.7 shows the areas where the strain field was measured. Table 3.3 shows the strains in the directions of the flow and perpendicular to it for the different areas in part #2.

The same uniformity is found in smaller areas than in the full part. This observation is in qualitative agreement with the simulated orientation field shown in fig.3.8. The simulation predicts an uniform distribution of the components of the orientation tensor. According to this

Strain component	Region	Mean (%)	Standard Deviation
e_{fd}	Region 1	1.99e-03	2.52e-04
	Region 2	1.69e-03	3.90e-04
	Region 3	1.06e-03	3.27e-04
e_{ft}	Region 1	-7.07e04	1.66e-04
	Region 2	-2.68e-04	2.48e-04
	Region 3	-6.14e-04	2.04e-04

Table 3.3: Components of the trace of the local Green-Lagrange strain tensor for 3 regions in part #2.

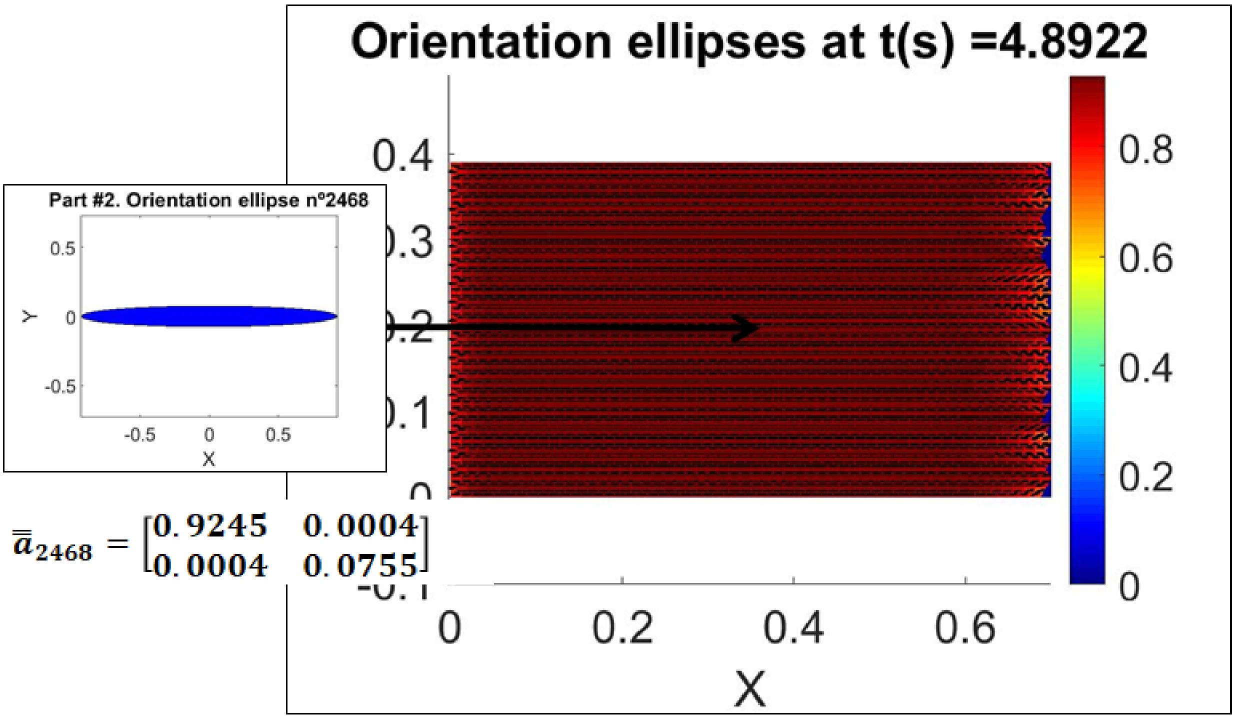

Figure 3.8: Simulated fibre orientation in part #2 (30% coverage rate of the charge, covering the left part of the mould).

result, for an uniform alignment of fibres in the part, the strain field should also be uniform when submitted to an uniform tensile loading.

The same analysis was performed on two parts produced from cylindrical SMC charges of SMC, which once compressed gave rise to a combination of radial and lineal flows. Table 3.4 reports the mean strain and standard deviation for parts #22 and #23, both produced with the same initial configuration of the charge and compression parameters (see table 3.2).

These values are also in good qualitative agreement with the predictions of the numerical model, shown in fig.3.9. In this case, the strain filed is more isotropic than in the case of unidirectional flow.

The strain field of the same regions than the ones picked for the part #2 were then analyzed for the part #23. Table 3.5 shows the components of the trace of the Green-Lagrange tensor for each region as well as the standard deviation of the strain in them.

The same uniformity of the components of the Green-Lagrange strain tensor, reflecting the isotropy of the distribution of the fibres orientation, is found in this local analysis. However,

Strain component	Part	Mean (%)	Standard Deviation
e_{fd}	Part #22	9.26e-04	2.22e-04
	Part #23	6.74e-04	3.32e-04
e_{ft}	Part #22	-2.97e04	1.90e-04
	Part #23	-4.15e-04	2.92e-04

Table 3.4: Components of the trace of the Green-Lagrange strain tensor for parts #22 and #23.

Strain compo-nent	Region	Mean (%)	Standard Deviation
e_{fd}	Region 1	9.77e-04	1.98e-04
	Region 2	9.90e-04	1.72e-04
	Region 3	9.55e-04	1.07e-04
e_{ft}	Region 1	-2.53e04	1.29e-04
	Region 2	-3.34e-04	1.65e-04
	Region 3	-6.59e-04	1.03e-04

Table 3.5: Components of the trace of the local Green-Lagrange strain tensor for 3 regions in part #23.

results of the numerical model obtained for the part #23 in fig. 3.9 show a very different fiber alignment in the regions studied. A higher degree of anisotropy is predicted.

In the light of the above results, two possible conclusions can be drawn. Either the tensile test on the full panel with DIC monitoring is not sensitive enough to capture the local elastic behaviour of the part, or the distribution of fibres orientation is more isotropic than what the numerical model predicts. Further validations are needed to really conclude on the accuracy of the proposed model. Then tensile tests are carried out on test coupons cut out from the SMC panels in the next section 3.4.

3.4 Tensile tests on coupons.

In addition to the previous tensile tests in elastic regime carried out on the full SMC panels, other tensile tests were performed on coupons cut out from similar panels. This allows to measure the whole stress-strain response of the material up to failure. The rectangular specimen had a length of 150 mm, a width of 25 mm, and a thickness of 2.50mm ± 0.3mm. The same universal testing machine was used were the cross-head velocity was of 1mm/min. Coupons were cut out from two panels produced with unidirectional flow (parts #8 and #35), and two panels produced with a combined radial and longitudinal flow (parts #19 and #21).

3.4.1 Results for part #8.

Part #8 was produced by unidirectional flow, with an initial charge coverage of 70%, (see table 3.2). The numerical simulation of the same configuration predicted a slight and uniform alignment of the reinforcement fibres in the direction of the flow. Fig. 3.10 shows the components of the orientation tensor, its elliptical representation and the distribution of the local orientation

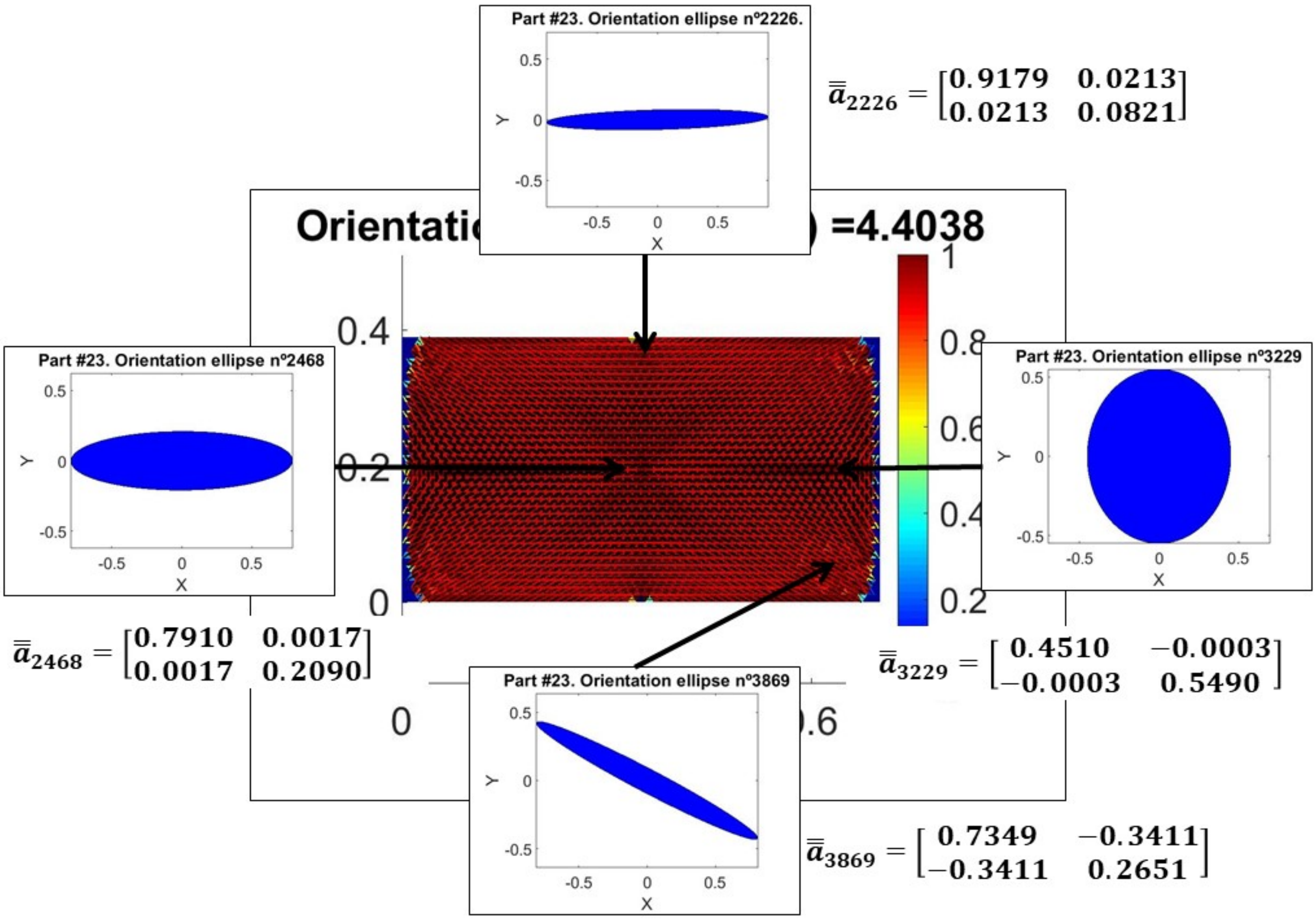

Figure 3.9: Simulated fibre orientation in part #23 (round charge of 265 mm of radius, placed in the center of the mould).

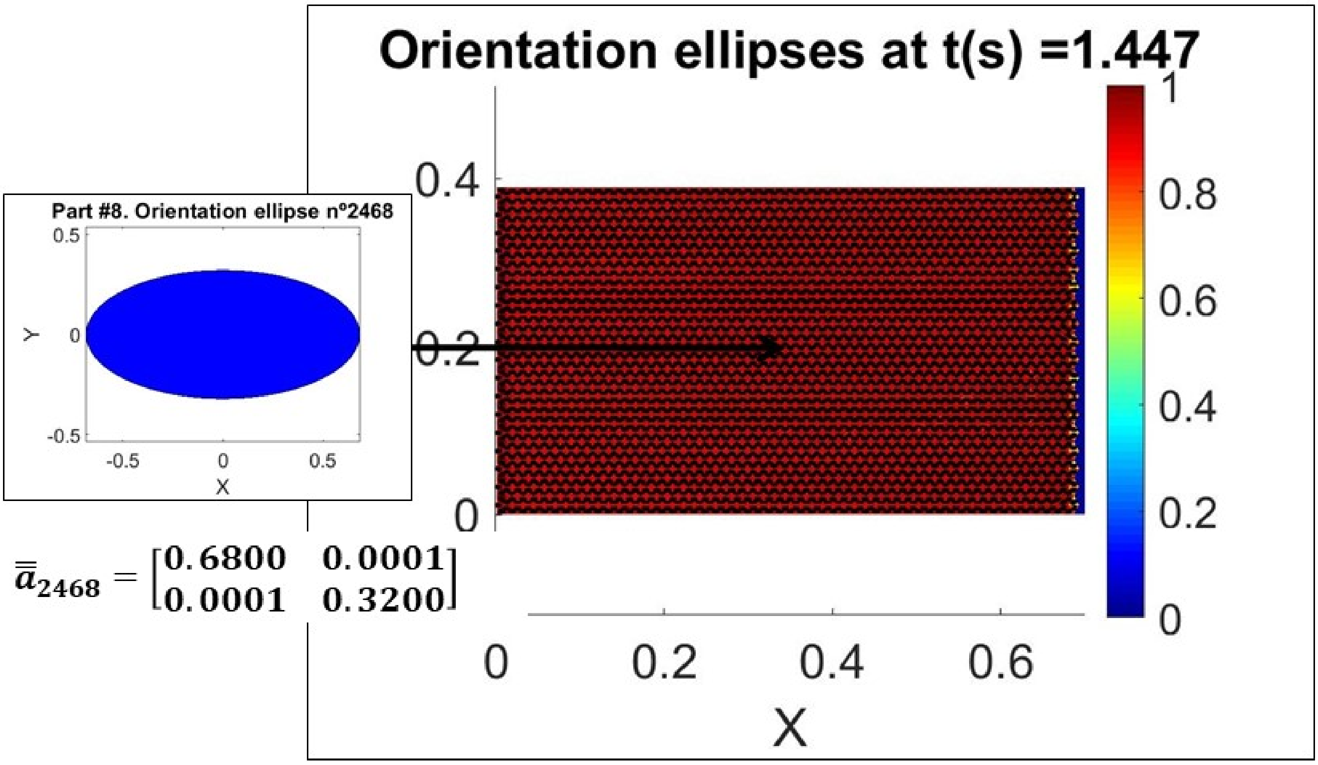

Figure 3.10: Simulated fibre orientation in part 8 (70% coverage rate of the charge, covering the left part of the mould).

ellipses in each finite element.

14 standardized tensile test coupons were cut out with a computer-controlled milling machine; 6 specimens in the flow direction and 8 specimens in the direction transverse (see fig.3.11).

The stress-strain curves resulting from the tensile test are displayed in fig.3.12, where the stress-strain curves for samples cut in the flow direction are in red and the ones in the transverse direction are in black. The trends are in qualitative agreement with the numerical model prediction, since the test coupons in the flow direction are stiffer and more resistant than the ones in the transverse direction. Table 3.6 shows that the scattering in stiffness for the same group of specimens is small. The scattering in strength is higher, which was expected. The same conclusions cannot be drawn for the ultimate strain at break. Some samples cut in the direction transverse to the flow have higher strain to failure than some samples aligned to the flow direction. Also the scattering is big, reflecting some finer changes in microstructures.

3.4.2 Results for part #35.

The part #35 was, as the part #8, produced by an unidirectional flow with an initial charge coverage of 10%, as shown in table 3.2. The numerical simulation predicted an almost perfect and uniform alignment of fibres in the direction of the flow. Fig.3.13 shows the components of the orientation tensor, its elliptical representation and the distribution of the local orientation ellipses in each finite element.

Fig.3.14 shows where and in which direction with respect to the main flow the tensile test coupons were cut out from the part #35.

The stress-strain curves resulting from the tensile tests are displayed in fig.3.15, where the same convention is adopted for the color. The same observations that the one made for the part #8 can be made here, except for the specimen 1 which is as stiffer as a coupon oriented in

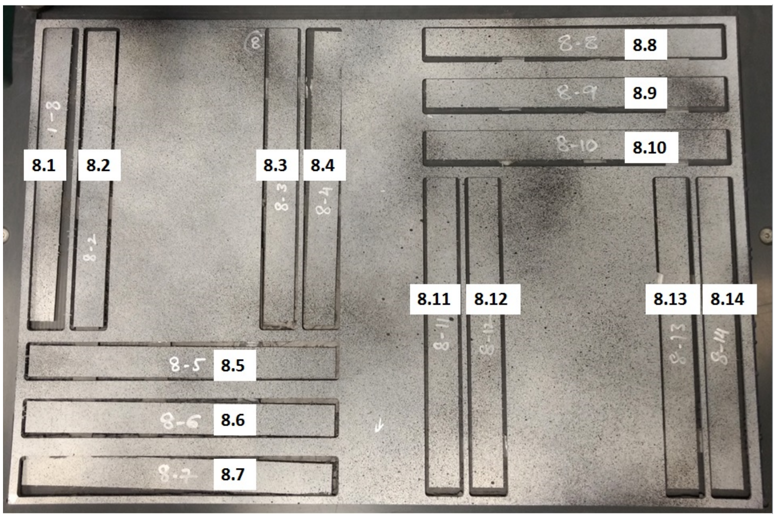

Figure 3.11: Tensile test coupons cut out from part #8.

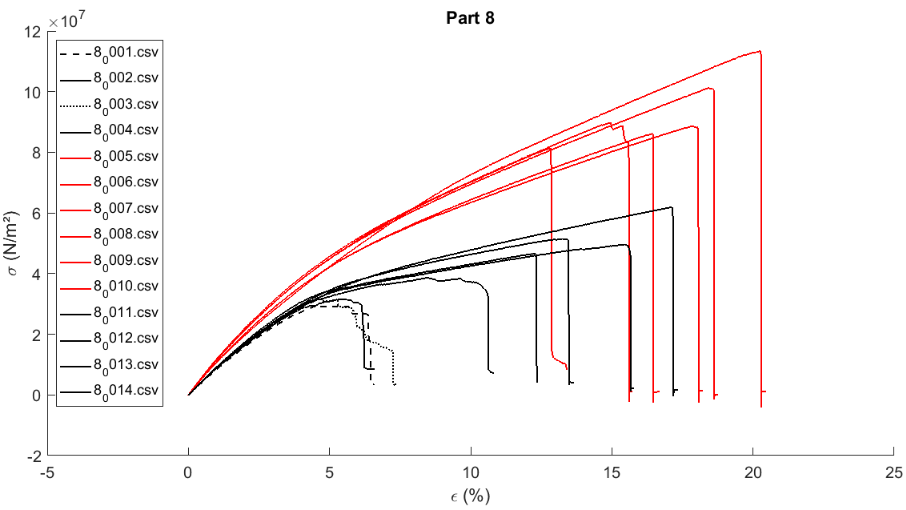

Figure 3.12: Stress-strain curves of the samples from part #8.

sample	Direction wrt. flow	Young modulus (Pa)	Stress at failure (Pa)
8_5	longitudinal	1.1509e+07	1.01e+08
8_6		1.2034e+07	8.97e+07
8_7		1.0780e+07	8.86e+07
8_8		1.1741e+07	8.13e+07
8_9		1.0591e+07	1.13e+08
8_10		1.0788e+07	8.61e+07
mean		1.1241e+07	2.15e+08
standard deviation		5.9848e+05	2.93e+08
8_1	transversal	8.1283e+06	2.95e+07
8_2		8.1923e+06	3.15e+07
8_3		8.8208e+06	3.16e+07
8_4		9.1956e+06	4.66e+07
8_11		8.9778e+06	4.95e+07
8_12		8.8749e+06	3.85e+07
8_13		8.9778e+06	5.14e+07
8_14		8.7486e+06	6.19e+07
mean		8.7395e+06	4.25e+07
standard deviation		3.8165e+05	1.16e+07

Table 3.6: Young modulus and strength for specimen cut out from part #8.

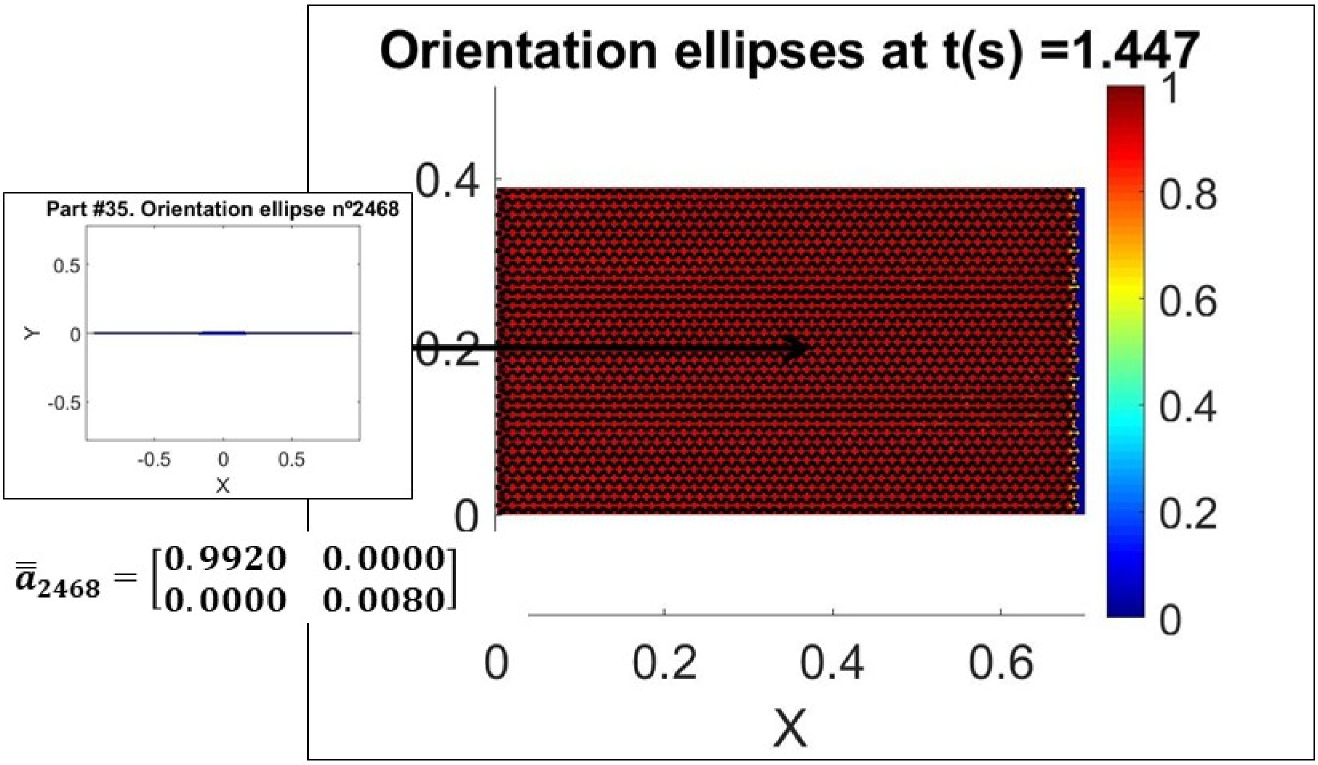

Figure 3.13: Simulated fiber orientation in part #35 (10% coverage rate of the charge, covering the left part of the mould).

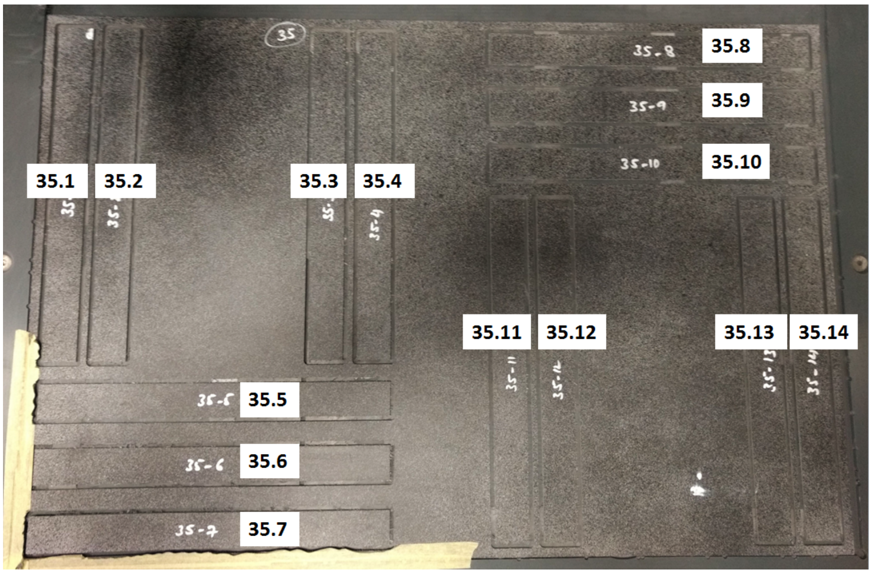

Figure 3.14: Tensile test coupons cut out from part #35.

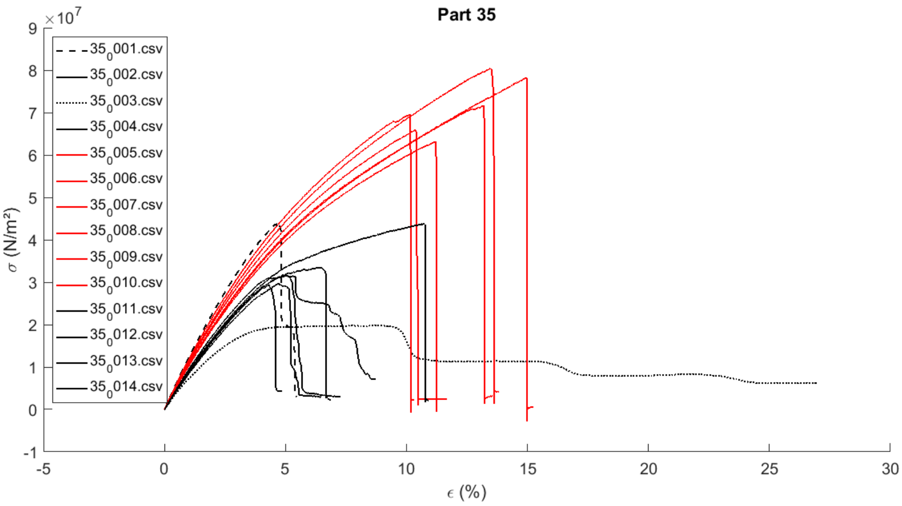

Figure 3.15: Tensile test : stress-strain curves for samples cut out from part #35.

the flow direction. This higher value may be caused by an edge effect because it is the closest to the mold edge where the charge where located and where fibres reorientate.

Sample #3 shows an abnormal low value that arises from the slipping of the sample inside the grip during the test. Fig.3.16 shows the scratch created by the sliding in the gripper.

Table 3.7 shows the values of the Young modulus measured from the stress-strain curve of each sample. As happened in the part #8, the point of failure for the different samples is also higher in the curves of the family of samples in the direction of the flow. In this case, the difference between samples when regarded from the point of view of the strain is more evident than for the sample #8, although it is still not determinant.

3.4.3 Results for part #19.

The part #19 was produced by a combination of a radial and linear flow, since the charge was circular and placed in the center of the rectangular mould. Its initial radius was 170 mm leading to an initial charge coverage of 32,4%, as shown in table 3.2.

Fig.3.17 shows the components of the orientation tensor at different locations of the final

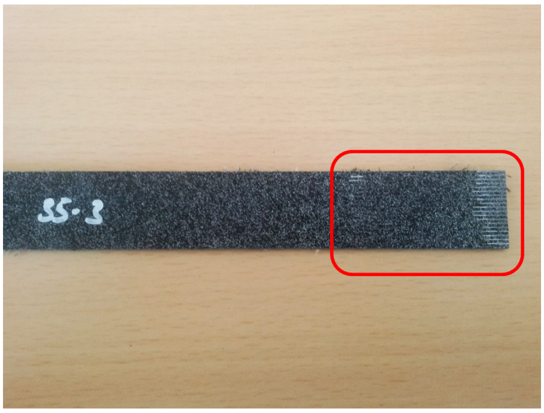

Figure 3.16: Scratch resulting from the sliding of specimen #3 during the test.

sample	Direction wrt. flow	Young modulus (Pa)	Stress at failure (Pa)
35_5	longitudinal	1.1844e+07	6.94e+07
35_6		1.1033e+07	6.58e+07
35_7		1.0282e+07	7.81e+07
35_8		1.1347e+07	8.03e+07
35_9		1.0073e+07	6.31e+07
35_10		1.0552e+07	7.13e+07
mean		1.0855e+07	7.13e+07
standard deviation		6.7580e+05	6.75e+06
35_1	transversal	1.2118e+07	4.39e+07
35_2		8.3868e+06	2.93e+07
35_3			
35_4		8.1748e+06	2.97e+07
35_11		8.6343e+06	3.34e+07
35_12		8.6905e+06	3.17e+07
35_13		9.3371e+06	3.15e+07
35_14		8.8306e+06	4.37e+07
mean		9.1689e+06	3.47e+07
standard deviation		1.3502e+06	6.33e+06

Table 3.7: Young modulus and strength for samples cut out from part #35.

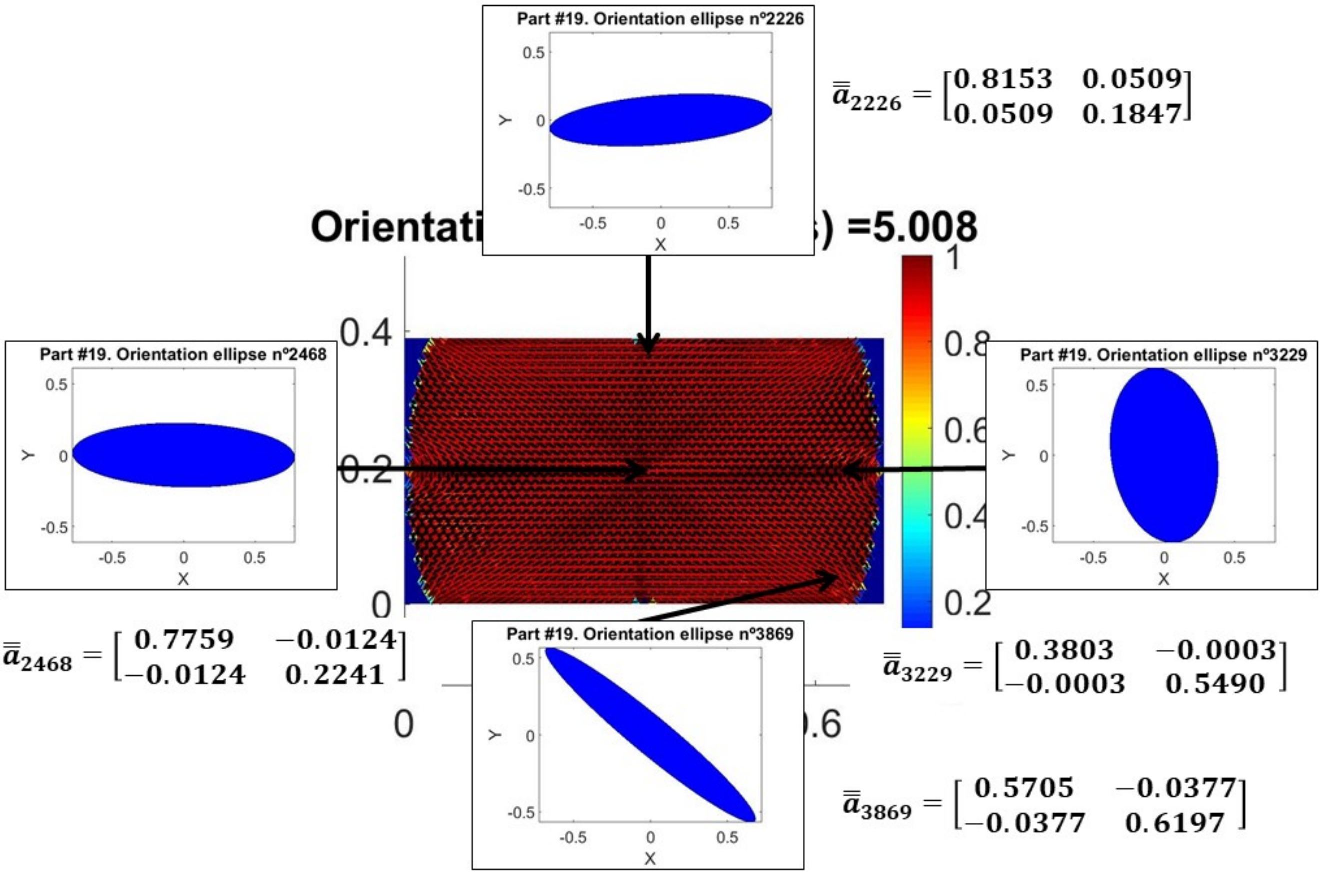

Figure 3.17: Simulated fibre orientation in part #19(round charge of 170 mm of radius, placed in the center of the mould).

SMC part, its elliptical representation and the distribution of the local orientation ellipses in each finite element.

Fig.3.18 shows where and in which direction with respect to the main flow the tensile test coupons were cut out from the part #19.

The stress-strain curves resulting from the tensile tests are displayed in fig. 3.19. In this case, since the flow is a combination between radial and longitudinal flow, no specific convention for the color to group them has been made. Table 3.8 shows the values of the Young modulus measured from the stress-strain curve of each sample. The stiffness is more homogeneous indicating a higher level of isotropy, which is agreement with the model prediction. The Young moduli are similar to the ones of samples cut in the transverse direction of the flow from parts #8 and #35. The strength is however more scattered than in the previous cases.

3.4.4 Results for part #21.

The part #21 was produced by a combination of radial and linear flow. The circular charge was placed in the center of the rectangular mould. The initial radius was of 265 mm what means an initial charge coverage of 78,7%, as shown in table 3.2.

Fig. 3.20 shows the components of the orientation tensor at different locations of the final SMC part, its elliptical representation and the distribution of the local orientation ellipses in each finite element.

Fig.3.21 shows where and in which direction with respect to the main flow the tensile test coupons were cut out from the part #21. A different configuration than for parts #8, #35 and #19 was performed.

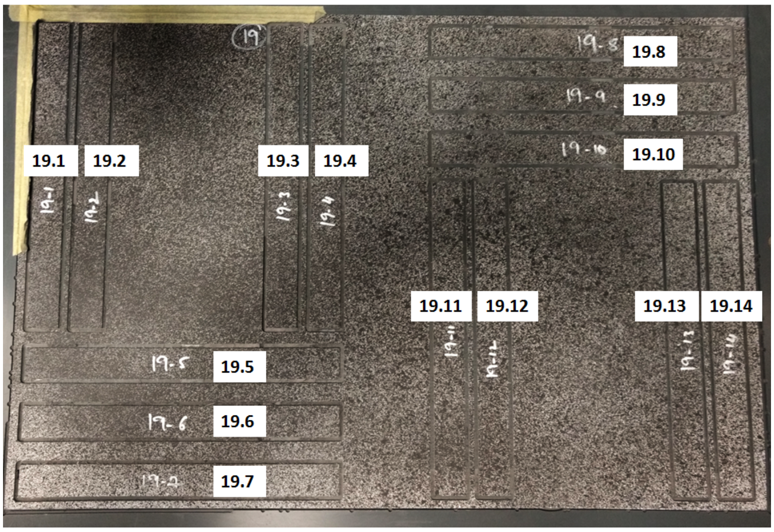

Figure 3.18: Tensile test coupons cut out from part #19.

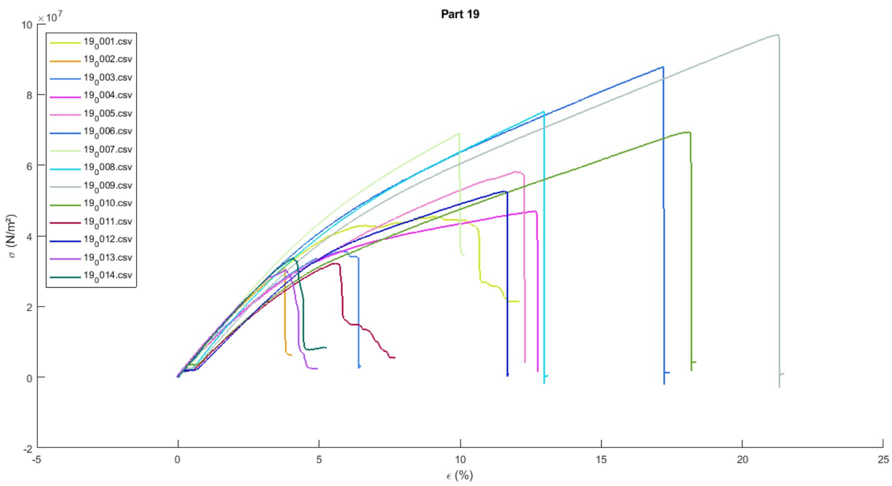

Figure 3.19: Tensile test : stress-strain curves for the samples cut out from part #19.

sample	Direction wrt. flow	Young modulus (Pa)	Stress at failure (Pa)
19_5	longitudinal	7.4183e+06	5.81e+07
19_6		8.3479e+06	8.78e+07
19_7		8.8341e+06	6.89e+07
19_8		8.5823e+06	7.05e+07
19_9		7.8069e+06	9.68e+07
19_10		6.7755e+06	6.93e+07
mean		7.9611e+06	7.52e+07
standard deviation		7.7757e+05	1.42e+07
19_1	transversal	7.4473e+06	4.28e+07
19_2		8.1818e+06	3.09e+07
19_3		6.9875e+06	3.56e+07
19_4		7.4121e+06	4.69e+07
19_11		6.8515e+06	4.54e+07
19_12		7.6788e+06	5.23e+07
19_13		8.5879e+06	3.02e+07
19_14		8.6612e+06	3.38e+07
mean		7.7260e+06	3.97e+07
standard deviation		6.8804e+05	8.21e+06

Table 3.8: Young modulus from the stress-strain curves of samples cut out from part #19.

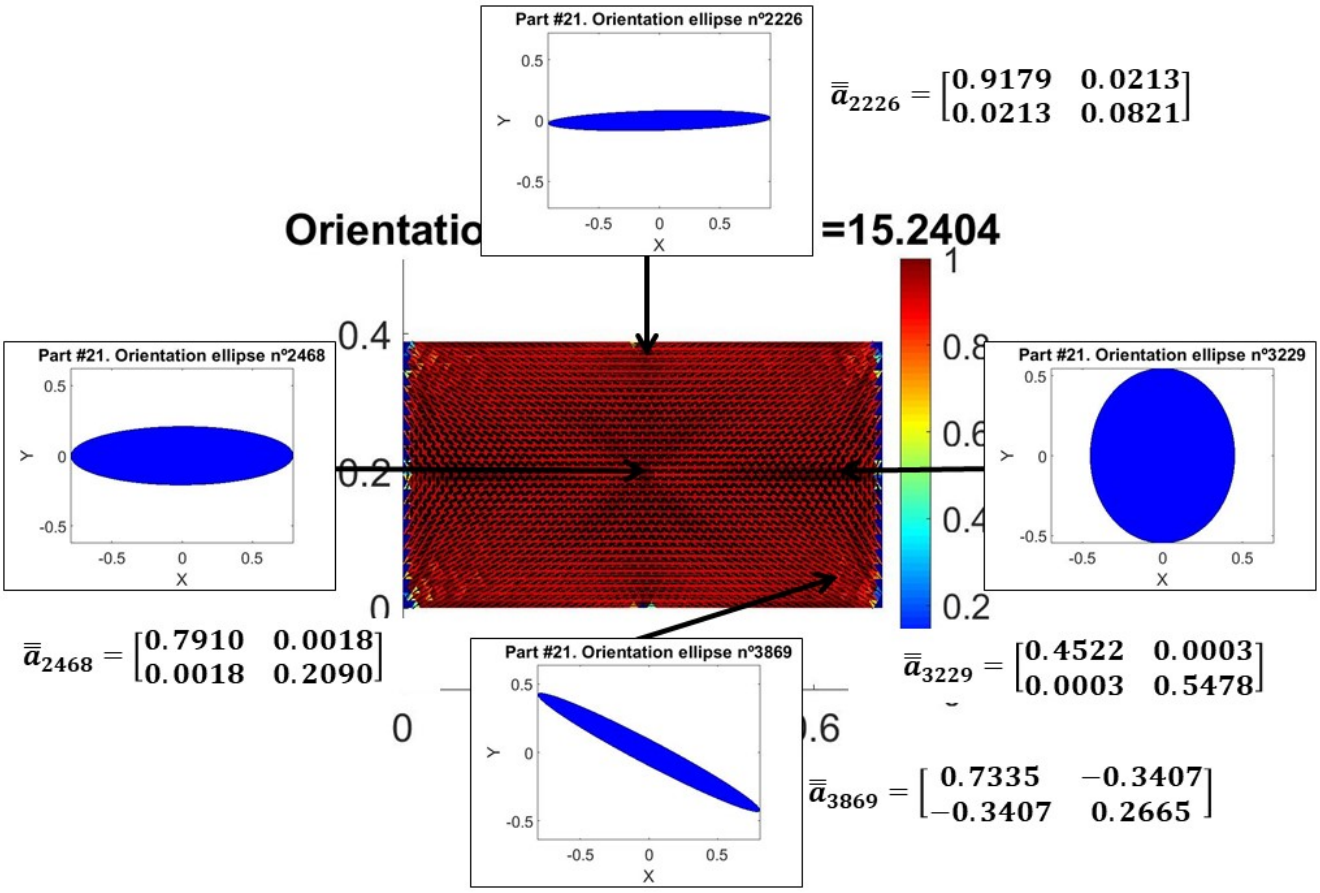

Figure 3.20: Simulated fibre orientation in part #21 (round charge of 265 mm of radius, placed in the center of the mould).

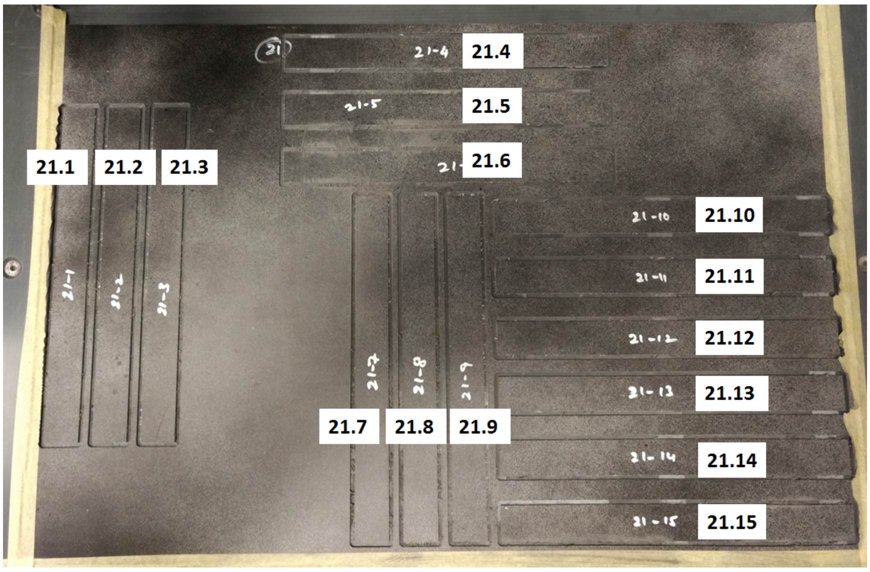

Figure 3.21: Tensile test coupons cut out from part #21.

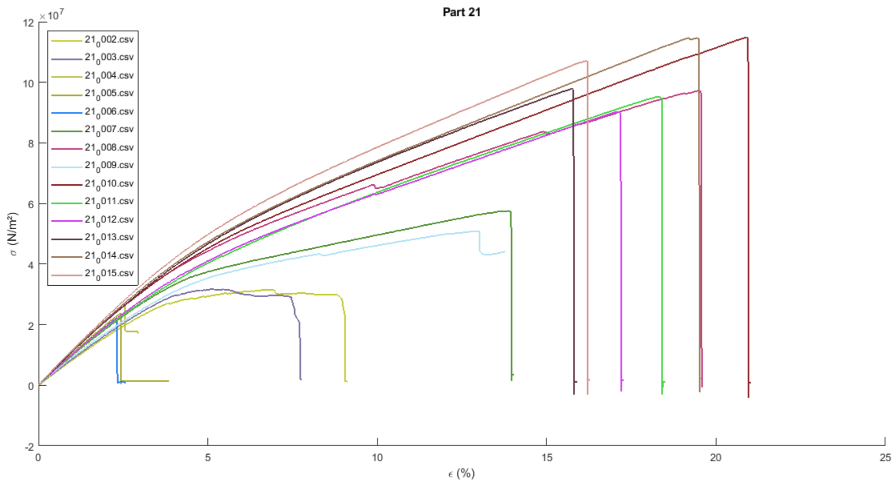

Figure 3.22: Tensile test : stress-strain curves for samples cut out from part #21.

In this case, a different configuration of cutting pattern for the samples has been set looking forward to find some difference form the part 19. The same observations than the one made for the part #19 can be made here.

The results are again in qualitative agreement with the numerical model prediction. Table 3.9 shows the Young moduli and strength for each sample.

The values of the Young modulus are again homogeneous between the curves, and still closer to the value of the Young modulus of the samples cut in transverse direction of the flow from samples 8 and 35. The dispersion of the values of the ultimate strength to failure shows, again, more dispersion than in the previous cases.

3.5 Through-thickness evolution of the fibre orientation.

From the parts manufactured in the campaign described in the subsection 3.2, part #1 and part #3 produced with unidirectional flow and 33% of initial charge coverage (see table 3.2) were selected for further analysis. The initial charge consisted in stack of 3 layers or sheets of SMC, of $7,8 \pm 1mm$ of total initial thickness. The SMC panels were processed with the

sample	Direction wrt. flow	Young modulus (Pa)	Stress at failure (Pa)
21_4	longitudinal	7.9159e+06	2.62e+07
21_5		7.2926e+06	2.37e+07
21_6		7.4794e+06	2.22e+07
21_10		7.5748e+06	1.15e+08
21_11		7.2415e+06	9.51e+07
21_12		7.1240e+06	9.01e+07
21_13		8.4023e+06	9.79e+07
21_14		9.2484e+06	1.14e+08
21_15		9.0019e+06	1.07e+08
mean		7.9201e+06	6.21e+07
standard deviation		7.8809e+05	4.24e+07
21_1	transversal		
21_2		6.1796e+06	3.15e+07
21_3		1.5847e+07	3.17e+07
21_7		8.5223e+06	5.75e+07
21_8		8.9873e+06	9.72e+07
21_9		8.7533e+06	5.03e+07
mean		9.6579e+06	5.36e+07
standard deviation		3.6387e+06	2.69e+07

Table 3.9: Young modulus and strength for samples cut out from part #21.

upper mould part heated at 165°C whereas the lower mould was maintained at 155°C. These asymmetric thermal boundary conditions are usual in SMC compression moulding of SMC. Actually it is advisable to maintain the upper mold at a higher temperature because of the longer time spent by the charge deposited first in the lower mould. The mould was closed with a force rate of 50 t/s for both parts. The final thickness of each part was $2 \pm 0, 2mm$. Circular samples of 30 mm in radius were cut out along the same theoretical streamline. Fig.3.23 shows the direction of the flow and the locations of samples in the SMC part. Finally the samples were scanned with a microtomograph (X-ray CT-scan device (Micro-XCT400 from Xradia) with the objective Macro70) to visualize in 3D the fiber bundle arrangement.

For each sample, a total of 1440 high resolution images of the cross-section of the samples were recorded (pixel size of $18, 14\mu m$). From these images, the 3D reinforcement structure of the sample was reconstructed using an image processing software; ImageJ in this case (see fig. 3.24). The reconstruction of the internal architecture of the whole sample revealed, as discussed in the introduction, several issues that lead the authors to question different aspects of the classical modelling of the squeeze flow of the SMC compression moulding. These observations are listed below.

1. The alignment or degree of orientation of fibres

- changes along the same flow line, unlike prediction of classical models.
- evolves in the trough-thickness direction of the sample following patterns that are in disagreement with the theoretical velocity profile of the fluid flow models.

2. Some fibre bundles widened and in more extreme situations filamentized into individual glass fibres. Therefore, two very different populations of fibres coexist in the same material: fibre bundles and individualized fibres.

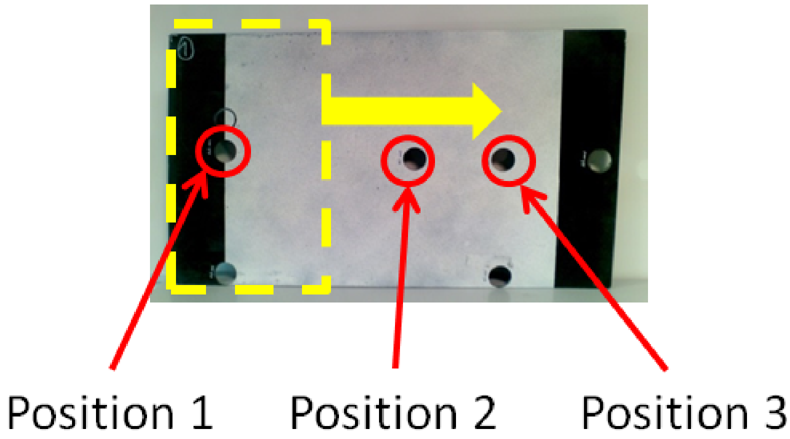

Figure 3.23: Flow direction and locations of samples in part #1.

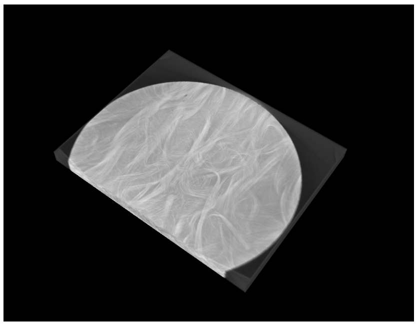

Figure 3.24: 3D reconstruction of the X-ray microtomograph cross-section images.

3. Some fibre bundles are strongly curved.

At each different position of each part, the scanned images from nine equidistant planes in the through thickness direction of the sample were discriminated and examined. The orientation of the reinforcement fibres was measured by three different means: manually and with two different image processing software packages: ImageJ and MountainsMap. The manual measure was done drawing lines following the direction of each tow or family of fibres, and measuring the angle of each one of the drawn lines with respect to the flow direction. ImageJ is a Java based public domain image processing software that allows a great versatility in the analysis of the orientation of objects in images. The plug-in OrientationJ for ImageJ was used in this case to analyse the orientation of the glass fibres (ref del. It provides an odf (orientation distribution function) of the fibres, giving the population of the fibres against their orientation in degrees. MountainsMap is an image analysis software designed to measure the surface topography or surface textures. It's directionality tool allows to plot the odf, either lineally or radially. The different methodologies of measurement are extensively analysed and discussed in the Chapter 5.

The components of the orientation tensor can be easily obtained from the odf of each image [2]. Fig.3.25 shows the evolution of the orientation of the reinforcement fibres measured by hand, represented by their orientation ellipse, for the series of samples cut out from each SMC part, at the positions indicated in fig.3.23.

At first sight, in the upstream locations where the initial charge was placed, the anisotropy in orientation seems to increase from the top to the bottom, whereas this trend is not verified at the positions downstream where the alignment tends to be higher in the midplane. Another finding is that the principal direction of alignment is not necessarily conserved from one location

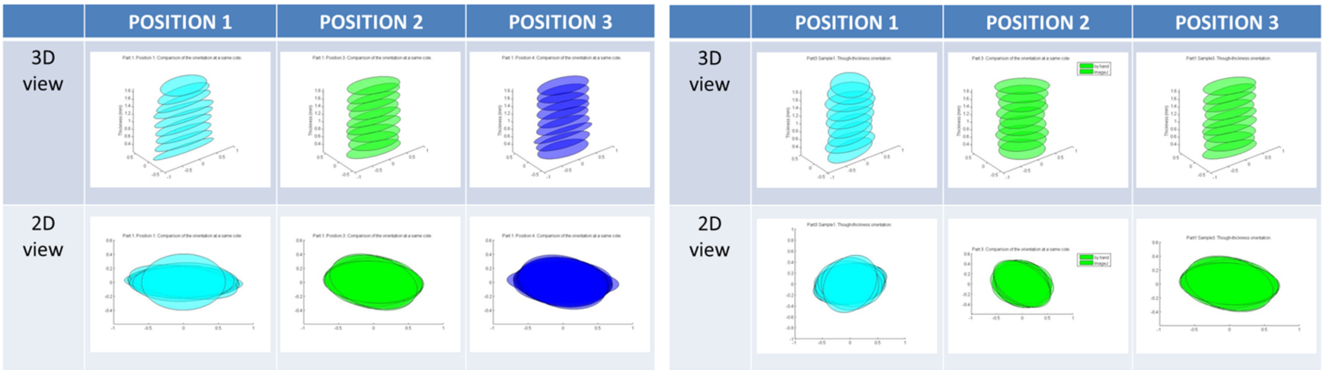

Figure 3.25: Orientation ellipses of samples cut out from part #1 (left) and part #3 (right).

to the next, even if they are in the same theoretical flow line. These findings are confirmed when analyzed plane by plane, it is clear that the alignment is more pronounced in the upstream positions, where this effect is more marked in part #1 (see table 3.10) than in part #3.

From these observations, one can conclude that the orientation distribution does not match the theoretical prediction of the proposed model, either in the through-thickness direction (since it should be symmetric) or in the main flow direction (since there should not be any evolution of the alignment). As already discussed, the best known and acknowledged theoretical models to describe the squeeze flow of a Newtonian fluid in a thin cavity are the Hele-Shaw model with either no-slip boundary conditions, total slip giving rise to the plug-flow model or the partial slip condition. For the partial slip condition case, the only scenario that would lead to a non symmetric velocity profile would be caused by a difference of the values of the slippage in the top and in the bottom interfaces charge-mould. No justification is found a priori for this difference since the mold cavity surface of the upper and lower moulds are the identical.

The difference of conditions between the upper and lower interfaces can then be sought in the heat transfer through the charge. The time from the SMC compound contacting the hot lower to the one when the hot upper mould comes in contact with the charge, an unbalanced heating condition is generated. The charge starts to be heated from its bottom, and a temperature gradient has been created through the thickness of the sample. This gradient is sometimes tried to be compensated by increasing the temperature of the upper half of the mould with respect to the lower half, so when it reaches the charge its higher temperature homogenizes the temperature in the charge faster. But the temperature of the upper platen can only be increased by some degrees, since the temperature needs to be in the range of the operational temperature of the SMC material. In addition the typical and mould closing and compression times are of 10 seconds in total.

3.6 Through thickness evolution of the filamentization of fibre bundles.

The analysis of the scanned images of SMC samples discussed in the subsection 3.5, revealed an evolution the fibre orientation distribution in the through-thickness direction, but also a gradient of the degree of filamentization of fibre bundles.

During the compounding (manufacturing) of the SMC sheets, the discontinuous reinforcement fibres are distributed in the matrix paste in the form of tows or fibre bundles of about 200 individual fibres each. Their length ranged in between 25 and 50 mm and their cross-section is usally approximated by an ellipsoidal shape whose major axis ranges from 500 μm to 1000 μm and its minor axis fluctuates between 60 μm and 200 μm ([61]). During the com-

z (mm)	ORIENTATION ELLIPSE OF PART #1	ORIENTATION ELLIPSE OF PART #3
1.89	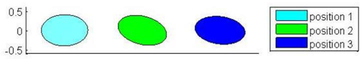	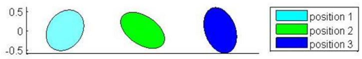
1.68	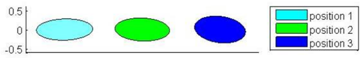	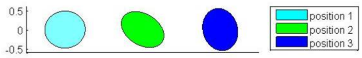
1.47	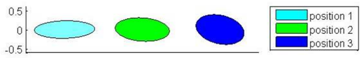	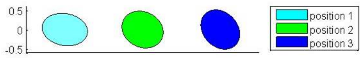
1.26	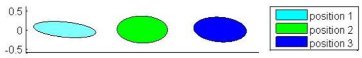	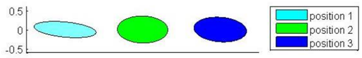
1.05	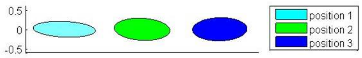	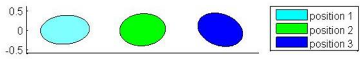
0.84	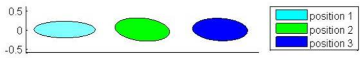	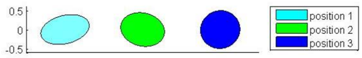
0.63	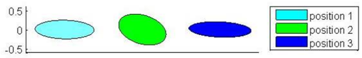	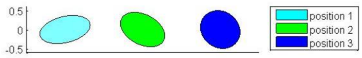
0.42	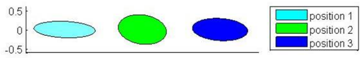	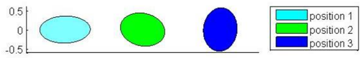
0.21	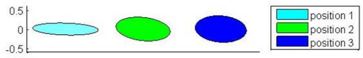	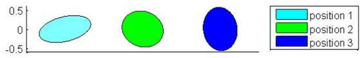

Table 3.10: Orientation ellipse of fibres of each image in the series.

pression phase in industrial conditions, the shear induced by the flow affects the integrity of fibre bundles, which tend to open up and individualize into single fibres in a process known as filamentization.

Images analysed in subsection 3.5 gave the evidence that this phenomenon does not occur uniformly neither in the through-thickness direction of each sample nor in the flow direction, as is also the case for the mechanism of fibre alignment. Fig. 3.26 illustrates the different degree of filamentization of fibre bundles in two images taken at two different altitude in the same sample in part#1. Moreover, these images show how the filamentization is a complex phenomena where the same bundle can be completely disintegrated or only partially opened up, either towards its ends or its center.

These observations raise a new question : are the filamentization and the fibre orientation distribution directly related? Both images in fig.3.26 show a preferential alignment fibres towards the direction of the flow. However the left hand side image taken close to the top surface

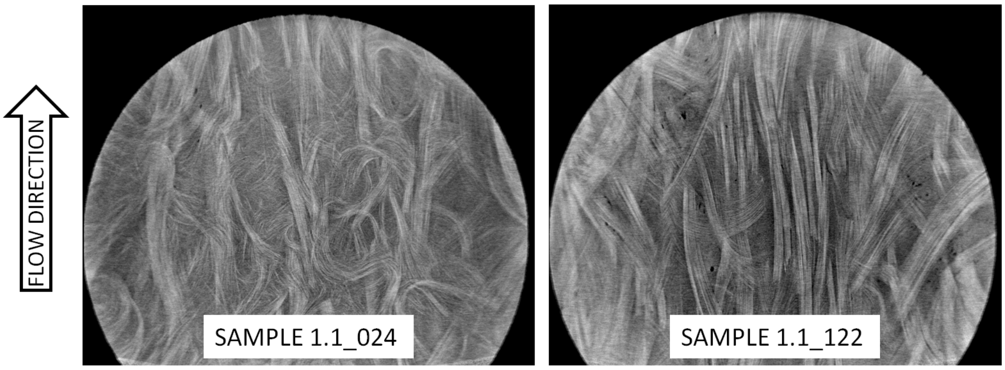

Figure 3.26: Different degrees of filamentization in images taken at two different altitudes in the same sample PART #1.

shows both a higher degree of isotropy and a higher level of filamentization than the right hand side image taken closer to the bottom surface. The force needed to drag and orientate a fibre bundle is necessarily higher than the one needed to convect and orientate a single fibre. However, the fibre alignment is more pronounced in the right hand side image where the degree of filamentization seems lower. Therefore, if there is a link between the two phenomena, it is direct and it would be necessary to determine the factors that rule the relation. It is worth to note that a symmetric through-thickness velocity field should lead to a symmetric degree of filamentization with a maximum in the vicinity of both mold surfaces, which is not observed here. Another characteristics is that the opening of the fibre bundles seems higher in the ones that are placed in the direction transverse to the flow front than in those which are in its direction.

To better understand the origin of filamentization and its possible relation with the fibre orientation, a manual measure of the degree of filamentization was performed in the same series of images from the sample 1, whose orientation was measured and shown in the subsection 3.5. A count of fibre bundles and a measure of their width was performed (fig.3.27) and compared with a reference image from a reference sample being an uncompressed polymerized sample of raw SMC material (see fig. 1.1). A uniform length was supposed for all bundles visible in the image. In fig.3.28, a first measure of the filamentization is proposed defined as the area occupied by the bundles in every image if its length was unitary. This measurement is made at various altitudes at the three locations defined in the table 3.10, for the part #1. No clear evolution can be deduced from this indicator. In position 1, the value of this indicator is greater in the upper half of the sample, and is bigger in the vicinity of the top charge-mould interface than in the vicinity of the bottom interface. In positions 2 and 3 there is an increase of the indicator towards the midplane, and is greater close to the bottom interface than close to the top interface.

In the light of these results, a more appropriate descriptor has been sought. Tables 3.11, 3.12 and 3.13 show the population of bundles of each image and an histogram with the distribution of the bundle widths. Fibre bundles whose width was greater than 5 mm were considered to be completely filamentized, where the mean bundle width in the reference sample was 0.7 mm. Since the bundle with may also vary along its length, a mean value has been assigned for each bundle.

Tables A.1,A.2,A.3, and A.6 and A.9 in appendix A show the histogram with the distribution of the width of the fibre bundles next to the image they were measured from.

From the analysis of the histograms in tables. 3.11, 3.12 and 3.13 , the following conclusions are drawn:

1. Two different mechanisms that cause a change of the fibre bundles width during the

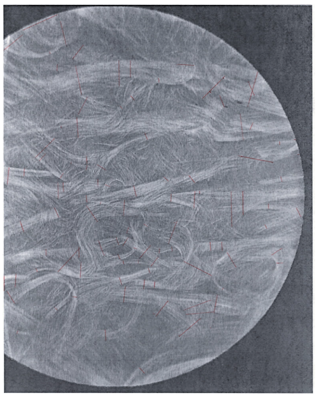

Figure 3.27: Manual measure of the width of the bundles from images at various altitudes.

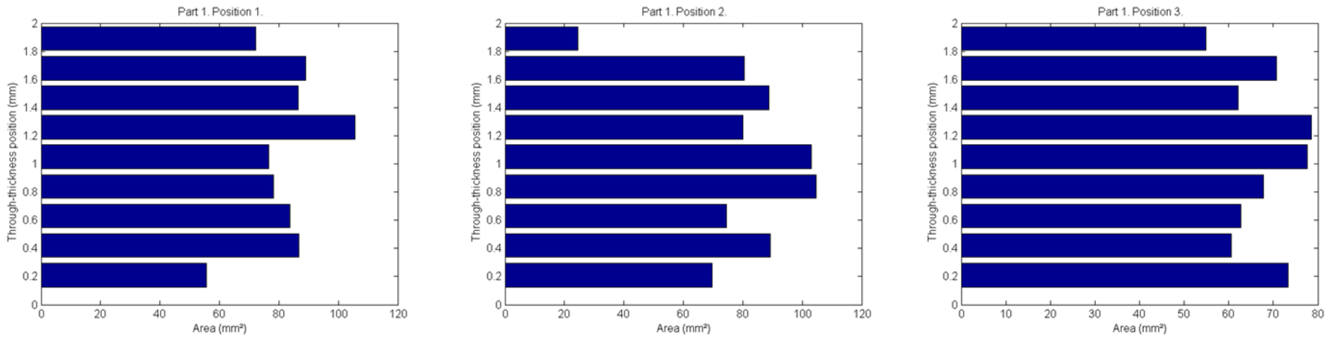

Figure 3.28: Area occupied by the bundles in every image if their length was unitary.

compression moulding were identified, dependent on the direction of the shear. The first is the filamentization phenomenon. Some bundles open up due to the transverse shear in the direction of the flow and the fibres spread, increasing the initial dimensions of the bundle. As the shear increases, the filamentization continues until the point where the bundle is not longer recognizable, turning into individual fibres or much smaller bundles of fibres. Second, there is a breakage along the longitudinal axis of the fibre bundle that might be caused by a severe bending in the transverse direction of the fibre bundle. The initial bundle subdivides in two or more smaller bundles.

2. The filamentization mechanism is the principal mechanism that leads to the individualization of fibre bundles close to the mould/charge interface. Because the shear stress is high close to the mould/charge interface, the mechanism of filamentization is predominant there and the breakage along the longitudinal axis is much less likely to happen. In these zones, the degree of filamentization is such that many bundles are completely split into individual fibres.

3. Close to the midplane of the part it is found that fibre bundles can widen but not the point where they split into individual fibres.

4. The degree of filamentization is asymmetric. Moreover, the face submitted to a greater shear stress is not necessarily always the bottom one, since the filamentization can be higher closer to the top surface.

4. The filamentization affects more intensively fibre bundles that are transverse to the main flow direction. The shear necessary to make the bundles spread when they are in this disposition is smaller than in the longitudinal direction.

5. The equivalent viscosity of a charge with individualized fibres is higher than the one of the original SMC charge. Since the filamentization is uneven over the part, an uneven viscosity field is also expected.

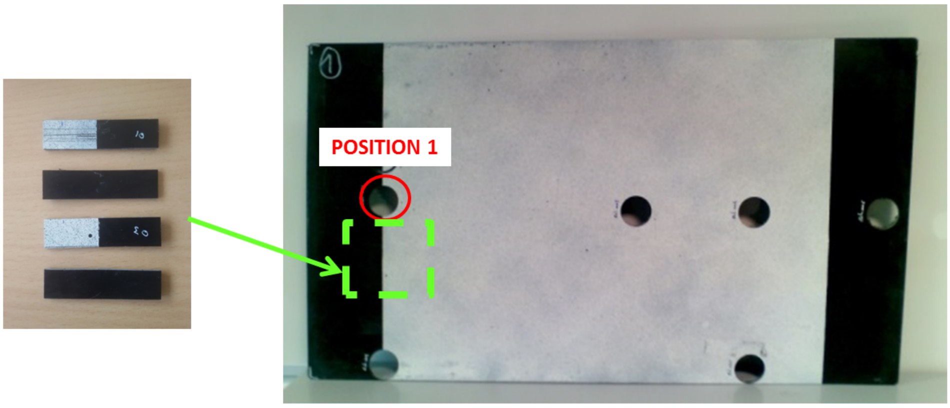

Figure 3.29: Position of the samples for the bending test in the part #1.

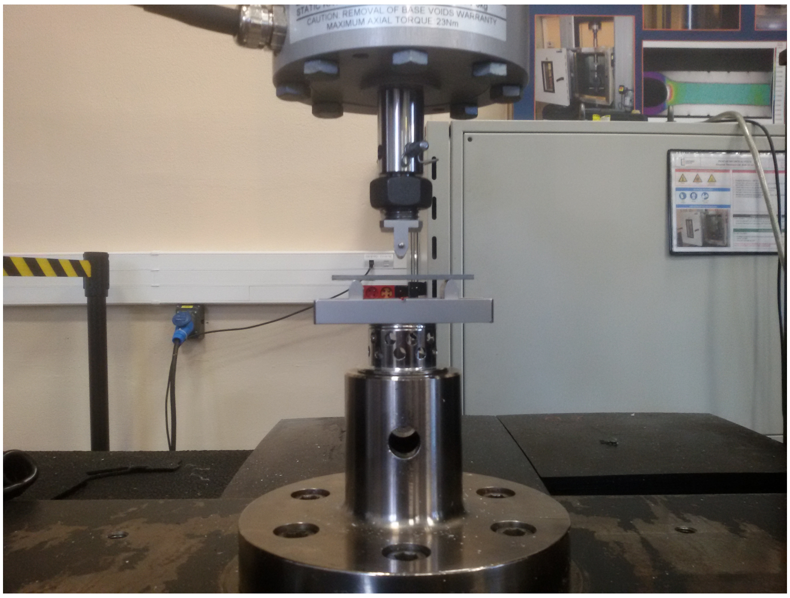

Figure 3.30: Set up for the 3-point bending test.

3.7 3-point bending test.

The asymmetric distribution of fibres can affect the bending response of the SMC when comparing the test coupons are turned upside down. Three-point bending tests were carried out on samples cut out from part #1 in region 1 where a marked asymmetric distribution was evidenced (see fig. 3.29). 4 samples of planar dimensions 60 mm x15 mm were tested according to the EN ISO 14125 standard. The distance between between supports was shortened to 40 mm instead of 64 mm to get higher transverse shear contribution as shown in Figures 3.30 and 3.31.

The specimens 1 and 3 were oriented in the test set-up so as to have their top surface (i.e. the surface in contact wit the upper part of the mould) in the compression zone, as indicated in fig.3.32. Samples 2 and 4 were turned upside down before testing. The objective is to check if the asymmetric through-thickness distribution of fibres was large enough to cause a different bending response. The four responses are shown in fig.3.33. The initial stiffness is very similar, however it is not possible to conclude about the strength due to the marked difference between the samples 1 and 3.

Then the asymmetric through-thickness distribution of fibres cannot be revealed by this test.

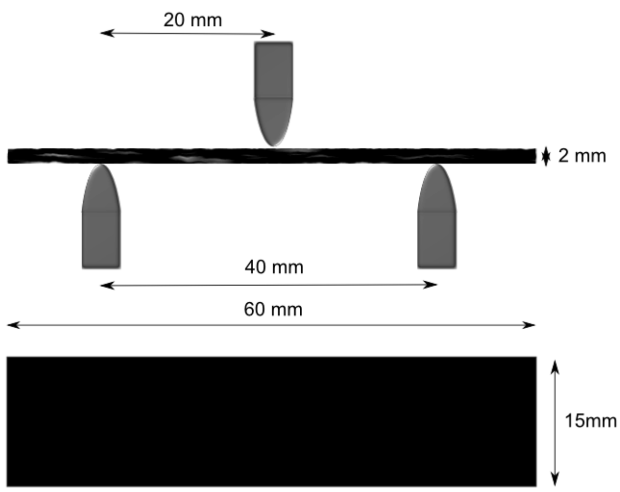

Figure 3.31: Set up for the three points bending test.

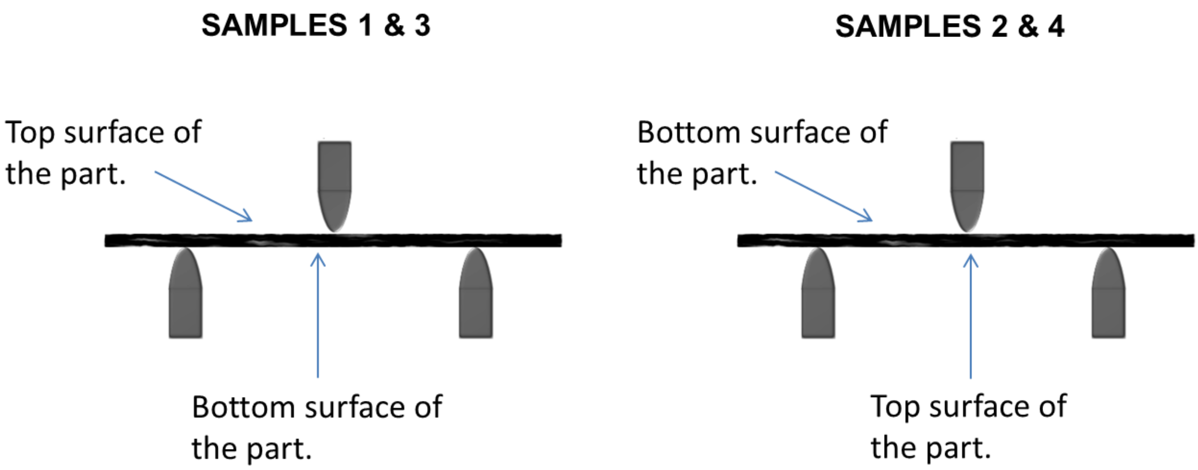

Figure 3.32: Specimen tested with the top surface up and upside down.

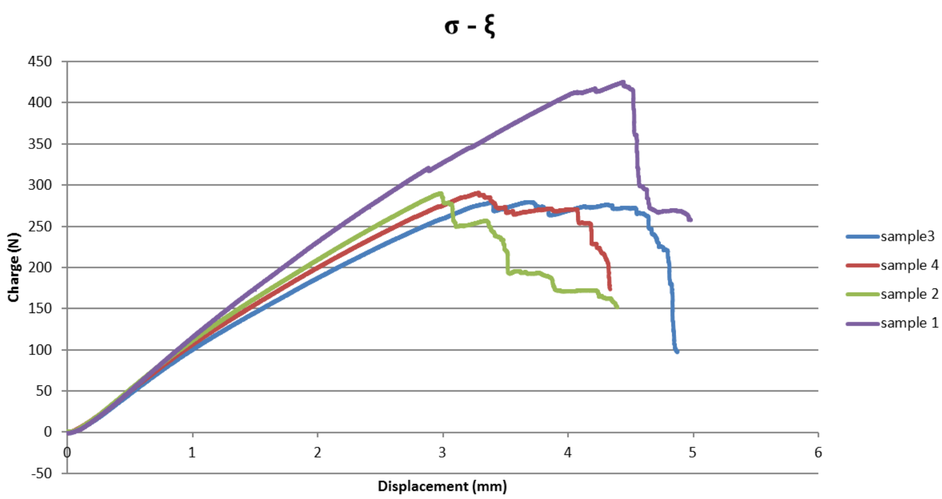

Figure 3.33: Mechanical responses of samples 1-4 subjected to 3-point bending test.

3.8 Conclusions of chapter 3.

The main conclusions of this chapter are listed below.

- The tests conducted are form SMC parts produced under actual industrial conditions.

Tensile tests on full parts test.

- The results of the test on full parts are in qualitative agreement with the predictions of the numerical model. Uniform values of the strain field are measured in parts where the model predicted uniform alignment of the fibers. The strain field show more isotropic values in parts where an isotropic distribution of the orientation of the fibers is expected.

  The results of the test on regions of the part show discrepancies with the local predictions of the numerical model in the parts where an isotropic distribution of the orientation is expected. Two possible causes can be considered: either the test is not sensitive enough to capture the local elastic behaviour of the part, or the distribution of fibres on the part is more isotropic than what the numerical model predicts.

Tensile tests on coupons.

- The trends observed in the tests are in qualitative agreement with the numerical model prediction.
- In the parts with unidirectional flow, the coupons are stiffer and more resistant in the direction of the flow. No determinant conclusions can be done from the ultimate strain at break.
- In parts with combined flow, the stiffness and the Young moduli are more homogeneous no matter the direction of the coupons. The dispersion of the values of the ultimate strength is bigger than in the previous case.

Microstructural analysis of scanned samples. Orientation.

- The alignment of the fibres changes along the same flow line in parts of unidirectional flow, and evolves in the through-thickness of the sample following patterns that disagree wiht the theoretical velocity profiles
- Two different populations of fibres co-exist in the same material: fiber bundles and filamentized individual fibres.

Microstructural analysis of scanned samples. Filamentization.

- The change of the width of the bundles can be caused either because of filamentization of because of a breakage along its longitudinal axis.
- The filamentization is the principal mechanism of individualization of the fibres close tho the mould/charge interface.
- The degree of filamentization is asymmetric in the through-thickness direction.
- The filamentization affects more intensively the fiber bundles transverse to the flow direction.
- An uneven viscosity field can be expected due to the uneven filamentization.

<table>
<tr><th>z (mm)</th><th>POSITION 1</th><th>POSITION 2</th><th>POSITION 3</th></tr>
<tr><td>1.89</td><td>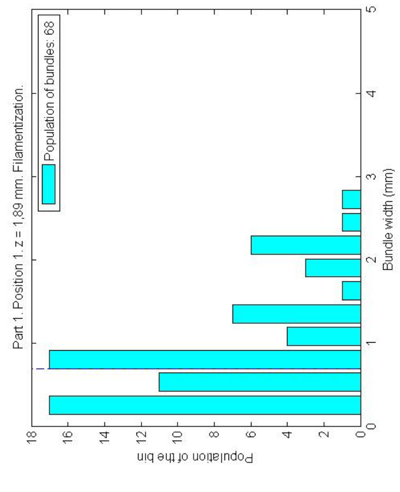
</td><td>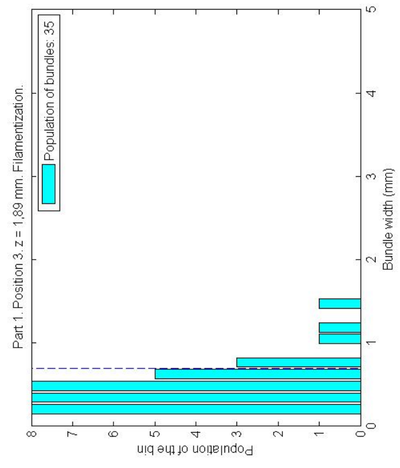
</td><td>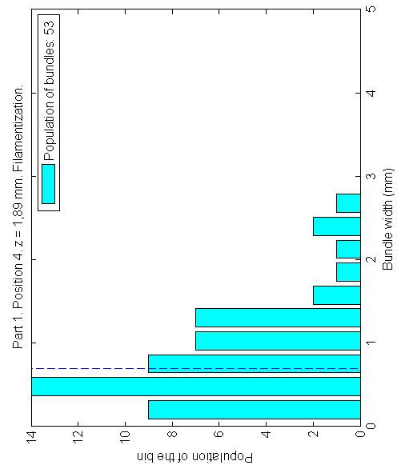
</td></tr>
<tr><td>1.68</td><td>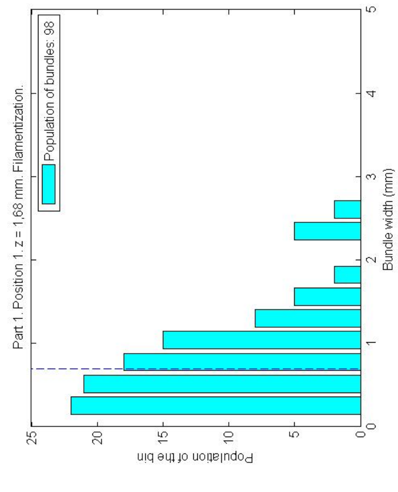
</td><td>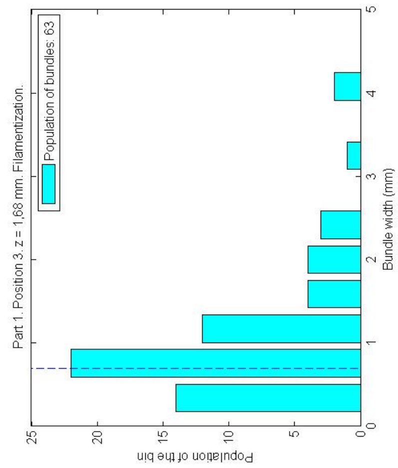
</td><td>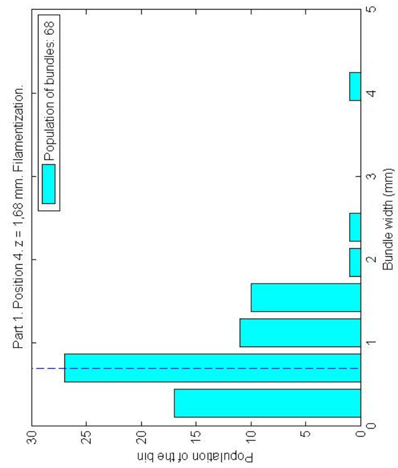
</td></tr>
<tr><td>1.47</td><td>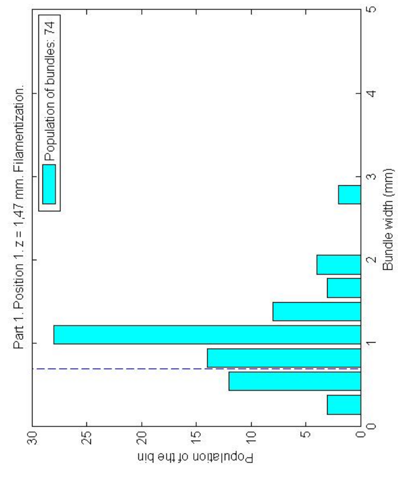
</td><td>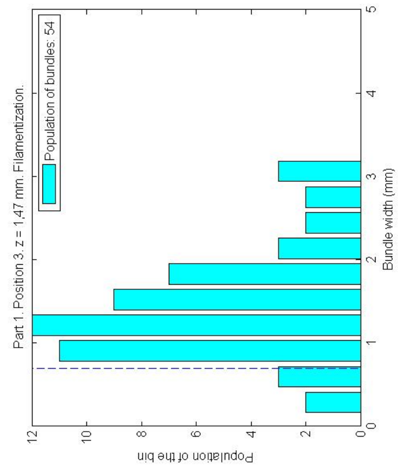
</td><td>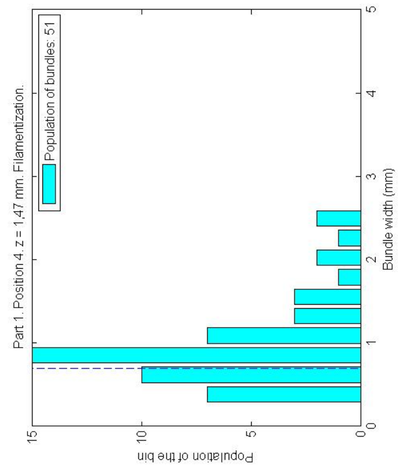
</td></tr>
</table>

Table 3.11: Distribution of the fibre bundle width at different altitudes in samples taken form 3 regions in part #1.

z (mm)	POSITION 1	POSITION 2	POSITION 3
1.26	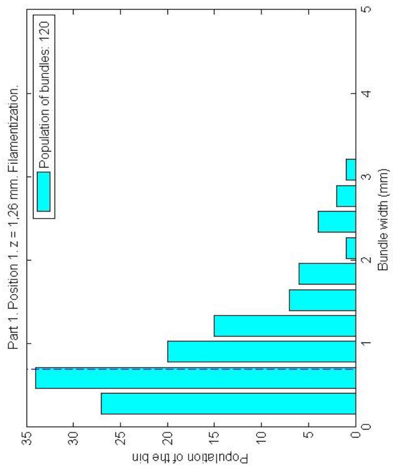	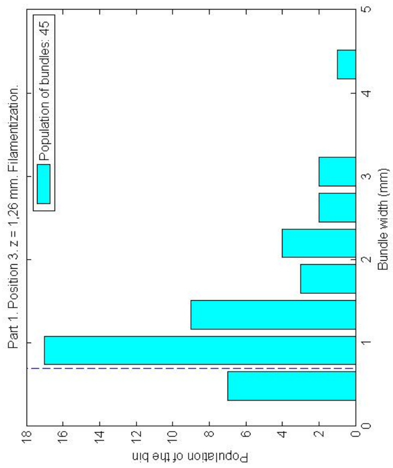	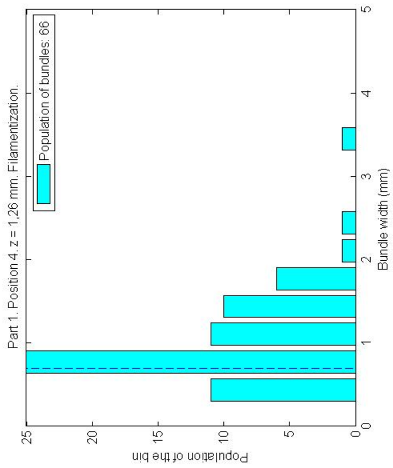
1.05	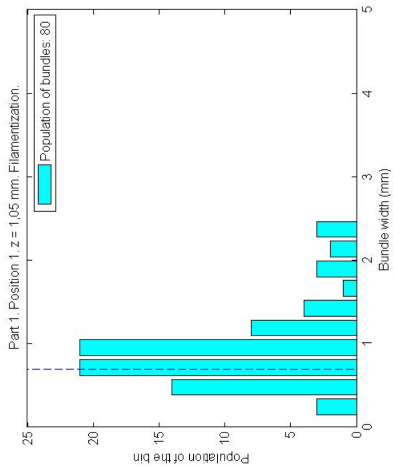	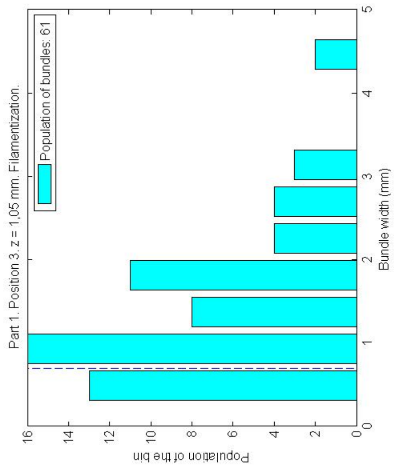	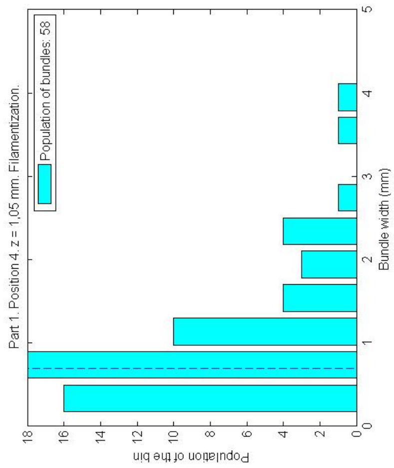
0.84	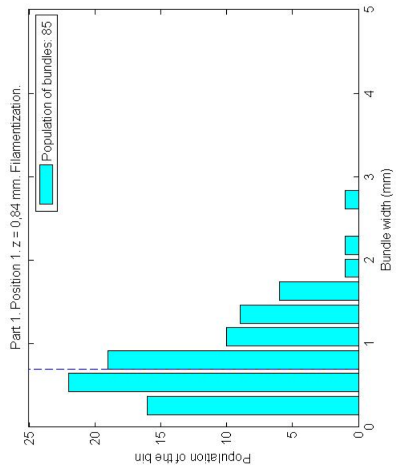	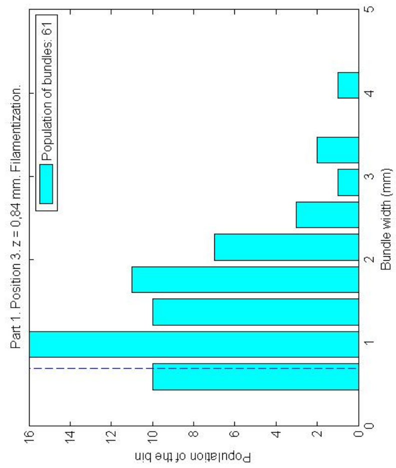	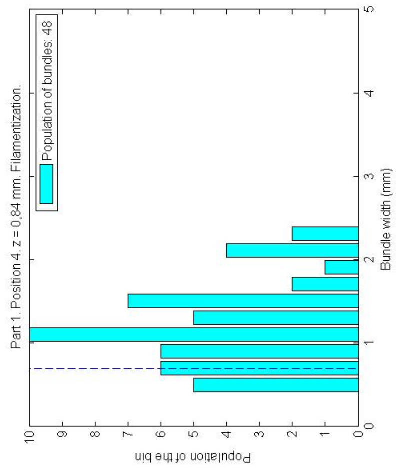

Table 3.12: Distribution of the fibre bundle width at different altitudes in samples taken form 3 regions in part #1.

<table>
<tr><th>z (mm)</th><th>POSITION 1</th><th>POSITION 2</th><th>POSITION 3</th></tr>
<tr><td>0.63</td><td>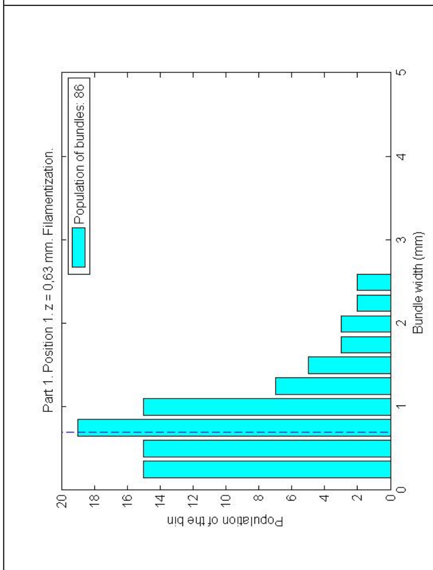
</td><td>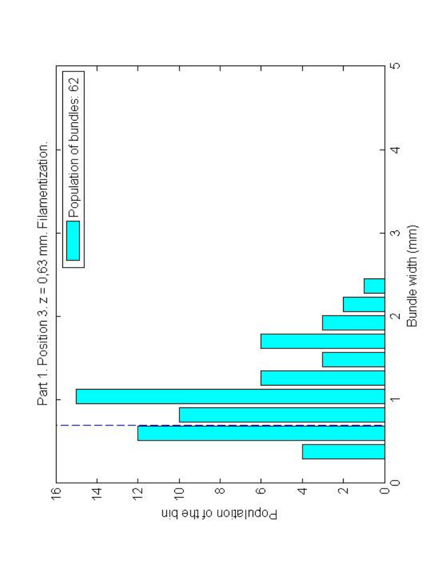
</td><td>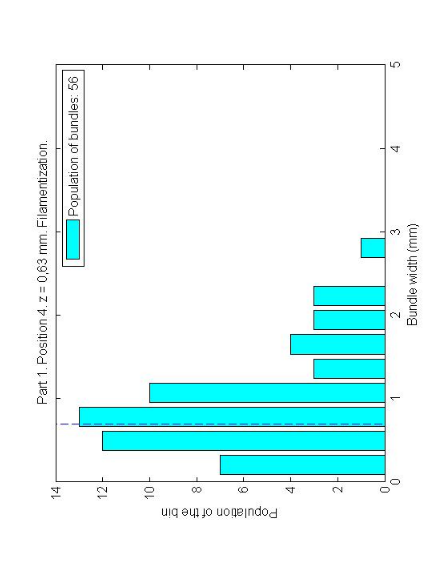
</td></tr>
<tr><td>0.42</td><td>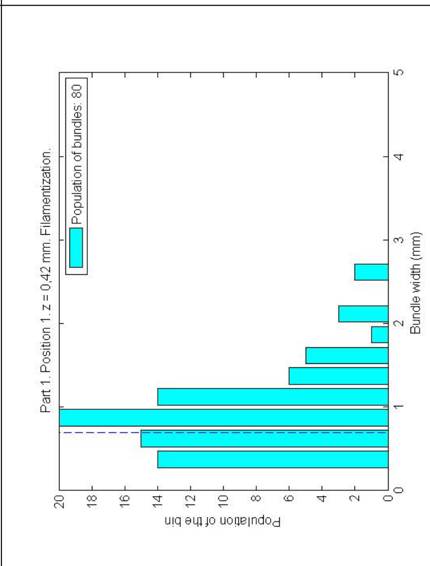
</td><td>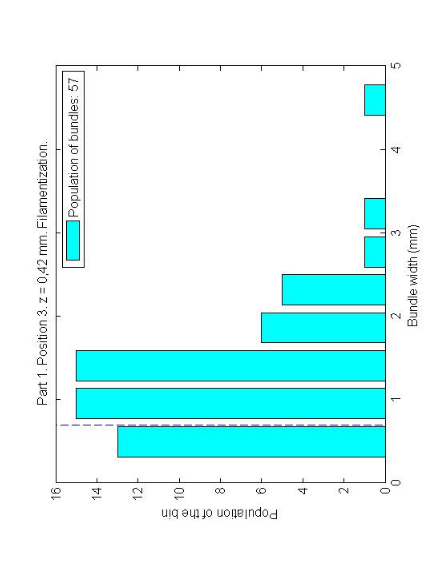
</td><td>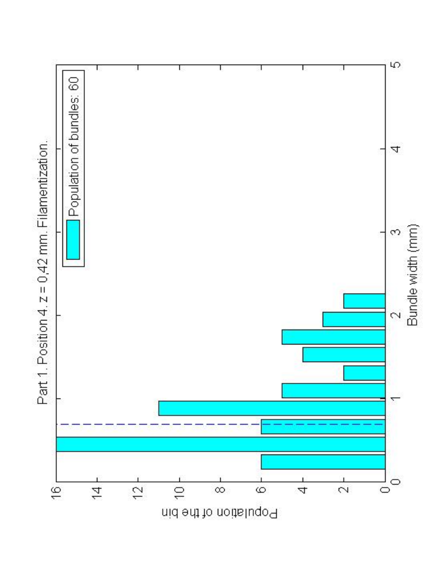
</td></tr>
<tr><td>0.21</td><td>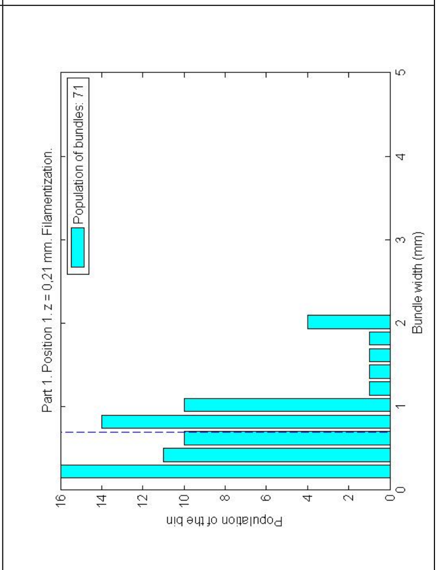
</td><td>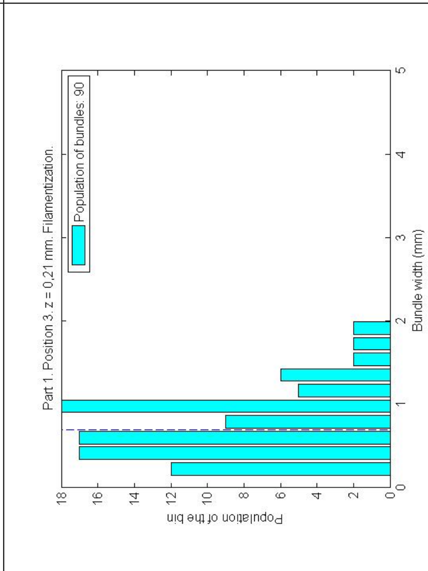
</td><td>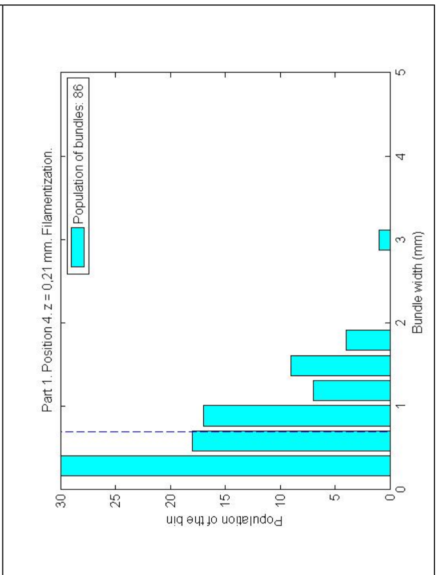
</td></tr>
</table>

Table 3.13: Distribution of the fibre bundle width at different altitudes in samples taken form 3 regions in part #1.

Chapter 4

2.5D non-isothermal numerical model.

4.1 Introduction.

The analysis of the microstructure of the samples indicated that a realistic through-thickness velocity profile is required to obtain the real through-thickness distribution of the fiber orientation. These experimental findings revealed that the velocity profile is not symmetric and that the maximal shear plane is not at a constant position in the through-thickness z direction. When looking for the source of such asymmetries, the two main factors that come to mind are the possible slippage at the mould/material interface, and/or the heat transfer through the SMC material. However, about the slippage, it should have a different value at the top and bottom contact surface to induce such a symmetric response. Since the SMC charge is initially (quasi)-isotropic and the material and treatment of both mould halves is identical, this scenario is not kept. Therefore, the decision was made to extend the numerical model to incorporate the heat transfer. The proposed model is based on the assumption that no significant curing occurs during the filling of the mould.

4.2 Heat transfer

The general heat equation reads as in equation 4.1.

$$\rho C_p \frac{\partial T}{\partial t} + u\frac{\partial T}{\partial x} + v\frac{\partial T}{\partial y} = K\frac{\partial T^2}{\partial z^2} \tag{4.1}$$

Where ρ is the density of the composite material, C_p its heat capacity under constant pressure, u and v are the in-plane components of the velocity of the material, and K is the thermal conductivity of the SMC charge. Assuming that the temperature profile is fully developed in the in-plane directions, the temperature gradients in the directions x and y are negligible, and 4.1 is simplified as 4.2.

$$\rho C_p \frac{\partial T}{\partial t} = K\frac{\partial T^2}{\partial z^2} \tag{4.2}$$

The heat transfer during the SMC compression moulding can be split in two separate phases, where the thermal boundary conditions change. The first stage consists in depositing the SMC charge over the bottom surface of the mould and close the mould to be in contact with the SMC charge. During this step, the bottom side of the charge is in contact with the hot mould, while the upper side of the charge will be heated by convection with the warm air between the charge and the hot mould. The boundary conditions during this first stage are then expressed as 4.3.

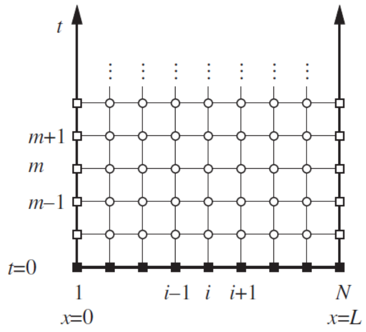

Figure 4.1: Mesh on a semi-infinite strip used for solution to the one-dimensional heat equation.[71]

$$-K\frac{\partial T^2}{\partial z^2} = h_\infty (T_S - T_\infty)$$
$$T = T_I \tag{4.3}$$

where T_S and T_I are the temperature of the upper and lower sides of the charge respectively, T_∞ is the temperature of the ambiance around the charge and h_∞ is the coefficient of heat transfer.

During the second stage the mould is closed, both mould halves are in contact with the charge . The related boundary conditions are expressed by 4.4.

$$T = T_S$$
$$T = T_I \tag{4.4}$$

The resolution of 4.2 along the thickness of the fluid charge inside the mould (variable in the time since the mould is closing), gives the distribution of the temperature in the material during the compression.

4.2.1 Approximation to the solution of the heat transfer equation by finite differences.

The Finite Difference Method (FDM) consists in replacing a continuous partial differential equation (PDF) with a *difference formula* whose discrete solutions approximate to the solutions of the PDF [78]. In the FDM method, the discrete solutions are obtained in points, called nodes as in the FEM), whose topography describes a regular mesh (see fig. 4.1).

While in the PDE there are spatial derivatives and time derivatives, the spacing of the mesh depends on the physical distance between the adjacent points, Δx, in one dimension, and their distance in time, or time step, Δt, in the other dimension.

If N is the total number of nodes in the space, and L is the length of the physical domain, Δz is defined in eq. 4.5.

$$\Delta z = \frac{L}{N-1} \tag{4.5}$$

Note that for the introduction of the FDM, the coordinate z is used to explain the formulation, instead of x as it is usually done, to be consistent with the reference system used here. In the same way, if t_{tot} is the time interval where the solutions are sought and M is the number of time intervals, Δt is defined in eq. 4.6.

$$\Delta t = \frac{t_{tot}}{M-1} \tag{4.6}$$

Finally, the finite formulas that replace the PDE are expressed in eq. 4.7.

$$\frac{\partial T}{\partial z} \approx \frac{T_{i+1} - T_i}{\Delta z} \qquad i = 1, 2, ...N \tag{4.7}$$

From the expansion in Taylor series of the dependent variable (as in eq. 4.8), and the use of the mean value theorem to replace the higher order derivatives in it (see [71] for the full development), the finite difference approximation of equation 4.2 can be obtained. The resulting equation 4.9 is called the Forward Time, Centered Space (FTCS) approximation to the heat equation.

$$T(z_i + \Delta z) = T(z_i) + \Delta z \frac{\partial T}{\partial z}|_{z_i} + \frac{\Delta z^2}{2!}\frac{\partial^2 T}{\partial z^2}|_{z_i} + \frac{\Delta z^3}{3!}\frac{\partial^3 T}{\partial z^3}|_{z_i} + ... \tag{4.8}$$

$$T_i^{m+1} = T_i^m + \frac{K}{\rho C_p}\frac{\Delta t}{\Delta z^2}\left(T_{i+1}^m - 2T_i^m + T_{i-1}^m\right) \tag{4.9}$$

where m is the actual time step. A too large time step can lead to unstable solutions that do not converge to the value of the actual PDE. To ensure the stability of the solution, the relation between Δz and Δt given in eq. 4.10, must be respected.

$$\frac{K}{\rho C_p}\frac{\Delta t}{\Delta z^2} < \frac{1}{2} \tag{4.10}$$

4.2.2 Distribution of the temperature profile in the through-thickness direction during the compression moulding process.

Fig.4.2 shows the temperature profile in the thickness of the SMC charge during the mould closing stage. For this simulation the thermal boundary conditions and the typical cycle time used to produce the SMC part, described in section 3.2, have been used. The temperature of the lower mould half is at 150°C, while the one of the upper mould half is at 160°C. To produce a part such as the part 1, described in section 3.2, with an initial coverage rate of the charge of 30%, the mould closing time (first stage of the compression process) is of 4 seconds, and the compression time (second stage of the process) is of 1.93 s. A discretization of the thickness into 50 nodes has been chosen. To conduct the simulation, the following values have been taken: a density of $1.42e + 06g/m3$, a heat capacity under constant pressure (Cp) of $0.9J/(gK)$ and a thermal conductivity of $0.3W/(m \cdot K)$.

The model shows that the influence of the ambient temperature is negligible, while the heat received by conduction from the bottom makes the temperature increase faster at the bottom compared to the top. The short duration of this step in industrial process (a few seconds) prevents the temperature to further homogenize.

As soon as the top mould is in contact with the charge to initiate the compression step, both sides of the SMC charge are at the mold temperature if we assume a perfect contact at the mould/material interface. The through-thickness temperature tends to be more uniform. This trend is further enhanced by the decreasing thickness of the charge that is being compressed. Fig. 4.3 shows the evolution of the temperature profile at different time steps.

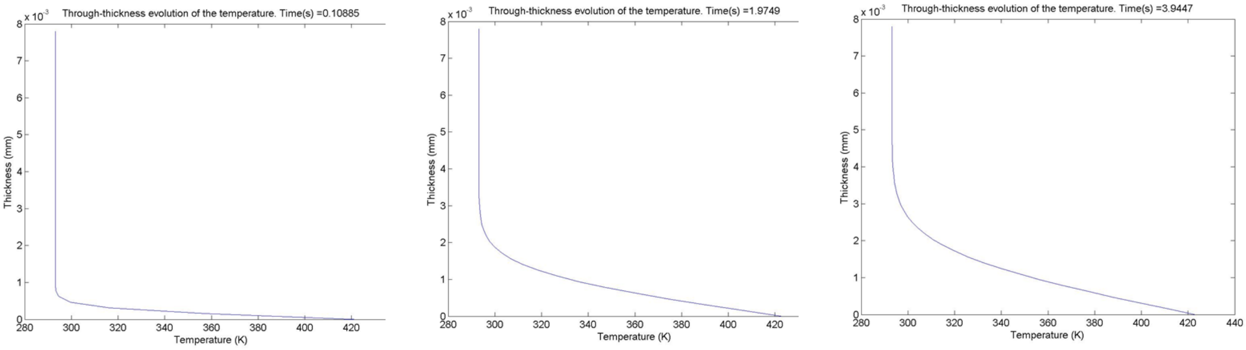

Figure 4.2: Through-thickness temperature distribution of the SMC material during the mould closing stage at times 0.108s, 1.975s and 3.945s from the beginning of the approaching phase.

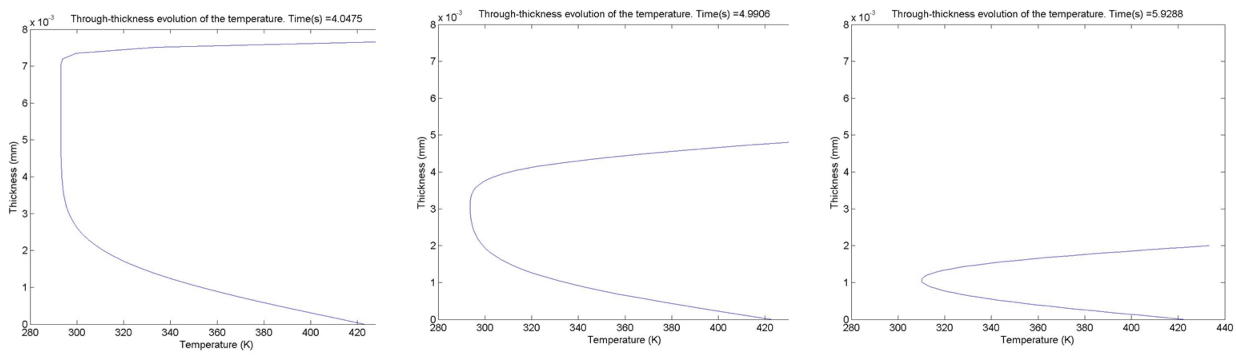

Figure 4.3: Through-thickness temperature distribution of the SMC material during the compression stage at times 4.047s, 4.99s and 5.928s from the beginning of the approaching phase.

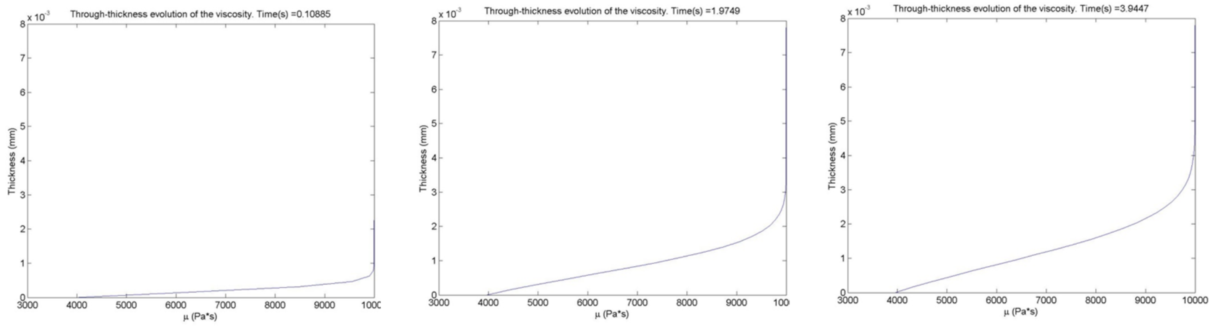

Figure 4.4: Viscosity distribution in the through-thickness direction of the SMC material during the mould closing stage at times 0.108s, 1.975s and 3.945s from the beginning of the approaching phase.

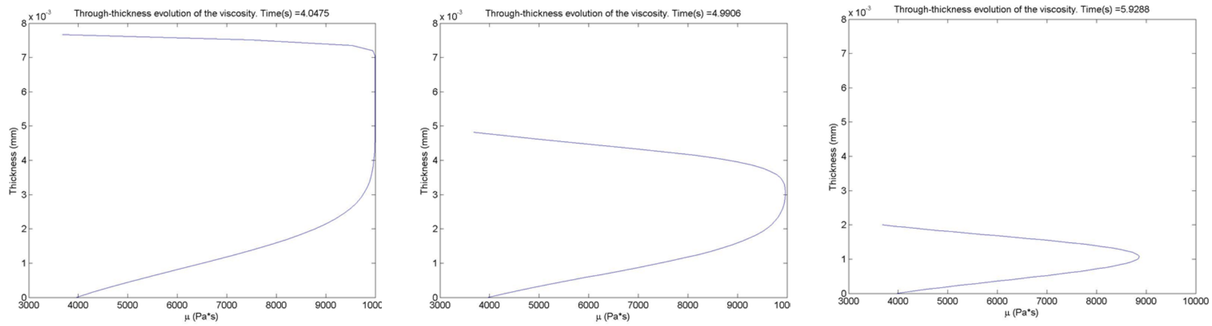

Figure 4.5: Viscosity distribution in the through-thickness direction of the SMC material during the compression stage at times 4.047s, 4.99s and 5.928s from the beginning of the approaching phase.

4.2.3 Evolution of the viscosity in the through-thickness direction of the SMC material during the compression stage.

The heterogeneous temperature field in the material translates into a heterogeneous viscosity field. An Arrhenius-type law is used to relate the material viscosity to the temperature during the compression process.

$$\mu = \mu_0 e^{-b\theta} \tag{4.11}$$

where μ_0 is the characteristic viscosity of the SMC charge, b is a phenomenological parameter whose value can be adjusted to each material through rheological measurement, and θ is a linearization in the thickness of the temperature to adimensionalize and approximate it to $\frac{z}{h}$. Once the evolution of the temperature at each node of the discretization made in subsection 4.2.2 is known, the variation of the through-thickness viscosity is obtained by direct computation of eq. 4.11 at each one of these nodes. Figures 4.4 and 4.5 show the evolution of the viscosity profile at the same time steps of plotting of the temperature profile in the subsection 4.2.2.Due to the lack of data provided by the supplier, a characteristic viscosity of 10000 Pa·s [76] and a unitary value of b have been taken to perform the simulation.

4.2.4 Through-thickness velocity profile under non-isothermal condition.

The objective of this subsection is to modify the current model to take into account the through-thickness evolution of the material viscosity, while applying the hydrodynamic lubrication approximation. The resulting velocity profile will be then averaged in the thickness direction to obtain a value of velocity for each finite element when solving for the material flow, however the full velocity field is used to compute the through-thickness orientation of fibers.

Considering now a non-constant viscosity , the Stokes equation is then modified to get Eq. 4.12.

$$\frac{\partial P}{\partial x} = -\frac{\partial \left(\mu\left(z\right)\frac{\partial u}{\partial z}\right)}{\partial z} \tag{4.12}$$

Eq. 4.12 cannot be solved to obtain an analytic expression of the distribution of the velocity u in the out-of-plane direction for the chosen viscosity model (4.11). The FEM method is then employed to solve for the viscosity dependent velocity profile. The derivation of the FEM model is presented in the following subsections.

4.2.4.1 Variational formulation.

In this subsection, the formulation of the problem is expressed into its weak form.

$$\int_0^h u^* \left(\frac{\partial P}{\partial x} + \frac{\partial \left(\mu\left(z\right)\frac{\partial u}{\partial z}\right)}{\partial z}\right) dz = 0 \tag{4.13}$$

Eq. 4.13 is integrated by parts to get

$$\int_0^h u^* \frac{\partial P}{\partial x} dz + \left[\left\{u^* \mu\left(z\right)\frac{\partial u}{\partial z}\right\}_0^h - \int_0^h \frac{\partial u^*}{\partial z}\mu\left(z\right)\frac{\partial u}{\partial z}dz\right] = 0 \tag{4.14}$$

Supposing that the no-slip condition is still verified, the velocity at boundaries is zero (Dirichlet boundary conditions) and the right-hand side term of Eq.4.14 can be neglected, since the function, the velocity in this case, takes a fixed value at the boundaries. Eq.4.14 reduces to Eq. 4.15.

$$\int_0^h u^* \frac{\partial P}{\partial x} dz - \int_0^h \frac{\partial u^*}{\partial z}\mu\left(z\right)\frac{\partial u}{\partial z}dz = 0 \tag{4.15}$$

The same approximation than the one made for the pressure in section 2.0.5.2, is proposed for the velocity function. In this case, the finite elements are uni-dimensional, since they are only defined in the z direction, and, therefore, they only have two nodes.

$$u \simeq \hat{u} = \sum_{j=1}^{2} u_j N_j \tag{4.16}$$

And also for the weight functions.

$$u_i^* = N_i \qquad i = 1, 2. \tag{4.17}$$

With this approximation and shape functions, eq.4.15 becomes Eq. 4.18.

$$\int_0^h [u_1^* \ u_2^*] \begin{bmatrix} N_1 \\ N_2 \end{bmatrix} \frac{\partial P}{\partial x} dz = \int_0^h [u_1^* \ u_2^*] \begin{bmatrix} \frac{\partial N_1}{\partial z} \\ \frac{\partial N_2}{\partial z} \end{bmatrix} \mu(z) \begin{bmatrix} \frac{\partial N_1}{\partial z} & \frac{\partial N_2}{\partial z} \end{bmatrix} \begin{bmatrix} u_1 \\ u_2 \end{bmatrix} dz \tag{4.18}$$

Eq. 4.18 can be rewritten in a compact form in Eq. 4.19

$$f_i = \sum_{j=1}^{2} k_{ij} u_j \tag{4.19}$$

where f_i is the *force vector* and k_{ij} are the components of the *stiffness matrix* of each finite element into which we discretize the domain (the thickness of the SMC charge in this case). The assembly of each element system defined for each element into a global lineal system allows to obtain the solution of the velocity at all nodes in the domain.

4.2.5 Formulation of the pressure field.

Eq. 4.19 expresses the planar dependency of the pressure through the term $\frac{\partial P}{\partial x}$. The linear system defined in subsection 2.0.5.2 to solve the pressure field is then no longer valid, since it was developed for a constant viscosity. Its adaptation to the variable viscosity case is necessary to obtain the through-thickness velocity distribution.

Let's consider the flow rate of the material through a cross-section. It is obtained by integration of velocity in the through-thickness direction, as in equations 2.21 and 2.22. Since the analytical expression to relate the viscosity to velocity is not known, it must be numerically integrated as a Riemann integral [6] [7]. If the mould gap is called H and discretized into small N intervals of the same length so that $H = \sum_{i=1}^{N} h_i = N \cdot h$, the in-plane components of the flow rate can be expressed as in Eqs.4.20.

$$Q_x = \frac{\partial P}{\partial x} h \sum_{j=1}^{N} \zeta_x^i = \zeta_x \frac{\partial P}{\partial x}$$

$$Q_y = \frac{\partial P}{\partial y} h \sum_{j=1}^{N} \zeta_y^i = \zeta_y \frac{\partial P}{\partial y} \tag{4.20}$$

This expression of the flow rate must satisfy the mass conservation Eq.2.20

$$\nabla \cdot \begin{bmatrix} \zeta_x \frac{\partial P}{\partial x} \\ \zeta_y \frac{\partial P}{\partial y} \end{bmatrix} = \dot{h} \tag{4.21}$$

where $\dot{h}$ is the squeeze ratio imposed by the press. Eq. 4.21 is transformed into its weak form following the same procedure as in subsection or subsection 4.2.4.1.

$$\int_\Omega P^* \begin{bmatrix} \zeta_x \frac{\partial P}{\partial x} \\ \zeta_y \frac{\partial P}{\partial y} \end{bmatrix} d\Omega = \int_\Omega P^* \dot{h} d\Omega \tag{4.22}$$

where Ω is the domain of integration. Integration by parts of Eq. 4.22 leads to Eq.

$$\int_{\partial\Omega} P^* \begin{bmatrix} \zeta_x \frac{\partial P}{\partial x} \\ \zeta_y \frac{\partial P}{\partial y} \end{bmatrix} \mathbf{n} d\partial\Omega - \int_\Omega \begin{bmatrix} \frac{\partial P^*}{\partial x} & \frac{\partial P^*}{\partial y} \end{bmatrix} \begin{bmatrix} \zeta_x \frac{\partial P}{\partial x} \\ \zeta_y \frac{\partial P}{\partial y} \end{bmatrix} d\Omega = \int_\Omega P^* \dot{h} d\Omega \tag{4.23}$$

Since the flow cannot cross the limits of the domain, the left-hand side left of Eq. 4.23 must be zero. It simplifies in Eq. 4.24.

$$\int_{\Omega} \left[\frac{\partial P^*}{\partial x} \ \frac{\partial P^*}{\partial y} \right] \begin{bmatrix} \zeta_x \frac{\partial P}{\partial x} \\ \zeta_y \frac{\partial P}{\partial y} \end{bmatrix} d\Omega = \int_{\Omega} P^* \dot{h} d\Omega \tag{4.24}$$

Using the definition of the pressure distribution (eq. 2.40), shape functions (eq. 2.41), pressure gradient (eq. 2.47) and derivative of the shape function (eq. 2.44) given in the subsection 2.0.5.2 to substitute in eq.4.24, the linear system that gives the pressure at the nodes is obtained as follows

$$\int_{y_1}^{y_2} \int_{x_1}^{x_2} (\mathbf{p}^*)^T \mathbf{B}^T \begin{pmatrix} \zeta_x & 0 \\ 0 & \zeta_y \end{pmatrix} \mathbf{B}\mathbf{p} dxdy = \int_{y_1}^{y_2} \int_{x_1}^{x_2} (\mathbf{p}^*)^T \mathbf{B}^T \mathbf{N} \dot{h} dxdy \tag{4.25}$$

$$(\mathbf{p}^*)^T \mathbf{B}^T \begin{pmatrix} \zeta_x & 0 \\ 0 & \zeta_y \end{pmatrix} \mathbf{B}\mathbf{p} A_e = (\mathbf{p}^*)^T \mathbf{B}^T \mathbf{N} \dot{h} \begin{pmatrix} A_e \\ A_e X_G \\ A_e Y_G \end{pmatrix} \tag{4.26}$$

where the stiffness matrix corresponds to the expression 4.27.

$$\mathbf{K}_e = \mathbf{B}^T \begin{pmatrix} \zeta_x & 0 \\ 0 & \zeta_y \end{pmatrix} \mathbf{B} A_e \tag{4.27}$$

and the force vector is given by the expression 4.28.

$$\mathbf{f}_e = \mathbf{B}^T \mathbf{N} \dot{h} \begin{pmatrix} A_e \\ A_e X_G \\ A_e Y_G \end{pmatrix} \tag{4.28}$$

The linear system expressed in matrix form for each finite element is then assembled in the global linear system as explained in subsection 2.0.5.2. Since the value of the constants ζ_x and ζ_y depends on the viscosity field but not on the pressure, the thickness and shape functions of each finite element at each time step suffices to solve for the linear system once for each time step. An unitary value is given to constants to calculate the value of the velocity at each element with the resultant pressure distribution. The Riemann integral of the through-thickness velocity field of each element is, actually, the value of the constants.

4.2.6 Results of the model and comparative with the isothermal 2D model.

In this subsection, the predictions of the non-isothermal model are presented and compared with the ones of the 2D isothermal model developed in chapter 2, for a rectangular part with unidirectional flow with the same geometric characteristics of the parts #1 to #3 described in the section 3.2. The same values of temperature and thermal parameters as in the section 4.2.2 have been defined for the simulation.

Table A.9 shows the orientation ellipse from equidistant in-plane cross-sections of the elements defined in fig. 4.6.

From the analysis of these results, one can conclude that

- The slight variation in the direction of the alignment is due to the triangular finite elements, and no because of the tortuosity of the streamlines. Therefore, the change of direction of the alignment of the fibers in the flow direction is not captured by the model.
- Regarding the orientation distribution in the through-thickness direction, the model predicts only a slight change in the vicinity of the charge/mould interface. The distribution in the rest of the thickness is uniform

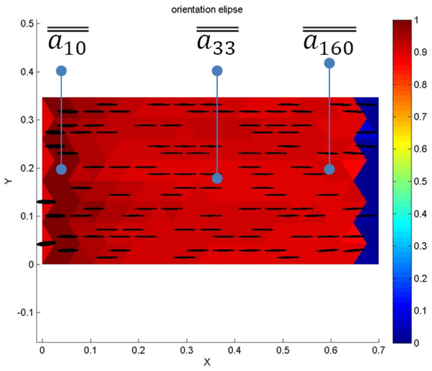

Figure 4.6: Positions of finite elements where the orientation tensor components are computed.

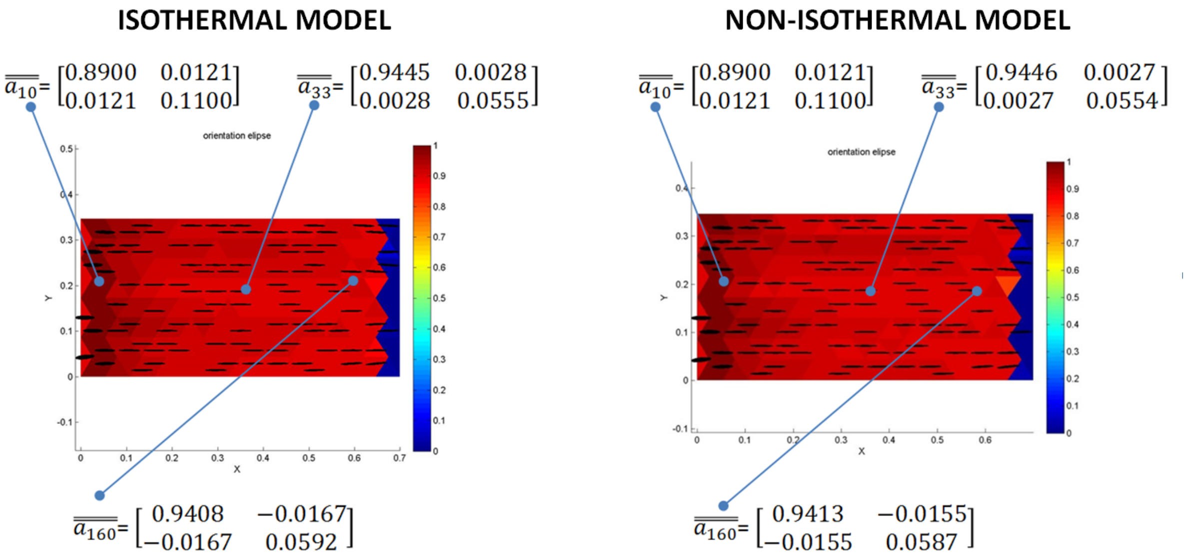

Figure 4.7: Simulated fiber orientation of part #1 from the isothermal 2D model vs. the anisothermal 2.5D model.

- The model does capture a change in fibre alignment at both charge/mould interfaces due to the difference of temperature, and it is more pronounced in the upstream positions.

Fig.4.7 shows the computed alignment of the orientation ellipses from both models, when the velocity is averaged in the through-thickness direction. No significant difference is found between the models and the principal direction of orientation of the fibers in the same streamline is conserved. The model does capture a small evolution of the alignment in the thickness direction, but very small compared to the experimental observations of the microstructure.

Fig.**??** shows that the loss of mass during the transport of fluid between elements, which is negligible in the non-isothermal 2.5D model, and it can be further reduced by refining the FEM mesh.

4.3 Laboratory scale SMC compression.

A new series of tests was performed in parallel to the development of the 2.5D model, to further understand

- role of the heat transfer during the SMC compression,
- the possible slippage at the mould/material interface,

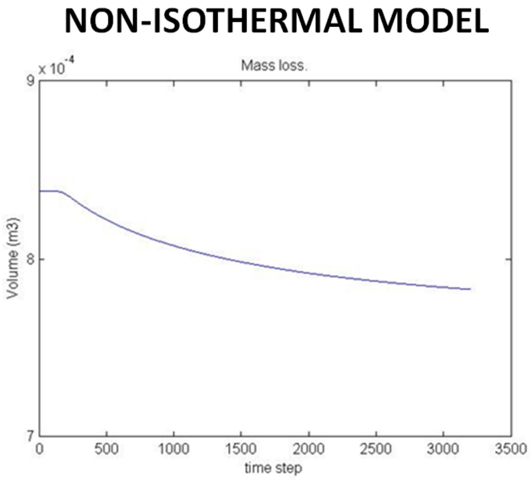

Figure 4.8: Balance of material during the transport of material between elements.

- determine to which extent the numerical model is able to capture the reality of the SMC compression moulding process.

This new series of experiments is explained below.

4.3.1 Material, experimental set-up and design of experiments

The material used was the ASTAR VERKIK LS-150.LD. This is a glass reinforced polyester SMC material that contains 29% in mass of 25 mm long fibres. This material is processed at a temperature in the range of 135° and 145°.

The test campaign was conducted with a rheological cell developed by Faurecia. It is made of two circular platens of 150 mm in diameter, equipped with electrical resistances to heat the surface to a controlled temperature. The rheological cell was mounted on an universal testing machine (Instron 5584) equipped with 100 kN cell force which mechanic and operational characteristics were described in the section 3.3.

This set up shown in figure 4.9) was designed to carry out compression of small sized SMC charge under conditions as similar as possible to the industrial production ones. The two main differences between this lab-scale experiment and the real industrial conditions are

- the planar dimensions of the charge
- the tooling edges that are open for the lab-scale rheological cell, whereas a punch die mould is used to produce SMC parts.

The same squeeze rate and volume to gap change (platen separation) than the ones usually applied in production are used during the lab-scale experiments.

A total of 64 SMC samples of 50 mm in diameter, made of 1 to 6 layers of SMC were analyzed during this campaign. Different conditions were applied by changing the squeeze ratio, the final thickness of the sample (degree of compression), the temperature of the platens and the initial temperature of the charge. Details of the different scenarios are explained hereafter. In order to remain in the volume-compression ratio of an industrial SMC process, the initial thickness of the samples was adjusted in the range of 18,5 mm to 12,5 mm. In addition, some samples with only one or two layers (3, 6 mm) were also squeezed. Tables 4.2 and 4.3 specify the boundary conditions and test conditions of each tested sample. Table 4.2 reports the conditions for a series of tests were the thermal boundary conditions were symmetric, whereas Table 4.3 shows the conditions for the samples produced under asymmetric boundary conditions.

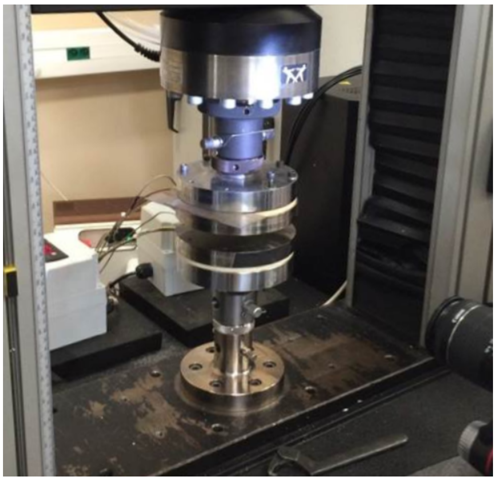

Figure 4.9: Lab-scale experimental set-up for the uniaxial compression test.

The degree of compression of samples ranged from only one millimetre (the initial thickness is reduced by 1 mm) to two millimetres of final thickness, to study the flow pattern along the compression moulding process of the sample to for a wide range of conditions.

Five different scenarios of temperatures were designed. In the first one, both platens of the rheological cell were heated at the same temperature, whereas the SMC charge was initially at room temperature. In the second, a ten degrees difference of temperature between the platens was enforced, where the highest temperature applied to the upper platen, whereas the SMC charge was initially at room temperature. In the third scenario, the temperature of platens were reversed with respect to the previous one. In the fourth, both the rheological cell and the charge were heated at the same temperature. Finally, some tests were done with the rheological cell and the charge at room temperature.

The squeeze ratios were changed from 5 to 0,33 mm/s.

The main conclusions drawn from the various tests are summarized hereafter.

4.3.2 Squish effect

When compression is carried out in the range of the recommended temperatures to process the SMC in industrial production, the bottom layer is squished (see fig.4.10). This phenomenon occurs even if the temperature of the upper platen is 10 degrees higher than the lower one to compensate the initial temperature gradient of the charge, or if the SMC charge is preheated. This lower layer flows much faster than the adjacent one. The second layer to squish is the upper layer once it comes in contact with the descending upper platen. This observation is in agreement with findings made by Barone and Cauk in [9] and [10]. This transverse velocity profile is the opposite of the classical shear-flow profile. The shear-flow type flow was observed when the SMC charge and the compression platens are kept at room temperature, i.e. as the viscosity of the SMC charge is homogeneous. Since the processing of SMC is always made by squeezing a SMC charge that was initially at room temperature and laid down in a hot mould (about 140°C), from these observations one can conclude that, in the the early stage of the compression, the transverse velocity profile is neither a pure shear flow nor a plug-flow due to the heat transfer effect. A possible consequence for this phenomenon would be a matrix transfer from the core towards the outer layer. It would enrich in matrix the outer layer, then lubricate the outer layers and would enhance their flow in comparison to the inner layers. This mechanism is further discussed in section 4.4.

For all the non-isothermal experiments, it is observed that the squished bottom layer bends towards the upper platen. In some more extreme situations the bending resulted in a folding

Figure 4.10: Sample #8 under uni-axial compression. The bottom layer (here in the back on this picture) shows a significant uniform squishing

Figure 4.11: Experimental evidence of the bottom layer folding (sample #45).

of the bottom layer up to the upper layers (see fig.4.11). This folding mechanism is prone to cause variations of the flow pattern, since the folded bottom layer can act as an obstacle for the inner layers. The strong difference in temperature between the bottom and inner layers, that translates into large through-thickness temperature and viscosity gradients, drives this mechanism. It is worth to note that the folding mechanism gives the evidence that the bottom layer behaves more as a shell-like structure than a fluid. This layer exhibits a non-zero bending stiffness because of the entanglement of the fiber bundles. It can also explain why some fibers are oriented out of the plane. This shell-like behaviour at the flow front at the early stage of the compression stage raises again the question about the validity of the classical models of squeeze flow in SMC compression. Even if they are suited to describe fully developed flow, they are inappropriate to model the squish and folding mechanisms at the early stage of the compression.

4.3.3 Accumulation of voids at the flow front.

A careful inspection of the flow front of samples, as shown in Fig.4.12 and Fig.4.13 reveals the presence of matrix concentration. It is observed in all samples consisting in more than two layers submitted to a limited reduction of their thickness, for any temperature scenario. This accumulation at the front seems to be steered by some air entrapped in porosities and especially in between layers. The compressed air is flushed out the compressed charge and force some

Figure 4.12: Experimental evidence of an accumulation of matrix at the front (sample 10)

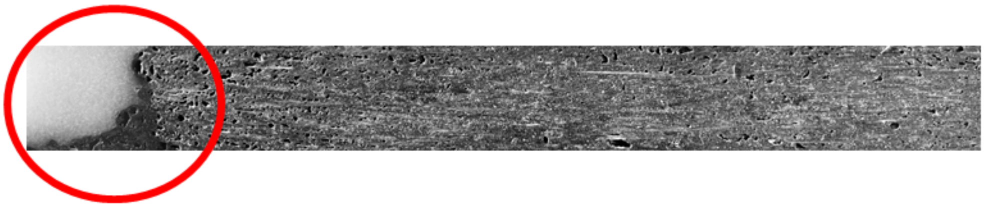

Figure 4.13: Sample 7 under hot uni-axial compression.

matrix to reach the flow front. Due to the presence of voids the charge is slightly compressible at the beginning and becomes gradually incompressible ([36]) as the voids are flushed out due to the high pressure built up during the compression. As the degree of compression grows, this accumulation increases to get an almost pure ring of matrix around the sample. When further compressing the charge, this matrix-rich zone starts redistributing until it disappears.

4.3.4 Charge/mould kinematic boundary condition.

In order to investigate whether a slippage can occur at the interface charge-mould, samples equipped with tracers were squeezed at different degrees of compression. The tracers consisted of 25 mm long carbon fibre bundles, taken from a carbon SMC charge. These bundles can be easily detected when they are placed at the surface of the glass SMC because of the strong brightness of the carbon fibres. The carbon bundles were placed on both sides of the sample, in the hoop direction of the circular sample. As shown in fig.4.14 a gap was created between them to avoid a direct contact between so that their movement is more independent (see fig.4.14). All samples were squeezed to reduce their initial thickness by 50% . Two different behaviours were observed depending on the initial charge thickness. On the one hand, the tracers placed in samples made of four layers of SMC (initial thickness 12,5 mm), experienced different degrees of displacement towards the flow front (see fig.4.15). The upper platen was heated at 140°C, whereas the lower one was at 130°C . On the other hand, samples made of 1 or 2 layers were squeezed being heated at 135°C at both mould surfaces. The tracers remained almost at their initial position (see fig4.16). Since the difference of temperature between the two experimental configurations is very small, the difference in slippage might be related to a transverse redistribution of matrix in the sample at the beginning of the compression. The amount of matrix at the mould/charge interface would be bigger in samples with more layers, and this higher concentrated of matrix could drag the tracers. The next subsection addresses the question of the possible out-of-plane matrix flow.

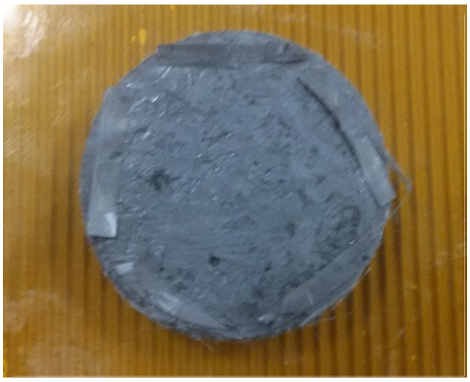

Figure 4.14: Carbon tracers on sample 51.

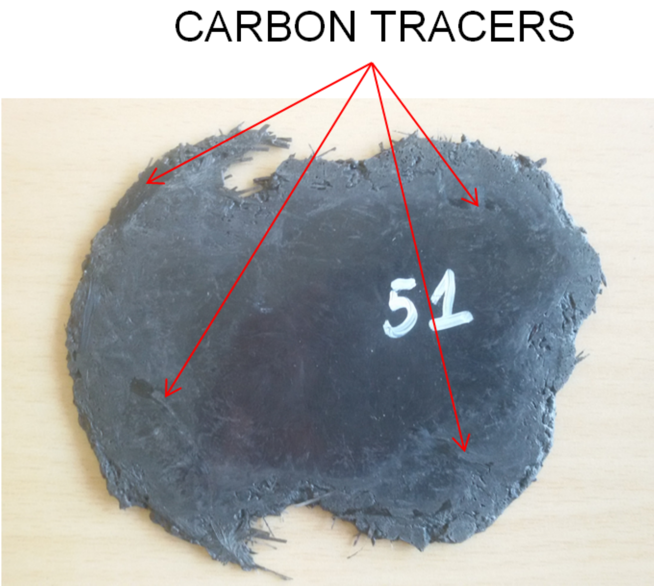

Figure 4.15: Sample 51 under hot uni-axial compression.

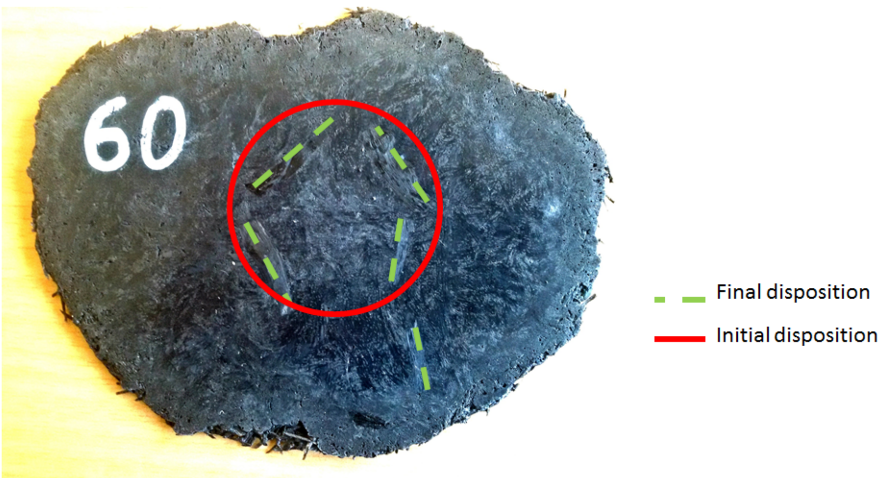

Figure 4.16: Sample 60 under hot uni-axial compression.

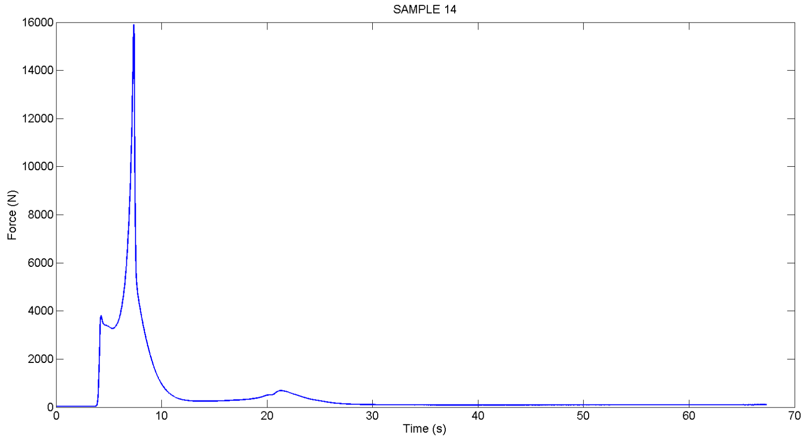

Figure 4.17: Compression response of sample 14.

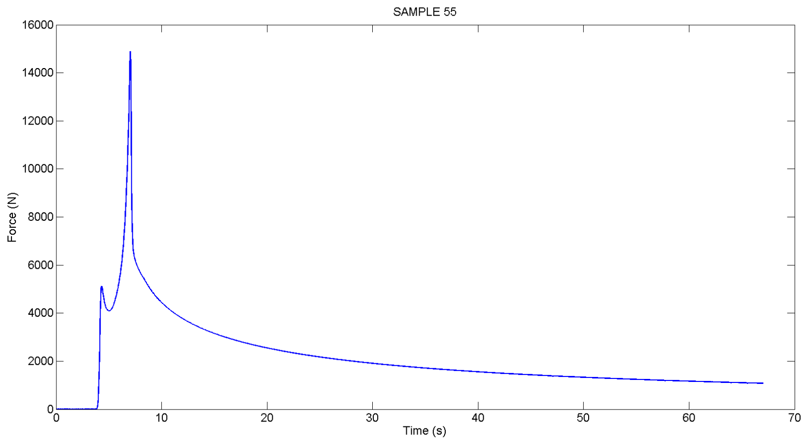

Figure 4.18: Compression response of sample 55.

4.3.5 Compression force vs time curves.

In this section some typical compression force vs time curves resulting from the compression of some samples described in section 4.3 are analyzed. Various thermal and mechanical testing conditions were selected to get different mechanical responses.

- Sample 14 (fig.4.17): Symmetric boundary conditions: compression platens at 135°C and charge at room temperature. 16% of thickness reduction. Squeeze rate of 3 mm/s.
- Sample 55 (fig.4.18) : Symmetric boundary conditions: compression platens and charge at room temperature. 24% of thickness reduction. Squeeze rate of 5 mm/s.
- Sample 42 (fig.4.19) : Symmetric boundary conditions: compression platens and charge at 135°C. 40% of thickness reduction. Squeeze rate of 5 mm/s.
- Sample 29 (fig.4.20) : Asymmetric boundary conditions: top compression platen at 140°C, bottom compression platen at 130°C and charge at room temperature. 24% of thickness reduction. Squeeze rate of 3 mm/s.
- Sample 30 (fig.4.21) : Asymmetric inverse boundary conditions: top compression platen at 120°C, bottom compression platen at 130°C and charge at room temperature. 40% of thickness reduction. Squeeze rate of 3 mm/s.

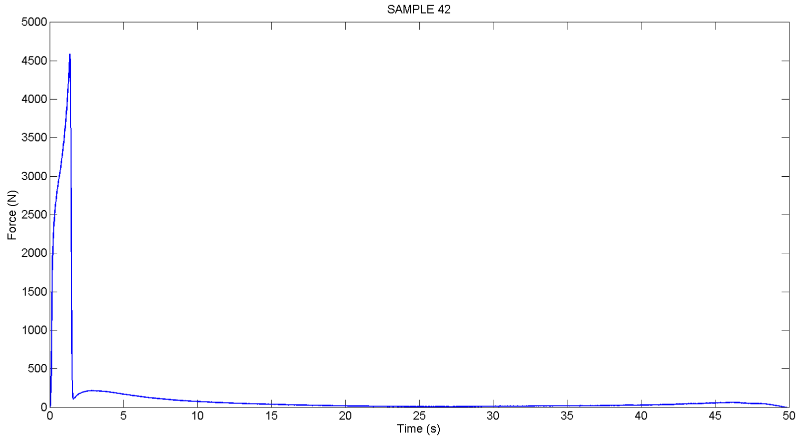

Figure 4.19: Compression response of sample 42.

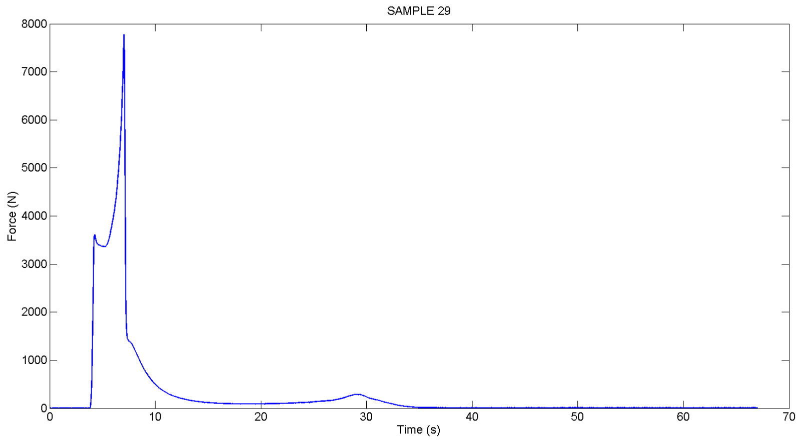

Figure 4.20: Compression response of sample 29.

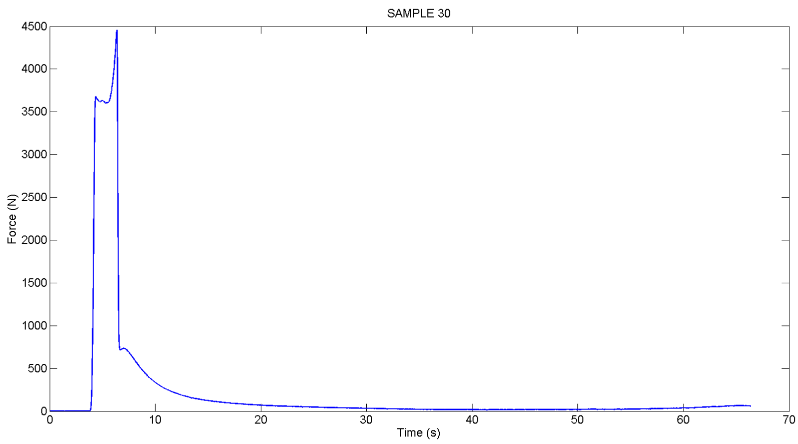

Figure 4.21: Compression response of sample.

The curves were contrasted with recordings of the compression realized during the tests. In view of the results, it can be concluded:

- The first force peak is due to the initial compressibility of the 4 layers of SMC. The compressible entrapped air between layers is flushed out at this stage. As the charge is preheated (sample 42), this first peak vanishes. This may be due to a better pre-consolidation of the stack due to a longer heat transfer during the sample pre-heating.
- Once the expulsion of the air is completed, the compression of the material begins until the target thickness is reached. The second force peak corresponds to the end of compression.
- Then a relaxation stage begins where the force returns gradually to zero. Hotter samples return faster to zero than colder ones.
- The compression force in non-isothermal conditions is higher for shorter compression times because the viscosity is higher.
- Small peaks at longer times may occur and correspond the exothermal curing of the polyester resin (see for instance the peak at 30s in sample 29 in fig.4.20).

4.4 Out-of-plane matrix flow.

Lab-scale squeeze flow experiments revealed the existence of a squish flow of the SMC charge near the heated mold surface, modifying the though-thickness velocity profile. This behaviour has been reported very early by many authors (see for instance [10] among others). The origin of such a behaviour is related to the temperature gradient across the charge thickness as the mould heats up the initially cold charge. This mechanism was discussed in the previous sections as a consequence of the non-isothermal compression moulding that created a lag of the inner layers compared to the bottom and top ones. The effect was modeled by introducing a through-thickness viscosity gradient. In this section we want to discuss another possible consequence of the viscosity drop from the mold wall toward the center of the charge. The lead-lag mechanism induces a transverse pressure gradient, which is combined with the viscosity drop. These conditions may induce a through-thickness transfer of matrix from the center of the charge towards the mold walls that will enrich the mold/charge interface with neat matrix. It can be viewed as a flow of the viscous matrix through the fiber bed made of chopped fibre bundles. This type of flow, sometimes called segregation, has been observed in ribs [56]. This extra amount of matrix at the mold/charge interface will act as a lubricant, changing the boundary conditions gradually from an initial non-slip condition to a mixed shear/plug flow. It may also favour the lead-lag mechanism. Another consequence of a such a mechanism is an increase of fiber volume fraction in the mid-plane of the moulding compound compared to the outer regions. This hypothesis was supported by some experimental evidence, where a higher concentration of resin was observed at the flow front at the early stages of the compression. That might suggest an initial redistribution of matrix in the SMC charge.

A dedicated experiment was designed to check if such a mechanism may happen. The compression moulding is performed on SMC charge in the same way that was done during the previous tests, except for a perforated high-temperature release film and a bleeder between the SMC charge and the platens of the rheological cell. These auxiliary materials are commonly used in autoclave moulding to store the excess of resin bled out the prepreg stack during the consolidation stage. They are peeled out once the composite is cured. By weighting the bleeder layer before and after peeling, one can determine the quantity of matrix transferred towards the outer plies. The test was performed on five charges of 50 mm in diameter and 9 mm of

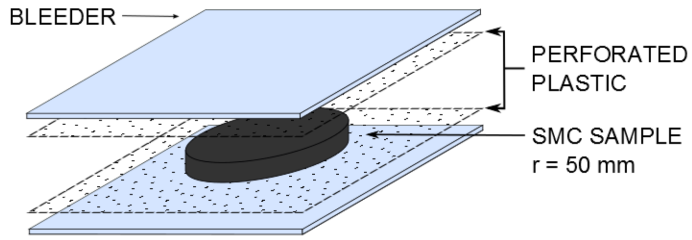

Figure 4.22: Scheme of the test.

initial thickness (3 layers of SMC). The five samples were compressed at a squeeze rate of 3 mm/s until a final thickness of 4,5 mm (half of their initial thickness). The temperature of the platens was increased up to 180°C because the bleeder is a poorly conductive material. This boundary condition allows to get a temperature of about 140°C on both sides of the charge.

As in the previous tests, the material used was the ASTAR VERKIK LS-150.LD. That consists of a glass reinforced SMC material that contains 29% by weight of 25mm-long fibres.

The bleeder layers were weighted before and after the compression moulding of the sample with a precision scale. Table 4.4 shows the results of the resin transfer in both sides of the sample.

The mean amount of resin transferred into the top and bottom bleeder layers is very small, respectively 0,22% and 0,15% of the initial bleeder weight. It is concluded that the transfer of matrix in the out-of-plane direction is negligible for that material under these experimental conditions. To go further on the possible fiber/matrix separation in a flat thin section (without any ribs), a model has been developed to investigate whether the fiber/matrix segregation might happen in regular SMC materials under representative moulding conditions. This mechanisms is known as jamming in SMC compression and has been observed in the vicinity of ribs or as the mould closing rate is low enough. Matrix flows through the network of fiber bundles as the viscous drag built during the compression is not big enough to convect the fiber bed. Such condition is encountered in the consolidation of continuous fiber reinforced thermoset prepregs where the squeeze rate and matrix viscosity are low enough. It is the case in the autoclave moulding where a generic 3D model was derived to predict the 3D resin flow while the prepreg is consolidating [37]. Here we suppose that the flow of viscous matrix through the network of fiber bundles is described by the Darcy's law,

$$\mathbf{v}_{\mathrm{m}} = -\frac{\mathbf{K}}{\mu}\nabla p \tag{4.29}$$

where $\mathbf{v}_{\mathrm{m}}$ is the Darcy's velocity, $\mathbf{K}$ the permeability tensor of the fibrous material, μ the matrix viscosity and ∇p the driving pressure gradient. Combining Darcy's law to the mass conservation of the matrix phase leads to the governing equation for the resin flow,

$$\frac{K_x}{V_f}\frac{\partial^2 p}{\partial x^2} + \frac{K_y}{V_f}\frac{\partial^2 p}{\partial y^2} + \frac{1}{V_0^2}\frac{\partial}{\partial z}\left(V_f K_z \frac{\partial p}{\partial z}\right) = \mu\frac{\dot{h}}{h} \tag{4.30}$$

where the K_i are the permeability components of the fibrous network and V_0 is the initial fiber volume fraction. For a random distribution of fiber bundles one can assume an in-plane isotropy of permeability, i.e. $K_x = K_y = K_r$. It writes in 2D and in cylindrical coordinates (r,z):

$$K_r\frac{1}{r}\frac{\partial}{\partial r}\left(r\frac{\partial p}{\partial r}\right) + K_z\left(\frac{h_0}{h}\right)^2\frac{\partial^2 p}{\partial z^2} = \mu\frac{\dot{h}}{h} \tag{4.31}$$

with p the fluid pressure, K_r and K_z the hydraulic permeability components of the tensor, h_0 the initial thickness, $\dot{h}$ the unidirectionnal compression velocity (negative, in the z-direction) and h the thickness of interest.

Considering that

$$\hat{r} = \frac{r}{R}, \quad \hat{z} = \frac{z}{h} \quad \text{et} \quad \hat{p} = \frac{p}{p_c} \tag{4.32}$$

and

$$p_c = -\frac{\mu \dot{h} R^2}{h K_r} \quad \text{and} \quad m = \frac{K_z h_0^2 R^2}{K_r h^4} \tag{4.33}$$

the non-dimensionalized pressure equation reads:

$$\frac{1}{\hat{r}}\frac{\partial}{\partial \hat{r}}\left(\hat{r}\frac{\partial \hat{p}}{\partial \hat{r}}\right) + m\frac{\partial^2 \hat{p}}{\partial \hat{z}^2} = -1 \tag{4.34}$$

In the special case of a cylindrical geometry, equation 4.30 can be solved by the Finite Difference Method (FDM) [20].

4.4.1 Materials' parameters and test configurations.

4.4.1.1 SMC and samples characteristics.

The SMC material is consituted of glass fibers, mineral fillers (hollow glass spheres) and a thermoset resin. The composition is given in table 4.5. Cylindrical samples have been cut from the SMC parts. The dimensions and main characteristics of the samples are given in table 4.6. The samples, initially at room temperature, are positionned on the platens (heated at 135°C) and compacted at 3 mm/s. Table 4.7 lists the four thicknesses that are considered for the resin flow analysis. It also gives the fiber, resin and filler volume fractions. The configuration at the thickness h_1 does not show interest since the material is highly porous (59.2%). Therefore during the consolidation stage, most of the movements at this thickness is driven by the closing of pores and the evacuation of air. The fluid motion is limited at that stage.

4.4.1.2 Resin viscosity

The resin is filled with mineral fillers in high content (M_{filler}=27% in the SMC and C_{filler}=32.2% in the resin). Therefore its viscosity is influenced by the presence and concentration C_{filler} of the filler. The relationship [18] can be used to model the influence of the fillers on the viscosity of the blend:

$$\mu_{filled} = \mu_0 \left[1 + \left(\frac{C_{filler}/C_\infty}{1 - C_{filler}/C_\infty}\right)^2\right] \tag{4.35}$$

with μ_0=0.5 Pa.s, C_{filler}=32.2% and C_∞=60%.

Then, the Williams Landel Ferry model [87] is used to take the temperature dependence of the viscosity into account:

$$\mu(T_K) = \mu_{filled} \exp\left(\frac{-C_1(T_K - T_0)}{C_2 + T_K - T_0}\right) \tag{4.36}$$

with C_1=8.86, C_2=101.4K, T_0=293K and T_K is the temperature of interest in K.

Using equations 4.35 and 4.36, the viscosity of the filled resin is displayed in fig.4.23

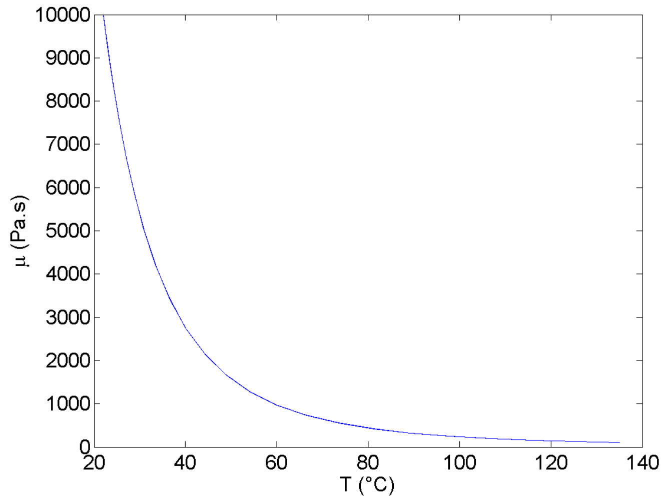

Figure 4.23: Evolution of the viscosity of the resin / fillers blend with respect to the temperature.

4.4.1.3 Temperature and viscosity profiles.

As soon as the SMC samples are positionned and compressed by the heated platens, the sample starts to heat-up. Fig.4.24 displays the temperature profiles and corresponding viscosities as the test is carried on (see also table 4.7).

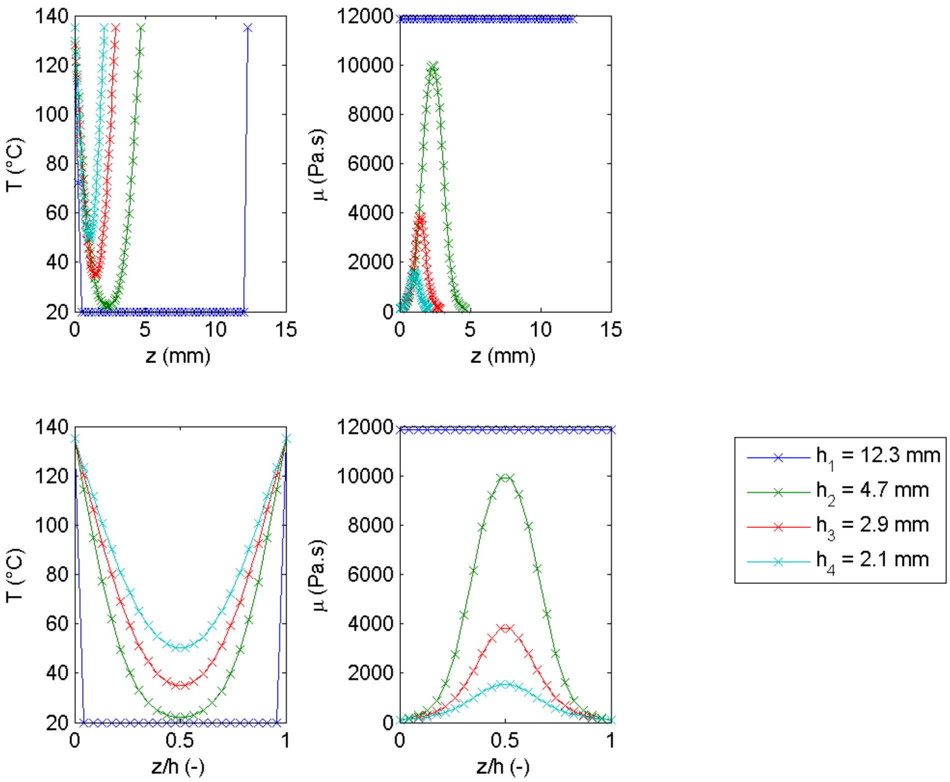

Figure 4.24: Evolution of the temperature (left) and viscosity (right) profiles through the sample thickness (top) and non-dimensionalized thickness (bottom).

z (mm)	POSITION 10	POSITION 33	POSITION 160
2	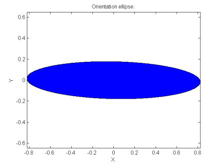	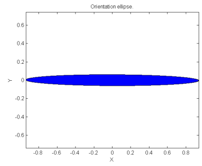	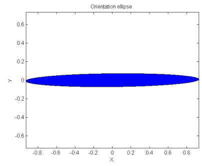
1.77	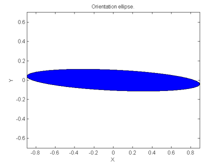	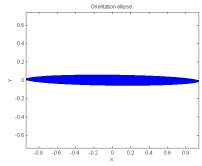	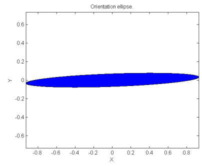
1.55	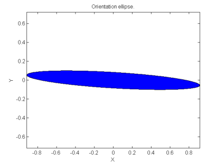	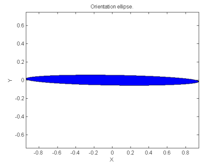	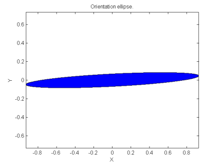
1.33	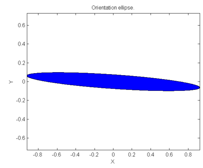	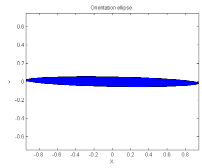	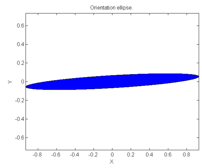
1.1	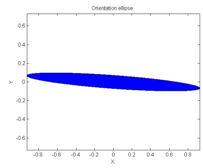	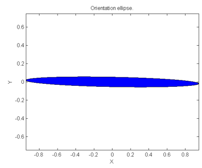	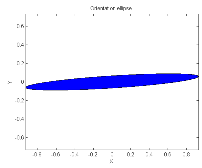
0.88	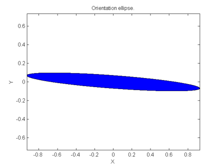	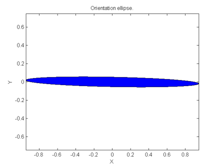	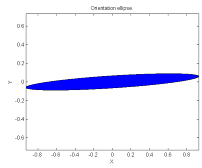
0.66	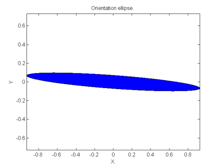	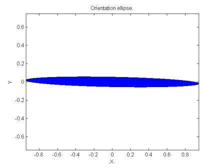	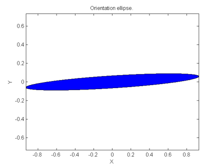
0.44	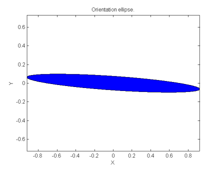	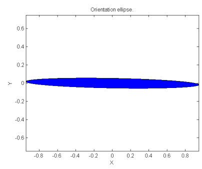	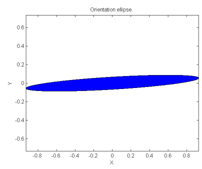
0.22	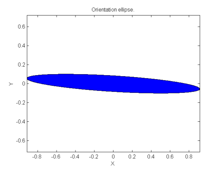	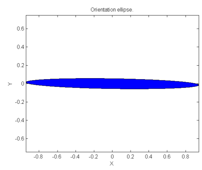	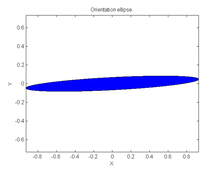
0	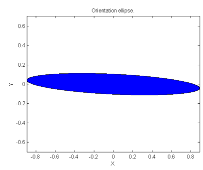	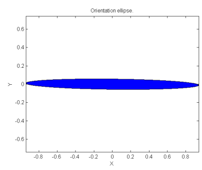	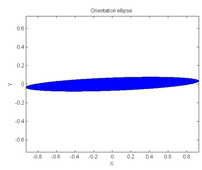

Table 4.1: Orientation ellipse at the elements defined in fig.4.6 at the defined in-plane cross-sections.

<table>
<thead>
<tr><th>sample</th><th>$H_{ini}/\#layers$</th><th>H_f</th><th>T platens (°C)</th><th>T charge(°C)</th><th>Squeeze rate (mm/s)</th></tr>
</thead>
<tbody>
<tr><td>1</td><td>18.8/6</td><td rowspan="4">2</td><td>130</td><td rowspan="21">room</td><td rowspan="16">3</td></tr>
<tr><td>2</td><td>9.4/3</td><td rowspan="21">135</td></tr>
<tr><td>3 to 4</td><td rowspan="10">12.5/4</td></tr>
<tr><td>5</td></tr>
<tr><td>6</td><td>10</td></tr>
<tr><td>7</td><td>11</td></tr>
<tr><td>8</td><td>9</td></tr>
<tr><td>9</td><td>8</td></tr>
<tr><td>10</td><td>7</td></tr>
<tr><td>11 to 12</td><td>6</td></tr>
<tr><td>13</td><td>5</td></tr>
<tr><td>14 to 15</td><td>2</td></tr>
<tr><td>16</td><td>3/1</td><td>0.5</td></tr>
<tr><td>17</td><td>6/2</td><td>1</td></tr>
<tr><td>18</td><td rowspan="3">1.25/4</td><td>4</td></tr>
<tr><td>19</td><td>3</td></tr>
<tr><td>34 to 36</td><td>5</td><td rowspan="3">5</td></tr>
<tr><td>37</td><td>9/3</td><td>4</td></tr>
<tr><td>38</td><td rowspan="7">12.5/4</td><td rowspan="4">5</td></tr>
<tr><td>39</td><td>1</td></tr>
<tr><td>40 to 41</td><td>0.33</td></tr>
<tr><td>42 to 43</td><td>135</td><td rowspan="2">5</td></tr>
<tr><td>55 to 57</td><td>3</td><td rowspan="2">room</td><td rowspan="5">room</td></tr>
<tr><td>58 to 59</td><td>6</td><td rowspan="4">3</td></tr>
<tr><td>60</td><td>2</td><td rowspan="3">135</td></tr>
<tr><td>61 to 62</td><td>3/1</td><td>0.5</td></tr>
<tr><td>63 to 64</td><td>6.5/2</td><td>1</td></tr>
</tbody>
</table>

Table 4.2: Uniaxial compression tests with symmetric thermal boundary conditions.

<table>
<tr><th>sample</th><th>$H_{ini}/\#layers$ (mm)</th><th>H_f (mm)</th><th>T top platen(°C)</th><th>T top platen(°C)</th><th>T charge (°C)</th><th>Squeeze rate (mm/s)</th></tr>
<tr><td>20</td><td rowspan="13">12.5/4</td><td rowspan="2">11</td><td>135</td><td>127</td><td rowspan="18">room</td><td rowspan="18">3</td></tr>
<tr><td>21</td><td rowspan="9">140</td><td rowspan="11">130</td></tr>
<tr><td>22</td><td>10</td></tr>
<tr><td>23</td><td>10</td></tr>
<tr><td>24</td><td>8</td></tr>
<tr><td>25</td><td>7</td></tr>
<tr><td>26</td><td>6</td></tr>
<tr><td>27</td><td>5</td></tr>
<tr><td>28</td><td>4</td></tr>
<tr><td>29</td><td>3</td></tr>
<tr><td>30</td><td>5</td><td rowspan="4">120</td></tr>
<tr><td>31</td><td rowspan="2">6</td></tr>
<tr><td>32</td><td rowspan="2">135</td></tr>
<tr><td>33</td><td>3/1</td><td>1</td></tr>
<tr><td>44</td><td rowspan="2">12.5/4</td><td rowspan="4">6</td><td rowspan="5">140</td><td rowspan="5">130</td></tr>
<tr><td>45 to 47</td></tr>
<tr><td>48</td><td>9/3</td></tr>
<tr><td>49</td><td rowspan="2">12.5/4</td></tr>
<tr><td>50 to 54</td><td>3</td></tr>
</table>

Table 4.3: Uniaxial compression tests with asymmetric thermal boundary conditions.

sample	initial bleeder weight (g)	Amount of matrix in the bottom bleeder (%)	Amount of matrix in the top bleeder (%)
1	24.5057	0.1481	0.2758
2	24.4941	0.1241	0.1600
3	24.4758	0.1438	0.1217
4	22.8945	0.1983	0.0161
5	24.2925	0.1276	0.5137
MEAN	–	0.1483	0.2175
SD	–	0.0297	0.1898

Table 4.4: Resin transfer.

Property	Value
Fiber mass fraction M_f	29%
Filler mass fraction M_{filler}	27%
Resin mass fraction M_r	44%
Fiber density ρ_f	2.54 g/cm^3
Filler density (hollow glass spheres) ρ_{filler}	1.42 g/cm^3
Resin density ρ_r	1.10 g/cm^3
Composite density ρ_c	1.42 g/cm^3

Table 4.5: SMC composition and constituents densities.

Parameter	Value
Sample initial radius R_0	25 mm
Sample initial thickness h_0	12.5 mm
Sample mass m_0	14 g
Sample initial residual porosity ϕ_0	59.8%
Sample initial V_{f0}	6.5%
Compaction speed $\dot{h}$	3 mm/s
Platen temperature	135°

Table 4.6: Sample and test parameters.

Configuration	h_1	h_2	h_3	h_4
Thickness h (mm)	12.3	4.7	2.9	2.1
Radius R (mm)	25.0	25.9	32.9	38.7
Average fiber volume fraction V_f	6.6%	16.2%	16.2%	16.2%
Average filler volume fraction V_{filler}	11.0%	26.9%	26.9%	26.9%
Average resin volume fraction V_r	23.2%	56.8%	56.8%	56.8%
Average filler concentration in resin C_{filler}	32.2%	32.2%	32.2%	32.2%
Porosity ϕ	59.2%	<1%	<1%	<1%

Table 4.7: Sample characteristics and compositions at four considered thicknesses.

4.4.1.4 Fibrous bed permeability.

The fibrous bed of SMC consists of chopped fibers which are randomly oriented in the plane of the sheet. Two analyses will be run. One with constant permeability fields, another one with $\Delta V_f/V_f = -2.5\%$ in the skins and $\Delta V_f/V_f = +5\%$ in the core.

The Kozeny-Carman empirical relationship [16] has been derived to estimate the permeability of a stack of spheres and can be written in various forms. For instance, the permeability K of a porous granular medium writes:

$$K = \frac{\phi^3}{36c(1-\phi)^2}d^2 \tag{4.37}$$

where $\phi = 1 - V_f$ is the porosity, d a particle diameter and c an empirical constant.

Collecting various in-plane permeability (K_r) measurements of fibrous reinforcements, an attempt is made to plot the Kozeny-Carman constant c with respect to the fiber volume fraction $V_f = 1 - \phi$. Fig.4.25 shows the variation of the constant c for in-plane permeability of mats constituted of either glass or carbon fibers. The nature of the fiber is simply taken into account through the fiber diameter.

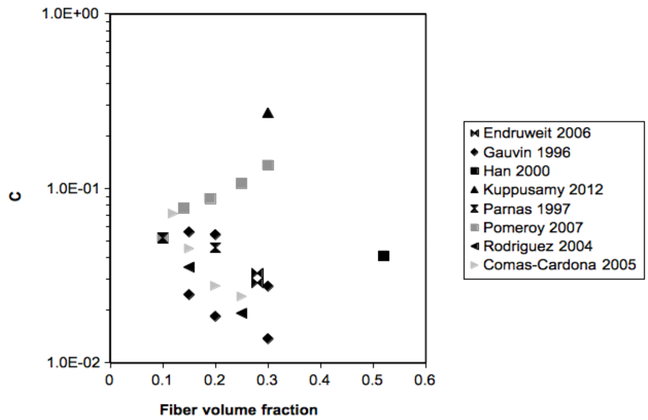

Figure 4.25: Kozeny-Carman constant evolution for fibrous mats with respect to fiber volume fraction.

For this study, a value of $c = 0.05$ and $d = 17\ \mu$m will be used. It gives for $V_f = 16.2\%$ the following permeabilities: $K_r = 3.6 \times 10^{-9}$ m^2. For the transverse value, $K_z = K_r/3 = 1.2 \times 10^{-9}$ m^2.

Configurations	Constant V_f	Skins $\Delta V_f/V_f = -2.5\%$	Core $\Delta V_f/V_f = +5\%$
K_r	3.60×10^{-9}	3.84×10^{-9}	3.16×10^{-9}
$K_z = K_r/3$	1.20×10^{-9}	1.28×10^{-9}	1.06×10^{-9}

Table 4.8: Permeabilities (m^2) of the fibrous bed for the configurations h_2, h_3 and h_4.

4.4.2 Numerical simulations.

4.4.2.1 Boundary conditions.

For given boundary conditions and materials' input parameters, the equation 4.34 can be solved with finite difference or finite element methods. Fig.4.26 displays the domain and boundary conditions for a unidirectional consolidation in z-direction with a compaction velocity $\dot{h}$ in a cylindrical geometry of radius R and thickness h. Material and testing parameters are detailed in the following section.

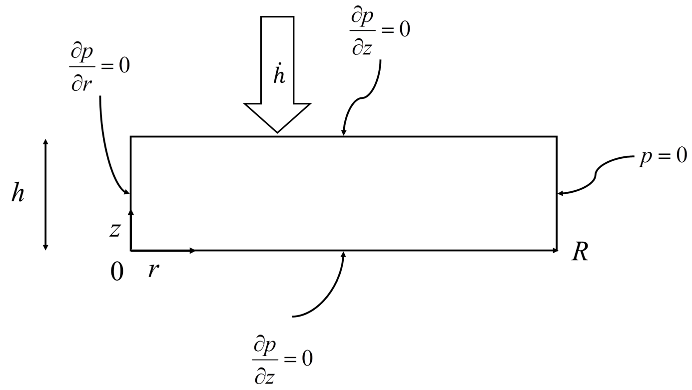

Figure 4.26: Domain and boundary conditions used to solve for a consolidation test between heated parallel platens.

4.4.2.2 Results with constant V_f and permeability

A first set of simulations have been run with constant V_f (no fiber segregation from skin to core) and transient heat transfer. Figures 4.27-4.28 show the viscosity field in the cross section of the compressed SMC sample. Also the resulting fluid pressure and interstitial velocities are displayed.

4.4.2.3 Results with segregation

A second set of simulations have been run with fiber segregation from skin to core and transient heat transfer. Figures 4.29-4.32 show the viscosity and permeability fields in the cross section of the compressed SMC sample. Also the resulting fluid pressure and interstitial velocities are displayed.

4.5 High performance SMC.

High performance SMC material is actually a compound reinforced with a higher fiber volume fraction. The material used to produce the parts was the IDI 19SP159 0AS, by IDITrans, consisting of a polyester matrix including some fillers reinforced with 55% by weigth of 25 mm long glass fibres. Flat rectangular parts were moulded at Faurecia under regular industrial conditions. A total number of 36 rectangular SMC of dimensions 700x400 mm where produced. Some short shots were also carried out, where spacers of different thickness were used to control the amount of squeeze applied to the charge. The 36 parts were classified into 2 different series, according to spacer thickness and the mould closing rate. The main characteristics of each series are described hereafter.

SERIES 1. A series of 27 parts was produced from an initial charge of 140 mm x 200 mm, with 10% of coverage rate, and a initial thickness of 15.4±2 mm. The charge was placed at the left hand side of the mould as shown in figure 4.33. 9 parts were produced with spacers of 7mm, 9 parts with spacers of 2mm and 9 parts with spacers of 1mm. The temperature of the upper mould part was kept at 160°C and the bottom platen was at 150°C. The closing force was 250 T, the total cycle time (from the placement of the charge into the mould up to the part demoulding) was of 120 s.

SERIES 2. A series of 7 parts, planar dimensions of 140 mm x 200 mm, 10% of coverage rate, and an initial thickness of 15.4±2 mm. The charge placed at the left side of the mould as indicated in figure 4.33. No spacers were used here. The temperature of the upper mould half was kept at 160°C and the lower one was at 150°C. Three of the parts were produced with a closing force rate of 20 T/s, another three with a closing force rate of 70 T/s and the last one with a closing force rate of 120 T/s.

In addition a single part was manufactured applying almost no compression force to get a reference part that kept the initial fibre orientation.

4.5.1 Irregularities at the flow front.

The flat parts moulded under industrial conditions showed repeatable characteristics.

1. The folding of some layers at the flow front, already observed on some sample with regular SMC material (see in section 4.3), happened in almost every parts where the thicker spacers were used, i.e. when the compression was at its early stage(see fig. 4.34).

2. The flow pattern became more and more irregular as the spacers get thinner, i.e. the squeeze ratio is increased (see fig.4.35). Such uneven flow pattern was recently observed for semi-structural SMC in [44], but no explanation was proposed to clarify the origin of this mechanism. A possible origin is proposed here: the above-mentioned strong folding of the bottom layer creates an obstacle to the adjacent upper layers. Since the fibre volume fraction is high, this folded layer is more cohesive than a regular SMC and then can withstand some stretching loading. The folded layer acts as a plug which modifies the flow kinematics at the flow front. The irregularity of the flow pattern is likely due to the variability in the folded material, where the load-bearing ability depends on the local fibre orientation. This mechanics might be enhanced by some jamming (segregation effects) due to the higher fibre content compared to regular SMC. This last argument is checked in the next subsection.

4.5.2 Material density

The structural high performance SMC contains a high content of fibre bundles. More bundle/bundle contacts are expected, which in turn could lead to a jamming (segregation) effect. A local zone enriched in matrix could modify the mould/charge contact and then induce some significant local change in the flow.

The objective is to measure after processing the material density field to check whether a fibre/matrix segregation occurred. The density measurement of the solid phase is determined by means of a fluid of known density. Here ethanol was used as a reference liquid to perform the test. The sample is first weighted at the dry state and then immersed in the auxiliary liquid and weighted again. The density of the material of the sample can then be obtained by expression 4.9.

$$\rho = \frac{A}{A-B}\left(\rho_0 - \rho_L\right) + \rho_L \tag{4.38}$$

where ρ is the density of the sample, A is the weight of the sample measured in the air, B is its weight measured as it immersed in the ethanol (0.7839 g/cm^3), ρ_0 is the ethanol density and ρ_L is the air density (0.0012 g/cm^3).

This test was performed on samples cut out from two parts manufactured with a 1mm thick spacer. This test condition was selected because very irregular flow front were observed.

A total of 33 samples of 25mm x 10 mm were cut out from the parts, in 12 different regions in the part 8 and part 10. Figure 4.36 shows where the samples were cut out. The averaged density of each local group is shown in the table 4.9.

Sample	Part 8	Part 10
1	1.7957	1.8455
2	1.8032	1.8354
3	1.7587	1.7787
4	1.9093	1.8483
5	1.9139	1.9825
6	1.8265	1.8330
7	1.0158	1.8114
8	1.8666	1.8406
9	1.8962	1.8432
10	1.6078	1.6357
11	1.5203	1.3003
12	1.6690	1.8140
MEAN	1.8167	1.7478
SD	0.1809	0.1330

Table 4.9: Local values of density (g/cm^3).

The low standard deviation reflects a low variability in the material density distribution over the part. To make sure that this uniformity is not actually due to a counterbalance between a fiber enrichment and a filler decrease, burn off test were carried out to get rid off the influence of mineral fillers that have the same density than the glass fibres.

Five samples of 30x15 mm were cut out from the part #15, 4 of them following the same theoretical stream line and an additional one in the flow front (see fig.4.37). Each sample was placed in an aluminum cup and put into a preheated calcination furnace. Then the samples were heated at 550°C during 3 hours. During this period the organic ingredients are burned off, leaving only the reinforcement fibres and mineral fillers. The mass of the sample and of the aluminum cup were measured with a precision scale before and after the burn off test. Results are reported in table.

Sample	Sample weight before calcination (g)	Sample weight after calcination (g)	% Remaining mass
1	1.249	0.8311	66.16
2	1.3858	0.9481	68.08
3	1.3836	0.96	69.04
4	1.0563	0.7375	69.29
5	1.2641	0.8943	70.46
MEAN	1.2677	0.8742	68.61
SD	0.0935	0.0719	1.1903

Table 4.10: Weigh of the samples before and after the calcionation and relative mass loss (g).

In view of the homogeneity of the burn-off test results, it can be concluded that there is no differential fibre/matrix flow. Results show a very similar distribution of the materials over the part since the percentage of remqining mass is similar for all the samples and the standard deviation of the distribution of the results from the mean is small. These results does not seem to reconcile a priori with previous evidences. The justification may be found in the lower content of matrix in the high performance SMC material, and a high content of reinforcement, of the 55% by weight in this case, as indicated in the description of the material, that constrains the redistribution of it over the part during the compression process.

4.6 Conclusions.

The initial 2D isothermal numerical model has been successfully extended to a 2.5D non-isothermal model. The through-thickness heat transfer and viscosity field have been successfully coupled to the initial flow model.

Laboratory scale SMC compression.

- In all the non-isothermal experiments, the bottom layer first and right after the top layer of the SMC charge squish from the rest of the layers.
- The squished bottom layer bends towards the upper platen and even folds over the upper layers. This can cause variations of the flow front behaviour since this mechanism is found to be non-uniform along the flow front. The bottom layer behaves more a a shell-like structure than as a fluid. This effect provided another evidence of the unsuitability of the classic models.
- The air entrapped in the porosities and in between layers flushes out from the compressed charge pushing some almost pure matrix to the flow front and forming a ring-like zone that surrounds the flow front. This frontal zone tends to disappear with further compression.
- In the samples made out of four layers, the carbon tracers placed on the surface of the charge experienced different degrees of displacement. In the samples made out of two layers, the tracers reminded almost at their initial position. This indicates that the actual charge/mould boundary condition is somehow random. The possibility of a transverse redistribution of matrix to enrich the mould/charge interface does not seem consistent with these experimental findings.
- The compression force-time curves have a similar structure with certain differences according to the scenario of the test: a first force peak due to the flushing out of the air entrapped between layers, a second force peak corresponding to the end of the compression phase and a relaxation stage begins where the force returns gradually to zero that is shorter in the hotter samples. Finally, the exothermal curing of the polyester may cause small peaks at longer times. The compression force in non-isothermal boundary conditions is higher for shorter compression times.

Out-of-plane matrix flow.

- A dedicated experiment evidences that the out-of-plane matrix transfer is negligible for the used material under the experimental conditions.
- A Darcy's law based numerical consolidation model has been used for further investigation of the possible fibre/matrix relative flow. Either the simulations run with constant volume fraction in the sample as the ones considering fiber segregation from skin to core, both scenarios considering transient heat transfer, show a negligible value of the through-thickness velocity of the matrix.

High performance SMC.
From the short shots of high performance SMC flat parts, it was observed that:

- The folding of the bottom layers over the flow front happens at all stages of the compression.
- The flow pattern shows more irregularity as the squeeze rate (compression velocity) and compression ratio (ratio of the initial to the final thickness) increase. This can be caused by the pronounced folding of some layers at the flow front.
- A very little change of material density, assessed by measuring the mass of the non-organic phase over the part, is observed .

h_1

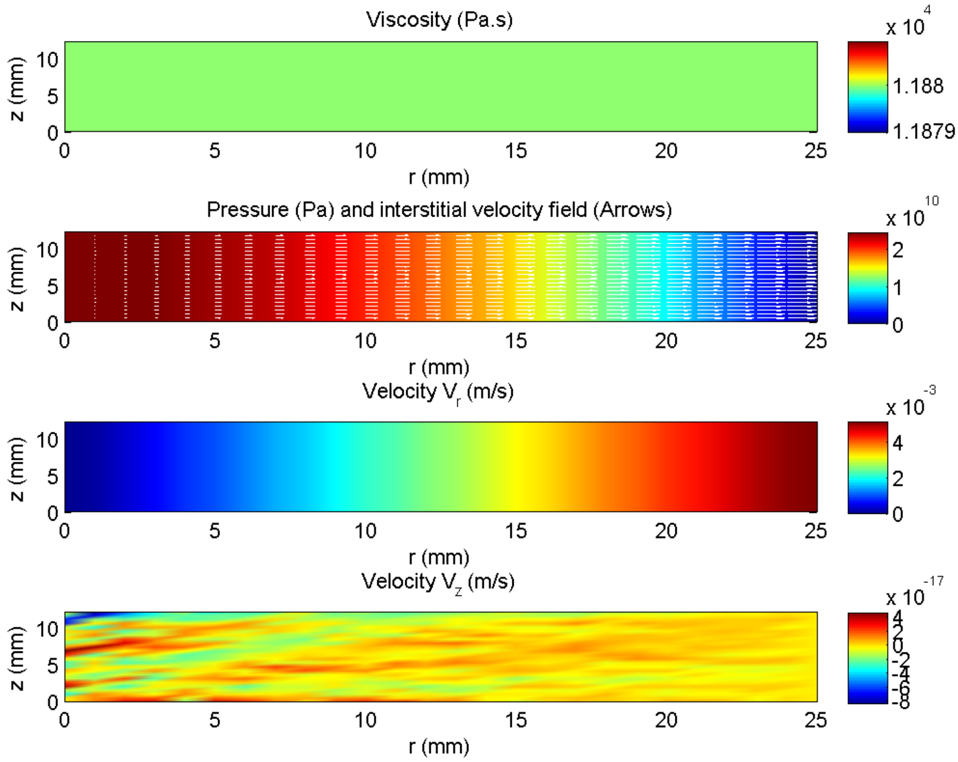

h_2

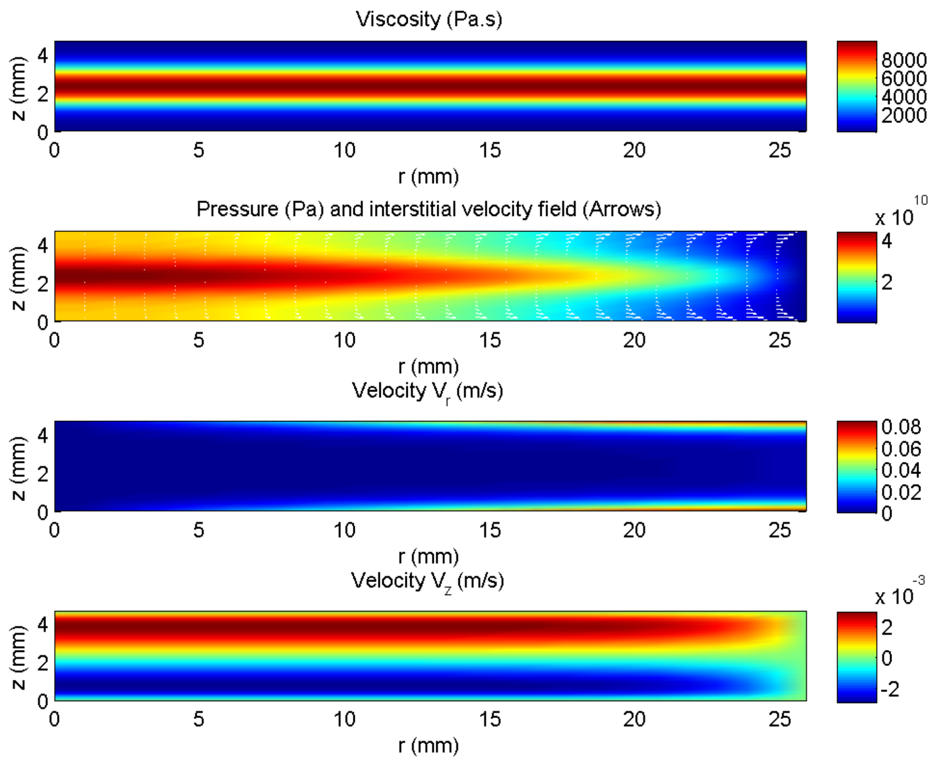

Figure 4.27: Simulation results without segregation for the thicknesses h_1 (top) and h_2 (bottom).

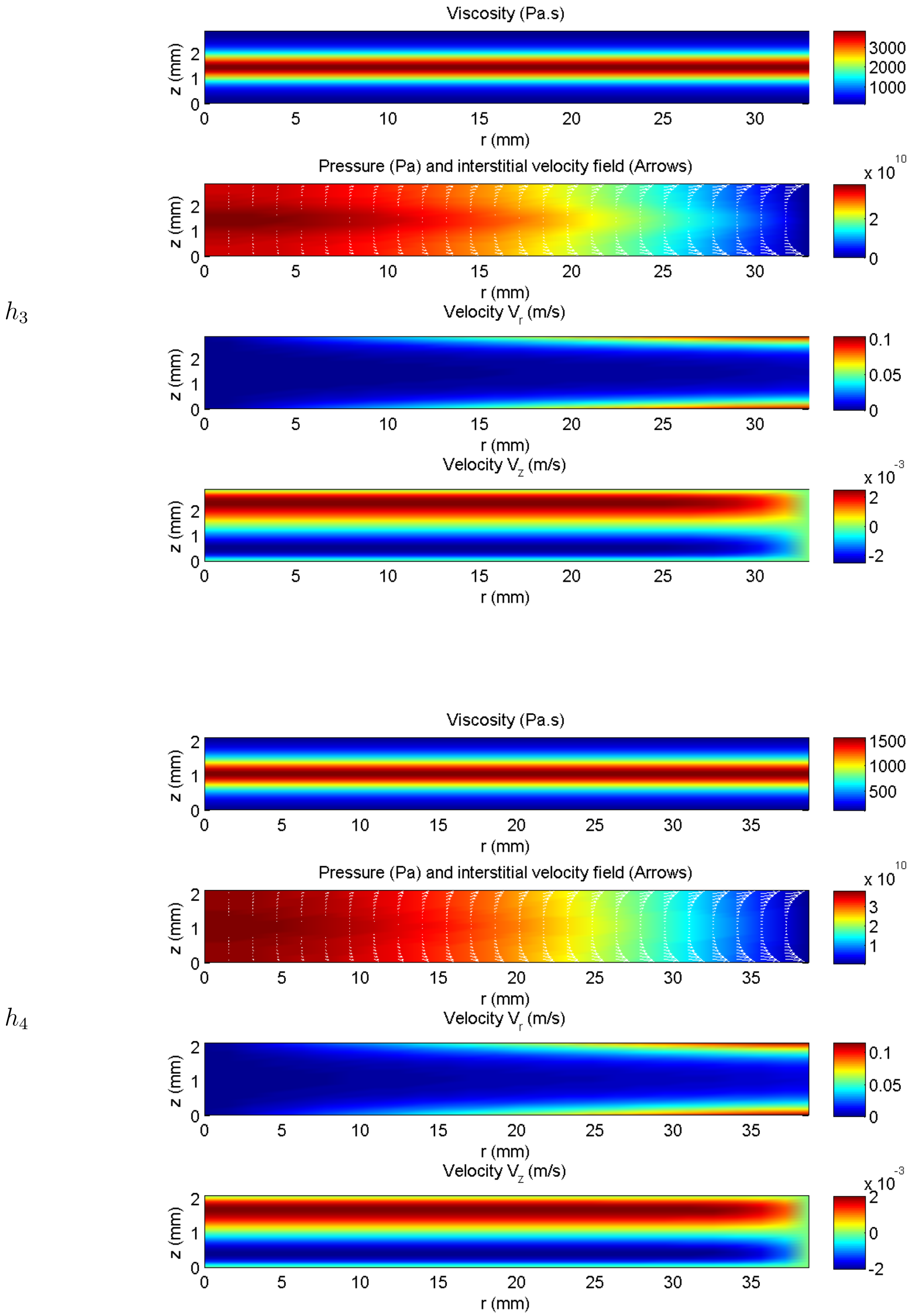

Figure 4.28: Simulation results without segregation for the thicknesses h_3 (top) and h_4 (bottom)

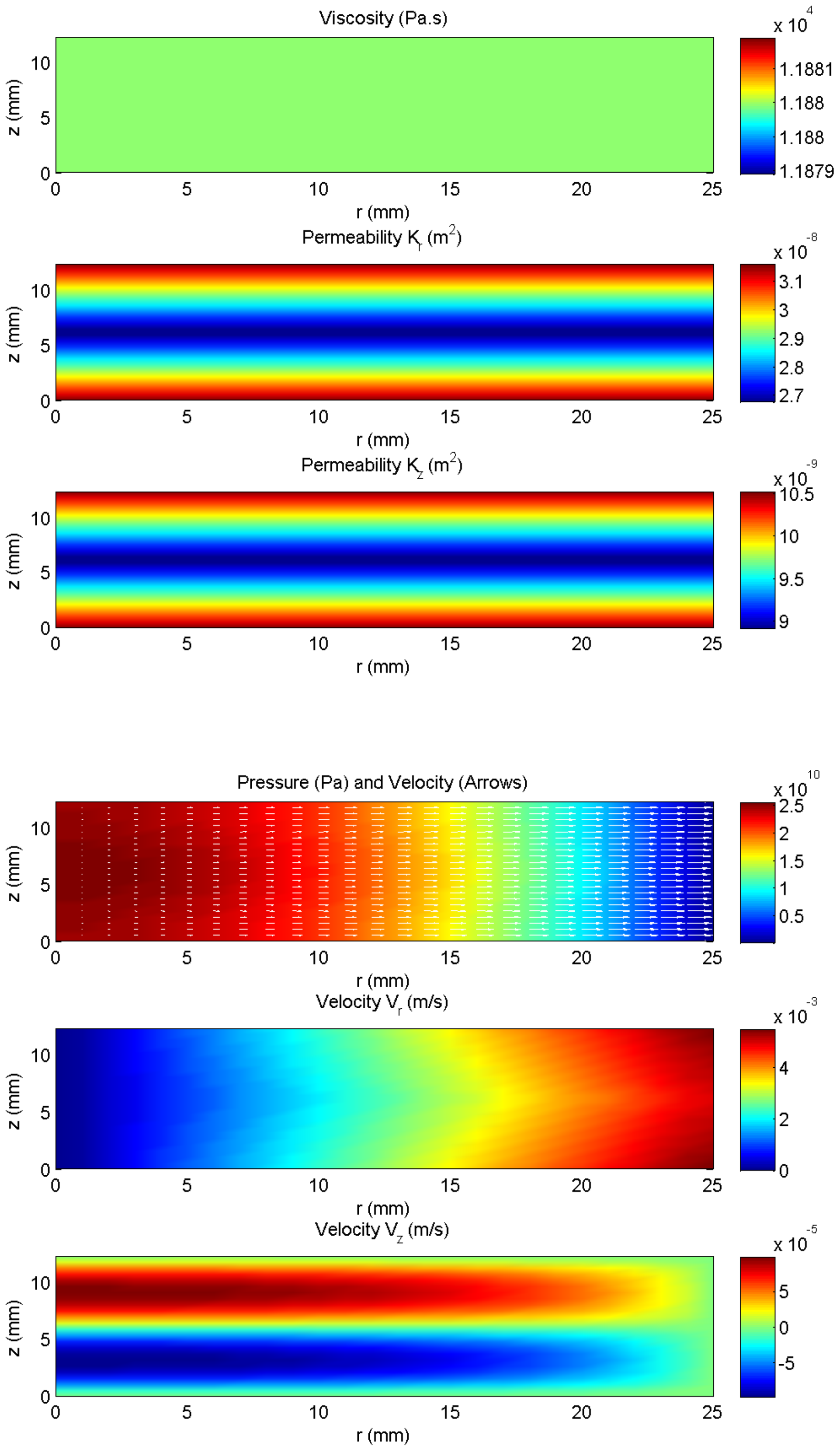

Figure 4.29: Simulation results with segregation for the thickness h_1.

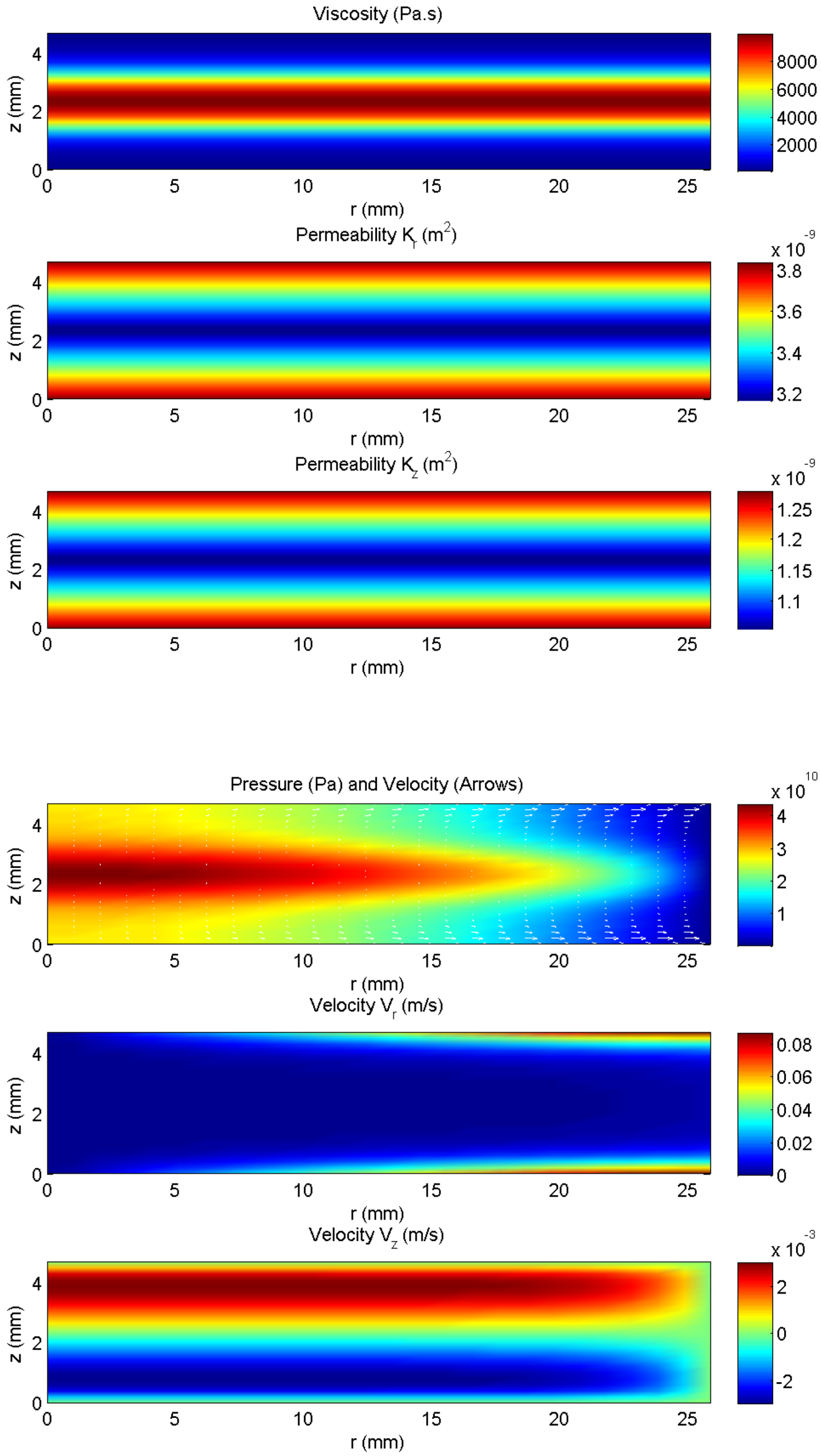

Figure 4.30: Simulation results with segregation for the thickness h_2.

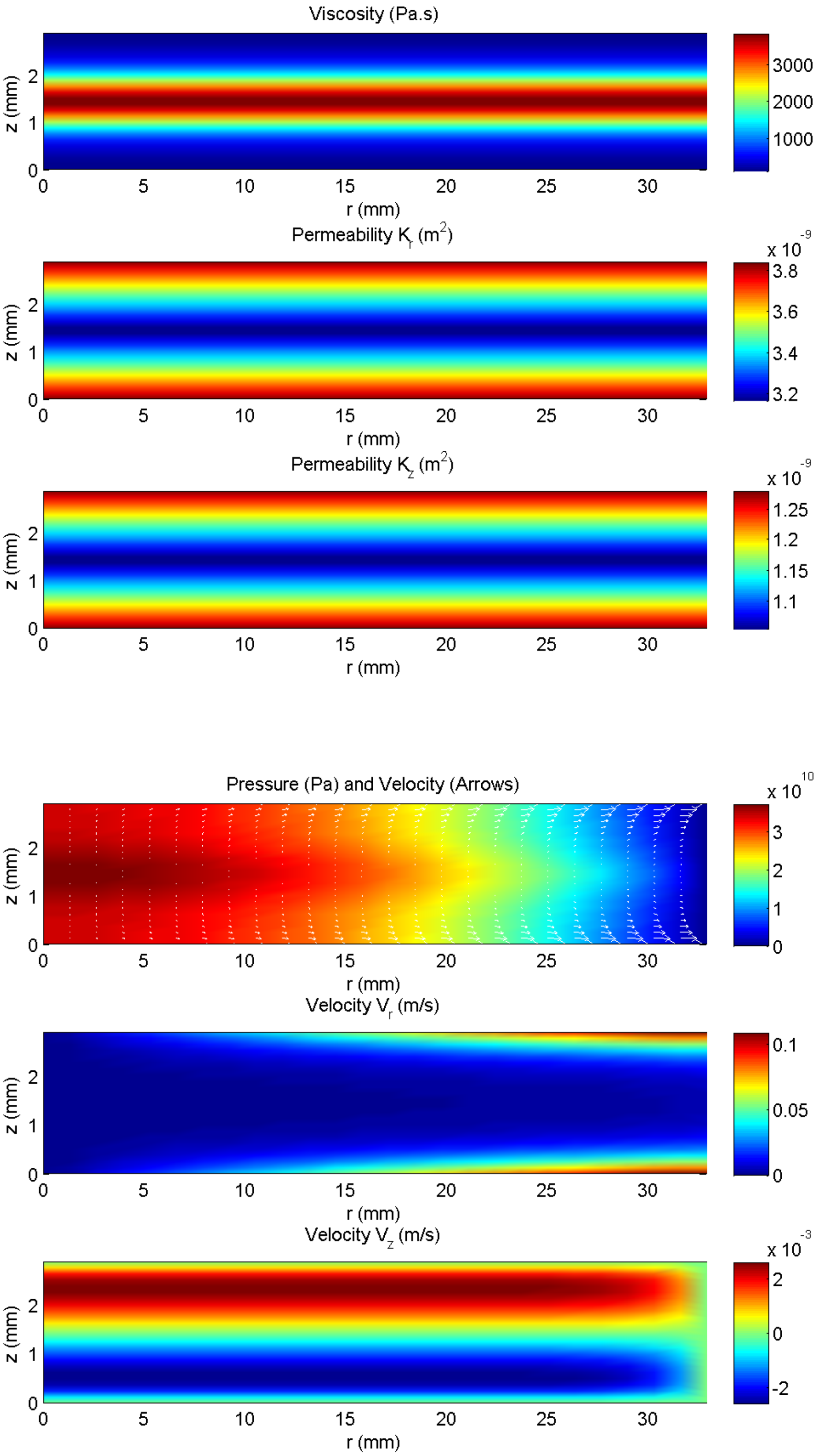

Figure 4.31: Simulation results with segregation for the thickness h_3.

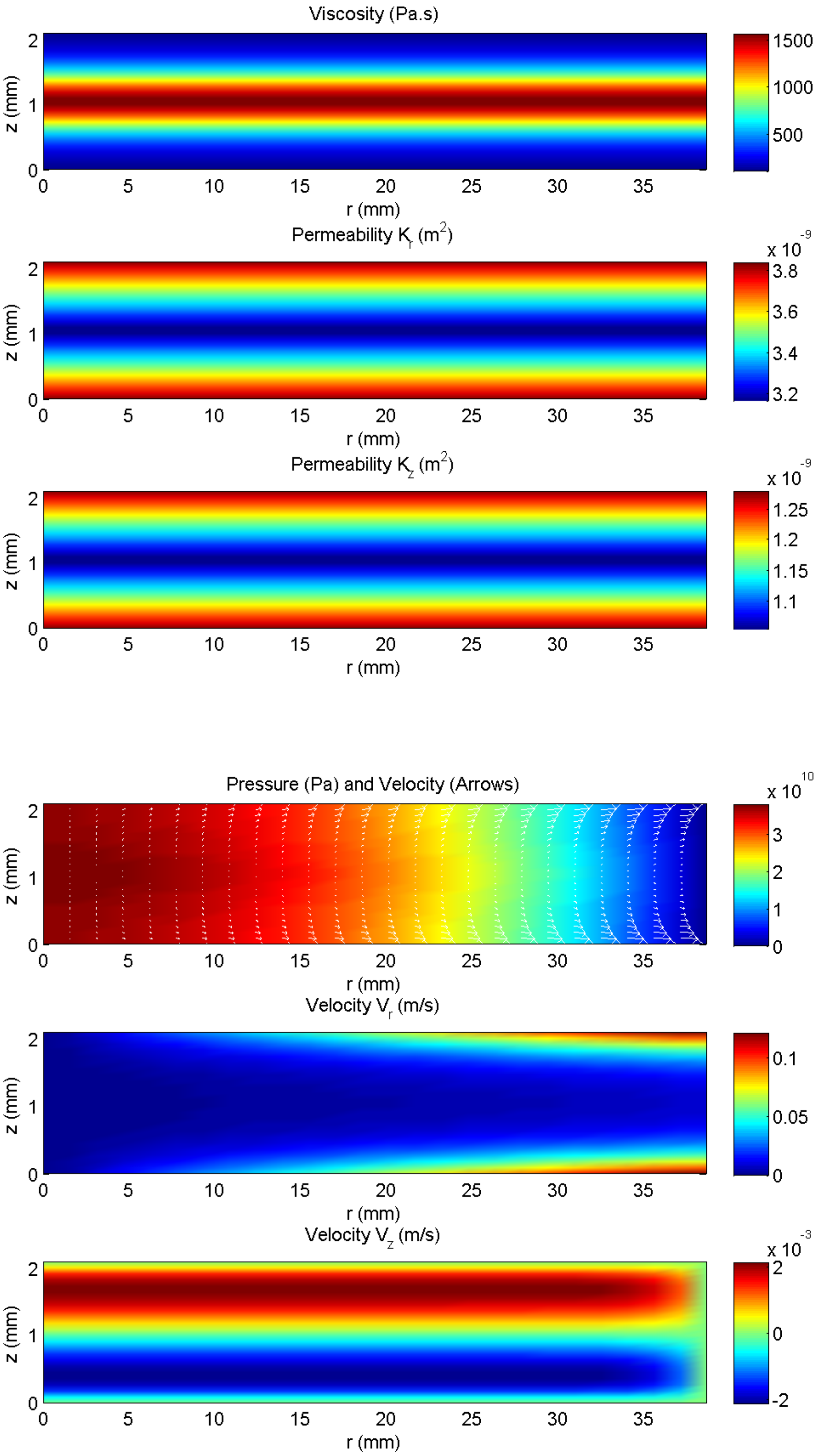

Figure 4.32: Simulation results with segregation for the thickness h_4.

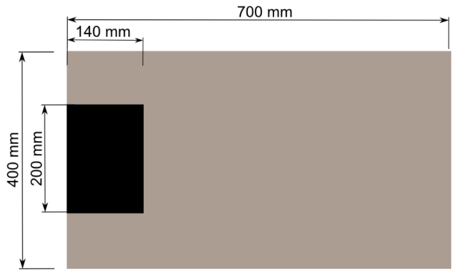

Figure 4.33: Distribution of the charge in the mould.

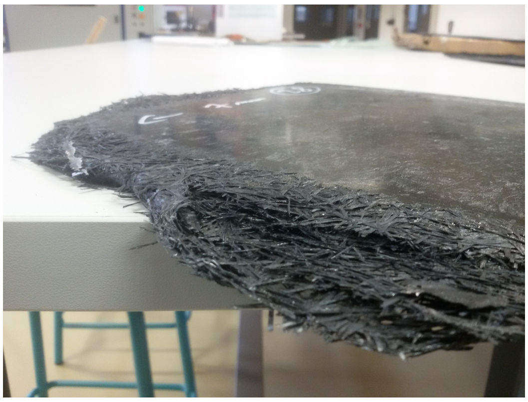

Figure 4.34: Folding of the bottom layer in sample 28.

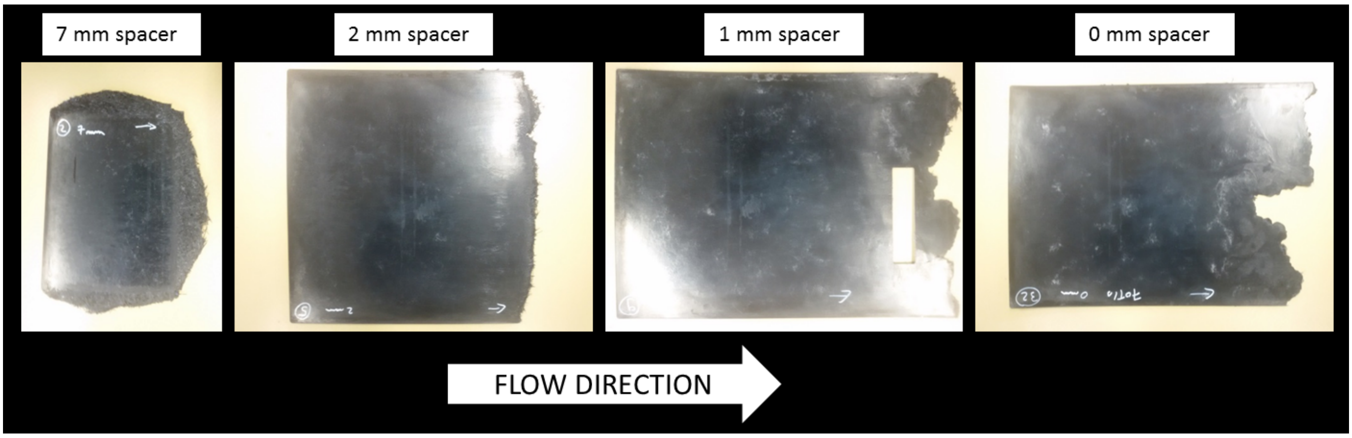

Figure 4.35: Evolution of the flow pattern vs the spacers thickness.

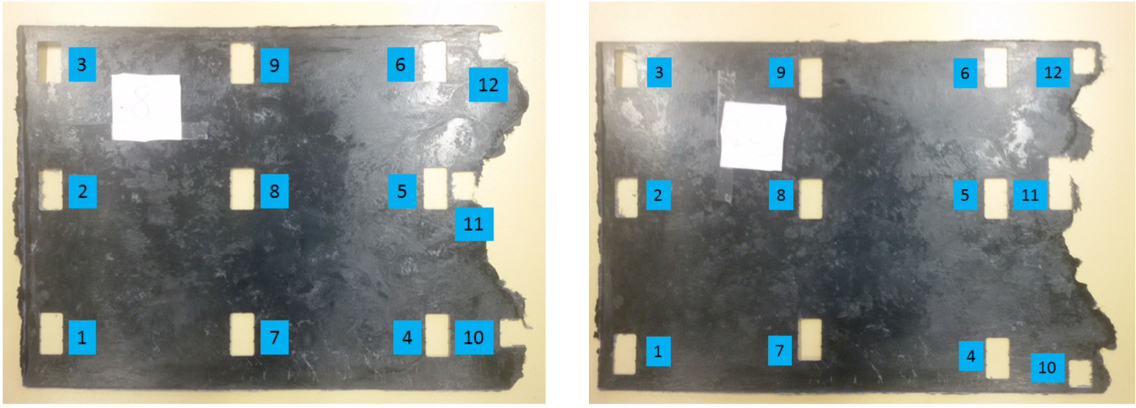

Figure 4.36: Placement of the samples from parts 8 (left) and 10 (right).

Figure 4.37: Disposition of the samples in the part #15.

Figure 4.38: Samples after the burn off test.

Chapter 5

Comparison of four image-based techniques to measure fibre orientation in SMC.

Mesurement of fibre content and orientation in SMC is of great importance for this work if a reliable validation of the model from the conducted part-based tests is to be achieved. A profound understanding of the available techniques of fibre orientation measurement is, therefore, capital to ensure truthful results. In this chapter we study diverse methodologies used to measure the fibre orientation in SMC parts. These methodologies are applied to samples cut out from the part #1 (see sections 3.2 and 3.5), manufactured by forcing an unidirectional flow pattern from a charge coverage of 30%. A survey on methods developed to measure the orientation distribution in suspensions from digital images shows a large variety of techniques and tools. It is believed that many factors can influence the outcomes. Then a critical comparison of different image-based techniques applied to the measurement of fiber orientation in SMC parts is developed in this chapter. Three different software packages; MountainsMap, ImageJ and MATLAB, are used to measure the fibre orientation along the squeeze flow direction and through the thickness. These measurements allowed us to compute the components of the orientation tensor. The goal of this analysis is to define which method is the most suitable to measure from high-resolution images obtained from a X-ray micro-tomograph the fibre orientation state in an SMC part manufactured under industrial conditions. As explained in section 3.5, 1440 images of the cross section of each sample from part #1 where recovered from the Imager of the micro-tomography, set in macro mode at 10 seconds exposure rate to get an image of pixel size 18.14 μm, from the X-ray at 40kV voltage and 8W power supply. The cross-sectioned images were then assembled with the Fiji image processing package of ImageJ, that allows to reconstruct the 3D sample from them, as shown in fig.3.24. In-plane images from different in-plane sections can then be observed with Fiji, to obtain the fibre orientation distribution in various in-plane sections. The outcome of this comparative study is some recommendations to improve this measurement.

5.1 Pre-processing of images.

Even though the images from the micro-tomograph have a high resolution, and also the SMC composite manufactured is a high industrial grade part, there is always some discrepancies in the images due to environmental conditions:

- **Blur effect at the edge of the sample**. The images obtained show a certain blur which caused discrepancies in the orientation analysis. This problem was sorted by simply cropping the blur region which was located at the boundary of the sample, but being careful to not lose important data or affect the fiber orientation analysis. Different patterns of cropping were analyzed and their effects on the orientation was studied for a few samples. The circular cropped sample images yielded the best results for the case of the SMC sample images and was thus, opted as most suitable.

- **Complexity of the SMC material rheology**. The complexity of the composition of the SMC material and of its manufactured composite itself present a challenge in image analysis as each image obtained from the micro-tomography have different particularities. There are many factors such as filamentization, widening, splitting or breaking of fibre bundles due to the effect of the shear that increase the initial complexity in the SMC part. The orientation analysis was performed only on fibre bundles to avoid introducing false measurements of the orientation, since it is believed, as concluded in section 3.5, that the orientation of the fibre bundles and of the single fibres may be happening at different rates. The removal of unwanted factors such as the filamentized fibres and noise in the images was done by pre-processing the images in MATLAB, applying an adaptive threshold to the image obtained from the micro-tomograph. A median filter was applied to further enhance the quality of the image and reduce the noise. The cropped pre-processed images were then used in MounatinMap and ImageJ to extract the distribution of the alignement of the fibres and to apply the FFT, coded in MATLAB.

- **Image masking and gaussian window**. The image masking and the gaussian window play a crucial role in orientation analysis. The mask for the input Image is created based on the parameters set for the minimum energy and minimum coherency parameters in the plug OrientationJ of ImageJ, and only the data within the mask is considered for the analysis. Since the SMC sample has many curved fibers of different intensities, difficulties can appear to adjust these parameters. The value of the standard deviation of the gaussian window greatly affects the accuracy of the analysis. It is based on the thickness of the area submited to analysis, which corresponds to the size of the fiber bundle which orientation is to be measured. After a thorough, quantitative analysis, these correct value of these parameters were set for the SMC sample images. A similar survey and review were also conducted by Püspöki [88], Goris [35], and Stergiopulos [72], for the selection of mathematical model and parameters.

Therefore, the following steps were taken to pre-process the initial SMC images:

1. Circular cropping of the initial images of the sample, obtained from the X-ray micro-tomograph, in order to remove the blur effect.

2. Adaptive threshold of each image to separate and remove the filamentized single fibers from fiber bundles.

3. Median filtering to further reduce noise effects and obviate the unwanted fiber fragments.

The final pre-processed images were then used to perform the orientation analysis with the different methods, described in in the next section. The increase of the accuracy from the pre-processed images for the orientation analysis was checked by comparing the results with analysis of an initial non-processed image.

Figure 5.1: Manual measure of the orientation of the reinforcement fibres.

5.2 Methodologies.

5.2.1 Manual measurement.

The manual measurement was performed by marking the orientation vector of fibre bundles directly over the image of the sample, as in fig.5.1, and measuring the angle of each one of the drawn lines with respect to the flow direction.

Once the orientation vector of each fibre bundle is known, the orientation tensor of each image can be obtained with equations 5.3, which is a discrete use of equation 2.60.

$$a_{11} = \frac{1}{N}\sum_{i=1}^{n}(cos\theta_i cos\theta_i) \tag{5.1}$$

$$a_{22} = \frac{1}{N}\sum_{i=1}^{n}(sin\theta_i sin\theta_i) \tag{5.2}$$

$$a_{12} = a_{21} = \frac{1}{N}\sum_{i=1}^{n}(sin\theta_i cos\theta_i) \tag{5.3}$$

The main drawbacks of this methodology are:

- It does not take into account the bundle length. Therefore, the orientation of a short or thin broken bundle has the same contribution as a complete long fibre placed entirely contained in the image plane.

- Subjectivity in defining when a bundle is totally filamentized. Sometimes bundles are very filamentized to an extent where single fibres can be detected, but it is still recognizable the bundle they belong to. Since the phenomenon is still not studied, it is difficult to define a threshold between the total individualization and the large widening of bundle. In this analysis, given the initial average width of the fibre bundles, about 0.74 mm, it was supposed that fibre bundles wider than 5 mm are completely filamentized.

- Orientation of the curved fibres. The length of fibre bundles, 25 mm, is long enough for them to bend due to the uneven shear along their length. In this analysis, the bent fibres were treated as an articulated slender body and the directions of each part of the slender body accounted for the measurement of the orientation.

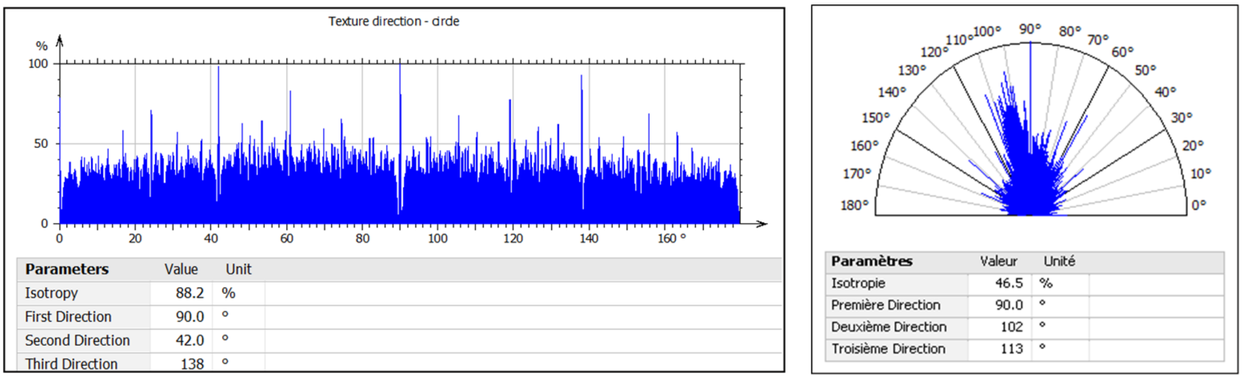

Figure 5.2: Types of histogram displayed by MountainsMap.

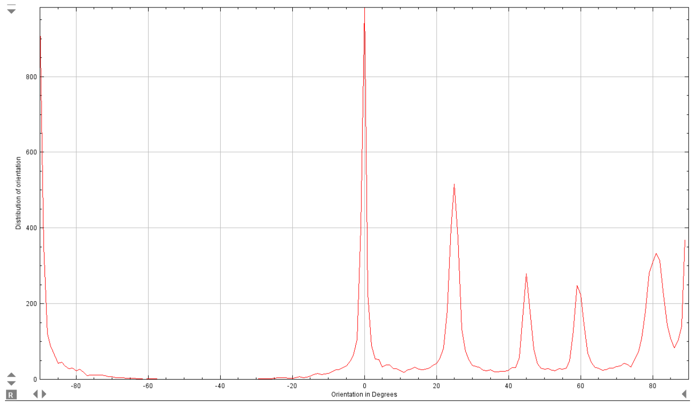

Figure 5.3: Orientation histogram in ImageJ.

5.2.2 Image analysis in MountainsMap.

MountainsMap is an image analysis software generally used to measure the topography or the texture of a surface from its image. The directionality tool in MountainsMap assists in plotting a histogram that represents the orientation angles in the x-axis from, 0° to 180°, and the percentage of bundles oriented with a certain angle in the y-axis . It also gives the possibility to draw the histogram radially, that gives a very intuitive idea of the principal directions of the orientation of the fibres (see fig.5.2). The orientation analysis in MountainMap is very quick and effective to find the principal orientations of the reinforcement fibres.

MounatinsMap provides the data form the histogram from with the obtaining of the orientation tensor of the fibre of the image is direct with equations 5.3.

5.2.3 Image analysis in ImageJ.

ImageJ is a Java based public domain image processing program, which allows further enhancing the quality of the sample images and gives more control over the analysis than MountainMap. Once the pre-processing of the sample image is done to enhance the image quality, the fibre orientation analysis in imageJ can be performed with the plug-in OrientationJ. It provides with a histogram that represents the fibre orientation angle, from -90° to 90° on the x-axis and fiber distribution function on the y-axis (see fig.5.3) . The histogram is plotted from the RGB color survey (see fig.5.4) and plotted as distribution of orientation vs orientation in degrees, obtained from the orientation plug-in, based on the parameters of gaussian window, minimum coherency, minimum energy and mathematical model. The value of these parameters for the case of the scanned images were set after a sensibility analysis of the value of different parameters and its effects on the fiber orientation measurements.

Figure 5.4: RGB color survey Image for a concentric circle.

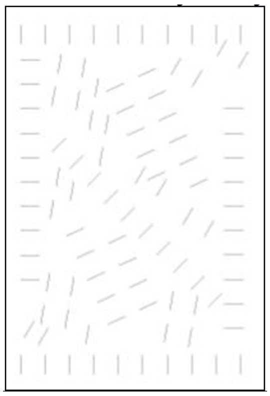

Figure 5.5: Test case.

5.2.3.1 Parameters calibration : gaussian window, coherency and minimum energy

A test case was used to perform a sensibility analysis of the values of the gaussian window, coherency and minimum energy for the fibre orientation measurement. Since these parameters define the mask, which plays a crucial role in analysis of the orientation, understanding how they work is of principal importance. Data are extracted from the test image shown in fig.5.5 by its masked color survey in fig.5.6. The mask of the test image, in fig.5.7, is created based on the parameters. In this case, they were set to : 40% of minimum coherency, 10% of minimum energy, and gaussian window = 1 (see fig.5.8). The structure tensor parameter of gaussian window is to be adjusted based on the thickness of the structure of interest, and on the mathematical model to measure the orientation, which in this case was set as the gaussian gradient, the most suited for the case of the scanned images. The minimum energy parameter is dependent on the intensity of the initial image. At zero minimum energy percentage the masked area is too small, and thereby computes large amount of unwanted data which leads to increased error; having a big minimum energy percentage creates a larger mask covering the essential data required for the analysis. The minimum coherency percentage helps in further refining the color survey, by masking the incoherent portion of the RGB color survey image, such as the round section that appears in the test images at the tip of a thick line. Hence, the proper selection of these parameters is mandatory before beginning the orientation analysis. Once these parameters are set, the histogram data for the orientation distribution vs the angle of orientation is extracted, and exported to MATLAB to calculate the orientation tensor.

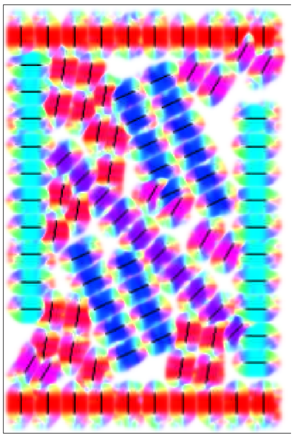

Figure 5.6: Color survey of the test case.

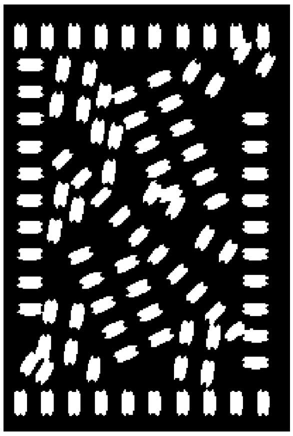

Figure 5.7: Mask of the test case.

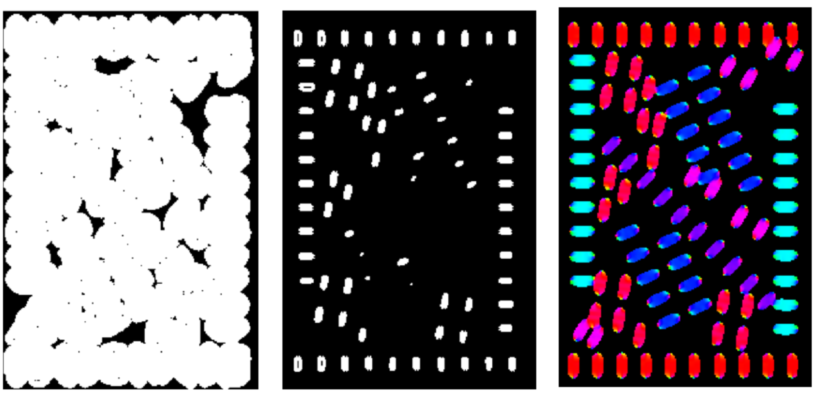

Figure 5.8: Mask of the test case created with the optimum parameters value.

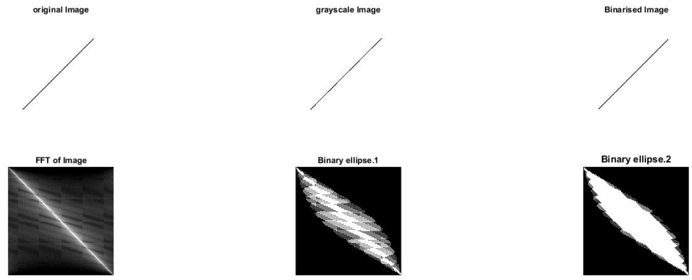

Figure 5.9: Test cases for the FFT method.

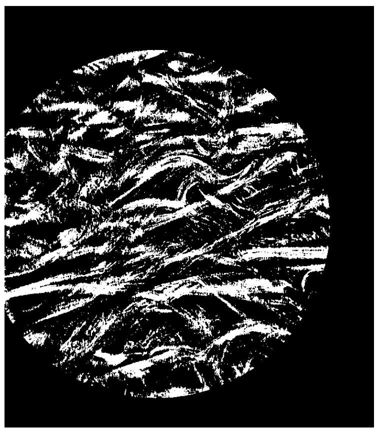

Figure 5.10: Binarized image of a scaned SMC sample image.

5.2.4 Image analysis with the Fast Fourier Transform (FFT) in Matlab.

The Fast Fourier Transform method in MATLAB is based on the concept of the Fraunhofer' s diffractometer: a line initially oriented at 45 degrees, when put under X-ray diffractometer single slit setup, causes a diffraction pattern that would be captured on the screen inverted at 135 degrees [23]. This diffraction pattern was found to be nothing but the FFT of the line. This method was tested for test cases of lines of known orientation in MATLAB. The procedure described by fig.5.9 was applied to the test cases, where the initial image is converted to grayscale image, after what it is binarized. The signal of the binarized image is obtained using the FFT function in MATLAB, that is then binarized and filtered to reduce the noise from the FFT image. The ellipse formed with-in the binarized image allows to obtain its orientation tensor [57]. The method was then applied to the sample images obtained from the X-ray micro-tomograph. To maintain the equality in comparison of the methods, the cropped pre-processed images were used, after what they were binarized and processed (see fig.5.10). The diffraction pattern was obtained using the FFT function (see fig.5.10). The major axis (X1) and minor axis (X2) of the diffracted ellipse define the eigenvalues and the eigenvectors of the orientation tensor of the image. The major challenges faced in this method are the data extraction from the diffraction pattern, due to the immense amount of noise in the FFT diffracted image.

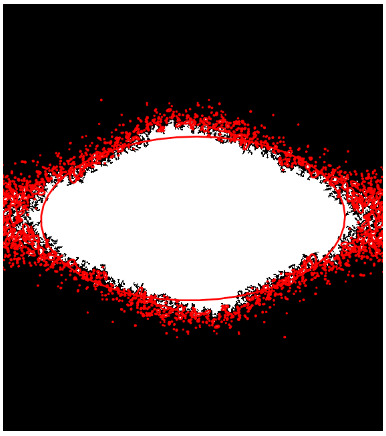

Figure 5.11: Diffracted ellipse of a scaned SMC sample image.

5.3 Quantitative comparison of results from the different methodologies.

The described methodologies were applied to obtain the orientation of a series of test cases consisting either in single lines and families of lines to emulate fibre bundles. Since the goal was to use the methodologies to measure the orientation of fibres in real SMC sample images, only the orientation of the fibre bundles should be taken into account by the methods to avoid wrong measurements, as explained in section 5.1.

In table 5.3, the results of each methodology for the series of test cases is summarized by confronting the images test case to the orientation ellipses obtained with the different methodologies.

TEST CASE	Manual	MountainsMap	ImageJ	FFT
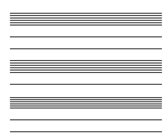	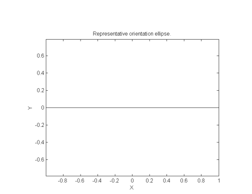	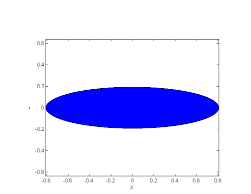	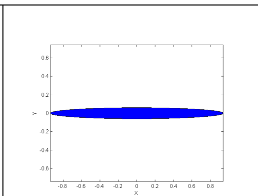	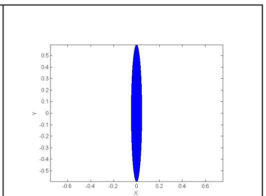
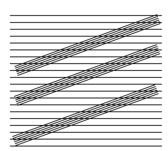	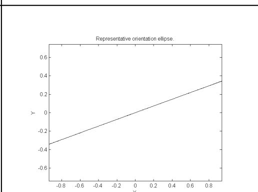	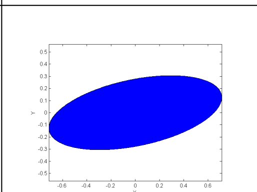	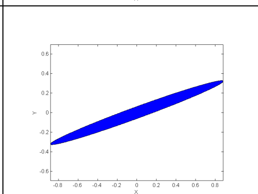	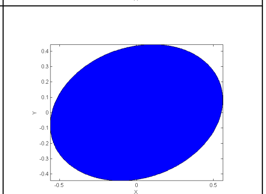
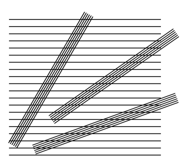	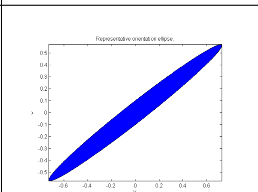	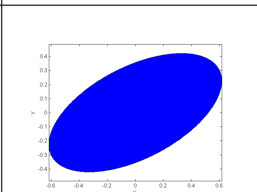	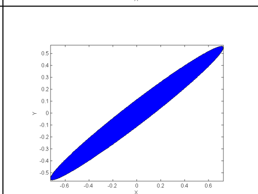	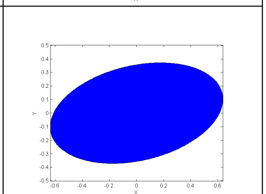
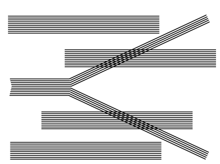	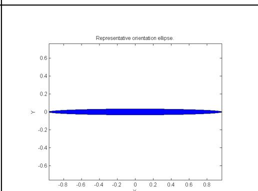	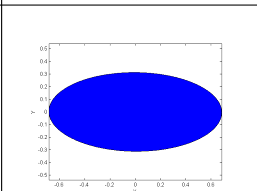	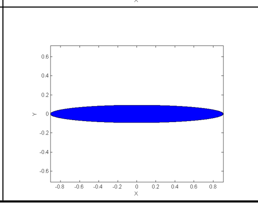	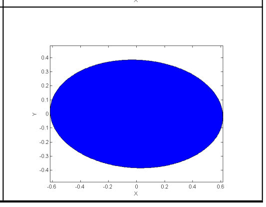

TEST CASE	Manual	MountainsMap	ImageJ	FFT

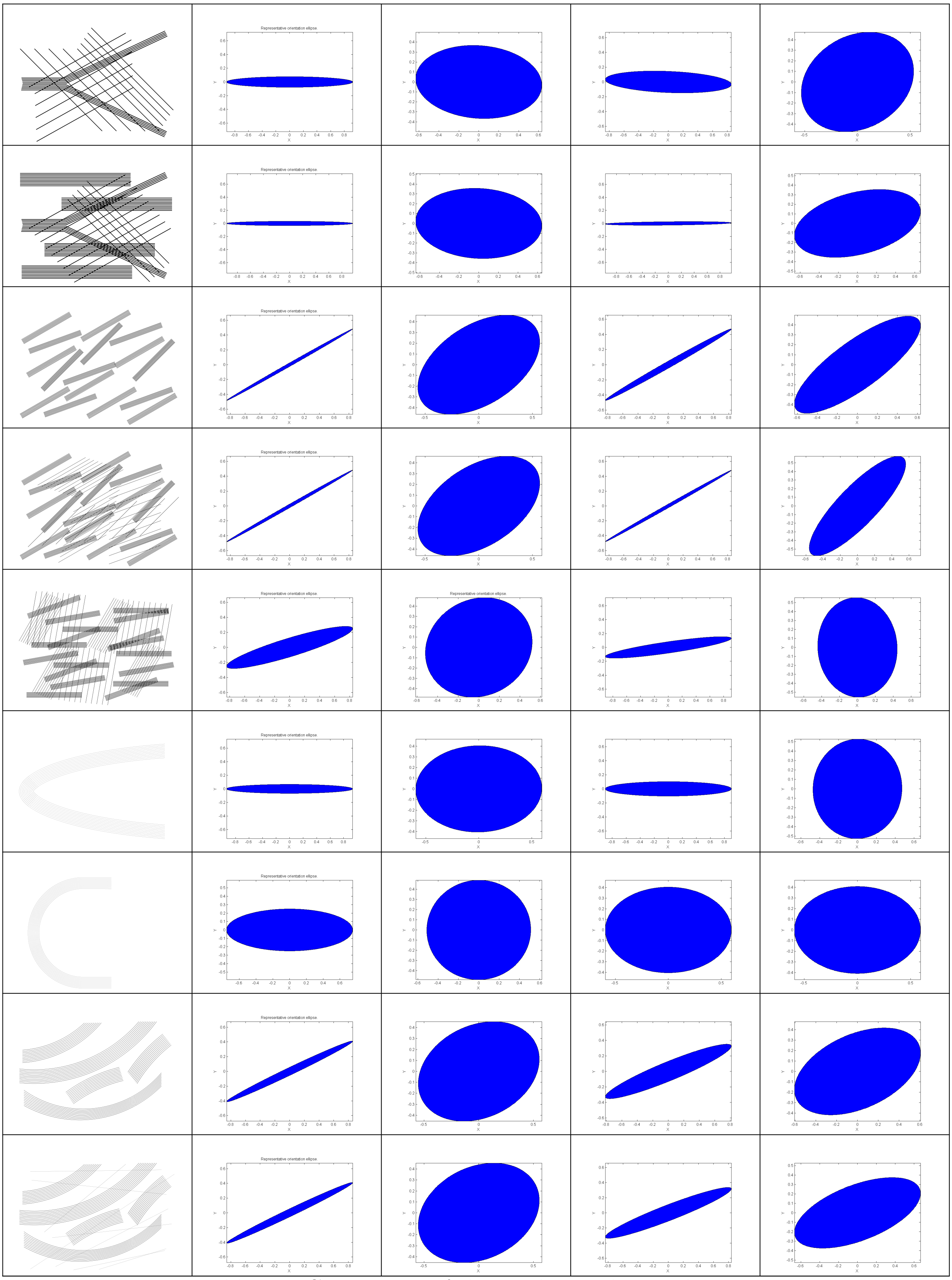

Table 5.1: Comparison of the results on the test layers.

In view of the results, the following conclusions are drawn:

- The results from ImageJ and the manual measurements are almost identical.
- The ImageJ and MountainsMap data extraction methods capture adequately the principal orientation of the fibre bundles of the test cases.
- The intensity of the alignment of the fibre bundles is better captured by ImageJ than by MountainsMap. MountainsMap seems to average between the fibrous region and clustered bundles.
- The FFT method fails to capture the orientation in the simplest cases, while its accuracy improves in direct relation of the population of bundles.
- For a clustered curved fiber bundle both MountainsMap and ImageJ show good overall orientation results, but its difficult to certify which one is the more accurate.
- For multiple clustered curved fiber bundles all three methods show good overall orientation results, but its difficult to certify which one is the more accurate.

In tables 5.3, 5.3 and 5.3, the same comparison was made for the images of the in-plane sections of the sample at the different positions in the part#1.

	$POS1_1$	Manual	MountainsMap	ImageJ	FFT
z=1.89	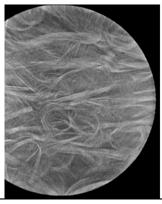	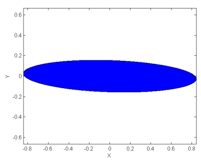	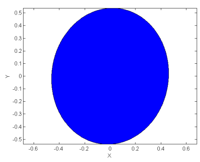	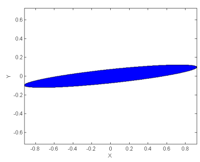	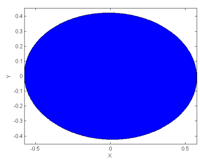
z=1.68	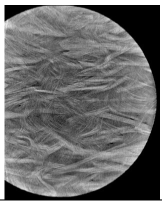	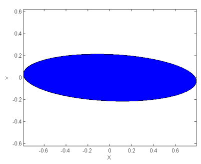	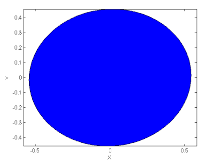	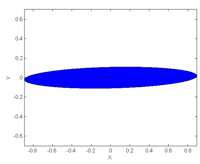	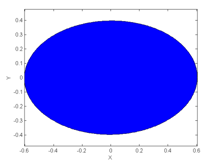
z=1.47	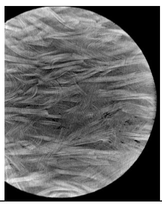	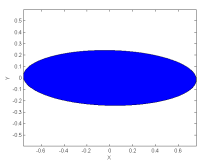	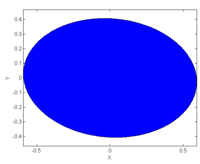	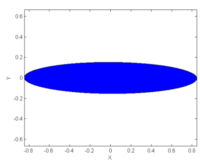	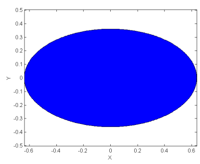
z=1.26	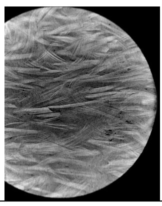	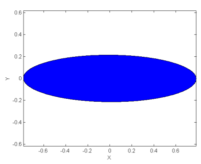	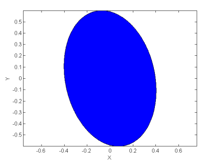	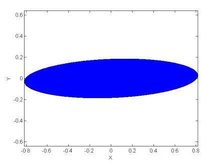	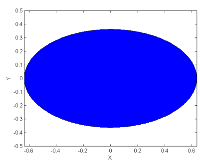
z=1.05	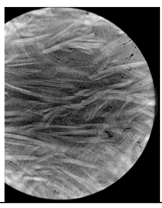	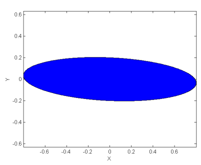	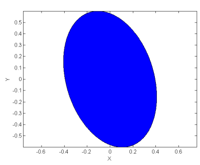	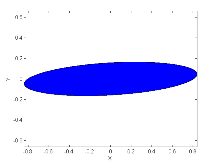	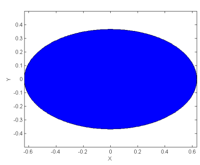

	$POS1_1$	Manual	MountainsMap	ImageJ	FFT
z=0.84	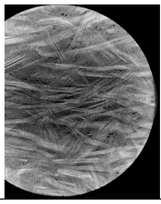	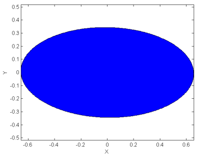	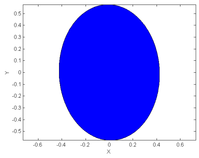	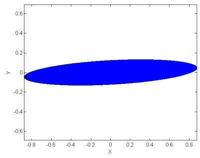	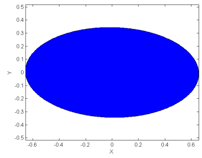
z=0.63	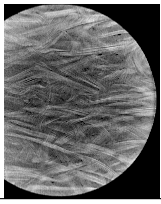	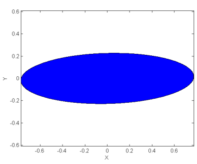	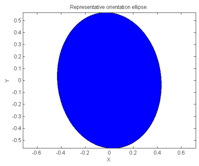	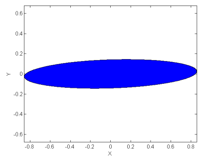	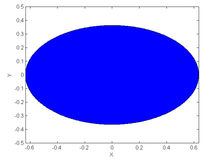
z=0.42	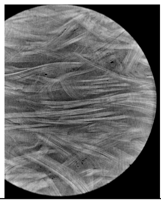	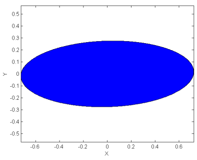	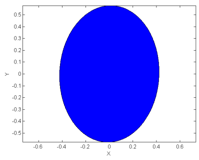	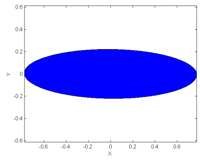	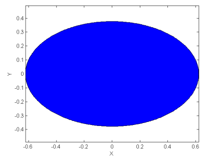
z=0.21	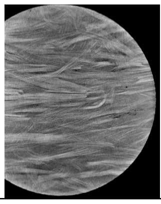	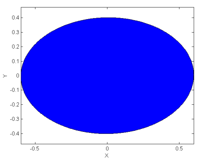	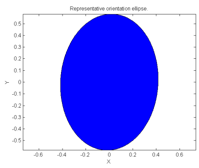	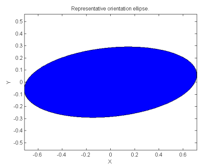	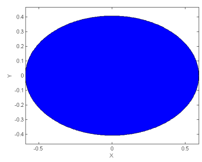

Table 5.2: Comparison of the results of the sample at the position 1 in the part 1.

	$POS1_2$	Manual	MountainsMap	ImageJ	FFT
z=1.89	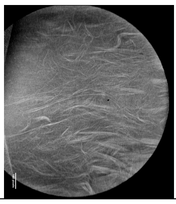	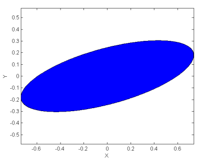	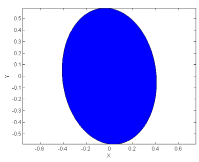	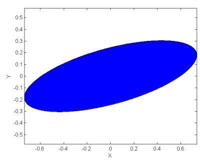	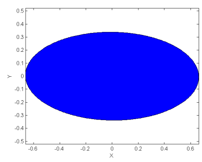
z=1.68	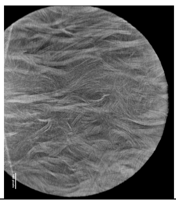	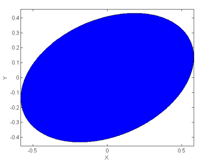	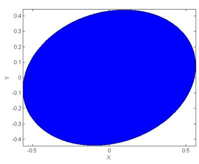	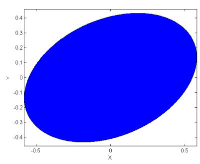	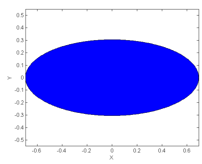
z=1.47	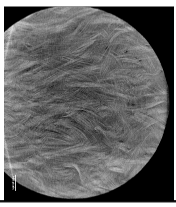	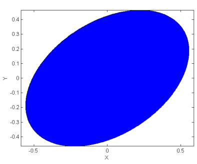	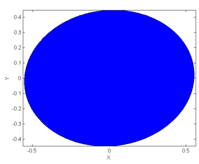	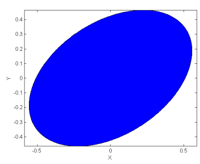	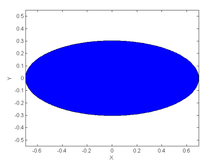

	$POS1_2$	Manual	MountainsMap	ImageJ	FFT
z=1.26	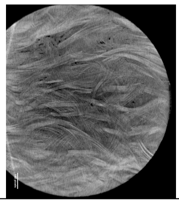	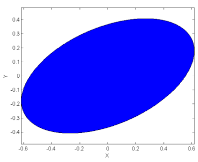	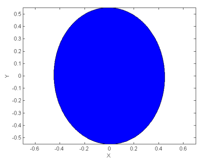	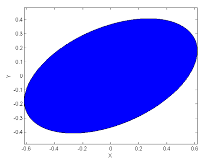	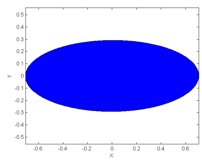
z=1.05		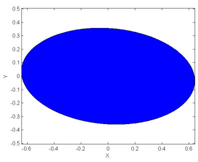	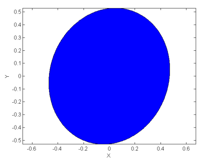	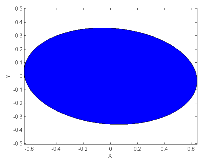	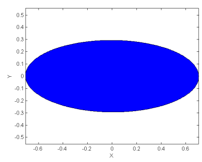
z=0.84	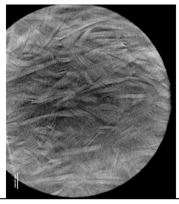	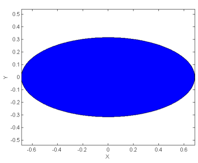	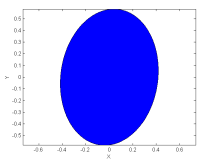	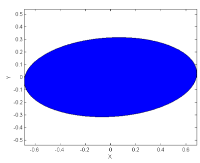	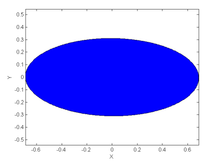
z=0.63	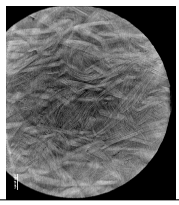	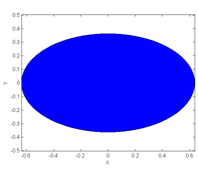	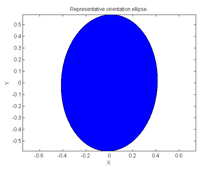	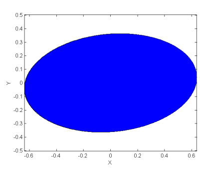	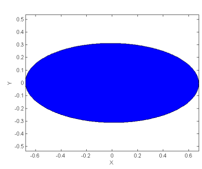
z=0.42	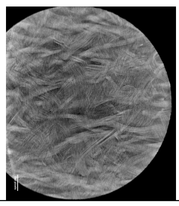	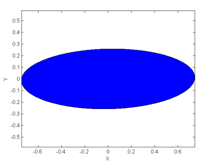	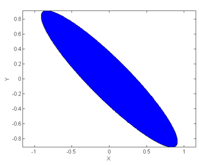	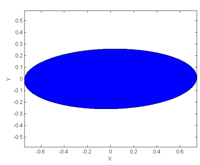	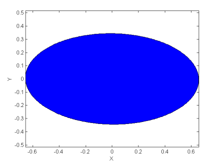
z=0.21	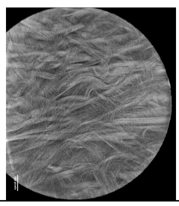	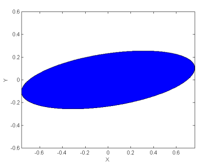	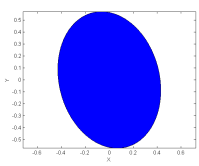	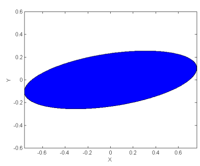	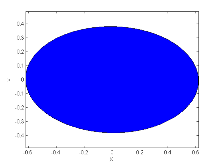

Table 5.3: Comparison of the results of the sample at the position 2 in the part 1.

	POS_3	Manual	MountainsMap	ImageJ	FFT
z=1.89	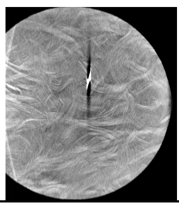	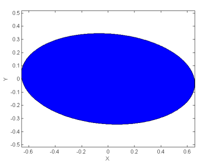	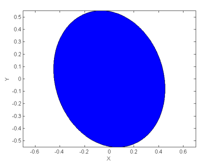	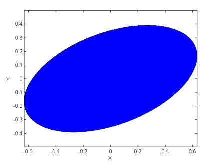	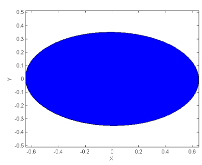

	POS_3	Manual	MountainsMap	ImageJ	FFT
z=1.68	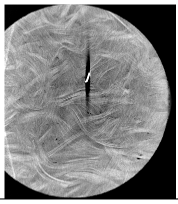	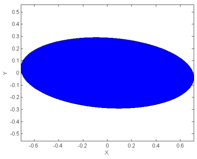	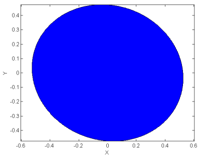	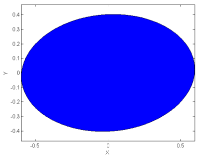	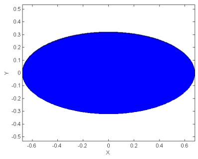
z=1.47	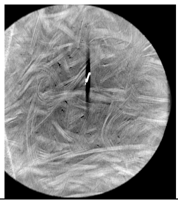	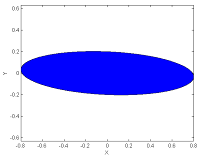	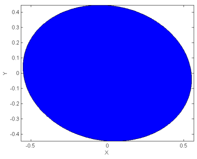	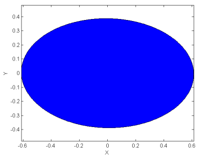	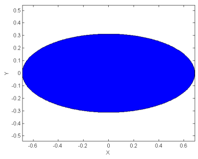
z=1.26		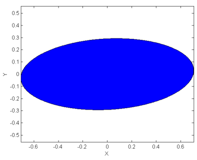	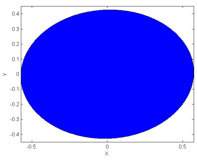	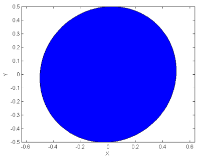	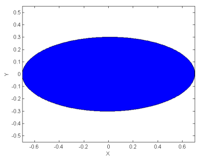
z=1.05	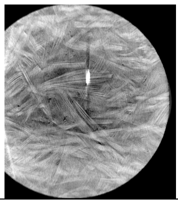	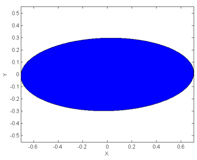	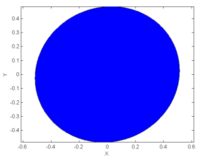	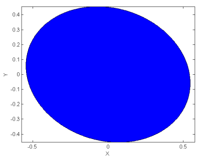	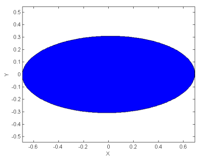
z=0.84		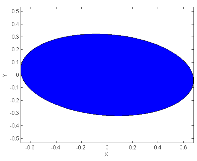	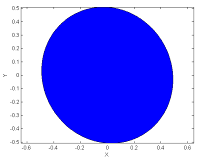	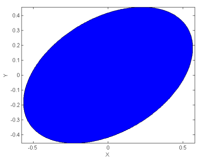	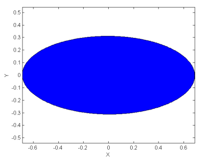
z=0.63	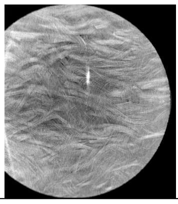	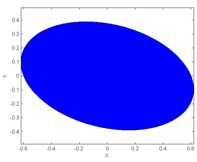	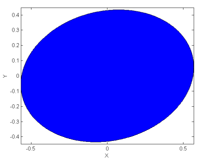	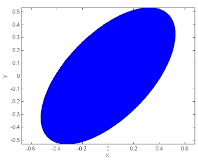	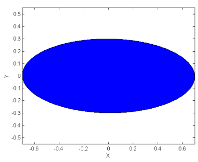
z=0.42	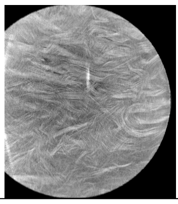	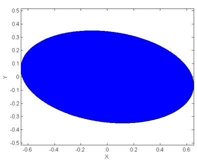	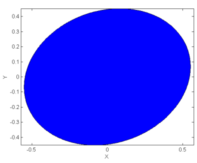	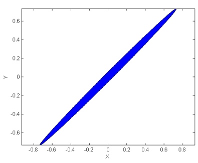	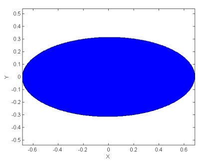
z=0.21	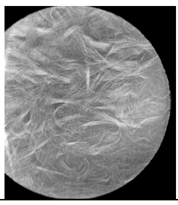	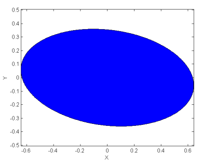	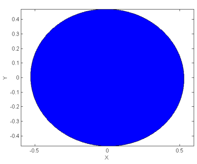	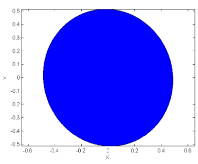	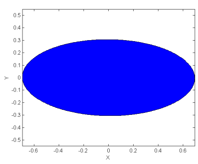

Table 5.4: Comparison of the results of the sample at the position 3 in the part 1.

In view of the previous results, the following conclusions are drawn:

- The discontinuity that can be seen in the images of the sample of position 3 are due to a copper tracer. Copper tracers were initially integrated between the SMC layers of the charge in some parts produced during the first campaign. The performance of the copper tracers in the test was unsuccessful, therefore they are not reported in this thesis. The reflection caused by the copper tracers hides the fibres and the image analysis is greatly affected. Therefore, only the manual measurement can be trusted as a estimation of the orientation of the fibre bundles at the position occupied by this sample.
- Either the manual measurement and ImageJ give a good estimation of the orientation tensor, compared to the manual method. The results obtained by ImageJ are the closest to the manual solution for the simple orientation analysis. ImageJ offers a great control over the SMC images, allowing more pre-processing options to enhance the image quality. Although the calibration of parameters can be laborious, once they are properly set the distribution of the orientation of the fibre bundles is the more accurate compared with the other methodologies. The small difference in the principal directions of alignment shown between these two procedures is due to the fact that the manual measurement does not take into account the length of the fibre bundles while it is accounted by ImageJ.
- The FFT method can be used as a directionality function to represent the principal directions of the orientation of the fibre bundles of an entire SMC sample, but not for a detailed analysis to obtain the individual fiber distribution.
- MountainsMap does not capture properly the orientation tensor of the images and cannot be used for this analysis.
- None of the digital procedures capture the orientation tensor in the presence of copper tracers. Only the manual technique is suited in this case.

Chapter 6

Conclusions and outlooks.

6.1 Conclusions.

To introduce SMC to structural applications, an advanced understanding and modeling of the mechanisms that govern the flow and transformation of the fibrous microstructure during the compression molding process is crucial. While a few commercial software packages are proposed to simulate the SMC compression, this study was meant to understand some discrepancies between predictions and real productions. To achieve this goal a general framework has been proposed and organized in different chapters. The following is a summary of the main findings we obtained, sorted out in chapter.

The main results obtained in chapter 2 are:

- **A simulation tool adapted to the peculiarities of the SMC compression moulding process has been developed.** The Hele-Shaw model was chosen as momentum equation to describe the flow of the SMC material [77] [52], which is acknowledged to be convenient to describe the squeeze flow of the SMC material in thin cavities [51]. It relies on the assumption of no-slip conditions between the contact point of the fluid and its enclosing domain. The fluid-flow model describes the position and evolution of the flow front pattern of the composite charge during the compression phase. As already mentioned, in compression moulding of SMC, the dominant type of flow that takes place is the so called 'squeeze flow'. The problem has been solved by the Finite Element Method (FEM), combined by the Control Volume (CV) approach to track the material flow front. The overall approach is the well-known FEM-CV methods used to model several composite processes involving flow of material over long distances. The code developed here was originally developed to address RTM flow problem and adapted here for the particular case of the squeeze flow of SMC material.

- **The proposed model is the best suited for the particular case of SMC compression moulding because it takes into account the physics to reproduce the effect of *confinement* of fibres in the thin mould gap.** The fibre orientation induced by the flow has been modelled with the Confined Rod Suspensions model [63], one of the newest and most advanced models for suspensions. This model was developed to take into account the effect of the *confinement* of fibres in thin mould gap.

- **The proposed compression moulding fluid flow model with confined chopped fibres is suitable for 2D and 3D geometries.** The capabilities of the numerical model have been illustrated through the simulation of the flow in different two and three-dimensional geometries, with different types of SMC charges and compressed with different squeeze rates. The validity of the model is demonstrated since it shows no mass loss during the process of transportation of fluid between the control volumes, and the computed pressure field matches the theoretical distribution.

The main results obtained in chapter 3 are:

- **Some tests have been performed on SMC panels produced under industrial conditions.** To validate the proposed model, a series of mechanical test and microscale observations were performed on rectangular panels produced in industrial conditions at the facility of Faurecia Group in Saint-Meloir-des-Ondes, France. Samples studied in the lab-scale rheological cell can be compressed by keeping the same squeeze rate but the resulting pressure will be much lower. Comparing microstructures of SMC produced with an industrial scale process and lab-scale protocol are not similar. Lab-scale samples had many voids and the fibre bundles are not transformed.

- **The results of the test on full parts are in qualitative agreement with the predictions of the numerical model.** A tensile test on the full parts combined with Digital Image Correlation (DIC) techniques was performed to measure the deformation field. Uniform strain field has been measured in parts where the model predicted uniform alignment of fibres. Strain fields were more isotropic in parts where an isotropic distribution of the orientation of fibres was predicted. However, when zooming to local regions in the part, some discrepancies with the local predictions of the numerical model in the parts appear. Two possible causes can be considered: either the test is not sensitive enough to capture the local elastic response, or the fibre distribution was more isotropic than what the numerical model predicts.

- **The trends observed in the tensile tests on coupons are in qualitative agreement with the numerical model prediction.** In parts moulded with unidirectional flow, the test coupons are stiffer and more resistant in the direction of the flow. In parts obtained with combined radial and longitudinal flows, the stiffness and the Young moduli are more homogeneous, whatever the orientation of the coupons. However, no conclusions can be drawn for the ultimate strain at break due to the high scattering in values. In the case of the combined flow, the dispersion of the values of the ultimate strength is even bigger than in the unidirectional flow case.

- **The fibre alignment changes along the same flow line in parts moulded with unidirectional flow. The through-thickness orientation distribution differs from the supposed velocity profiles.** A micro-structural analysis of samples cut out from panels was made by means of 3D images taken with a X-ray micro-tomograph. The fibre orientation in SMC parts with unidirectional flow revealed an evolution that is in disagreement with the predictions of models, which predict the same exact orientation for all the fibres in the same flow line and a symmetry with respect to the mid-plane in the through-thickness direction. This kind of distribution cannot be explained by the current fluid flow models, which describe symmetric velocity profiles in the out-of-plane direction that necessarily lead to symmetric distributions of the orientation of the fibres in the same direction.

- **Two different populations of fibres co-exist in the same material: fiber bundles and filamentized individual fibres.**. The same micro-structural analysis revealed a change of the width of the bundles that can be caused either by the filamentization that makes the fibre bundles break due to the shear in the flow direction, opening the tows and allowing the fibres to spread, or because of a breakage along its longitudinal axis. The quantity and magnitude of filamentization of fibre bundles is in direct relation to the shear stress and, therefore, with the velocity profile. Therefore, the filamentization is the principal mechanism of individualization of the fibres close tho the mould/charge interface. It also evidenced that, if the degree of filamentization is asymmetric in the through-thickness direction, as it has been observed, the through-thickness velocity distribution is uneven. The phenomena affects more intensively the fibre bundles transverse to the flow direction. Indeed, there are two different reinforcement types coexisting in the material during the compression: on the one hand fibre bundles and on the other hand the individualized fibres. It is expected that the degree of fibre bundles opening will have a significant effect on the mechanical performance of parts. An uneven viscosity field can be expected due to the uneven filamentization. This phenomenon constitutes another evidence of the lack of physics of the actual orientation models, that cannot describe the microstructural complexity of the material.

The main results obtained in chapter 4 are:

- **The initial 2D isothermal numerical model has been successfully extended to a 2.5D non-isothermal model.** In view of the experimental results, the numerical model was enriched in order to take into consideration some experimental observations. The initial formulation of the 2D velocity field, obtained by averaging the planar components of the velocity through the thickness (the out-of-plane independence of the velocity value in the Hele-Saw model allows to do so), was generalized in order to be able to reconstruct the velocity profile in the thickness, to allow to describe the orientation of the fibres in the out-of-plane direction, becoming a 2.5D model. The through-thickness heat transfer and viscosity field distribution in the SMC charge were modeled and coupled, in order to study the influence of the temperature on the fibre orientation distribution in the through-thickness direction.

In parallel to the development of the code, additional lab-scale tests were carried out to have a better understanding of mechanisms that led to the above mentioned phenomena
From laboratory scale SMC compression tests, the following results were obtained.

- **In all the non-isothermal experiments, the bottom layer of the SMC charge squishes from the rest of the layers at the beginning of the compression, followed by the top layer.**

- **The squished bottom layer bends towards the upper platen and even folds over the upper layers.** This can cause variations of the flow front behaviour since this mechanism is found to be non-uniform along the flow front. The bottom layer behaves more a a shell-like structure than as a fluid. This effect provided another evidence of the unsuitability of the classic models.

- **A concentration of matrix is found around the flow front at the beginning of the compression.**The air entrapped in the porosities and in between layers flushes out from the compressed charge pushing some almost pure matrix to the flow front and forming a ring-like zone that surrounds the flow front. This frontal zone tends to disappear with further compression.

- **There is a difference of behaviour in the carbon tracers placed on the surface of certain samples that depends on their initial thickness.**In the samples made out of four layers, the carbon tracers placed on the surface of the charge experienced different degrees of displacement. In the samples made out of two layers, the tracers reminded almost at their initial position. This indicates that the actual charge/mould boundary condition is somehow random. The possibility of a transverse redistribution of matrix to enrich the mould/charge interface does not seem consistent with these experimental findings.

- The compression force-time curves showed similar responses with certain differences according to the scenario of the test: a first force peak due to the flushing out of the air entrapped between layers, a second force peak corresponding to the end of the compression phase and a relaxation stage begins where the force returns gradually to zero that is shorter in the hotter samples. Finally, the exothermal curing of the polyester may cause small peaks at longer times. The compression force in non-isothermal boundary conditions is higher for shorter compression times.

From a analysis of the out-of-plane matrix flow, the following results were obtained.

- **No differential fibre/matrix flow in the through thickness direction happens in the compression test.** A dedicated experiment was carried out that evidenced that the out-of-plane matrix transfer is negligible for the used material under the experimental conditions. For further study of the possible fibre/matrix relative flow, a Darcy's law based numerical consolidation model has been used for further investigation. In simulations run with constant volume fraction in the sample or the ones considering fibre segregation from skin to core, both scenarios considering the transient heat transfer, a negligible through-thickness velocity of the matrix was obtained.

From the short shots made under industrail conditions on high performance SMC (55% by weight of glass fibres), the following results were obtained.

- **The folding of the bottom layers over the flow front happens with great intensity at the beginning of the compression.**. Spacers of different thickness were used for the short shots, in order to control the compression ratio applied to the charge. In the samples were the compression was stopped at early stages, an pronounced folding between layers happens in almost all the specimens.

- **The flow pattern shows more irregularity as the squeeze rate (compression velocity) and compression ratio (ratio of the initial to the final thickness) increase.** This can be caused by the folding of some layers at the flow front, that obstacles the flow of the material and forces the material to change the direction of the stream lines to find the path of of minimum energy. A study of the distribution of the density in the final incomplete parts showed that, however, there is no differential fibre/matrix flow. This may be justified by the lower content of matrix in the high performance SMC material.

The main results obtained from chapter 5 are:

The manual measurement of the direction of the fiber bundles and the OrientationJ plug-in of ImageJ are the most convenient methodologies to measure the orientation of the reinforcement fibres. Finally, a chapter of this thesis is dedicated to the analysis of the different methodologies of measurement of the orientation of the fibres from images. Four methodologies were analyzed on test cases and on X-ray micro-tomograph scanned images of samples from the industral-scale regular SMC parts: the manual measurement of the direction of the fiber bundles, the analysis of the orientation of the fibers with two commercial image-processing packages, ImageJ and MountainsMap, and the FFT method implemented in Matlab. The analysis is challenging due to diversity and the amount of factors and parameters to be defined and calibrated in order to optimize the results. From the comparison of four classical image-based techniques to measure fibre orientation in SMC, it can be concluded that the most suited methodologies are either the manual measurement or the OrientationJ plug-in in ImageJ. Any software-based technique requires a very careful determination of the calibration parameters to get reliable results.

6.2 Outlooks.

The proposed model does not include important ingredients that are mandatory to predict the process-induced microstructure in industrial SMC compression.

- First the matrix was supposed to behave as a Newtonian fluid. A power-law model or shear-thinning model would be more suitable.
- A one-way fluid flow/fibre orientation coupling was proposed in this thesis. A full coupling is necessary due to the high concentration in fibres.
- The mechanism of filamentization should be modelled and implemented in the numerical simulation.
- A new model of viscosity is required to include the influence of the filamentization on the local equivalent viscosity field [69] [83] [84] [58] [21] [54].

Bibliography

[1] Advani, S. G., & Sozer, E. M. (Eds.). (2002). Process modeling in composites manufacturing (Vol. 59). CRC press.

[2] Advani, S. G., & Tucker III, C. L. (1987). The use of tensors to describe and predict fiber orientation in short fiber composites. Journal of rheology, 31(8), 751-784.

[3] Advani, S. G., & Tucker III, C. L. (1990). Closure approximations for three-dimensional structure tensors. Journal of Rheology, 34(3), 367-386.

[4] Advani, S. G., & Tucker III, C. L. (1990). A numerical simulation of short fiber orientation in compression molding. Polymer composites, 11(3), 164-173.

[5] Advani, S. G., & Hsiao, K. T. (Eds.). (2012). Manufacturing techniques for polymer matrix composites (PMCs). Elsevier.

[6] Apostol, T. M. (1967). Calculus, Vol. 1: One-Variable Calculus, with an Introduction to Linear Algebra. Waltham, MA: Blaisdell.

[7] Apostol, T. M. (1969). Calculus, vol.II. Editora Reverté SA, Barcelona, Buenos Aires, Caracas, MÃ©xico, MCMLXXII.

[8] Azaiez, J., Chiba, K., Chinesta, F., & Poitou, A. (2002). State-of-the-art on numerical simulation of fiber-reinforced thermoplastic forming processes. Archives of Computational Methods in Engineering, 9(2), 141-198.

[9] Barone, M. R., & Caulk, D. A. (1985). Kinematics of flow in sheet molding compounds. Polymer composites, 6(2), 105-109.

[10] Barone, M. R., & Caulk, D. A. (1986). A model for the flow of a chopped fiber reinforced polymer compound in compression molding. Journal of applied mechanics, 53(2), 361-371.

[11] Batchelor, G. K. (1970). The stress system in a suspension of force-free particles. Journal of fluid mechanics, 41(3), 545-570.

[12] Batchelor, G. K. (1976). An introduction to fluid mechanics. Cambridge University Press.

[13] Bronstein, I. N., & Semendyaev, K. A. (1981). Handbook of mathematics for engineers and students of technical colleges.

[14] Books, R. (1997). Materials Properties Modeling and Design of Short Fibre Composite, In: T.D. Papathanasiou, D.C. Guell (eds). Flow-induced alignement in composite materials, 293pp., Woodhead Pub., England.

[15] Binetruy, C., Chinesta, F., & Keunings, R. (2015). Flows in Polymers, reinforced polymers and composites: A multi-Scale approach. Springer.

[16] Carrier III, W. D. (2003). Goodbye, hazen; hello, kozeny-carman. Journal of geotechnical and geoenvironmental engineering, 129(11), 1054-1056.

[17] Chinesta, F. (2013). From single-scale to two-scales kinetic theory descriptions of rods suspensions. Archives of Computational Methods in Engineering, 20(1), 1-29.

[18] Chong, J. S., Christiansen, E. B., & Baer, A. D. (1971). Rheology of concentrated suspensions. Journal of applied polymer science, 15(8), 2007-2021.

[19] Comas-Cardona, S. (2005). Modélisation, simulation et contrôle du couplage hydromécanique pour le moulage de composites (Doctoral dissertation, Lille 1).

[20] Comas-Cardona, S., Binetruy, C., & Krawczak, P. (2007). Unidirectional compression of fibre reinforcements. Part 2: A continuous permeability tensor measurement. Composites Science and Technology, 67(3-4), 638-645.

[21] Costa, F. S., Cook, P. S., & Pickett, D. (2015). A framework for viscosity model research in injection molding simulation, including pressure and fiber orientation dependence. SPE ANTEC Tech. Papers.

[22] Cox, R. G., & Brenner, H. (1971). The rheology of a suspension of particles in a Newtonian fluid. Chemical Engineering Science, 26(1), 65-93.

[23] Pourdeyhimi, B., Dent, R., & Davis, H. (1997). Measuring fiber orientation in nonwovens Part III: Fourier transform. Textile Research Journal, 67(2), 143-151.

[24] Dinh, S. M., & Armstrong, R. C. (1984). A rheological equation of state for semiconcentrated fiber suspensions. Journal of Rheology, 28(3), 207-227.

[25] Dumont, P., OrgÃ©as, L., Favier, D., Pizette, P., & Venet, C. (2007). Compression moulding of SMC: In situ experiments, modelling and simulation. Composites Part A: Applied Science and Manufacturing, 38(2), 353-368.

[26] Eik, M., Puttonen, J., & Herrmann, H. (2016). The effect of approximation accuracy of the orientation distribution function on the elastic properties of short fibre reinforced composites. Composite Structures, 148, 12-18.

[27] Endruweit, A., McGregor, P., Long, A. C., & Johnson, M. S. (2006). Influence of the fabric architecture on the variations in experimentally determined in-plane permeability values. Composites Science and Technology, 66(11-12), 1778-1792.

[28] Engmann, J., Servais, C., & Burbidge, A. S. (2005). Squeeze flow theory and applications to rheometry: a review. Journal of non-newtonian fluid mechanics, 132(1-3), 1-27.

[29] Dumont, P., Orgéas, L., Le Corre, S., & Favier, D. (2003). Anisotropic viscous behavior of sheet molding compounds (SMC) during compression molding. International Journal of Plasticity, 19(5), 625-646.

[30] Fan, X., Phan-Thien, N., & Zheng, R. (1998). A direct simulation of fibre suspensions. Journal of Non-Newtonian Fluid Mechanics, 74(1-3), 113-135.

[31] Folgar, F., & Tucker III, C. L. (1984). Orientation behavior of fibers in concentrated suspensions. Journal of reinforced plastics and composites, 3(2), 98-119.

[32] Gauvin, R., Trochu, F., Lemenn, Y., & Diallo, L. (1996). Permeability measurement and flow simulation through fiber reinforcement. Polymer composites, 17(1), 34-42.

[33] Geerling Gamboa, E.L. Reducción del error experimental en los campos de deformación obtenidos por un sistema de correlación de imágenes digitales. Facultad de Ciencias Físicas y Matemáticas. Universidad de Chile (2015).

[34] Ghnatios, C., Chinesta, F., & Binetruy, C. (2015). 3D Modeling of squeeze flows occurring in composite laminates. International Journal of Material Forming, 8(1), 73-83.

[35] Goris, S., & Osswald, T. (2015). Fiber orientation measurements using a novel image processing algorithm for micro-computed tomography scans. In Proceedings of SPE ANTEC.

[36] Guiraud, O., Dumont, P. J. J., Orgéas, L., & Favier, D. (2012). Rheometry of compression moulded fibre-reinforced polymer composites: rheology, compressibility, and friction forces with mould surfaces. Composites Part A: Applied Science and Manufacturing, 43(11), 2107-2119.

[37] Gutowski, T. G., Morigaki, T., & Cai, Z. (1987). The consolidation of laminate composites. Journal of Composite Materials, 21(2), 172-188.

[38] Affdl, J. H., & Kardos, J. L. (1976). The Halpin-Tsai equations: a review. Polymer Engineering & Science, 16(5), 344-352.

[39] Han, K. K., Lee, C. W., & Rice, B. P. (2000). Measurements of the permeability of fiber preforms and applications. Composites science and Technology, 60(12-13), 2435-2441.

[40] HERMXNS, P. (1946). Contribution to the Physics of Cellulose Fibers.

[41] Herrmann, H., & Beddig, M. (2018). Tensor series expansion of a spherical function for the use in constitutive theory of materials containing orientable particles. Proceedings of the Estonian Academy of Sciences, 67(1), 73-92.

[42] Hinch, E. J., & Leal, L. G. (1975). Constitutive equations in suspension mechanics. Part 1. General formulation. Journal of Fluid Mechanics, 71(3), 481-495.

[43] Hinch, E. J., & Leal, L. G. (1976). Constitutive equations in suspension mechanics. Part 2. Approximate forms for a suspension of rigid particles affected by Brownian rotations. Journal of Fluid Mechanics, 76(1), 187-208.

[44] Hohberg, M., K´arger, L., Henning, F., & Hrymak, A. (2017). Rheological measurements and rheological shell model Considering the compressible behavior of long fiber reinforced sheet molding compound (SMC). Composites Part A: Applied Science and Manufacturing, 95, 110-117.

[45] M. Imbert (2017). High speed reactive RTM with on line mixing in du al scale fibrous reinforcements: experimental and numerical developments and investigations. Ecole Central de Nantes.

[46] Jackson, W. C., Folgar, F., & Tucker, C. L. III. (1982). Prediction and control of fiber orientation in molded parts. Polymer Blends and Composites in Multiphase Systems, 279-299.

[47] Jackson, W. C., Advani, S. G., & Tucker, C. L. (1986). Predicting the orientation of short fibers in thin compression moldings. Journal of Composite Materials, 20(6), 539-557.

[48] Jeffery, G. B. (1922). The motion of ellipsoidal particles immersed in a viscous fluid. Proc. R. Soc. Lond. A, 102(715), 161-179.

[49] Kleindel, S., Salaberger, D., Eder, R., Schretter, H., & Hochenauer, C. (2015). Prediction and validation of short fiber orientation in a complex injection molded part with chunky geometry. International polymer processing, 30(3), 366-380.

[50] Kuppusamy, R. R. P., Shinde, V. M., & Neogi, S. (2012). Measurement of effective permeability of reinforcement mats using sensitivity analysis. Polymer Composites, 33(8), 1445-1454.

[51] Lee, C. C., & Tucker III, C. L. (1987). Flow and heat transfer in compression mold filling. Journal of non-newtonian fluid mechanics, 24(3), 245-264.

[52] Lee, C. C., Folgar, F., & Tucker, C. L. (1984). Simulation of compression molding for fiber-reinforced thermosetting polymers. Journal of engineering for industry, 106(2), 114-125. Ind.,106 (1984) 114.

[53] Lebel-Lavacry, A. (2012).Modélisation et simulation de la saturation en milieux fibreux a double echelle de pores pour la mise en oeuvre des matériaux composites. Université du Havre.

[54] Li, T., & Luyé, J. F. (2017). Flow-fiber coupled viscosity in injection molding simulations of short fiber reinforced thermoplastics. International Polymer Processing.

[55] Lionello, G., & Cristofolini, L. (2014). A practical approach to optimizing the preparation of speckle patterns for digital-image correlation. Measurement Science and Technology, 25(10), 107001.

[56] Londono-Hurtado A., Hernandez-Ortiz, J. P., & Osswald, T. A. (2007). Mechanism of fiber-matrix separation in ribbed compression molded parts. Polymer composites, 28(4), 451-457.

[57] Lovrich M., T.C.L. Automated Measurments of fiber orientation in short fiber composites. Annual Tecnical Conference and Exhibition - Society of Plastic Engineers, pp. 1119-1122, 1985.

[58] Mazahir, S. M., Vélez-García, G. M., Wapperom, P., & Baird, D. (2013). Evolution of fibre orientation in radial direction in a center-gated disk: Experiments and simulation. Composites Part A: Applied Science and Manufacturing, 51, 108-117.

[59] McCormick, N., & Lord, J. (2010). Digital image correlation. Materials today, 13(12), 52-54.

[60] McGee, S. H. (1983). The Influence of Microstructure on the Elastic Properties of Composite Materials.

[61] Orgéas, L., & Dumont, P. J. (2011). Sheet molding compounds. Wiley Encyclopedia of Composites, 1-36.

[62] Parnas, R. S., Flynn, K. M., & Dal-Favero, M. E. (1997). A permeability database for composites manufacturing. Polymer Composites, 18(5), 623-633.

[63] Perez, M., Scheuer, A., Abisset-Chavanne, E., Chinesta, F., & Keunings, R. (2016). A multi-scale description of orientation in simple shear flows of confined rod suspensions. Journal of Non-Newtonian Fluid Mechanics, 233, 61-74.

[64] Phan-Thien, N., Fan, X. J., Tanner, R. I., & Zheng, R. (2002). Folgar-Tucker constant for a fibre suspension in a Newtonian fluid. Journal of Non-Newtonian Fluid Mechanics, 103(2-3), 251-260.

[65] Phelps, J. H., & Tucker III, C. L. (2009). An anisotropic rotary diffusion model for fiber orientation in short-and long-fiber thermoplastics. Journal of Non-Newtonian Fluid Mechanics, 156(3), 165-176.

[66] Byron Pipes, R., McCullough, R. L., & Taggart, D. G. (1982). Behavior of discontinuous fiber composites: fiber orientation. Polymer Composites, 3(1), 34-39.

[67] Pomeroy, R., Grove, S., Summerscales, J., Wang, Y., & Harper, A. (2007). Measurement of permeability of continuous filament mat glass-fibre reinforcements by saturated radial airflow. Composites Part A: Applied Science and Manufacturing, 38(5), 1439-1443.

[68] Pratt, W. K. (1973). Bibliography on digital image processing and related topics.

[69] Ranganathan, S., & Advani, S. G. (1991). Fiber-fiber interactions in homogeneous flows of nondilute suspensions. Journal of Rheology, 35(8), 1499-1522.

[70] Ranganathan, S., & Advani, S. G. (1993). A simultaneous solution for flow and fiber orientation in axisymmetric diverging radial flow. Journal of Non-Newtonian Fluid Mechanics, 47, 107-136.

[71] Recktenwald, G. W. (2004). Finite-difference approximations to the heat equation. Mechanical Engineering, 10, 1-27.

[72] Rezakhaniha, R., Agianniotis, A., Schrauwen, J. T. C., Griffa, A., Sage, D., Bouten, C. V., ... & Stergiopulos, N. (2012). Experimental investigation of collagen waviness and orientation in the arterial adventitia using confocal laser scanning microscopy. Biomechanics and modeling in mechanobiology, 11(3-4), 461-473.

[73] Reynolds, O. (1885). On the Theory of Lubrication and Its Application to Mr. Beauchamp Tower's Experiments, Including an Experimental Determination of the Viscosity of Olive Oil. Phil. Trans. Roy. Soc., 1, 157.

[74] Rodriguez, E., Giacomelli, F., & Vazquez, A. (2004). Permeability-porosity relationship in RTM for different fiberglass and natural reinforcements. Journal of composite materials, 38(3), 259-268.

[75] Santos, A. H. A., Pitangueira, R. L. S., Ribeiro, G. O., & Caldas, R. B. (2015). Study of size effect using digital image correlation. Revista IBRACON de Estruturas e Materiais, 8(3), 323-340.

[76] Sepehr, M., Ausias, G., & Carreau, P. J. (2004). Rheological properties of short fiber filled polypropylene in transient shear flow. Journal of Non-Newtonian Fluid Mechanics, 123(1), 19-32.

[77] Silva-Nieto, R. J., Fisher, B. C., & Birley, A. W. (1980). Predicting mold flow for unsaturated polyester resin sheet molding compounds. Polymer composites, 1(1), 14-23.

[78] Smith, G. D. (1985). Numerical solution of partial differential equations: finite difference methods. Oxford university press.

[79] Solutions, C. (2009). Digital Image Correlation: Overview of Principles and Software. University of South Carolina.

[80] Sutton, M. A., McNeill, S. R., Helm, J. D., & Chao, Y. J. (2000). Advances in two-dimensional and three-dimensional computer vision. In Photomechanics (pp. 323-372). Springer, Berlin, Heidelberg.

[81] Tandon, G. P., & Weng, G. J. (1984). The effect of aspect ratio of inclusions on the elastic properties of unidirectionally aligned composites. Polymer composites, 5(4), 327-333.

[82] Tseng, H. C., Chang, R. Y., & Hsu, C. H. (2017). Improved fiber orientation predictions for injection molded fiber composites. Composites Part A: Applied Science and Manufacturing, 99, 65-75.

[83] VerWeyst, B. E., & Tucker III, C. L. (2002). Fiber suspensions in complex geometries: flow/orientation coupling. The Canadian Journal of Chemical Engineering, 80(6), 1093-1106.

[84] Vincent, M., Giroud, T., Clarke, A., & Eberhardt, C. (2005). Description and modeling of fiber orientation in injection molding of fiber reinforced thermoplastics. Polymer, 46(17), 6719-6725.

[85] Wang, J., O'Gara, J. F., & Tucker III, C. L. (2008). An objective model for slow orientation kinetics in concentrated fiber suspensions: Theory and rheological evidence. Journal of Rheology, 52(5), 1179-1200.

[86] Wedgewood, A., Zhang, Z., Sulmoni & Kang, S. (2017). Addressing practical challenges in developing Digimat material laws. In Digimat Users' Meeting, Berlin, Germany.

[87] Williams, M. L., Landel, R. F., & Ferry, J. D. (1955). The temperature dependence of relaxation mechanisms in amorphous polymers and other glass-forming liquids. Journal of the American Chemical society, 77(14), 3701-3707.

[88] Püspöki, Z., Storath, M., Sage, D., & Unser, M. (2016). Transforms and operators for directional bioimage analysis: a survey. In Focus on Bio-Image Informatics (pp. 69-93). Springer, Cham.

[89] Zienkiewicz, O. C., & Taylor, R. L. (1977). The finite element method (Vol. 36). London: McGraw-hill.

Appendix A

Filamentization.

<table>
<tr><th>z (mm)</th><th>POSITION 1</th><th>SCANNED IN-PLANE IMAGE</th></tr>
<tr><td>1.89</td><td>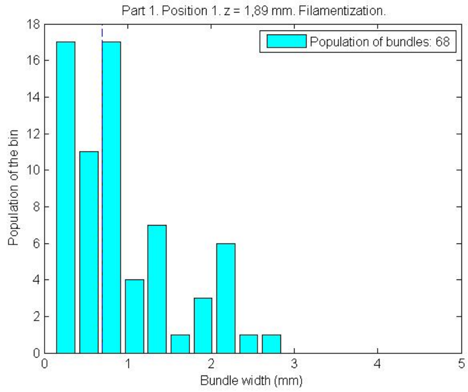
</td><td>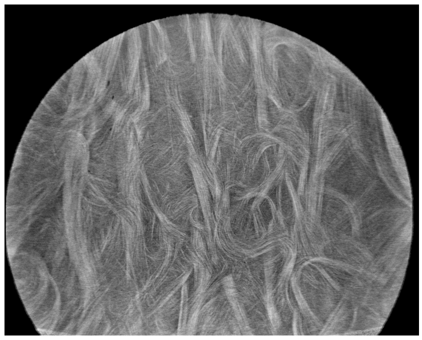</td></tr>
<tr><td>1.68</td><td>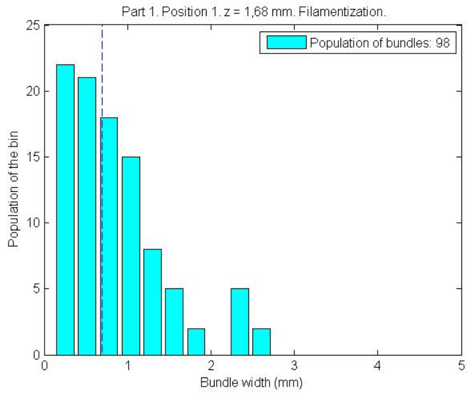
</td><td>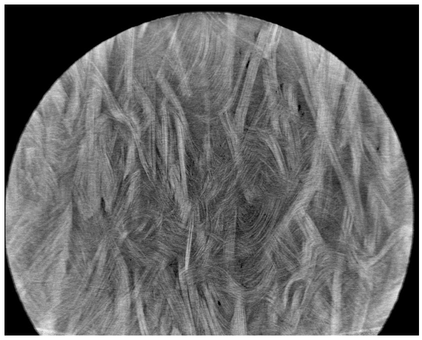</td></tr>
<tr><td>1.47</td><td>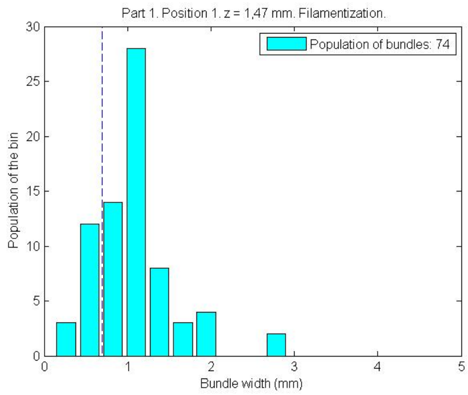
</td><td>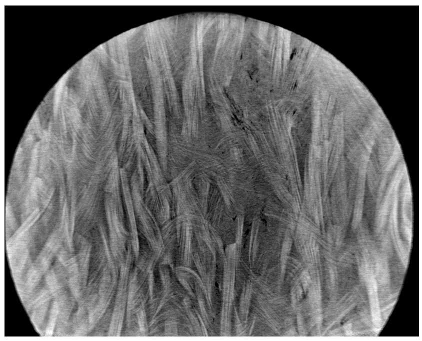</td></tr>
</table>

Table A.1: Distribution of the width of the fibre bundles at the position 1. Part I.

z (mm)	POSITION 1	SCANNED IN-PLANE IMAGE
1.26	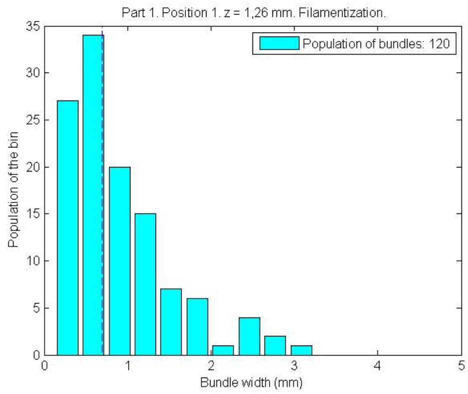	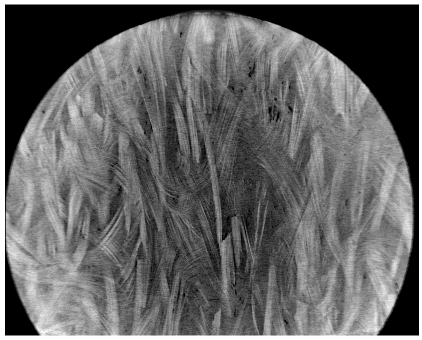
1.05	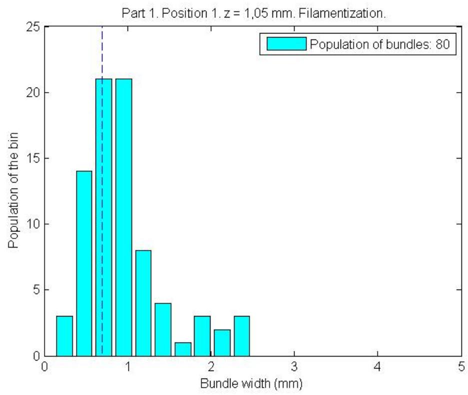	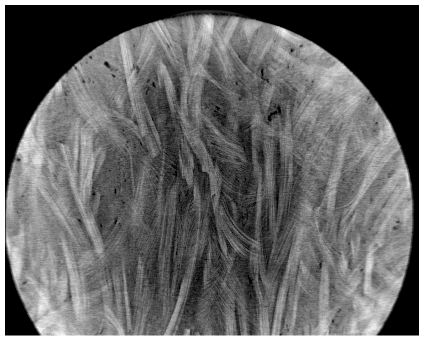
0.84	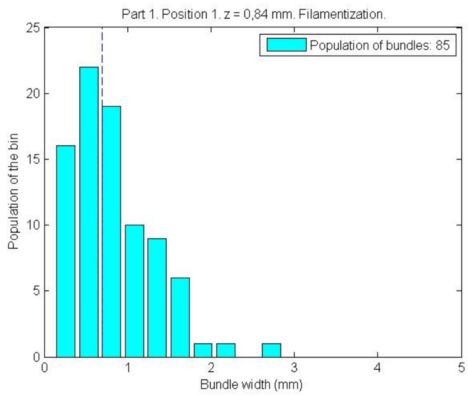	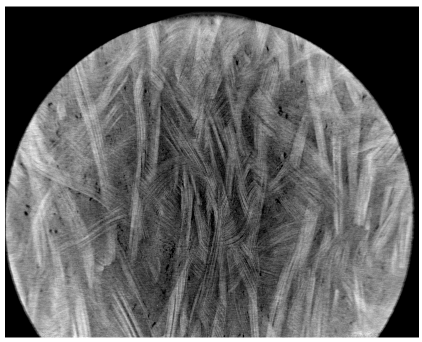

Table A.2: Distribution of the width of the fibre bundles at the position 1. Part II.

z (mm)	POSITION 1	SCANNED IN-PLANE IMAGE
0.63	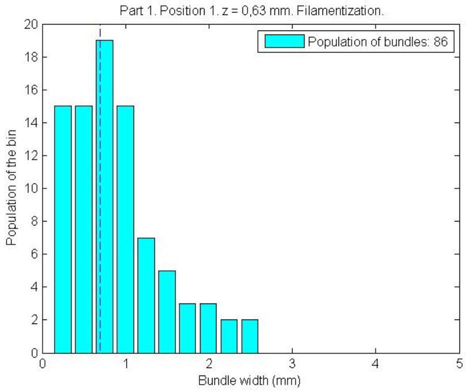	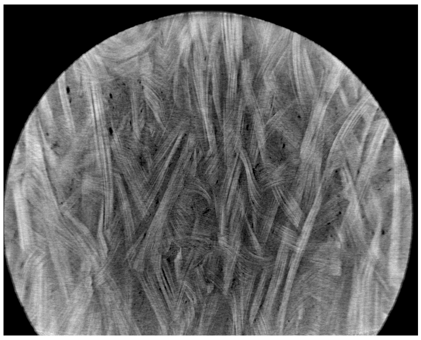
0.42	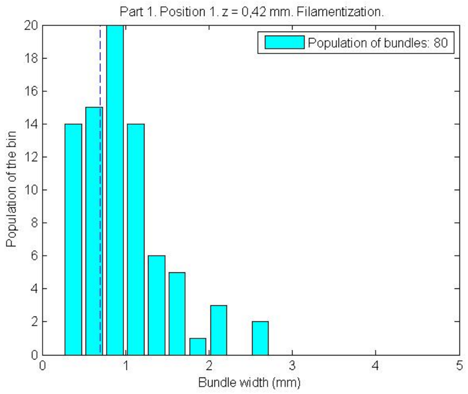	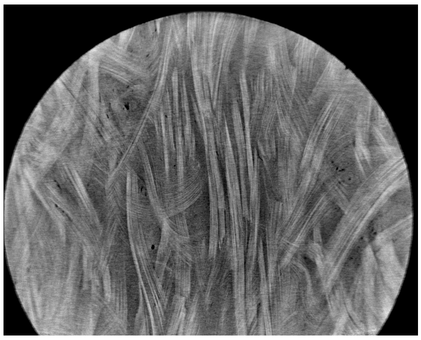
0.21	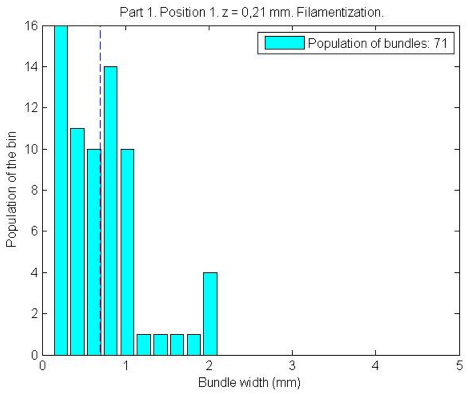	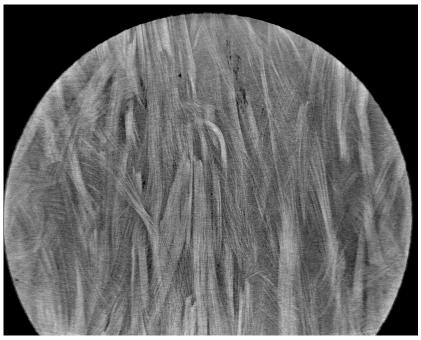

Table A.3: Distribution of the width of the fibre bundles at the position 1. Part III.

z (mm)	POSITION 2	SCANNED IN-PLANE IMAGE
1.89	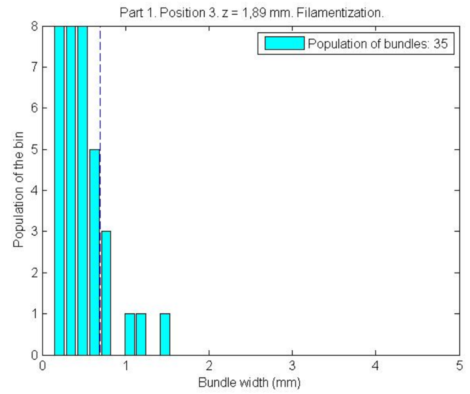	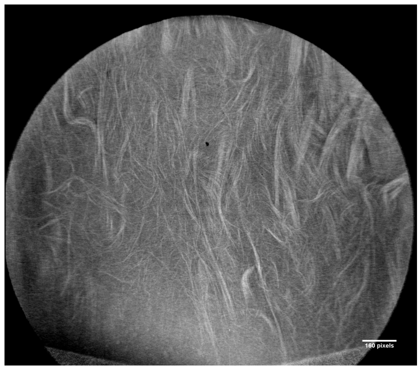
1.68	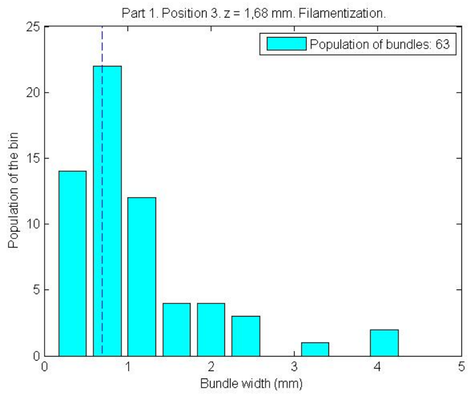	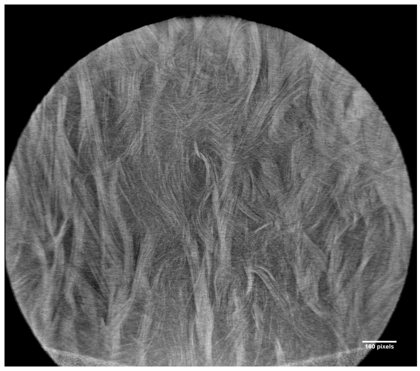
1.47	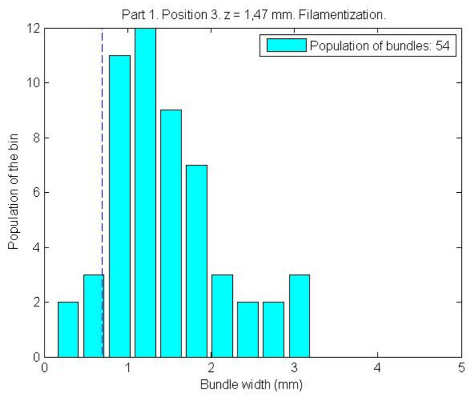	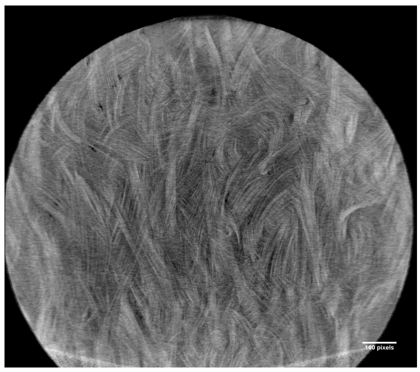

Table A.4: Distribution of the width of the fibre bundles at the position 2. Part I.

<table>
<tr><th>z (mm)</th><th>POSITION 2</th><th>SCANNED IN-PLANE IMAGE</th></tr>
<tr><td>1.26</td><td>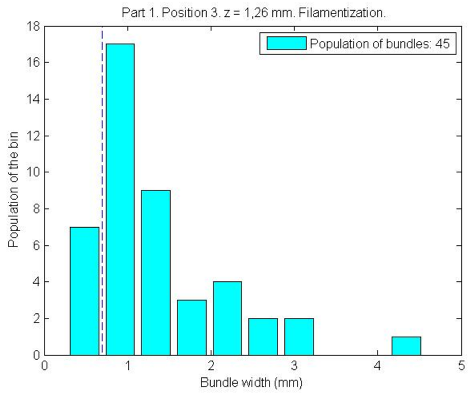
</td><td>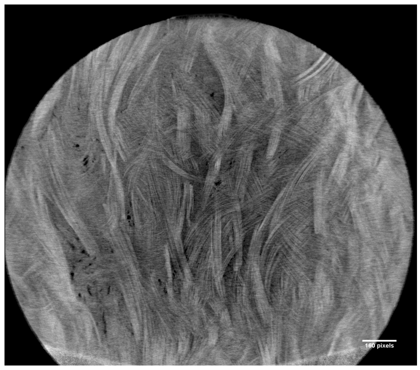</td></tr>
<tr><td>1.05</td><td>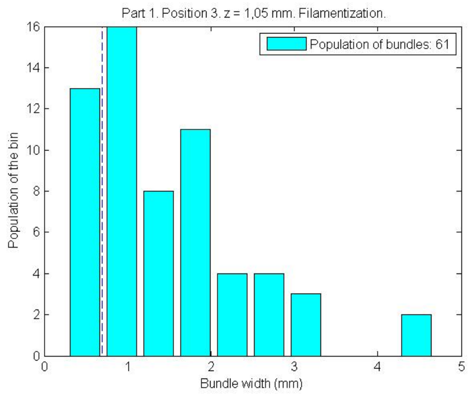
</td><td>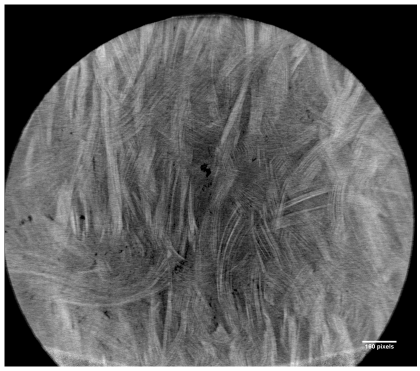</td></tr>
<tr><td>0.84</td><td>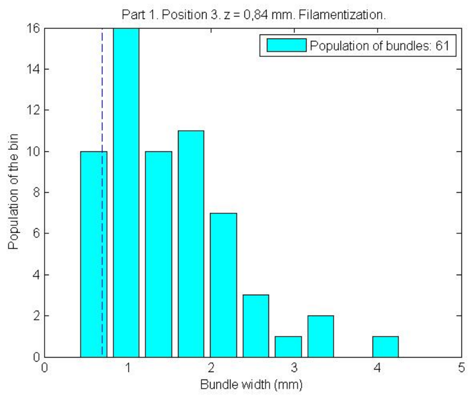
</td><td>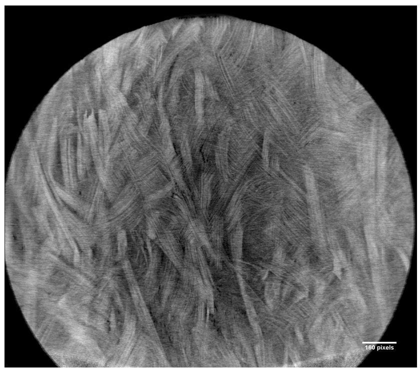</td></tr>
</table>

Table A.5: Distribution of the width of the fibre bundles at the position 2. Part II.

z (mm)	POSITION 2	SCANNED IN-PLANE IMAGE
0.63	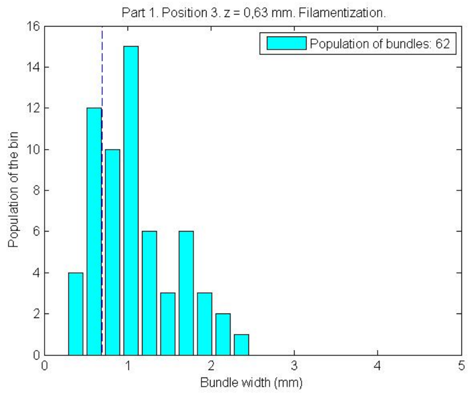	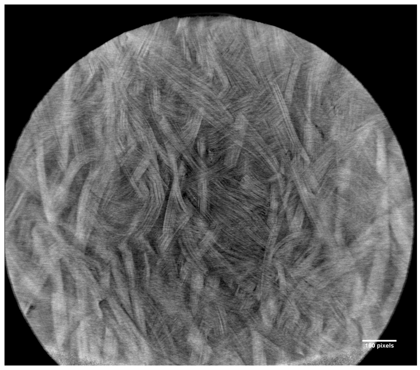
0.42	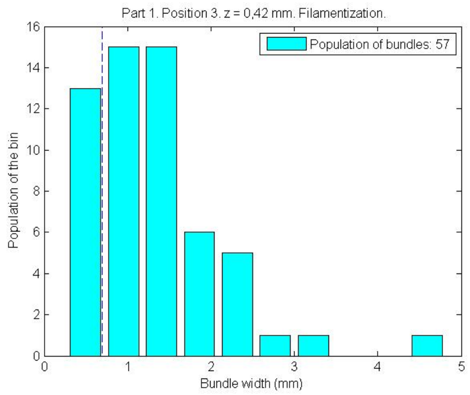	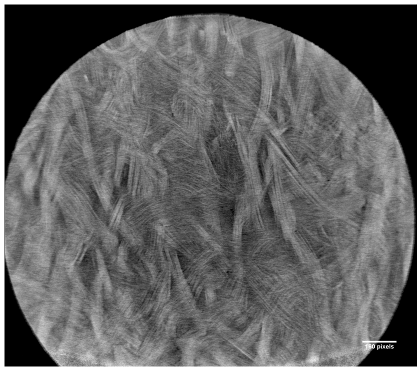
0.21	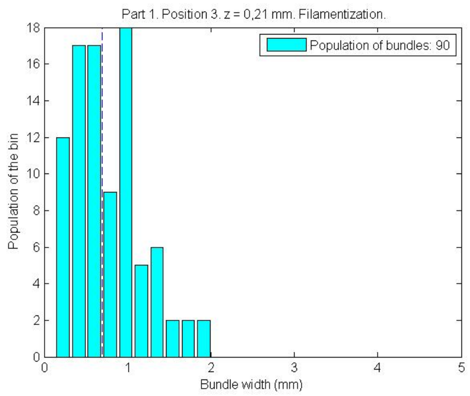	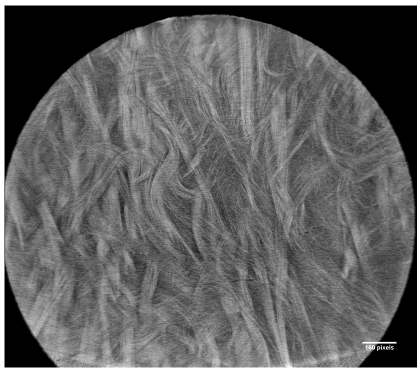

Table A.6: Distribution of the width of the fibre bundles at the position 2. Part III.

z (mm)	POSITION 3	SCANNED IN-PLANE IMAGE
1.89	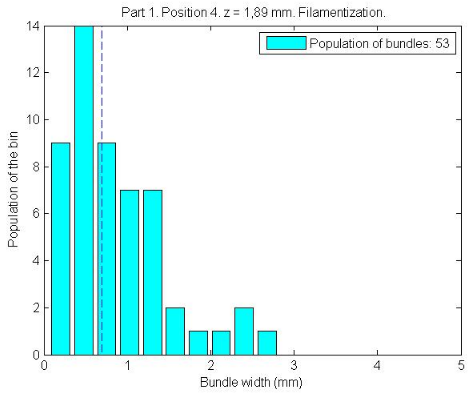	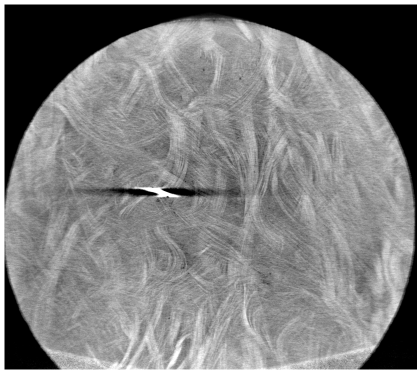
1.68	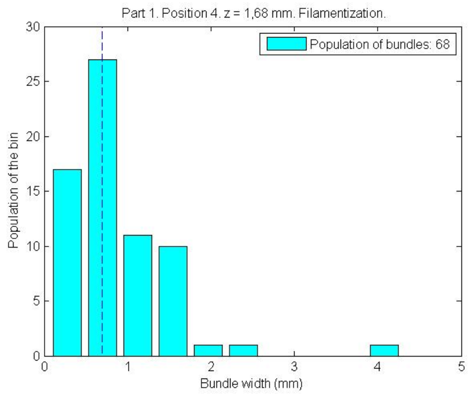	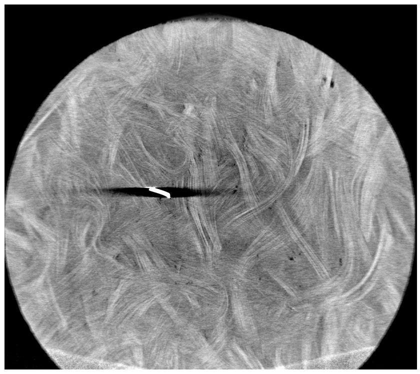
1.47	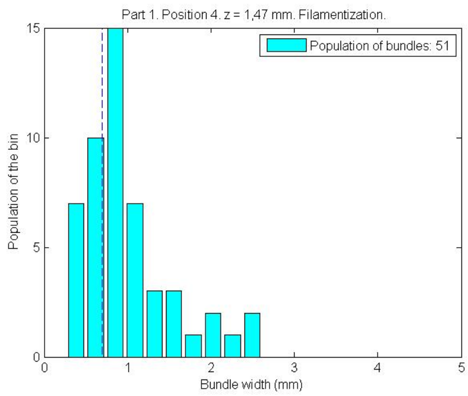	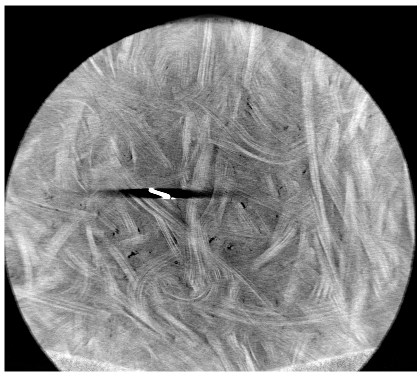

Table A.7: Distribution of the width of the fibre bundles at the position 3. Part I.

z (mm)	POSITION 3	SCANNED IN-PLANE IMAGE
1.26	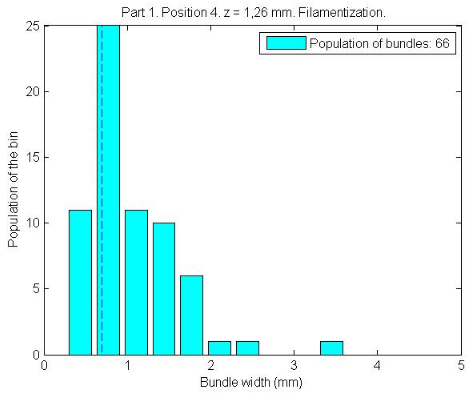	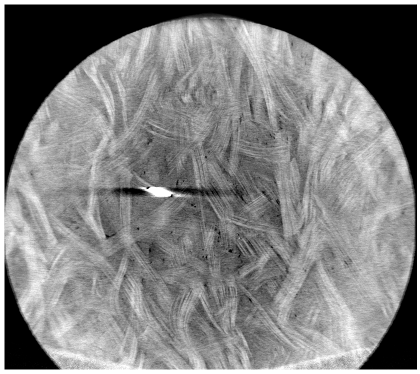
1.05	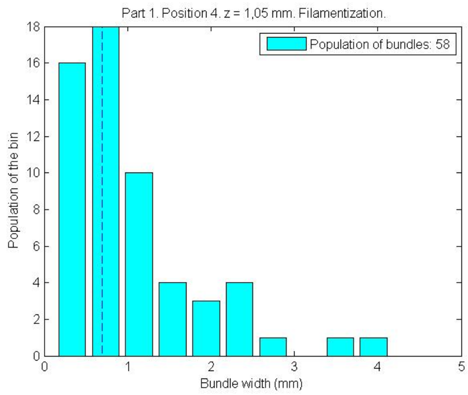	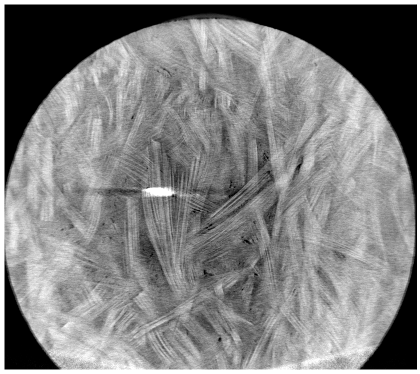
0.84	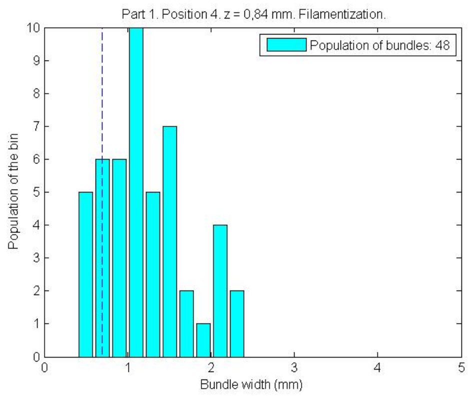	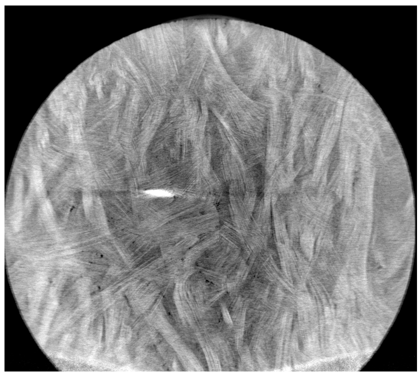

Table A.8: Distribution of the width of the fibre bundles at the position 3. Part II.

z (mm)	POSITION 3	SCANNED IN-PLANE IMAGE
0.63	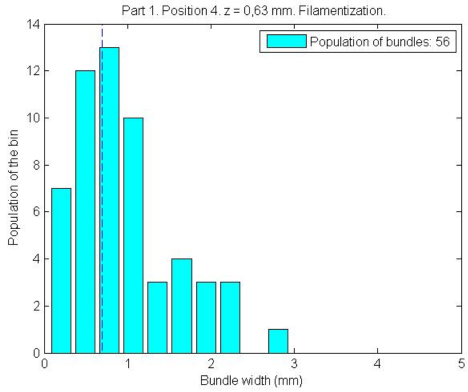	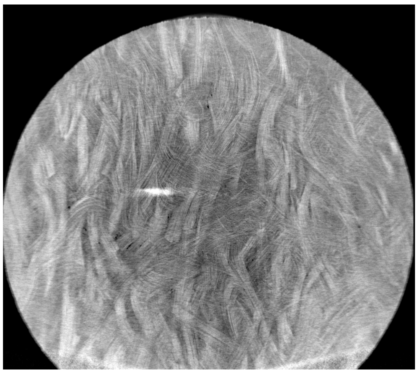
0.42	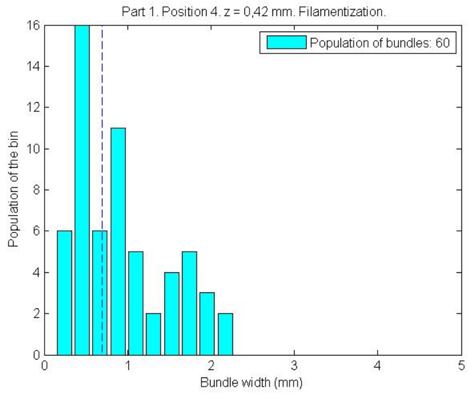	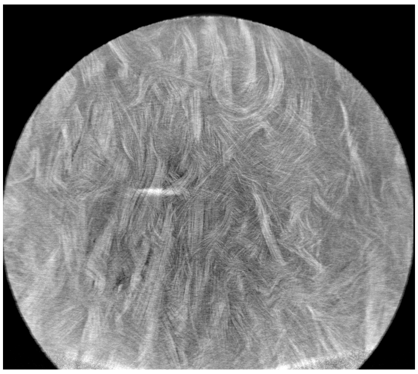
0.21	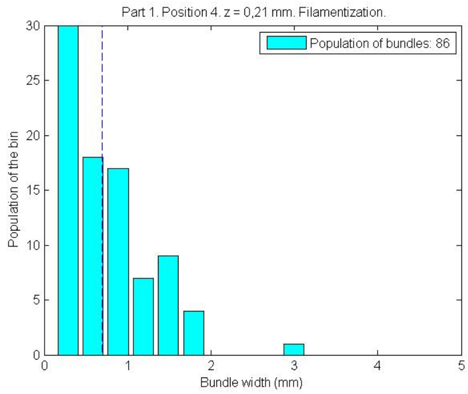	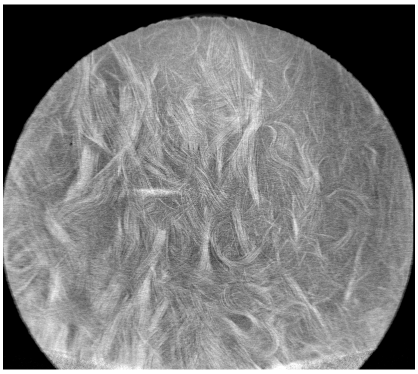

Table A.9: Distribution of the width of the fibre bundles at the position 3. Part III.

Titre : **Analyse descriptive quantitative et modélisation numérique de la microstructure de composite SMC moule par un procédé de compression industriel.**

Mots clés : SMC, moulage par compression, microstructure, modélisation numérique, échelle industrielle

Résumé : Le moulage par compression du SMC est une technologie de mise en œuvre des polymères réactifs renforcés de fibres coupées pour fabriquer une pièce en matériau composite. Le matériau SMC déposé et chauffé dans un moule métallique monté sous presse est mis en mouvement par la compression qu'il subit. Le matériau s'écoule dans la cavité et polymérise pour obtenir la forme finale. L'état final d'orientation des fibres joue un rôle important dans les performances mécaniques de la pièce SMC. L'adaptation de la forme, de la position de la charge SMC dans le moule, ainsi que de la microstructure du matériau dans la pièce finale permet d'optimiser à la fois les propriétés structurelles de la pièce et le procédé de fabrication. Un besoin majeur est de comprendre comment l'écoulement du matériau impacte les caractéristiques mécaniques des pièces moulées.

Dans cette thèse, un modèle numérique 2.5D non isotherme qui inclut les dernières contributions théoriques de la modélisation des écoulements de suspensions a été développé. Les prédictions des modèles sont comparées aux observations expérimentales et aux propriétés mécaniques sur des échantillons à l'échelle du laboratoire, mais aussi sur des pièces SMC produites à l'échelle industrielle. Il est démontré que les modèles théoriques actuels ne peuvent pas saisir certains mécanismes identifiés dans la compression SMC à l'échelle industrielle. Parmi eux, le comportement asymétrique du matériau ainsi que sa très forte transformation au cours de l'écoulement sont mis en évidence et discutés.

Title : **Process-induced microstructure in industrial SMC compression: quantitative descriptive analysis and predictability of a state-of-the-art numerical model.**

Keywords : SMC, compression moulding, microstructure, numerical modeling, industrial-scale

Abstract : Compression moulding of SMC is a processing technology for reactive polymers reinforced with chopped fibres in a composite material. It involves both the flow and deformation of the raw material to transform it into its final shape, thanks of heat and pressure applied to a matched metal moulds mounted under press. The final fibre orientation state plays an important role in the mechanical performance of the SMC part. Adapting the shape and position of SMC charge in the mould, as well the material microstructure in the final part leads to an optimization of both structural properties of the part and manufacturing process. A major need is to understand how the flow affects the structural characteristics of moulded parts.

In this thesis a 2.5D non-isothermal numerical model that includes the latest theoretical contributions to the squeeze flow modeling has been developed. Model predictions are compared with physical observations and mechanical properties on lab-scale specimens but also on industrial-scale SMC parts. It is shown that the current theoretical models cannot captured some mechanisms revealed by the industrial-scale SMC compression. Among them, the asymmetric behaviour of the material as well as its strong transformation during the flow, are highlighted and discussed.